

**KOCAELI UNIVERSITY**  
**GRADUATE SCHOOL OF NATURAL AND APPLIED SCIENCE**

**DEPARTMENT OF MECHATRONICS ENGINEERING**

**DOCTORAL THESIS**

**A NEW MULTIDISCIPLINARY DESIGN APPROACH FOR A  
NOVEL EDDY CURRENT ELECTROMAGNETIC BRAKE**

**MEHMET GÜLEÇ**

**KOCAELI 2019**

KOCAELI UNIVERSITY  
GRADUATE SCHOOL OF NATURAL AND APPLIED SCIENCES

DEPARTMENT OF MECHATRONICS ENGINEERING

DOCTOR OF PHILOSOPHY

IN

MECHATRONICS ENGINEERING

A NEW MULTIDISCIPLINARY DESIGN APPROACH FOR A  
NOVEL EDDY CURRENT ELECTROMAGNETIC BRAKE

MEHMET GÜLEÇ






Assoc.Prof.Dr. Metin AYDIN  
Supervisor, Kocaeli Univ.

Prof.Dr. Zafer BİNGÜL  
Jury member, Kocaeli Univ.

Prof.Dr. Mehmet Timur AYDEMİR  
Jury member, Gazi Univ.

Prof.Dr. Erkan MEŞE  
Jury member, Ege Univ.

Prof.Dr. Hasan KARABAY  
Jury member, Kocaeli Univ.

  
.....  
  
.....  
  
.....  
  
.....  
  
.....

Thesis Defense Date: 12.07.2019

## FOREWORD

I would like to express my gratitude to my mentor Associate Professor Metin AYDIN for his endless guidance and patience during my studies. Working with him over 10 years has been a great pleasure and honor.

I am grateful to my lab mate Mr. Ersin YOLAÇAN for his support and feedbacks during experimental studies. I am also thankful to Mr. Oğuzhan OCAK and Mr. Yücel DEMİR for their friendliness. I also would like to thank all my colleagues in the Department of Mechatronics Engineering in Kocaeli University.

I express my gratitude to Professor Zafer BİNGÜL and Professor Mehmet Timur AYDEMİR for their valuable comments during my studies. I also would like to thank my defense committee Professor Erkan MEŞE and Professor Hasan KARABAY for their time and valuable comments.

I would like to thank The Scientific and Technological Research Council of Turkey – TÜBİTAK and Kocaeli University BAP Unit for funding my research. This thesis was supported partly by TÜBİTAK under the Grants 2130158, 7150639 and 116E603, and Kocaeli University BAP Unit under the Grant 2018/096.

I wish to thank Finnish National Agency for Education for the scholarship they provided to complete a part of my study in Lappeenranta University of Technology (LUT). I am also grateful to Professor Juha PYRHÖNEN, Professor Pia LINDH and Professor Janne NERG for the valuable feedbacks during my study at LUT.

I am very grateful to my parents for their supports through my life. Last but not least, my lovely wife Berna: Thank you for your love, support and everything you have given me. You always have been there when I needed help. This thesis is dedicated to you all.

July – 2019

Mehmet GÜLEÇ

## TABLE OF CONTENTS

FOREWORD .....	i
TABLE OF CONTENTS .....	ii
LIST OF FIGURES .....	iv
LIST OF TABLES .....	ix
LIST OF SYMBOLS AND ABBREVIATIONS .....	x
ÖZET .....	xiv
ABSTRACT .....	xv
INTRODUCTION .....	1
1. ELECTROMAGNETIC BRAKES .....	4
1.1. Friction-based Electromagnetic Brakes .....	6
1.2. Frictionless Electromagnetic Brakes .....	8
1.3. Review of ECBs .....	10
1.4. AF-ECBs .....	17
1.5. PM-ECBs .....	19
1.6. Objectives and Contributions of the Thesis .....	21
2. MODELING AND ANALYSIS OF EDDY CURRENT BRAKES .....	23
2.1. Braking Torque Governing Calculation .....	23
2.2. Influence of Design Parameters on Braking Torque .....	26
2.3. Magnetic Equivalent Circuit Modeling .....	29
2.4. Root-Finding Algorithms for Nonlinear Analysis .....	33
2.4.1. Gauss-Siedel approach .....	33
2.4.2. Newton-Raphson approach .....	34
2.4.3. Relaxation method .....	35
2.5. Modeling and Analysis of an AF-ECB .....	37
2.5.1. Introduction .....	37
2.5.2. Nonlinear MEC modeling .....	39
2.5.3. 3D-FEA .....	43
2.5.4. Prototype, experimental results and comparison .....	46
2.6. Modeling and Analysis of a Radial-Flux PM-ECB .....	52
2.6.1. Introduction .....	52
2.6.2. Nonlinear 2D reluctance network modeling .....	54
2.6.3. 3D-FEA .....	60
2.6.4. Prototype, experimental results and comparison .....	63
2.7. Summary .....	64
3. NOVEL NONLINEAR MULTIDISCIPLINARY DESIGN APPROACH .....	65
3.1. Introduction .....	65
3.2. Novel NMDA .....	67
3.2.1. Nonlinear magnetic modeling .....	69
3.2.2. Nonlinear thermal modeling .....	73
3.2.3. Nonlinear structural modeling .....	77
3.2.4. Results of NMDA .....	79
3.3. Case Studies .....	80
3.3.1. Case-1: 4.5 kW AF-ECB .....	81

3.3.2. Case-2: 10.5 kW AF-ECB .....	85
3.3.3. Investigation of braking time by the proposed NMDA .....	89
3.4. Summary .....	90
4. A NEW AF-PMA-ECB AND ITS DESIGN OPTIMIZATION.....	92
4.1. Introduction .....	92
4.2. The Proposed AF-PMA-ECB.....	93
4.3. Analytical Modeling of the Proposed AF-PMA-ECB .....	94
4.4. Nonlinear Analysis of the Proposed AF-PMA-ECB.....	97
4.5. MO-PSO of the Proposed AF-PMA-ECB .....	101
4.6. 3D-FEA Validation of the Optimized AF-PMA-ECBs .....	104
4.7. Summary .....	108
5. NMDA OF THE NEW AF-PMA-ECB.....	110
5.1. NMDA of the Proposed AF-PMA-ECB .....	110
5.1.1. Nonlinear magnetic modeling .....	111
5.1.2. Nonlinear thermal modeling .....	113
5.1.3. Nonlinear structural modeling .....	115
5.2. Investigation of the Optimized AF-PMA-ECB by NMDA .....	116
5.3. Summary .....	124
6. THE PROTOTYPE AND EXPERIMENTAL WORK.....	125
6.1. Prototype of the optimized AF-PMA-ECB .....	125
6.2. Test Setup .....	125
6.3. Cold-Case Experimental Work .....	126
6.4. Hot-Case Experimental Work .....	128
6.5. Summary .....	136
7. CONCLUSIONS AND RECOMMENDATIONS.....	138
REFERENCES.....	141
PUBLICATIONS AND WORKS.....	149
CURRICULUM VITAE.....	152

## LIST OF FIGURES

Figure 1.1.	The classification of the electromagnetic brakes.....	4
Figure 1.2.	The structure of friction-based electromagnetic brake .....	5
Figure 1.3.	Rotational type frictionless electromagnetic brake .....	6
Figure 1.4.	The structure of magnetically engaged electromagnetic brake .....	7
Figure 1.5.	The structure of spring engaged electromagnetic brake .....	7
Figure 1.6.	The structure of electromagnetic particle brake .....	8
Figure 1.7.	Hysteresis brake structure.....	9
Figure 1.8.	Double-rotor single-stator axial flux eddy current brake .....	10
Figure 1.9.	The classification of ECBs .....	17
Figure 1.10.	AF structures: (a) single-rotor single stator, (b) double-rotor single stator, (c) single-rotor double-stator and (d) multi-rotor multi-stator .....	18
Figure 1.11.	Industrial AF-ECB having double-rotor single-stator .....	19
Figure 1.12.	Typical PM-ECB examples: (a) moving stator and (b) moving brake disc .....	20
Figure 1.13.	Industrial PM-ECB product having outer rotor topology.....	20
Figure 1.14.	Working principles of the magnetarder: (a) braking and (b) nonbraking.....	21
Figure 2.1.	Magnetic flux density variation over one pole pitch .....	26
Figure 2.2.	Braking torque variation as a function of stator teeth-to-pole ratio.....	27
Figure 2.3.	Braking torque variation as a function of conductive region thickness .....	27
Figure 2.4.	Braking torque variation as a function of number of poles .....	28
Figure 2.5.	Braking torque variation as a function of outer radius .....	28
Figure 2.6.	Variation of braking torque characteristic for various conductive materials .....	29
Figure 2.7.	(a) Magnetic circuit with single air gap and (b) MEC modeling.....	30
Figure 2.8.	(a) BH curves and (b) permeability curves of various magnetic materials .....	32
Figure 2.9.	Investigation of various relaxation factors: (a) $\alpha=1$ , (b) $\alpha=0.75$ , (c) $\alpha=0.5$ , (d) $\alpha=0.25$ and (e) $\alpha=0.1$ .....	36
Figure 2.10.	Layout of an AF-ECB in a commercial truck.....	38
Figure 2.11.	3D model and one flux path of AF-ECB.....	39
Figure 2.12.	BH curve of ST37 low carbon steel.....	39
Figure 2.13.	2D symmetry model and the magnetic equivalent circuit modeling of AF-ECB .....	40
Figure 2.14.	The flow chart of Gauss-Siedel approach.....	42
Figure 2.15.	The magnetic flux density in the yoke and the stator teeth obtained by nonlinear magnetic modeling .....	43
Figure 2.16.	Braking torque profile of AF-ECB at rated excitation current.....	43
Figure 2.17.	(a) Full and (b) symmetry 3D-FE models of AF-ECB.....	44

Figure 2.18. Magnetic flux density profiles of AF-ECB for rated excitation current.....	44
Figure 2.19. Braking torque profiles of AF-ECB for various excitation currents .....	45
Figure 2.20. Temperature variation of the disc during braking .....	45
Figure 2.21. (a) Manufactured stator, brake disc and assembled AF-ECB and (b) test setup .....	47
Figure 2.22. Comparison of the braking torque profiles of the AF-ECB obtained from nonlinear magnetic modeling, 3D-FEA and the experiments .....	47
Figure 2.23. Comparison of the temperature rise in the brake disc obtained from thermal 3D-FEA and the experiments .....	48
Figure 2.24. Real-time control system of AF-ECB .....	49
Figure 2.25. Responses of torque control at the speed of 1000 min <sup>-1</sup> : (a) 30 Nm step, (b) 0-30 Nm sine and (c) 0-30 Nm square wave loads .....	50
Figure 2.26. Responses of torque control at the 600-1400 of sine speed (a) 25 Nm step, (b) 0-25 Nm sine and (c) 0-25 Nm square wave loads .....	51
Figure 2.27. Responses of torque control at the 600-1400 min <sup>-1</sup> of triangular speed (a) 25 Nm step, (b) 0-25 Nm sine and (c) 0-25 Nm square wave loads .....	52
Figure 2.28. 3D view of the RF-PM-ECB .....	53
Figure 2.29. 2D reluctance network model of the RF-PM-ECB considering a flat-shaped PM.....	54
Figure 2.30. Comparison of the braking torque profiles obtained from the rectangular-shaped PM geometry and the arc-shaped trapezoid geometry .....	55
Figure 2.31. The flowchart of the nonlinear method for the 2D reluctance network model.....	57
Figure 2.32. 3D Magnetic flux density profile of the reference PM-ECB in the middle of the air gap obtained by the analytical and 3D-FEA considering overhang .....	58
Figure 2.33. 2D-FE symmetry model of the PM-ECB: (a) mesh structure, (b) magnetic flux density profile, and (c) current density profile at the speed of 330 min <sup>-1</sup> .....	59
Figure 2.34. Comparison of the reference and the optimized PM-ECB: (a) normal and (b) tangential components of the magnetic flux density in the air gap with both nonlinear reluctance network modeling and 3D-FEA approaches .....	60
Figure 2.35. FE modeling approaches of PM-ECB: (a) 2D-FEA, (b) 3D-FEA and (c) 3D-FEA with overhang structure .....	61
Figure 2.36. Braking torque profiles obtained from 2D-FEA, 3D-FEA and 3D-FEA with overhang structure .....	62
Figure 2.37. 3D magnetic flux density distribution of PM-ECB.....	62
Figure 2.38. Photo of the prototype .....	63
Figure 2.39. Comparison of the braking torque results obtained from the quasi-3D analytical and 3D-FEA and experimental data.....	63

Figure 3.1.	The novel NMDA. $\sigma$ is the conductivity, $k_{con}$ is the thermal conductivity, $c_p$ is the heat capacity, $\rho_{bd}$ is the volume density of the brake disc .....	67
Figure 3.2.	Variation of nonlinear parameters of ST37: (a) BH curve at room temperature, (b) effect of temperature on peak polarization (c) resistivity, (d) heat capacity, (e) thermal conductivity and (f) temperature factor.....	68
Figure 3.3.	(a) 2D symmetry and (b) reluctance network model of the AF-ECB.....	70
Figure 3.4.	Flowchart of the nonlinear magnetic modeling for AF-ECBs.....	71
Figure 3.5.	(a) The schematic drawing and (b) thermal resistance network of AF-ECB. $T_a$ represents the ambient temperature .....	74
Figure 3.6.	Variation of braking torque and temperature in time .....	79
Figure 3.7.	Influence of slot opening-to-pole pitch ratio on braking torque.....	80
Figure 3.8.	4.5 kW of AF-ECB: (a) FE model with mesh profile, (b) magnetic flux density, (c) thermal and (d) structural profiles.....	81
Figure 3.9.	4.5 kW AF-ECB prototype: (a) Disc, (b) stator with windings, (c) assembled prototype, and (d) test system .....	83
Figure 3.10.	(a) Braking torque and (b) temperature variations for various excitation currents at the speed of $1400 \text{ min}^{-1}$ .....	84
Figure 3.11.	10.5 kW of AF-ECB: (a) FE model with mesh profile, (b) magnetic flux density, (c) thermal and (d) structural profiles.....	85
Figure 3.12.	10.5 kW AF-ECB prototype: (a) Stator core made of solid ST37, (b) stator with windings, (c) assembled prototype and test system .....	87
Figure 3.13.	(a) The braking torque and (b) temperature variations of 10.5 kW AF-ECB at the speed of $1000 \text{ min}^{-1}$ and the excitation current of 20 A.....	88
Figure 3.14.	Temperature variation of (a) Case-1 and (b) Case-2 when the brake disc thickness are doubled at the rated speed and excitation current.....	89
Figure 4.1.	(a) The proposed AF-PMA-ECB topology and (b) its flux paths .....	93
Figure 4.2.	Reduction of 3D AF-PMA-ECB geometry to 2D linearized symmetry models .....	95
Figure 4.3.	The reluctance network model of the proposed AF-PMA-ECB (focusing only symmetry model). The DC excitation coils are not shown for better demonstration.....	96
Figure 4.4.	HB cure of the low carbon steel used in the AF-PMA-ECB.....	97
Figure 4.5.	The flow chart of the Newton-Raphson method .....	99
Figure 4.6.	Flowchart of the particle swarm optimization .....	102
Figure 4.7.	3D-Pareto surface of the Case-1 .....	105
Figure 4.8.	3D-Pareto surface of the (a) Case-2 .....	105
Figure 4.9.	3D-FEA model with mesh structure, and magnetic flux density profile of (a) Case-1 and (b) Case-2 at the time zero PM width.....	106
Figure 4.10.	Transient variation of braking torque for Case-1 and Case-2 obtained from 3D-FEA.....	107
Figure 4.11.	Magnetic flux density variation of Case-1 and Case-2 for one-pole pitch at the steady state.....	108
Figure 4.12.	Current density variation of (a) Case-1 and (b) Case-2.....	109



Figure 5.1.	The revised NMDA. Demagnetization curve of the PM is updated by temperature rise .....	111
Figure 5.2.	Demagnetization curves of the N30UH grade NdFeB .....	111
Figure 5.3.	(a) Symmetry model and (b) the magnetic modeling of the proposed AF-PMA-ECB .....	112
Figure 5.4.	(a) The schematic drawing and (b) heat transfer flow definition and (c) thermal resistance network of the proposed AF-PMA-ECB. $T_a$ represents the ambient temperature .....	114
Figure 5.5.	(a) The 3D model and (b) symmetry model of the optimized AF-PMA-ECB.....	117
Figure 5.6.	Braking torque variation of the optimized AF-PMA-ECB for Scenario-A (1000 $\text{min}^{-1}$ and 7.7 A fixed).....	118
Figure 5.7.	Temperature variation of the brake disc and the PM for Scenario-A (1000 $\text{min}^{-1}$ and 7.7 A fixed).....	118
Figure 5.8.	Braking torque variation of the optimized AF-PMA-ECB for Scenario-B (1000 $\text{min}^{-1}$ and 5.8 A fixed).....	119
Figure 5.9.	Temperature variation of the brake disc and the PM for Scenario-B (1000 $\text{min}^{-1}$ and 5.8 A fixed).....	119
Figure 5.10.	Braking torque variation of the optimized AF-PMA-ECB for Scenario-C (1000 $\text{min}^{-1}$ and 3.5 A fixed).....	120
Figure 5.11.	Temperature variation of the brake disc and the PM for Scenario-C (1000 $\text{min}^{-1}$ and 3.5 A fixed).....	120
Figure 5.12.	Braking torque variation of the optimized AF-PMA-ECB for Scenario-D (500 $\text{min}^{-1}$ and 7.7 A initial).....	121
Figure 5.13.	Temperature variation of the brake disc and the PM for Scenario-D (500 $\text{min}^{-1}$ and 7.7 A initial).....	121
Figure 5.14.	Braking torque variation of the optimized AF-PMA-ECB for Scenario-E (1000 $\text{min}^{-1}$ and 7.7 A initial).....	122
Figure 5.15.	Temperature variation of the brake disc and the PM for Scenario-E (1000 $\text{min}^{-1}$ and 7.7 A initial).....	122
Figure 5.16.	Braking torque variation of the optimized AF-PMA-ECB for Scenario-F (2000 $\text{min}^{-1}$ and 7.7 A initial).....	123
Figure 5.17.	Temperature variation of the brake disc and the PM for Scenario-F (2000 $\text{min}^{-1}$ and 7.7 A initial).....	124
Figure 6.1.	Prototype of the optimized AF-PMA-ECB .....	126
Figure 6.2.	Test setup.....	126
Figure 6.3.	Braking torque comparison at the speed of 500 $\text{min}^{-1}$ .....	127
Figure 6.4.	Braking torque comparison at the rated speed of 1000 $\text{min}^{-1}$ .....	127
Figure 6.5.	Braking torque comparison at the speed of 2000 $\text{min}^{-1}$ .....	128
Figure 6.6.	Braking torque comparison at the speed of 3000 $\text{min}^{-1}$ .....	128
Figure 6.7.	The revised test setup with temperature measuring and capturing tools .....	129
Figure 6.8.	Braking torque variation for Scenario-A (1000 $\text{min}^{-1}$ and 7.7 A fixed) .....	130
Figure 6.9.	Temperature rise of the brake disc and PM for Scenario-A (1000 $\text{min}^{-1}$ and 7.7 A fixed).....	130
Figure 6.10.	Braking torque variation for Scenario-B (1000 $\text{min}^{-1}$ and 5.8 A fixed) .....	131

Figure 6.11. Temperature rise of the brake disc and PM for Scenario-B (1000 min <sup>-1</sup> and 5.8 A fixed).....	131
Figure 6.12. Braking torque variation for Scenario-C (1000 min <sup>-1</sup> and 3.5 A fixed) .....	132
Figure 6.13. Temperature rise of the brake disc and PM for Scenario-C (1000 min <sup>-1</sup> and 3.5 A fixed).....	132
Figure 6.14. Braking torque variation for Scenario-D (500 min <sup>-1</sup> and 7.7 A initial) .....	133
Figure 6.15. Temperature rise of the brake disc and PM for Scenario-D (500 min <sup>-1</sup> and 7.7 A initial).....	133
Figure 6.16. Braking torque variation for Scenario-E (1000 min <sup>-1</sup> and 7.7 A initial) .....	134
Figure 6.17. Temperature rise of the brake disc and PM for Scenario-E (1000 min <sup>-1</sup> and 7.7 A initial).....	134
Figure 6.18. Braking torque variation for Scenario-F (2000 min <sup>-1</sup> and 7.7 A initial) .....	135
Figure 6.19. Temperature rise of the brake disc and PM for Scenario-F (2000 min <sup>-1</sup> and 7.7 A initial).....	135
Figure 6.20. Thermal image of the prototype: (a) in the beginning, (b) after 40 seconds, (c) after 74 seconds and (d) after 120 seconds of braking.....	136

## LIST OF TABLES

Table 2.1. Analogy between the magnetic and the electric circuits.....	30
Table 2.2. Key parameters of single-rotor-single-stator AF-ECB .....	38
Table 2.3. Reference signals for braking torque and speed values .....	50
Table 2.4. Key parameters of the PM-ECB .....	53
Table 2.5. Validation of the quasi-3D analytical modeling .....	59
Table 3.1. Comparison of the results for Case-1 .....	82
Table 3.2. Results for Case-1 .....	84
Table 3.3. The design parameters of Case-2 .....	86
Table 3.4. Comparison of the results for Case-2.....	86
Table 4.1. Key parameters of the proposed AF-PMA-ECB .....	94
Table 4.2. Variable parameters of MO-PSO .....	103
Table 4.3. Cost functions of MO-PSO .....	103
Table 4.4. Optimized Design Parameters.....	104
Table 4.5. Results comparison .....	107
Table 5.1. Temperature characteristics of NdFeB grades .....	113
Table 5.2. Key parameters of the optimized AF-PMA-ECB.....	116
Table 5.3. Studied scenarios of the optimized AF-PMA-ECB .....	117

## LIST OF SYMBOLS AND ABBREVIATIONS

$a$	: Temperature coefficient of remanent induction
$A$	: Cross-sectional area of the surface, ( $m^2$ )
$b$	: Temperature coefficient of intrinsic coercivity
$B$	: Magnetic flux density, (T)
$B_0$	: Magnetic flux density when the speed is zero, (T)
$B_{ave}$	: Average magnetic flux density, (T)
$B_g$	: Air gap magnetic flux density, (T)
$B_n$	: Normal magnetic flux density, (T)
$B_s$	: Saturation level of magnetic flux density, (T)
$B_r$	: Residual flux density, (T)
$B_{rint}$	: Remanent induction at room temperature, (T)
$c_1$	: Personal acceleration coefficient
$c_2$	: Global acceleration coefficient
$c_p$	: Heat capacity, (J/K)
$C$	: Thermal capacitance matrix
$C_{max}$	: Axial flow coefficient, ( $m^3/h$ )
$d$	: Stack length, (m)
$E$	: Electric field, (V/m)
$E_m$	: Modulus of elasticity, (Pa)
$F$	: Force, (N)
$F_r$	: Tangential component of electromagnetic force, (N)
$g$	: Axial air gap length, (m)
$g_f$	: Gravitational attraction force, (N)
$G$	: Thermal conductance matrix
$Gr$	: Grashof number
$h$	: Convection coefficient, ( $Wm^{-2}K^{-1}$ )
$h_{Cu}$	: Copper thickness, (m)
$h_{disc}$	: Disc thickness, (m)
$H$	: Magnetic field, (A/m)
$H_0$	: Applied maximum magnetic field strength, (A/m)
$H_{Cint}$	: Intrinsic coercivity, (A/m)
$i$	: Particle index
$I$	: Current, (A)
$I_m$	: Area moment of inertia of the disc, ( $m^4$ )
$J$	: Current density, ( $A/mm^2$ )
$k$	: Iteration number
$k_a$	: Surface condition modification factor
$k_b$	: Size modification factor
$k_c$	: Load modification factor
$k_{con}$	: Thermal conductivity, ( $Wm^{-1}K^{-1}$ )
$k_d$	: Temperature modification factor,
$k_e$	: Reliability factor
$k_f$	: Miscellaneous-effects modification factor

$k_{ff}$	: Fringing factor
$k_C$	: Carter's factor
$l$	: Length, (m)
$l_c$	: Characteristic length
$l_{oh}$	: Axial overhang length, (m)
$l_{stk}$	: Total axial PM length, (m)
$M$	: Bending moment, (Nm)
$n$	: Factor of safety
$N$	: Turn number
$Nu$	: Nusselt numbers
$P$	: Power loss vector, (W)
$P_{br}$	: Braking power, (W)
$Pr$	: Average Prandtl number
$Q$	: Slot number
$r$	: Radius, (mm)
$r_1$	: Randomly generated number between 0 and 1
$r_2$	: Randomly generated number between 0 and 1
$r_i$	: Inner radius, (m)
$r_o$	: Outer radius, (m)
$r_{PM}$	: Radius of permanent magnet, (m)
$r_{shaft}$	: Shaft radius, (m)
$R$	: Thermal resistance, (K/W)
$R_m$	: Magnetic Reynolds number
$Re$	: Reynolds number
$S$	: Surface area, (m <sup>2</sup> )
$S_{disc}$	: Disc surface, (m <sup>2</sup> )
$Se$	: Endurance limit
$Sut$	: Tensile stress
$S'e$	: Test specimen endurance limit
$S_y$	: Yield stress, (N/m <sup>2</sup> )
$t$	: Time, (s)
$t_1$	: Slot pitch
$T$	: Temperature, (°C)
$Ta$	: Taylor numbers
$T_{br}$	: Braking torque, (Nm)
$v$	: Circumferential speed of the brake disc, (m/s)
$v_c$	: Characteristic velocity
$v_\delta$	: Kinematic viscosity of the air, (m <sup>2</sup> /s)
$V_{disc}$	: Disc volume, (m <sup>3</sup> )
$w$	: Width, (m)
$w_{pole}$	: Pole width, (m)
$w_{st}$	: Teeth width, (m)
$x$	: Particle position
$z$	: Vertical distance away from the neutral axis, (m)
$z_a$	: Transformation variable
$\alpha$	: Relaxation factor
$\alpha_{PM}$	: PM angular width, (Degree)
$\beta$	: Coefficient of cubical expansion
$\Im$	: Current linkage, (Ampere turns)

$\mathfrak{I}_{eq}$	: Equivalent current linkage, (Ampere turns)
$\delta$	: Skin depth, (m)
$\mu_0$	: Vacuum permeability, (H/m)
$\mu_d$	: Brake disc magnetic permeability, (H/m)
$\mu_{PM}$	: Permanent magnet permeability, (H/m)
$\mu_r$	: Magnetic permeability, (H/m)
$\mu_{sb}$	: Yoke magnetic permeability, (H/m)
$\mu_{st}$	: Teeth magnetic permeability, (H/m)
$\xi_{iw}$	: Inertia weight
$\rho$	: Electrical resistivity, ( $\Omega m$ )
$\rho_{bd}$	: Volume density of the brake disc, ( $kg/m^3$ )
$\rho_d$	: Mass density of the air, ( $kg/m^3$ )
$\mathfrak{R}$	: Reluctance, ( $H^{-1}$ )
$\mathfrak{R}_d$	: Brake disc reluctance, ( $H^{-1}$ )
$\mathfrak{R}_{eq}$	: Equivalent reluctance, ( $H^{-1}$ )
$\mathfrak{R}_g$	: Air gap reluctance, ( $H^{-1}$ )
$\mathfrak{R}_{pm}$	: Permanent magnet reluctance, ( $H^{-1}$ )
$\mathfrak{R}_{sb}$	: Yoke reluctance, ( $H^{-1}$ )
$\mathfrak{R}_{sl}$	: Reluctance of core lamination, ( $H^{-1}$ )
$\mathfrak{R}_{st}$	: Teeth reluctance, ( $H^{-1}$ )
$\sigma$	: Electrical conductivity, (S/m)
$\sigma_a$	: Amplitude stress, ( $N/m^2$ )
$\sigma_b$	: Bending stress ( $N/m^2$ )
$\sigma_{Ftan}$	: Tangential stress, ( $N/m^2$ )
$\sigma_m$	: Midrange stress, ( $N/m^2$ )
$\varphi$	: Magnetic flux, (Wb)
$\varphi_{PM}$	: Permanent magnet flux, (Wb)
$\omega$	: Angular speed, ( $sec^{-1}$ )
$\omega_{el}$	: Electrical angular speed, ( $sec^{-1}$ )

## Abbreviations

2D	: 2-Dimensional
3D	: 3-Dimensional
AC	: Alternative Current
AF	: Axial Flux
DC	: Direct Current
EC	: Eddy Current
ECB	: Eddy Current Brake
EMF	: Electromotive Force
FE	: Finite Element
FEA	: Finite Element Analysis
FEM	: Finite Element Method
MEC	: Magnetic Equivalent Circuit
MMF	: Magnetomotive Force
MO	: Multi Objective
NMDA	: Nonlinear Multidisciplinary Design Approach
PI	: Proportional Integral
PM	: Permanent Magnet

PMA : Permanent Magnet Assisted  
PMW : Pulse Width Modulation  
PSO : Particle Swarm Optimization  
RF : Radial Flux



## ÖZGÜN BİR ELEKTROMANYETİK GİRDAP AKIM FRENİ İÇİN YENİ BİR ÇOK DİSİPLİNLİ TASARIM YAKLAŞIMI

### ÖZET

Girdap akım frenleri (GAF) çoğunlukla DC sargılardan meydana gelmektedir ve içinde sürekli mıknatıs (SM) barındıran GAF konvansiyonel frenlere göre daha fazla frenleme moment yoğunluğuna sahip olduğu açıktır. Ne yazık ki, SM-GAF kontrol dezavantajları mevcuttur ve bunlar frenleme momenti kontrol etmek için harici bir sisteme ihtiyaç duyarlar. Bu tez kapsamında yeni bir eksenel akılı (EA) sürekli mıknatıs uyarımlı (SMU) GAF topolojisi bu kontrol dezavantajını elimine etmek için önerilmiştir. Önerilen topolojide, mıknatıslar oluk açıklıklarına yerleştirilmiş ve bu sayede frenleme momenti sadece uyarım akımları ile kontrol edilebilir hale gelmiştir. Önerilen yapıda, mıknatıs boyutları çok büyük bir önem arz etmektedir ki eğer doğru mıknatıs boyutları kullanılmazsa, mıknatıs akısı tam anlamıyla kontrol edilemez ve akı verimsiz bir şekilde kullanılır. Bu yüzden, en iyi mıknatıs ve manyetik sistem boyutları belirlenmelidir. Bu tez çalışması kapsamında, çok amaçlı optimizasyon ile en uygun fren tasarım özelliklerinin belirlenmesi gerçekleştirilmiş ve 3 boyutlu sonlu elemanlar analizleri önerilen tasarımı doğrulamak için gerçekleştirilmiştir.

Frenleme momenti ve sıcaklık artışının zamana göre değişimini belirlemek için yeni bir doğrusal olmayan çok disiplinli tasarım yaklaşımı GAF için önerilmiştir. Yeni önerilen metod doğrusal olmayan analitik manyetik-termal-yapısal modellemeden oluşmakta ve girdap akım frenlerinin çalışma koşullarını bulmayı amaçlamaktadır. Yeni tasarım yaklaşımı 2 farklı eksenel akılı girdap akım frenine ve tabii ki önerilen eksenel akılı sürekli mıknatıs uyarımlı girdap akım frenine uygulanmıştır. Önerilen yeni frenin prototipi üretilmiş ve laboratuvarında test edilmiştir. Soğuk durum ve sıcak durum testleri yapılmış ve deneysel olarak elde edilen sonuçların önerilen yeni metod ile uyum içerisinde olduğu gözlemlenmiştir.

**Anahtar Kelimeler:** Çok Amaçlı Optimizasyon, Doğrusal Olmayan Çok Disiplinli Tasarım, Eksenel Akılı Sürekli Mıknatıs Uyarımlı Girdap Akım Freni, Girdap Akım Freni, Parçacık Sürü Optimizasyonu.



## **A NEW MULTIDISCIPLINARY DESIGN APPROACH FOR A NOVEL EDDY CURRENT ELECTROMAGNETIC BRAKE**

### **ABSTRACT**

Eddy current brakes (ECBs) mostly consist of only DC windings and it is certain that ECBs having permanent magnets offer more braking torque density as to conventional topologies. Unfortunately, permanent magnet ECBs have a control drawbacks that they need an external system to control the braking torque. New axial-flux (AF) permanent magnet assisted (PMA) ECB topology is proposed in this thesis to eliminate the control drawbacks. In the proposed topology, magnets are placed into the slot openings in which the size of the magnet becomes very important. If the correct magnet dimensions are not used, magnet flux cannot be fully controlled and flux will be wasted resulting in less breaking torque. Therefore, optimum magnet size as well as the dimensions of the magnetic materials in the magnetic system should be determined. In this thesis, multiobjective optimization is accomplished to find out the optimum brake design parameters and 3-dimensional finite element analyses are performed to validate the optimized design.

A new nonlinear multidisciplinary design approach is proposed for ECBs to determine the braking torque and temperature variation in time. The new proposed design method consists of nonlinear analytically coupled magnetic-thermal-structural modeling and it aims to find the working limits of ECBs. The new design approach is applied to 2 different AF-ECBs and also the proposed novel AF-PMA-ECB. Prototype of the proposed ECB is manufactured and tested in the laboratory. The cold-case and hot-case experimental studies are performed, and good agreement between the test data and developed model has been achieved.

**Keywords:** Multiobjective Optimization, Nonlinear Multidisciplinary Design, Axial Flux Permanent Magnet Assisted Eddy Current Brake, Eddy Current Brake, Particle Swarm Optimization.

## INTRODUCTION

Energy efficiency and the sustainability are the most essential components of today's engineering world. The design of the innovative products and their application to the industry definitely shape our world and the future. Most of the reports state that the energy requirement in the future can be only supplied by electrical energy. The electric-based products have already taken an important part of our life such as electrical goods, electric machines, generators and electric vehicles etc. It is clear that the energy efficient products will definitely become more critical and the old-technology products will be replaced with the innovative ones in the long run.

Eddy current brakes have been used as braking components in various areas almost for a century. These brakes provide frictionless and environmental-free braking with maintenance free structures. This thesis proposes a new axial flux permanent magnet assisted eddy current brake topology for braking applications. The proposed brake provides higher braking torque density as to conventional eddy current brakes by its unique design. The permanent magnets are used in the brake to increase the braking torque characteristics and to increase the efficiency of the magnetic system. The permanent magnets in the proposed design are placed into slot openings, therefore, the magnet flux can be controlled by excitation current. The thesis contains a detailed review of the electromagnetic brakes particularly eddy current brakes, design and analysis of various eddy current brake topologies, multiobjective optimization and nonlinear multidisciplinary design approach of the new proposed brake. The experimental validation has also been provided in this work.

The first chapter of the thesis deals with the overview of electromagnetic brakes. Working principles, types and classification of the electromagnetic brakes are described. A detailed literature survey of eddy current brakes is provided and the structure of the eddy current brakes is investigated. The contribution of the thesis is presented.

The second chapter investigates the modeling and the analysis of different types of conventional eddy current brakes. Firstly, a brief introduction about the eddy current brake theory and the braking torque calculations are given. The influence of design parameters on braking torque is explained in a practical example for various design cases. Then, an analytical modeling approach based on magnetic equivalent circuit and nonlinear solver methods are described. Lastly, two different eddy current brakes having axial flux and radial flux structures are analytically and numerically modeled, analyzed and experimentally verified.

The third chapter of the thesis presents a novel multidisciplinary design approach for eddy current brakes. The proposed novel design methodology covers actual brake behaviors by considering all of the magnetic, thermal and structural aspects all together. Nonlinear analytical magnetic, thermal and structural models are developed and coupled in the time domain to determine the braking torque and temperature rise. Two different design cases of axial flux eddy current brake are examined by the proposed new design procedure to define the working limits of the brakes.

The fourth chapter of the thesis proposes a new axial flux permanent magnet eddy current brake and its multiobjective optimization. The proposed design structure is firstly explained. Then, particle swarm based multiobjective optimization is developed to find out the optimum brake parameters by nonlinear reluctance network based modeling. Two different design cases are targeted, and the optimized design parameters are found and validated by 3-dimensional finite element analyses.

The fifth chapter of the thesis presents the proposed nonlinear multidisciplinary design approach of the novel axial flux permanent magnet assisted eddy current brake. The proposed design procedure presented in Chapter 3 is revised and applied to one of the optimized cases in Chapter 4. The number of 6 different scenarios are investigated to clarify the braking torque reduction and temperature rise in time for the optimized design.

The last chapter focuses on the prototype manufacturing and the experimental studies. The investigated optimized design in Chapter 5 is manufactured and tested in a special set-up. Cold-case and hot-case experimental studies are performed to compare the results obtained from analytical and numerical approaches. The temperature rise is not

allowed in the cold-case studies that experimental braking torque data are compared with the results obtained from nonlinear magnetic modeling and 3-dimensional finite element analyses. In the hot-case tests, the temperature rise and the braking torque variation in time are measured, and the experimental results are compared with the results obtained from nonlinear multidisciplinary design approach proposed in this thesis.

In summary, the aim and the contribution of the thesis is to propose a new axial flux permanent magnet assisted eddy current brake topology to eliminate the drawbacks of the conventional permanent magnet eddy current brakes and to obtain more braking torque characteristic as to conventional eddy current brakes. In addition, in this thesis a new design procedure for eddy current brakes to obtain the actual brake performance by regarding temperature rise and braking torque variation in time is proposed for the first time in literature for such magnetic systems.

## 1. ELECTROMAGNETIC BRAKES

Due to the rapid developments in the industry, the use of electromagnetic brakes have been dramatically increased in the last decades. Electromagnetic brakes can be implemented into various areas such as aerospace, defense, robotics, medical, traction and even in domestic applications, where the designers are willing to stop or hold or control a moving system. The classification of the electromagnetic brakes is given in Figure 1.1. Electromagnetic brakes can be classified by two main groups: (1) friction-based and (2) frictionless brakes. The friction-based electromagnetic brakes have three subgroups as magnetically engaged, spring engaged and electromagnetic particle brakes. Frictionless electromagnetic brakes consist of hysteresis and eddy current brakes. Whether the topology is friction-based or not, the electromagnetic brakes are used for the security reasons in most applications [1, 2].

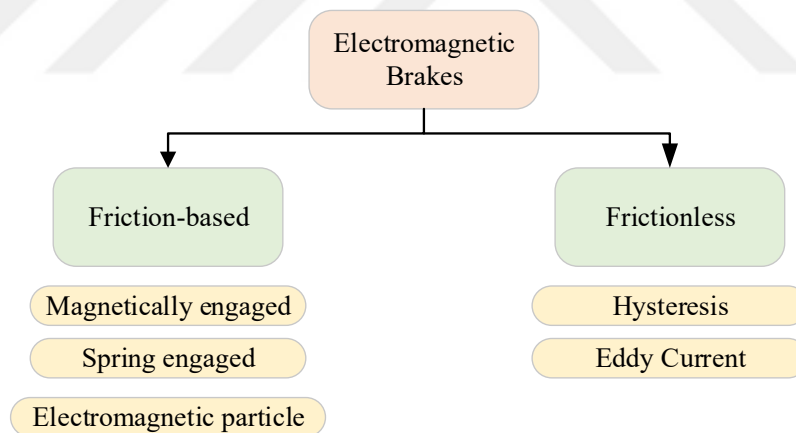


Figure 1.1. The classification of the electromagnetic brakes

The working principle of the friction-based brakes relies on the fundamental electromagnetic laws. Friction-based brakes can be also classified by their working principles as power-off and power-on brakes. To give a brief information, the structure of a power-on type friction-based brake is given in Figure 1.2 [3]. In this topology, coils are wound in a C-core named as field. When the coils are energized, the field pulls a disc called armature, and therefore the braking can be achieved. When the power is off, the springs pushes the armature and an air gap is generated between the

field and the armature. Depending on the application type, the friction material can be used or only armature can be preferred. The details about friction-based brakes will be discussed later in the thesis.

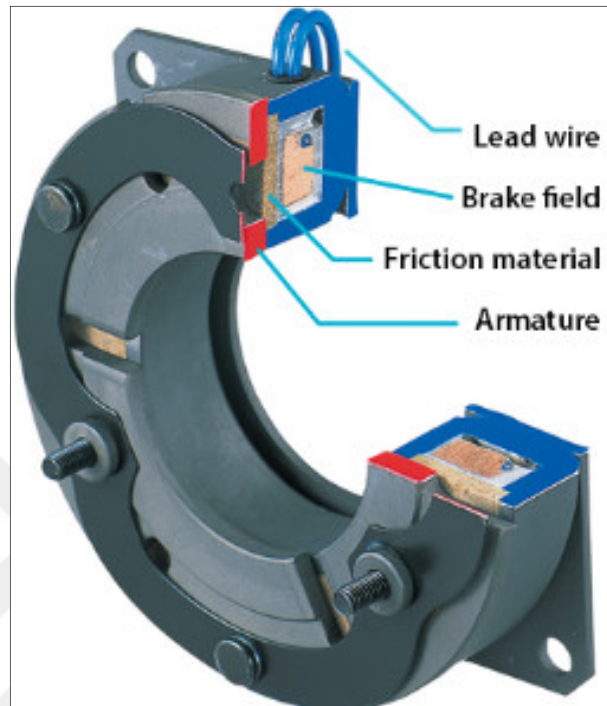


Figure 1.2. The structure of friction-based electromagnetic brake [3]

Frictionless brakes are the other main group of the electromagnetics brakes. The working principle of frictionless brakes can be explained by the eddy current theory. According to Lenz's law, moving magnetic fields in a conductive region create circulating eddy currents and these currents generate reverse magnetic field, which provides retarding. In the literature and the market, linear and rotational type frictionless brakes exist and they are generally used as an auxiliary braking component. A typical example of rotational type frictionless brake is given in Figure 1.3 [4]. This structure is called as hysteresis brake. The brake consists of a conductive cup and a stator, wherein the coils are wounded. The magnetic fields produced by coils are completed their magnetic paths over the conductive cup and during rotating, eddy currents are generated in the disc. Therefore, braking can be achieved. The frictionless brakes will be investigated in detail later.

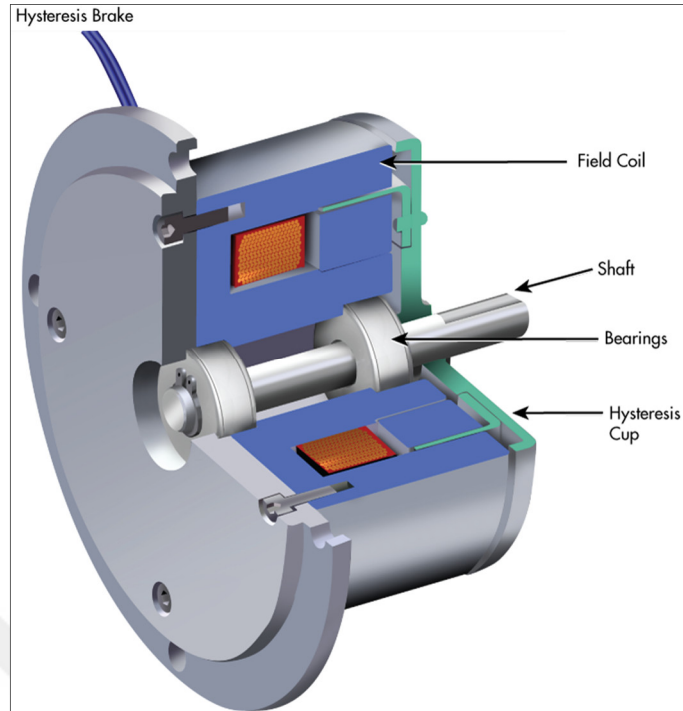


Figure 1.3. Rotational type frictionless electromagnetic brake [4]

### 1.1. Friction-based Electromagnetic Brakes

Friction-based brakes are also known as electromechanical brakes in the industry due to working principles. Electromechanical brakes can be grouped by three categories: (1) magnetically engaged (power-off type), (2) spring engaged (power-on type) and (3) electromagnetic particle brake [5]. The magnetically and the spring engaged electromechanical brakes consist of almost the same components as armature, springs, DC coils and the field whilst electromagnetic particle brake has different structure contrary to the others. Electromagnetic particle brakes do not require springs or armature for braking due to its unique design.

The working operations of magnetically engaged electromagnetic brake is given in Figure 1.4. When the power is on, the field pulls the armature to itself and the brake is engaged. When the power is off, springs are released and they pull the armature and an air gap is occurred between the armature and the field. Therefore, the brake is disengaged and rotating is possible.

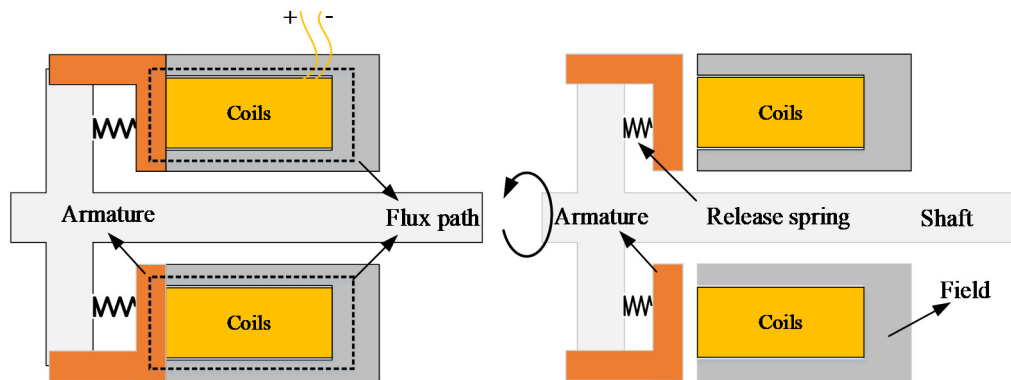


Figure 1.4. The structure of magnetically engaged electromagnetic brake

The working operations of spring engaged electromagnetic brake is given in Figure 1.5. When the power is on, the field pulls the armature itself and the brake is disengaged with the output plate. During this operation, the springs are tightened and the rotating is possible. When the power is off, the springs are released and they push the armature to the output plate. So, the armature is connected with the output plate and the brake is disengaged.

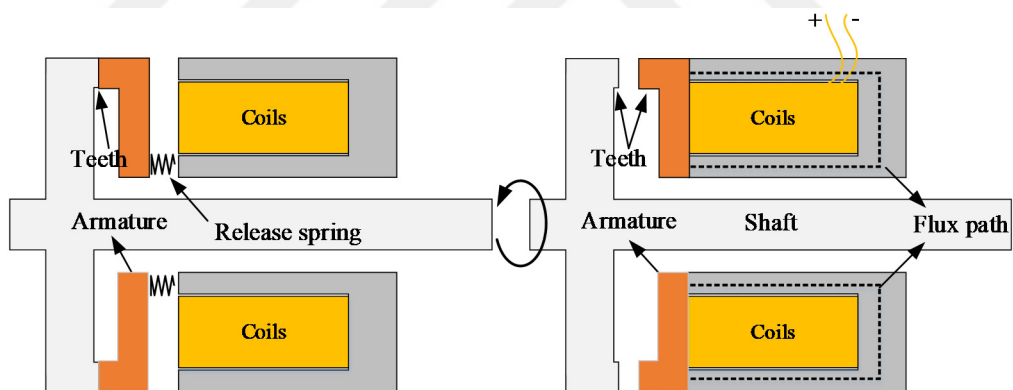


Figure 1.5. The structure of spring engaged electromagnetic brake

Lastly, the working operations of electromagnetic particle brake is given in Figure 1.6. The electromagnetic particle brake has different structure from the above mentioned electromagnetic brakes. Contrary to conventional electromechanical brakes, electromagnetic particle brake do not require any springs or armature. The particles, which have ferromagnetic properties, are located in the air gap or a special cavity that they are free to flow until the coils are energized. When the power is on, the magnetic fields attract the particles and force them to bind. The rotor tries to rotate through the particles therefore slowing and stopping can be obtained. The most important benefit



of electromagnetic particle brake is that the braking can be fully controlled by altering the excitation current contrary to other electromechanical brakes.

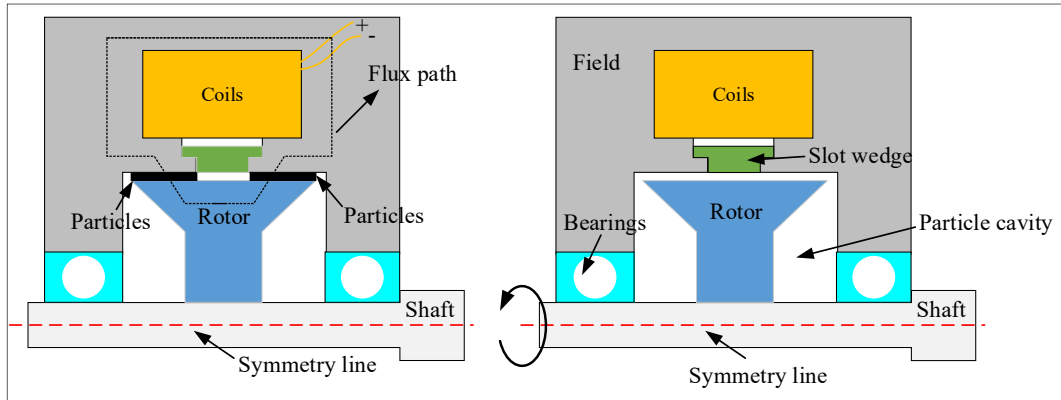


Figure 1.6. The structure of electromagnetic particle brake

As a conclusion, magnetically engaged and electromagnetic particle brakes can stop the rotating plate when the coils are energized, and contrary to these, spring engaged brake allow the plate to rotate when the coils are energized. The placement of the springs with respect to the armature determines the electromechanical brake type by means of power-on or power-off. Magnetically and spring engaged brakes can only stop and hold the rotating plate while electromagnetic particle brake can also slow the rotating plate.

## 1.2. Frictionless Electromagnetic Brakes

Frictionless electromagnetic brakes provide long term and maintenance free working conditions compared to friction-based brakes. Due to the unique structure, there is no mechanical contact between the fixed and the rotating components. Therefore, nearly infinite working life can be achieved with environment friendly structures. The working principle of frictionless brakes relies on Lenz's law. Briefly, according to Lenz's law, variable magnetic fields create circulating electric currents in a conductive component, which are called as eddy currents. These currents create opposite magnetic fields that provide retarding or braking based on Faraday's law of induction.

Frictionless electromagnetic brakes can be categorized by two main design groups. These are named as hysteresis and eddy current brakes. Contrary to electro mechanical brakes, hysteresis and eddy current brakes are not effective in very low speeds and

they cannot hold the rotating components. However, they can provide high and smooth braking torque for the speeds between  $100\text{-}10000\text{ min}^{-1}$  [6].

A typical hysteresis brake structure is given in Figure 1.7. Hysteresis brakes consist of coils, field and a rotating hysteresis cup, which is made of conductive material as copper or aluminum. There is an air gap between the field and the hysteresis cup that can rotate in the field. When the coils are energized, flux completes its path over the hysteresis cup, and the braking torque can be observed without no mechanical contact. It has to be reminded that the braking torque cannot be obtained at very low speeds. In addition, a great amount of energy is generated in the cup during braking so that most of the industrial products have cooling systems and the manufacturers determine the maximum braking time.

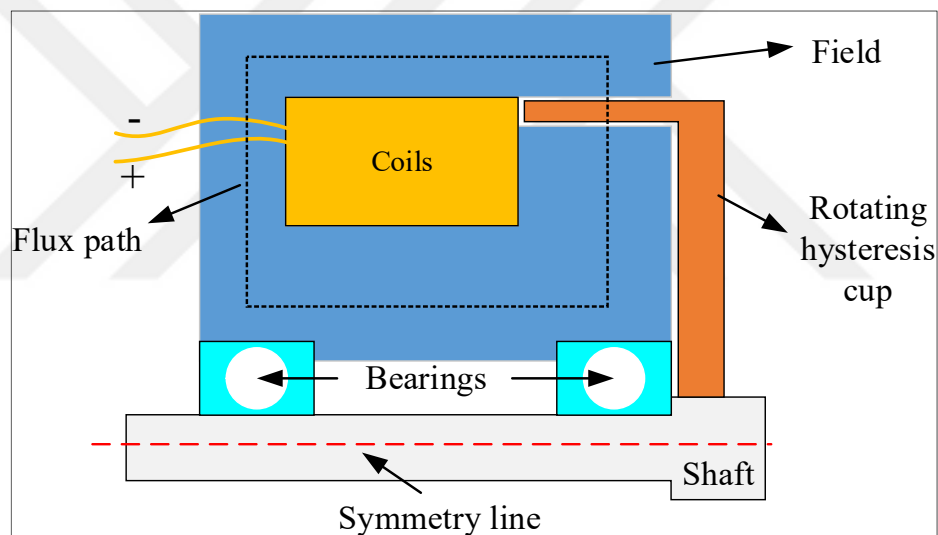


Figure 1.7. Hysteresis brake structure

The second frictionless electromagnetic brake option is called eddy current brakes. The structure of a double-rotor single-stator eddy current brake is given in Figure 1.8. Eddy current brakes consists of stator, coils and rotor (brake disc). Rotor is usually called as brake disc in axial flux topologies. When the coils are energized, flux completes its path over the brake disc and the braking can be attained. It has to be stated that the brake disc material has a great influence on braking torque characteristic in eddy current brakes. The influence of brake disc material will be covered later.

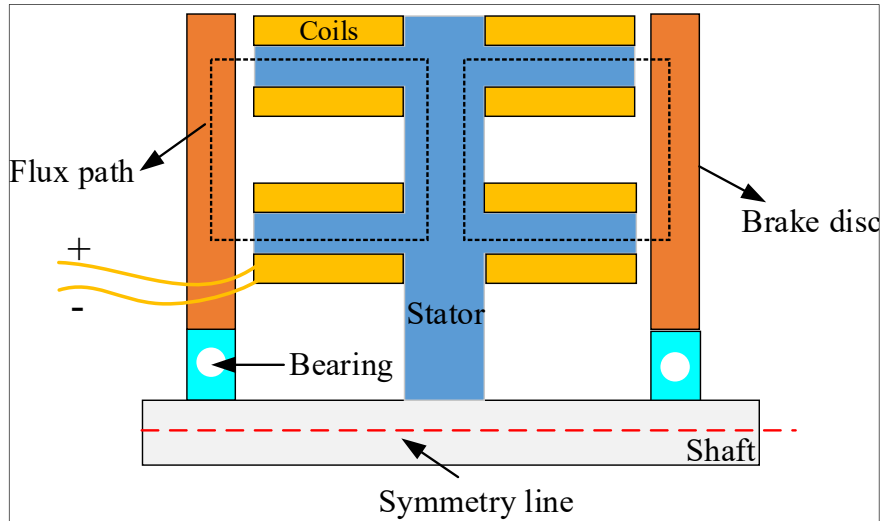


Figure 1.8. Double-rotor single-stator axial flux eddy current brake

As conclusion, the main difference between hysteresis and eddy current brakes is based on their structures and operating principles. In hysteresis brakes, a rotating cup, which is settled into the field, provides braking torque. The design structure is almost same for all types of hysteresis brakes. Contrary to hysteresis brakes, eddy current brakes can have numerous design alternatives. The structure of eddy current brakes is similar to electric machines. They can have axial- or radial-flux topologies, and rotational or linear type design structures. In addition, based on the placement of the brake disc, thermal forces in eddy current brakes can be removed more easily than that of hysteresis brakes. Therefore, eddy current brakes get more attention for high power density applications as opposed to conventional EMBs [4-6].

### 1.3. Review of ECBs

Eddy current brakes (ECBs) have been used in numerous applications over a century. One of the first studies of ECBs was reported in the beginning of 20<sup>th</sup> century by Morris and Lister [7]. The authors proposed that ECBs were more suitable for motor testing than the other mechanical and fluid based equipment. They also focused on testing problems of the motors and clearly explained the advantages of the ECBs. They performed several experimental studies related to the dynamic behaviors of ECB for various ampere-turns per coil and rotational speeds, and provided practical comparison.

Smythe presented a study related to analytical modeling of eddy currents in a rotating disc in 1942 [9]. The author used Maxwell-Ampere law equation to demonstrate the currents flow in a conductive part, and combined the equations with Maxwell-Faraday's law and Gauss' law to obtain the induced currents in the disc. The study was so interesting that the author concluded that the eddy currents can cause a reduction of the magnetic fields on the electromagnets that results in an irregularity in the eddy current distribution.

The eddy current phenomena in ferromagnetic materials was investigated by McConnell [10] in 1954. The paper dealt with the saturation effect in ferromagnetic materials and investigation of linear and nonlinear limiting theories focusing on induced eddy currents. The author provided detailed comparison of classical and proposed theories for various case studies. In addition, proposed theory was tested for an inductive heating application.

Davies reported an experimental and theoretical study of eddy current brakes and couplings [11] in 1963. The steady-state theory of the eddy current machines particularly eddy current couplings with homogenous ferromagnetic disc was proposed in this study. The author explained the relations between the flux, torque and speed, and provided well-covered information about the effect of the armature reaction by analytical estimation and experimental data. The measured flux density distribution in the brake disc as a function of skin depth was also provided in the study.

ECB was analyzed with the definition of braking torque characteristic by Gonen and Stricker in 1965 [12]. The authors reported that the braking torque was proportional to DC magnetization current and the authors' proposed theory was validated by experimental data. The authors also provided information about the effect of geometric parameters on the braking torque and selection of ECB as a test equipment, which can be used for testing motor at high speed ranges.

Contrary to all above studies, Schieber investigated braking torque on a rotating nonmagnetic metal disc by DC magnetic field in 1973 [13]. The object of the paper was to present a general calculation method for ECBs. He used magnetic analogy and direct integration of the relevant differential equation to describe the theory. An extended general approach was presented and validated by experimental work.

Ripper and Endean reported a study related to torque measurements on a thick rotating copper disc in 1974 [14]. In this study, contrary to previous works, fields of permanent magnets (PM) were used in the ECB system instead of coils. Two different PM-ECB designs were used in practice to obtain various braking torque characteristics and the tests were performed at the speed range of 50-1800  $\text{min}^{-1}$ . The contribution of the author was to clarify the braking torque characteristic by low and high magnetic Reynolds number asymptote similar to induction motor characteristics.

In 1975, Schieber also studied optimal dimensions of a single rectangular electromagnet for braking purposes [15]. Two different conductive metal sheets were studied in order to highlight the rectangular shaped pole dimensions over the material cost. The author investigated various length-to-width ratios of rectangular-shaped pole to reduce the material cost for a defined braking force. The study concluded with some practical information about the determinations of rectangular pole dimensions for a specific braking range.

Singh presented a study related to generalized theory of braking torque for ECBs, which has nonmagnetic thick rotating disc in 1977 [16]. He clearly described the lack of modeling assumption of the previously published papers and proposed a new model. The used ECB in the paper had a single-rotor double-stator axial flux topology with electromagnets. The author aimed to present a general theory related to braking torque characteristic of ECB particularly for very high speeds. He combined the skin effects and transverse edge effects and obtained a quasi-3D equivalent modeling for such magnetic systems.

In the same year with Singh work, Venkatartnam and Ramachandra studied analysis of ECBs with nonmagnetic rotors by conformal mapping method [17]. The authors presented z, t and W planes of conformal mapping to calculate the air gap field in 2D model and then clarify the normalized force/speed and flux/speed characteristics of the ECBs. To validate the mathematical expressions, resistivity factors for different ECB configurations were given and validated by experimental studies.

One of the first work related to finite element analysis (FEA) of ECB was studied by Bigeon et al. in 1983 [18]. Analysis based on nonlinear finite element (FE) computation was investigated to describe the eddy current distribution in the ECB by

the velocity vector. The authors used upwind triangular FE mesh elements in their model with integration mesh points connecting of velocity direction. The flux lines of ECB obtained from FEA at various speeds were also provided in the paper and experimental data were compared with the FEA results.

In 1985, Zhi-ming et al. presented FE solution of transient axisymmetric nonlinear eddy current field problems [19]. The transient diffusion equation was discretized by Galorkin projective and implicit forward differential schema in time. The authors used Newton-Raphson nonlinear solving approach and clearly explained the flow diagram of the iterative procedure with the optimization of an accelerating converging factor, which has a great effect on the speed and the stability of the solution. The authors reported that the proposed method was suitable for arbitrary varying source voltage.

Wouterse reported a research paper in 1991 related to critical torque and speed of ECB with widely separated soft iron pole [20]. The author performed some high speed experimental tests to obtain a theoretical model and to compare results with the well-known ECB modeling techniques. The proposed theory by the authors determines the critical braking torque and speed proportional to the air gap. He found out that the proposed equations could predict the critical braking torque and speed better than previously proposed approaches.

In 1994, Nehl et al. studied nonlinear 2D finite element modeling (FEM) of PM ECB [21]. An axial-flux (AF) single-rotor single-stator PM-ECB topology with 16 poles was investigated in the study. The authors made a comparison between the results obtained from Maxwell stress tensor and the eddy current loss by braking torque calculation. The investigated PM-ECB was simulated up to  $10000 \text{ min}^{-1}$  and tested up to  $4000 \text{ min}^{-1}$ . All 2D-FEA results agreed well with the experimental data. Authors suggested some design criteria for various ECB configurations.

Albertz et al. studied calculation of 3D nonlinear eddy current (EC) field in moving conductors and its application to linear ECB systems, which are used in the magnetic levitation systems and high speed trains in 1996 [22]. The tetrahedral mesh elements were applied to consider the rectangular shaped geometry and only one-pole was taken into consideration to avoid the heavily computation efforts. The rough mesh and fine

mesh cases were also employed and the results obtained from train and test setup were provided.

Lequense et al reported a study related to EC machines with PMs and solid rotors in 1997 [23]. The authors investigated various types of brake disc constructions, with a single layer iron, aluminum or copper and with a composite layer or iron/aluminum or iron/copper and compared the braking torque characteristics of these configurations. The authors used 2D-FEA and compared the numerical results with experimental data. In addition, the authors examined the optimization of the PM-ECB by parametric studies with changing the number of poles and magnet thickness. The study was proposed that PM-ECB with solid-rotor was better suited to application where the linear torque-speed characteristic was needed.

In 1999, Muramatsu et al studied 3D EC analysis in moving conductor of PM type of retarder using moving coordinate system [24]. The authors used different approaches from the above studies that contrary to time-step analysis, FEA were performed at DC steady state and the results were obtained directly without time iteration by summation of  $F_r \cdot r$  ( $F_r$ : tangential component of electromagnetic force and  $r$ : radius). The authors presented experimental studies up to  $5000 \text{ min}^{-1}$  and validated the proposed 3D-FEA approach with experimental data.

Jang et al studied the application of linear halbach array to eddy current rail brake system in 2001 [25]. Halbach array and segmented magnet-iron array types of linear PM-ECBs were investigated by 2D-FEAs with Galerkin FEM approach and the authors clarified the benefits of the halbach array linear PM-ECB compared to segmented brake. Extended version of [25] was reported by Jang and Lee in 2003 [26]. The authors investigated PM linear ECBs with different magnetization patterns by analytical field solution. The authors proposed that halbach magnetized ECB had higher braking force characteristic as opposed to vertically and horizontally magnetized ECB.

In 2004, Anwar studied a parametric model of an ECB for automotive braking applications [27]. The author proposed a parameter estimation scheme to identify the model parameters. The steady-state torque-speed characteristic of ECB was captured by parametric model and two-stage estimation procedure was performed to define the

coefficients. The author presented that no look-up table was needed once the model parameters has been identified.

Gay and Ehsani investigated parametric analysis of ECB performance by 3D-FEA in 2006 [28]. Single-rotor single-stator axial flux PM-ECB was studied in the paper and the influence of design parameters of inner and outer radius, disc thickness, air gap width, brake conductivity, ferromagnetic properties, and magnet properties on braking torque and critical speed was clarified by 3D-FEAs.

In 2008, Gosline and Hayward published a study related to design, identification and control of an ECB for haptic interfaces [29]. Above all studies, for the first time, the authors applied an ECB to unconventional field. Generally, ECBs have been implemented into traction or testing applications for braking purposes. The authors used ECB as a viscous damper for haptic interfaces that linear and programmable physical damping at high frequency can be obtained by ECBs.

Ye et al studied design and performance of a water-cooled PM-ECB for heavy vehicles in 2011 [30]. The author proposed a novel outer rotor RF-PM-ECB topology that uses water cooling to improve the braking torque capability. Magneto-thermal FEAs were carried out to describe the performance of the authors' proposed topology and clarify the benefits of the structure. The authors also provided an experimental comparison of the conventional air cooling and the water cooling methods.

Shin et al investigated analytical torque calculations and experimental testing of AF-PM-ECB in 2013 [31]. The authors used an analytical field calculation by a space harmonic method to compute the investigated brake performances. The investigated brake had AF topology with PMs in the stator and the braking torque can be controlled by a moving component that the air gap length is adjusted by the moving component. The experimental results obtained at low speed ranges were also provided and agreed well with the FEA and analytical results.

Karakoc et al studied optimized braking torque generation capacity of an ECB with the application of time-varying magnetic fields in 2014 [32]. The authors investigated an optimized ECB, which can retard at very low speed with an AC field with varying frequency. The study was proposed a feasible solution to one of the most important



drawback of insufficient braking torque generation of ECBs at low speeds by applying the AC fields on optimized multi pole projection areas. The authors presented that significant improvement in the braking torque can be observed with the proposed ECB at very low speeds.

In 2014, Kou et al studied analysis and design of hybrid excitation linear ECB [33]. The authors proposed a hybrid excitation linear ECB, which consists of coils and PMs. Analytical field solution was performed and the results obtained by analytical, FEA and experimental agreed well. The authors proposed that higher force density, low loss and high reliability can be obtained by hybrid excitation ECB.

Yazdanpanah and Mirsalim investigated a hybrid electromagnetic brake in 2015 [34]. The investigated brake had an axial flux topology and consisted of two kind of electric machines as regenerative brake and ECB. The study proposed a combined topology. When the ECB isn't working, the energy can be observed by regenerative braking. The investigated proposed topology has a great potential to be implemented into the electric vehicles.

In 2015, Lubin and Rezzoug studied 3D analytical model for AF-PM-ECB under steady-state conditions [35]. The authors used a magnetic scalar potential formulation to solve 3D boundary value problem. The 3D analytical flux density distribution, induced currents, braking torque and axial force can be predicted by the proposed model. The authors showed that the proposed analytical model can determined the brake performances in a few milliseconds, whereas it took several hours in 3D-FEA.

Ye et al investigated multi field coupling analysis and demagnetization experiment of permanent magnet retarder for heavy vehicles in 2018 [36]. The authors used a double-rotor single-stator AF-PM-ECB topology and controlled the braking torque by an external mechanism. The electromagnetic-thermal fluid multiphysics coupling model by FEA was performed to determine the braking torque and temperature variation in time.

Jin et al studied thermal analysis of a hybrid excitation linear ECB in 2019 [37]. The authors proposed a thermal network model of the ECB and before the analytical thermal network model, they simulated computational fluid dynamic analysis to obtain

the thermal parameters. Later, the authors used these parameters in thermal network model. The temperature variation in time was investigated by analytical approach and experimental studies.

As a conclusion, various types of ECBs have been studied for a very long time and used in different industrial applications. As to above mentioned studies, ECBs can be classified by several manners similar to the electric machines. The classification schema of ECBs is given in Figure 1.9. They can be categorized by three main categories: (1) flux direction, (2) movement type and (3) source of magnetic field. According to flux direction, ECBs can have axial-flux or radial-flux topologies. Most ECBs have axial-flux topologies due to high braking torque density ratios and cooling benefits in practical applications. As to movement type, ECBs can be implemented into rotating or linear motion applications. Rotational as well as linear type ECBs are both used in the industrial applications such as traction. Related to magnetic field source, ECBs could have an electrical excitation or PM or hybrid type (electrical excitation and PM) magnetic field. It has to be born in mind that most ECBs in the market are only working with electrical excitation. However, PM-ECBs and hybrid type ECBs offer feasible and high efficiency design alternatives compared to conventional ones due to rapid and steady-state growth in the industry.

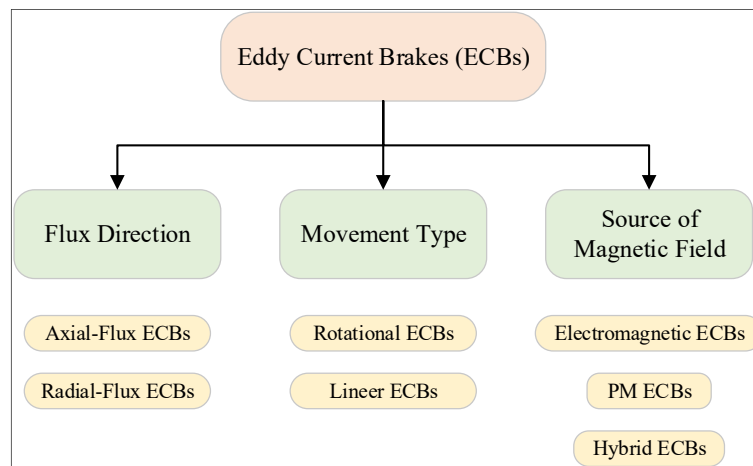


Figure 1.9. The classification of ECBs

#### 1.4. AF-ECBs

The very first applications of ECBs were related to test the motors in the beginning of 1990s [7, 8] and generally ECBs had AF structures due to the design and

manufacturing benefits. The first vehicle application of AF-ECB was performed in France in 1936 [38]. With the speedy and stable growth in traction applications, AF-ECBs have been frequently used in heavy vehicles as an auxiliary braking component since 1940s [39]. Almost all of the industrial AF-ECB products have double-rotor single-stator structure. It has to be stated that AF-ECBs could also have several topologies as single-rotor single-stator, single-rotor double-stator or multi-rotor multi-stator. These topologies are illustrated in Figure 1.10. Based on rotor material, geometric limitations and application requirements, AF-ECB structure or topology can vary. However, braking torque governing equation and fundamentals of AF-ECB topologies are investigated with the same approach.

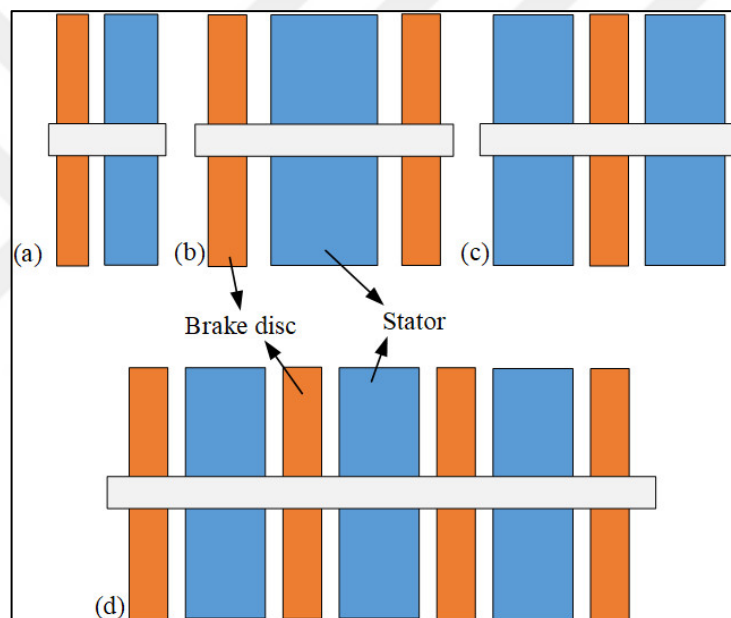


Figure 1.10. AF structures: (a) single-rotor single stator, (b) double-rotor single stator, (c) single-rotor double-stator and (d) multi-rotor multi-stator

AF-ECBs in the market are generally called as electromagnetic retarders, and they are mostly implemented into heavy vehicles. The general structure of the industrial AF-ECB is shown in Figure 1.11 [39]. The electromagnetic retarder shown in the figure has double-rotor single-stator structure and consists of DC windings with solid-steel stator and rotor material. Most industrial AF-ECB products in the market consist of 8 stator poles with 4 independent windings.

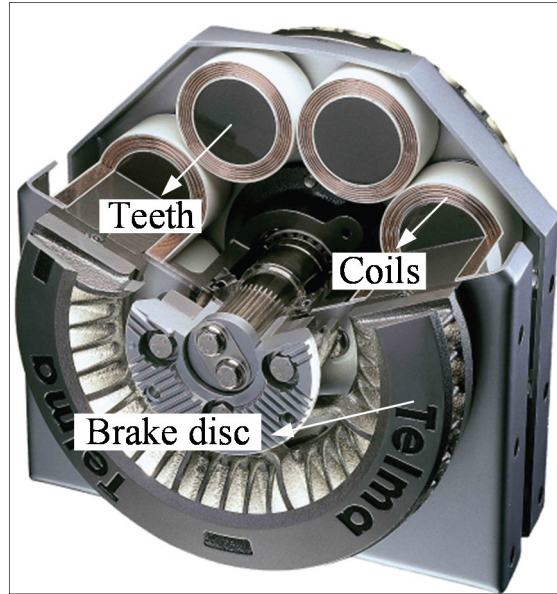


Figure 1.11. Industrial AF-ECB having double-rotor single-stator [39]

### 1.5. PM-ECBs

Due to the rapid development in the PM technology, PMs have been implemented into almost all electromagnetic applications since 1970s [40-42]. Parallel to this trend, PM based ECB studies have been rapidly increased in 1990s. However, it can be stated that most studies related to PM-ECBs have been performed for the academic purposes. Generally, PM-ECBs need an external system to control the braking torque. External system adjusts the position of PMs to control the magnetic field of the magnet. To give a practical example, two different type of PM-ECB are given in Figure 1.12 [31, 36]. As seen from the figure that external systems regulate the air gap length to control the braking torque.

Due to the control drawbacks, the industrial companies do not take attention to the PM-ECBs. Only one industrial PM-ECB, named as magnetarder [43], exists in the market. The structure of the magnetarder is given in Figure 1.13. The magnetarder has a radial flux topology and consists of PMs, a pole piece and a brake disc. PMs are settled to the stator surface, and a pole piece, which composes of magnetic and nonmagnetic segments, is placed in the front of magnets. Brake disc has both magnetic and conductive properties and there is an air gap between the brake disc and the pole piece.

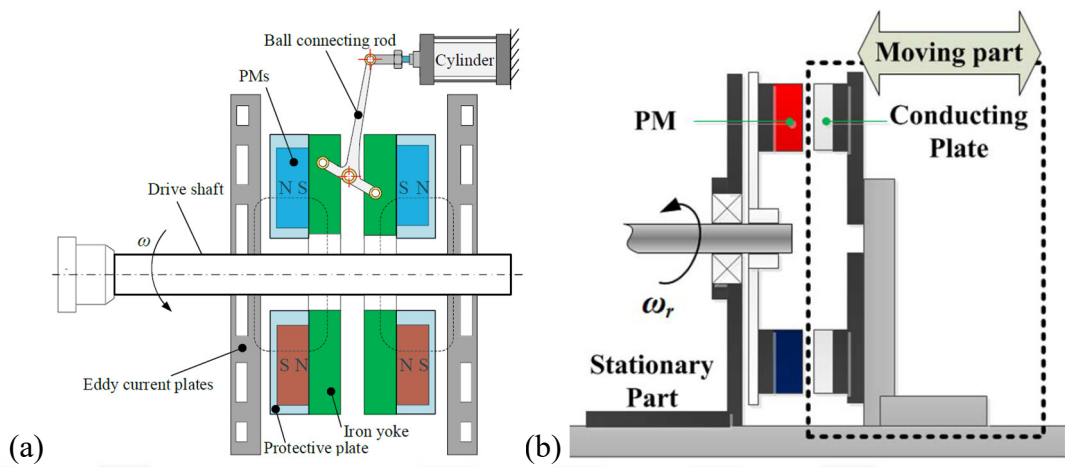


Figure 1.12. Typical PM-ECB examples: (a) moving stator [36] and (b) moving brake disc [31]

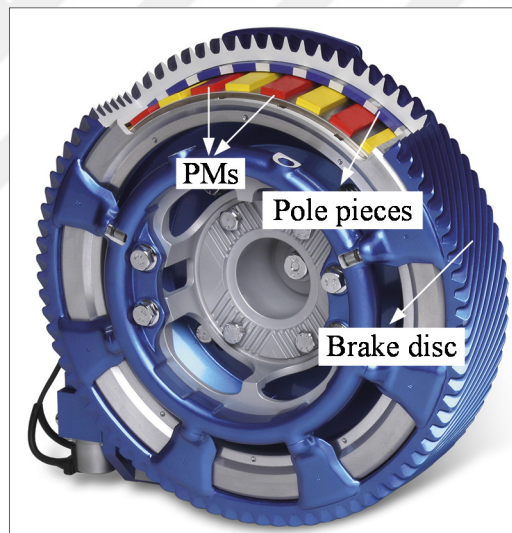


Figure 1.13. Industrial PM-ECB product having outer rotor topology [43]

To clarify the working principles of the magnetarder, the flux paths of braking and nonbraking operations are given in Figure 1.14. The working principle of the magnetarder relies on the moving of the pole piece. When the magnetarder is in braking operation (Figure 1.14-(a)), PMs are paired with the magnetic segments of the pole piece. In this case, the PM flux is completed its path over the brake disc. This enables the braking operation. When the magnetarder is not working (Figure 1.14-(b)), the PMs are matched with the nonmagnetic segments and the PM flux is completed over the pole piece and there is no flux passing through the brake disc. This is the

nonbraking operation. The control of the pole piece is performed by an external pneumatically system.

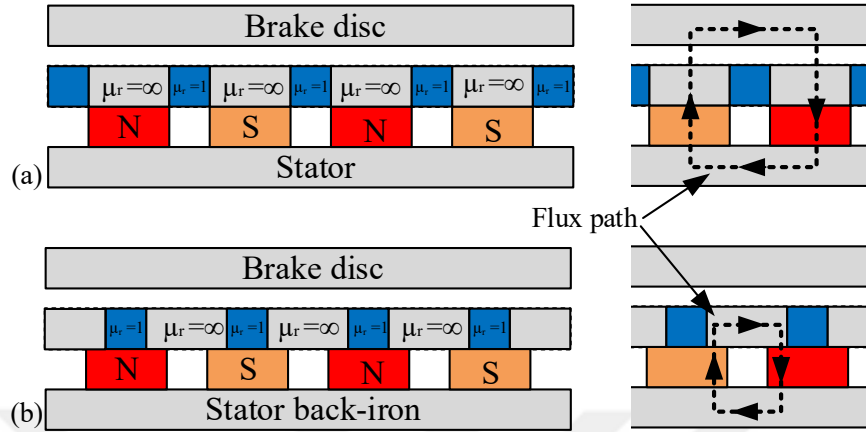


Figure 1.14. Working principles of the magnetarder: (a) braking and (b) nonbraking

## 1.6. Objectives and Contributions of the Thesis

The main objective of this research is to propose and develop a new permanent magnet biased eddy current brake for braking applications particularly for traction applications. Conventional eddy current brakes consists of only DC windings and the braking torque characteristic relies on the excitation current. More braking torque can be obtained by implementing permanent magnets into the magnetic system. However, permanent magnet type eddy current brakes have control shortcomings that an external mechanism is needed to control the magnet field by altering the air gap length or the position of the permanent magnets. Permanent magnet biased eddy current brakes, which consist of DC windings and permanent magnets, can be a viable solution to the control drawback. Permanent magnets could be implemented into various places as teeth tips, yoke, inside the teeth and slot openings. The most suitable one is to place the permanent magnets into the slot openings. Thus, controllable magnet flux can be achieved and braking torque characteristic can be improved.

Another objective of this research is to propose a new analytical-based multidisciplinary design methodology, which consists of coupled nonlinear magnetic-thermal-structural modeling in the time domain. A great amount of energy occurs in the brake disc during retarding and this energy leads the temperature rise in the brake disc. For conventional eddy current brakes, thermal analysis is enough to investigate

the temperature rise and its effects on braking torque. However, in the proposed eddy current brake, permanent magnets placed in the slot openings are directly affected by the disc temperature. In addition, structural analysis is also needed to determine the safety factor and the bending stresses. Therefore, a new multidisciplinary design approach is developed and proposed to determine the braking time, braking torque variation, temperature rise in permanent magnets and brake disc.

The contributions of this thesis can be summarized as follows:

- A detailed review of eddy current brakes from the application and technology point of view
- Design and analysis of radial flux and axial flux eddy current brakes using nonlinear magnetic equivalent circuit modeling approach and finite element analysis, and experimental comparison of the brakes
- 3D finite element analysis of eddy current brakes to determine the braking torque profile at various speeds and excitation currents
- Proposal of a new multidisciplinary design approach for eddy current brakes particularly for axial flux topologies, which consist of coupled analytical-based magnetic-thermal-structural nonlinear modeling in the time domain
- Proposal of a new axial flux permanent magnet biased eddy current brake and multiobjective optimization of the proposed brake by nonlinear magnetic equivalent circuit modeling and its FEA validation
- Cold-case experimental study of the proposed new axial flux permanent magnet biased eddy current brake to determine the braking torque profile at the room temperature
- Hot-case experimental study of the proposed new axial flux permanent magnet biased eddy current brake to determine the braking torque variation, temperature rise in brake disc and the magnets and the excitation current variation in time.

## 2. MODELING AND ANALYSIS OF EDDY CURRENT BRAKES

This chapter deals with the modeling, analysis and experimental verification two different ECBs. Axial-flux (AF) and radial-flux (RF) ECB topologies are investigated by the nonlinear analytical modeling and 3-dimensional (3D) finite element analyses (FEAs). A brief introduction of braking torque governing calculation, influence of design parameters on braking torque, magnetic equivalent circuit (MEC) modeling and root-finding algorithms for nonlinear analysis will firstly be presented. An open-slotted single-rotor single-stator AF-ECB and a RF permanent magnet (PM)-ECB will be investigated in details by nonlinear analytical modeling and 3D-FEA. Prototypes of AF-ECB and RF-PM-ECB will be presented and the comparison of the results obtained from nonlinear analytical modeling, 3D-FEA and the tests will be provided in this chapter.

### 2.1. Braking Torque Governing Calculation

It is clear that an eddy current brake consists of a rotating part and a fixed part. The eddy currents occur in the rotating part because of the motion, and the time varying magnetic flux density produces an electric field according to Lenz's law and defined by 3<sup>rd</sup> equation of Maxwell as

$$\nabla \times \vec{E} = - \frac{\partial \vec{B}}{\partial t} \quad (2.1)$$

where E is the electric field, B is the magnetic flux density. This electric field results in circulating currents called current density, J, and according to Ohm's law defined as

$$\vec{J} = \sigma \vec{E} \quad (2.2)$$

where  $\sigma$  is the electrical conductivity. Interaction between the current density and the magnetic flux density results in a retarding force defined as



$$\vec{F} = \vec{J} \times \vec{B} \quad (2.3)$$

For linear eddy current brake, retarding force can be used. Otherwise, for radial flux or axial flux topologies, the braking torque can be defined as

$$\vec{T} = r \vec{F} \quad (2.4)$$

where  $r$  is the radius. The braking torque can be computed by two approaches: (1) field analysis [44, 45] and (2) magnetic equivalent circuit modeling [46, 47]. In this thesis, analytical modeling is performed by magnetic equivalent circuit approach. Governing equations of the braking torque in ECBs are relied on the calculation of the power dissipation in the conductive part. The power dissipation in the conductive part can be defined by

$$P_{br} = \rho J^2 V_{disc} \quad (2.5)$$

where  $P_{br}$  represents the braking power,  $\rho$  represents the electrical resistivity of the conductive part and  $V_{disc}$  symbolizes the volume. The current density in the conductive part is defined by

$$J = \sigma (r \cdot \omega \cdot B_n) e^{(h_{disc}/\delta)} \quad (2.6)$$

where  $\omega$  represents the angular speed,  $B_n$  represents the normal magnetic flux density,  $h_{disc}$  represents the disc thickness and  $\delta$  represents the skin depth. The analytical skin depth calculation is relied on whether the material has linear or nonlinear magnetic characteristic. The skin depth for the linear case is defined by

$$\delta = \sqrt{\frac{2\rho}{\omega \mu_0 \mu_r}} \quad (2.7)$$

where  $\mu_0$  represents the vacuum permeability and  $\mu_r$  represents the magnetic permeability. The above approach can be used in the materials, which have linear magnetic properties as copper and aluminium etc. Generally, ferromagnetic materials have nonlinear characteristic as typically described by BH curve. Therefore, skin effect for the nonlinear case needs a special attention [48] and is described by

$$\delta = \sqrt{\frac{2H_0\rho}{\omega B_s}} \quad (2.8)$$

where  $H_0$  represents the applied maximum magnetic field strength and  $B_s$  represent the saturation level of magnetic flux density respect to BH curve. Contrary to conventional skin effect approach, Agarwal et al propose that if the time varying magnetic field applies to a conductive material, the magnetic flux density is  $+B_s$  or  $-B_s$  [49]. This approach is found by the empirical methods and it is shown that more accurate results can be obtained for the materials, which have nonlinear behaviors. Finally, the braking torque is obtained by

$$T_{br} = \frac{P_{br}}{\omega} \quad (2.9)$$

It is clearly seen that the magnetic flux density plays an important role in the calculation of the braking torque. Generally, steel laminations are used in the electric machines to reduce the eddy currents and they have high magnetic permeability and resistivity values. Opposite to conventional electric machines, the aim of the ECBs is to generate eddy currents and the current density as much as possible for the braking purposes. Therefore, low resistivity in the brake disc is preferred. As a consequence of that, the armature reaction is naturally occurred in the ECBs and this reaction leads to decrease of the magnetic flux density as the increase of the speed. When the speed is zero, which is equals to the magnetostatic case, the flux can easily pass from the air gap to the brake disc but when the speed is increased, the flux reflects from the surface of the brake disc due to the armature reaction. Thus, the mean magnetic flux density is decreased by the speed. This issue can be investigated by nondimensional Reynolds number defined by

$$B_n = B_0 e^{-\mu_0 \sigma \omega \delta} \quad (2.10)$$

where  $B_0$  represents the magnetic flux density when the speed is zero. In some design cases, Reynolds number might be dominant and it has a great influence on the braking torque. It is crucial to consider the magnetic Reynolds number in analytical braking torque computation. A demonstration related to decrease of the magnetic flux density is given in Figure 2.1 to highlight this issue. The magnetic flux density variation over

one pole pitch at the speed of zero and  $1000 \text{ min}^{-1}$  obtained are shown in the figure. The armature affect is clearly seen that the 0.91 T of mean magnetic flux density at the speed of zero is reduced to 0.48 T of mean magnetic flux density at the speed of  $1000 \text{ min}^{-1}$ .

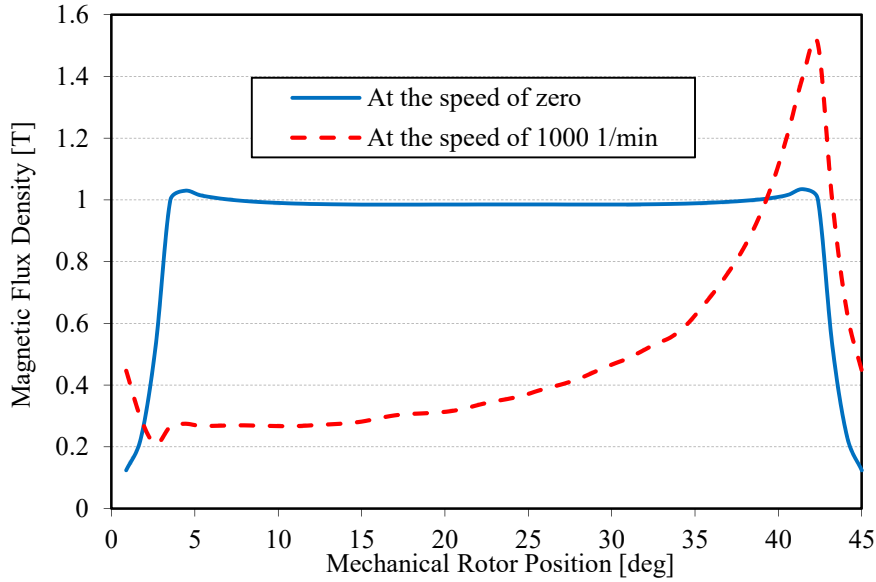


Figure 2.1. Magnetic flux density variation over one pole pitch

## 2.2. Influence of Design Parameters on Braking Torque

The geometric parameters play critical role to determine the output performances in all kind of electric machines [50-52]. In this section, the influence of geometric parameters on braking torque will be investigated for a reference radial-flux conventional eddy current brake. The studied reference model or design consists of 8 poles, 0.5 mm of air gap length, 0.2 mm of conductive region thickness, 2.3 mm of yoke thickness, 0.5 of stator teeth-to-pole ratio and 50 mm of outer radius and the conductive region has copper material. The current density is set to  $4 \text{ A/mm}^2$  and is kept same for all design cases. The rated braking torque is 2.25 Nm and the rated speed is  $1000 \text{ min}^{-1}$  (the tangential speed of 5.25 m/s) in the reference model. The geometric parameters of stator teeth-to-pole ratio, conductive region thickness, pole number, outer radius, rated speed and conductive materials are parametrically altered in order to demonstrate the variation of braking torque.

The braking torque variation as a function of stator teeth-to-pole ratio is given in Figure 2.2. It has to borne in mind that the current density is kept the same for all cases. It

means that current linkage is changed with this ratio. It is shown that the maximum braking torque is obtained at the stator-teeth-to-pole ratio of 0.3. The braking torque is very low compared to reference design in high stator teeth-to-pole ratios, which is close to 1.

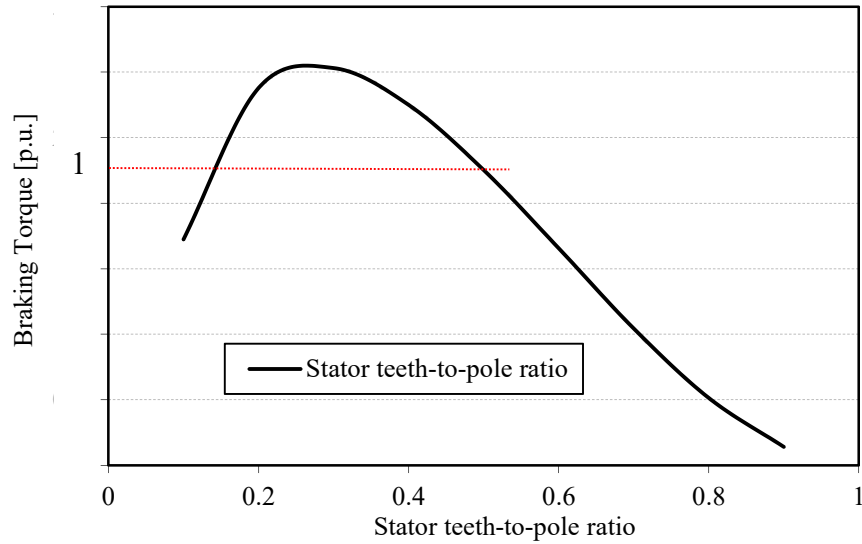


Figure 2.2. Braking torque variation as a function of stator teeth-to-pole ratio

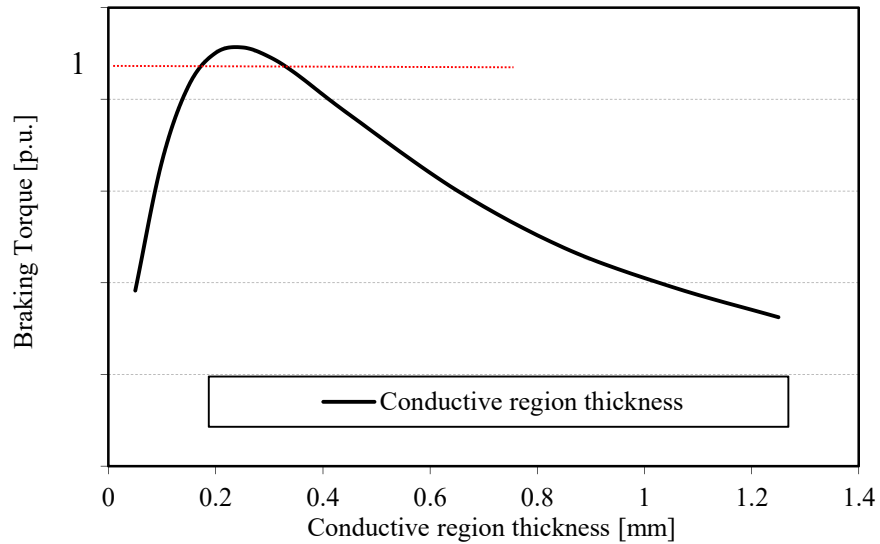


Figure 2.3. Braking torque variation as a function of conductive region thickness

The braking torque variation as a function of conductive region thickness is given in Figure 2.3. The conductive region is very important since the eddy currents occur in here. However, the increase of the conductive region also leads the increase of the magnetic air-gap. Therefore, magnetic flux density is decreased by the increase of the

conductive region. The figure shows that 0.25 mm of conductive region thickness gives the maximum braking torque while the reference design has 0.2 mm of conductive region thickness. It has to be reminded that mechanical constraints and production capability has to be considered while determining the thickness of the conductive region.

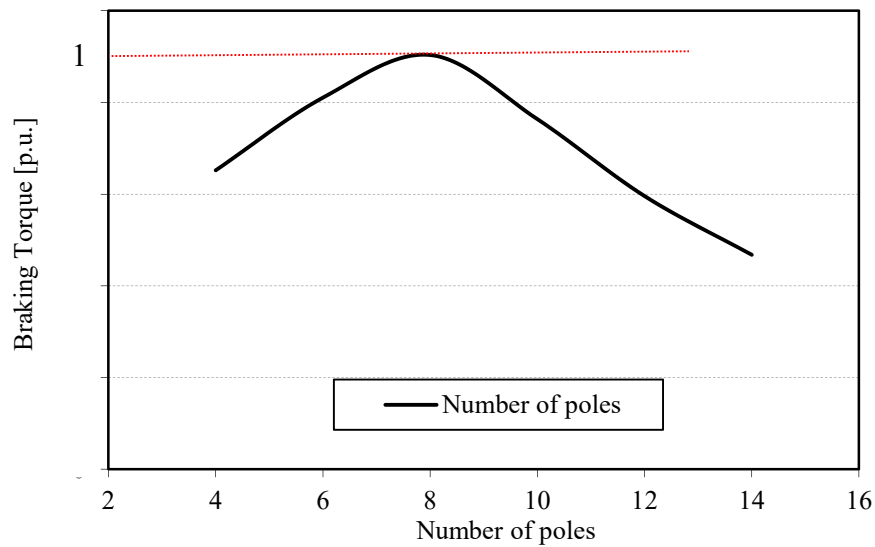


Figure 2.4. Braking torque variation as a function of number of poles

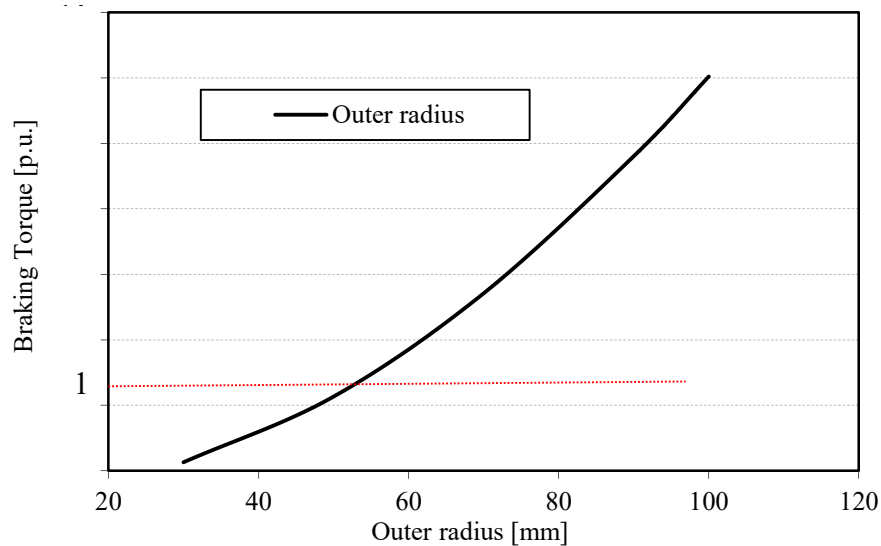


Figure 2.5. Braking torque variation as a function of outer radius

The braking torque variation as a function of pole number is given in Figure 2.4. The pole number differs from 4 to 14 and it is seen that the maximum braking torque is obtained for 8 poles. It has to be reminded that nearly all industrial eddy current brakes

have 8 poles. The braking torque variation as a function of outer radius is given in Figure 2.5. It is clearly seen that the braking torque relies on outer radius. Increase of outer radius results in braking torque increase considerably.

The braking torque characteristic of the reference eddy current brake is given in Figure 2.6. The conductive region is made by copper in the reference model and the braking torque is investigated up to  $5000 \text{ min}^{-1}$  and it is seen that the braking torque is in decreasing region after the speed of  $2000 \text{ min}^{-1}$ . Variation of braking torque characteristic for various conductive materials is also given in Figure 2.6. Aluminum, zinc, nickel and low carbon steel materials are used in the conductive region, respectively and the braking torque characteristics obtained from these material are provided. It is seen from the figure that electrical property of the conductive region affects the braking torque characteristic dominantly. For example, for copper and aluminum conductive regions, the braking torque decreases after the speed of  $1500 \text{ min}^{-1}$  and  $2500 \text{ min}^{-1}$ , respectively. It has to be pointed out that the linear braking torque profile is obtained for zinc, nickel and low carbon steel conductive regions.

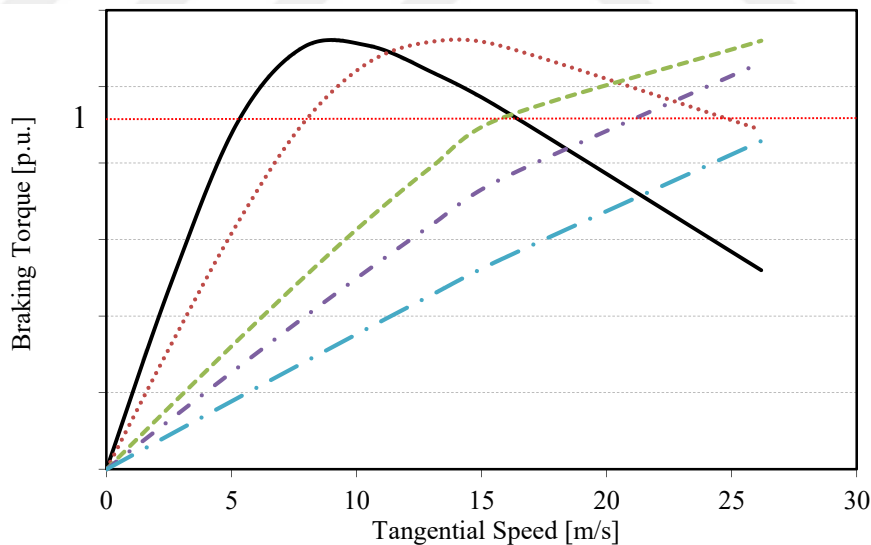


Figure 2.6. Variation of braking torque characteristic for various conductive materials

### 2.3. Magnetic Equivalent Circuit Modeling

Electric machines can be analytically modeled by several manners. Main approaches are: 1) magnetic equivalent circuit (MEC) modeling, 2) Fourier based modeling and 3) hybrid type combined modeling, which consists of MEC and the Fourier based

modeling [53, 54]. Here, MEC is used for the analytical modeling of the ECBs. 5The MEC modeling relies on representing an electric machine with magnetic circuit analogous to an electric circuit. The analogy between the magnetic and the electric circuits is given in Table 2.1.

Table 2.1. Analogy between the magnetic and the electric circuits

Magnetic			Electric	
Name		Units	Name	Units
Magneto	motive	Ampere-turn	Electromotive force	Volt
Magnetic field		Ampere/meter	Electric field	Volt/meter
Magnetic flux		Weber	Electric current	Ampere
Reluctance		1/Henry	Resistance	Ohm
Magnetic flux density		Tesla	Current density	A/m <sup>2</sup>
Permeability		Henry/meter	Conductivity	Siemens/meter

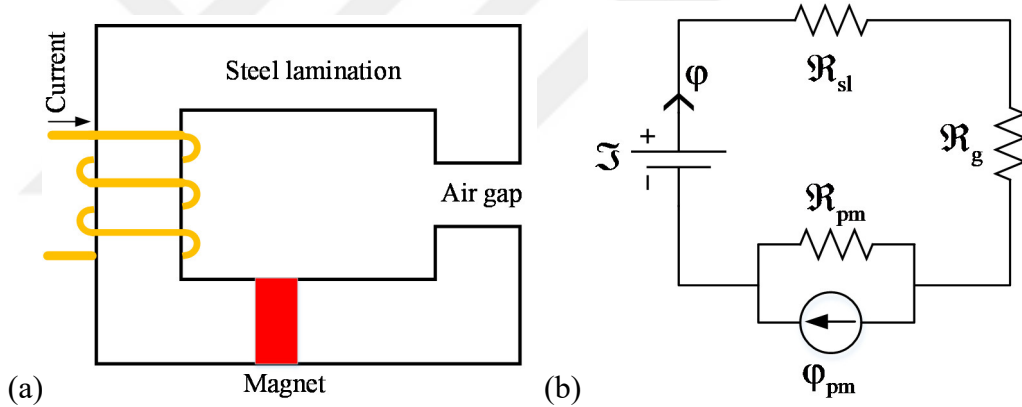


Figure 2.7. (a) Magnetic circuit with single air gap and (b) MEC modeling

A simple C-core magnetic circuit with single air gap is given in Figure 2.7-(a). C-core magnetic circuit consists of windings and a magnet with a single air gap. The steel laminations are assumed to be used in the core stack. The MEC modeling of the C-core structure is given in Figure 2.7-(b). Similarly electromotive force in electric equivalent circuit, magneto motive force in the magnetic circuit is the line integral of magnetic field strength along a closed path described by

$$\mathcal{F} = \oint H dl \quad (2.11)$$

where  $H$  is the magnetic field and  $l$  is the closed loop length. According to the Ampere's law,  $\mathcal{F}$  is also defined by

$$\mathfrak{I} = \oint \mathbf{H}d\mathbf{l} = \oint \mathbf{J}d\mathbf{S} = \sum \mathbf{NI} \quad (2.12)$$

where  $\mathbf{J}$  is the current density and  $\mathbf{S}$  is the surface area and the  $\mathbf{NI}$  is the current linkage. In this study,  $\mathfrak{I}$  names as the current linkage in IEC60050 standard. The MEC model consists of current linkage, reluctances and magnetic flux. The reluctance is defined by

$$\mathfrak{R} = \frac{1}{\mu_0 \mu_r} \frac{l}{A} \quad (2.13)$$

where  $\mu_0$  is the vacuum permeability,  $\mu_r$  is magnetic permeability of the material,  $l$  is length and the  $A$  is the cross-sectional area of the surface. Flux in the MEC modeling is defined as

$$\varphi = \frac{\mathfrak{I}_{eq}}{\mathfrak{R}_{eq}} = \frac{\mathfrak{I} + \mathfrak{R}_{pm} \varphi_{pm}}{\mathfrak{R}_{sl} + \mathfrak{R}_{pm} + \mathfrak{R}_g} \quad (2.14)$$

where  $\varphi$  is the magnetic flux,  $\mathfrak{I}_{eq}$  is the equivalent current linkage and  $\mathfrak{R}_{eq}$  is the equivalent reluctance in the modeling,  $\mathfrak{R}_{sl}$  is the reluctance of core lamination,  $\mathfrak{R}_g$  is the air gap reluctance,  $\mathfrak{R}_{pm}$  is the PM reluctance and  $\varphi_{pm}$  is the PM flux, which equals to residual flux density ( $B_r$ ) multiply by the cross-sectional areas ( $A$ ). Equation (2.14) is similar to Ohm's law and it is called as Hopkinson's law or Rowland's law.

It has to be stated that magnetic properties of the materials has a great influence on the electric machine's performance. Generally, steel laminations are frequently used in the electric machines and as an alternative solution to specific designs, solid steels are also preferred. The magnetic property is defined by BH curve of the material defined as

$$\mathbf{B} = \mu_0 \mu_r \mathbf{H} \quad (2.15)$$



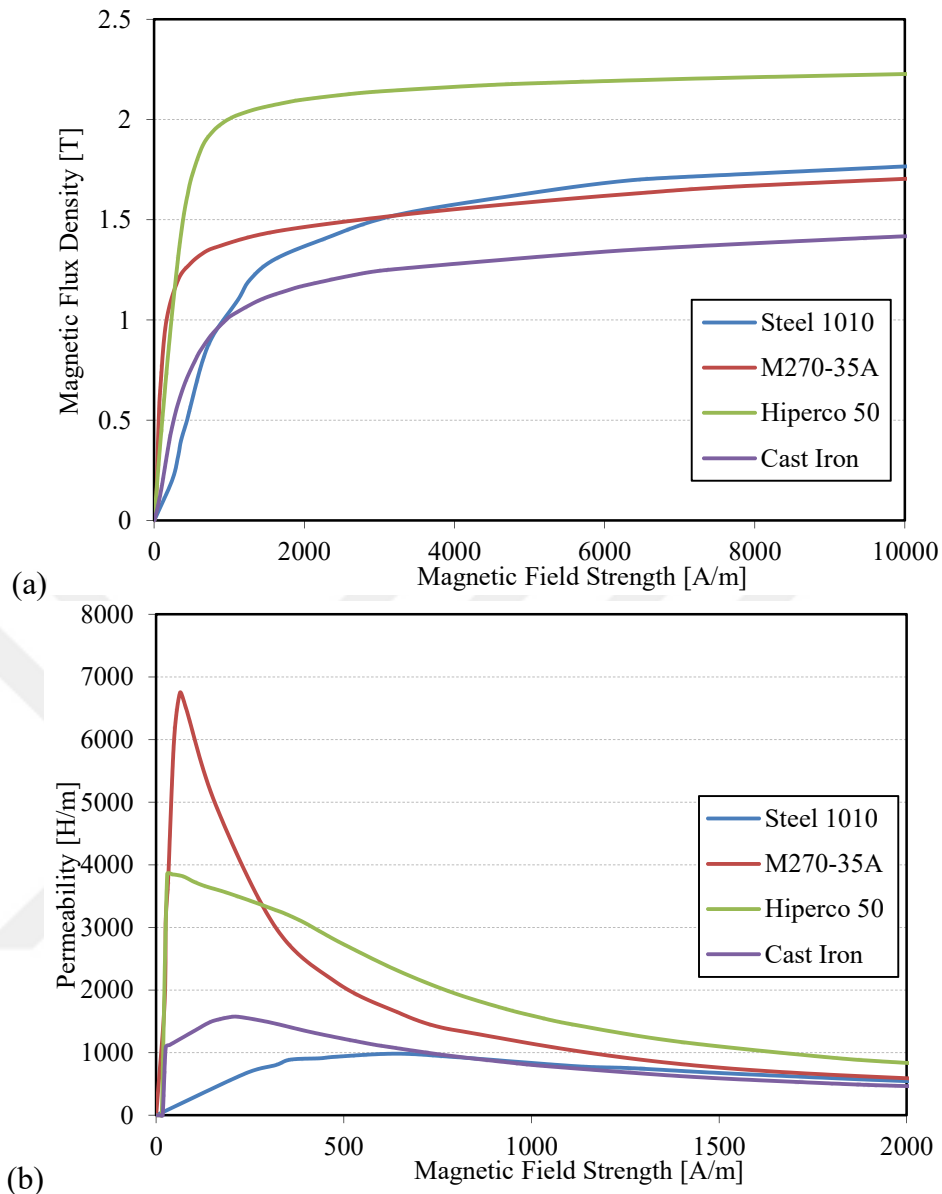


Figure 2.8. (a) BH curves and (b) permeability curves of various magnetic materials

where  $B$  is the magnetic flux density. BH and permeability curves of the most common materials in the market are given in Figure 2.8. In the figure, cast iron, solid steel 1010, electrical steel M270-35A and cobalt-iron soft magnetic allow Hiperco 50 are provided. It is seen from the figure that materials have different BH curve characteristic as Hiperco 50 has the highest saturation level among all while the cast iron has the lowest one. In addition, for magnetic permeability curves, M270-35A has the highest peak permeability value as nearly 7000 H/m among all while solid steel 1010 has the lowest magnetic permeability as 1000 H/m.

## 2.4. Root-Finding Algorithms for Nonlinear Analysis

The materials used in the electric machines have nonlinear behaviors related to magnetic, electrical or structural based properties. It is clear that BH curve of the magnetic materials is the most important property among all. BH curve characterizes the magnetic properties of materials, and is defined by the variation of the magnetic flux density with the external magnetization field. The magnetic materials have various BH curve characteristics as previously shown in Figure 2.8-(a). The accurate consideration of BH curve is a crucial task for electric machine designers in the preliminary design stage. The BH curve characteristic can be taken into account by various approaches. The most common nonlinear approaches used in the literature are Gauss-Siedel and Newton-Raphson approaches.

### 2.4.1. Gauss-Siedel approach

Gauss-Siedel approach is the most preferred solving approach of nonlinear systems due to its simple structure. Gauss-Siedel approach can convergence a solution if the equation sets are close to linear and solving matrix is diagonal dominance. Gauss-Siedel approach is frequently used in the literature since it has good converging ability and can be easily implemented to energy conversion problems by its simple structure [55-57]. Generally, Gauss-Siedel approach is preferred in the nonlinear magnetic modeling of the electric machines, which are working in the nonsaturated design points. The system equation is considered as

$$Ax=B \quad (2.16)$$

where A is a given  $n \times n$  matrix, B is a given  $n \times 1$  vector and x is the  $n \times 1$  solution vector. If it is assumed that the matrix n is equal to 3, the system equation and the solution are defined by

$$\begin{bmatrix} a_{11} & a_{12} & a_{13} \\ a_{21} & a_{22} & a_{23} \\ a_{31} & a_{32} & a_{33} \end{bmatrix} \begin{bmatrix} x_1 \\ x_2 \\ x_3 \end{bmatrix} = \begin{bmatrix} b_1 \\ b_2 \\ b_3 \end{bmatrix} \quad (2.17)$$

$$x_1^{k+1} = \frac{b_1 - a_{12}x_2^k - a_{13}x_3^k}{a_{11}} \quad (2.18)$$

$$x_2^{k+1} = \frac{b_2 - a_{21}x_1^{k+1} - a_{23}x_3^k}{a_{22}} \quad (2.19)$$

$$x_3^{k+1} = \frac{b_3 - a_{31}x_1^{k+1} - a_{32}x_2^{k+1}}{a_{33}} \quad (2.20)$$

where  $k$  is the iteration number. Gauss-Siedel approach starts with the initial guess of the parameters and the results are firstly obtained by the initial values in the first iteration. The new calculated values are used in the same iteration in Gauss-Siedel therefore low computation effort is obtained. In each iteration, the calculated results are compared with the previous values. If the error percentage is less than the desired value, the iteration will end. If not, the iteration will continue until the desired error is achieved.

#### 2.4.2. Newton-Raphson approach

Although Gauss-Siedel approach is a simple and a feasible solution for the nonlinear analysis, Gauss-Siedel cannot converge a solution if the system matrix is nondominance diagonal. For example, if an electric machine works in the saturated region, Gauss-Siedel approach cannot converge and fails. More sophisticated approaches are needed for such kind of systems. Newton-Raphson approach is one of most effective method for this task. Newton-Raphson approach is an iterative based root finding algorithm and the fundamental of Newton-Raphson approach relies on describing a function by Taylor series [58]. Newton-Raphson approach uses only first order Taylor series and is defined as

$$x_{k+1} = x_k - \frac{f(x_k)}{f'(x_k)} \quad (2.21)$$

where  $k$  is the iteration number,  $x$  is the unknown value and the  $f$  is the function and  $f'$  is its derivative. Newton-Raphson starts with the initial parameters and error percentage is compared in every iteration as Gauss-Siedel approach. It has to borne in mind that Newton-Raphson approach has more computation effort than Gauss-Siedel since it has a derivative operation. However, owing to its derivative operation,

Newton-Raphson approach can convergence a solution in the nonlinear dominant cases. The equation with n number of variables is described by

$$f(x_1, \dots, x_n) = \begin{bmatrix} f_1(x_1, \dots, x_n) \\ \vdots \\ f_n(x_1, \dots, x_n) \end{bmatrix} \quad (2.22)$$

and Newton-Raphson functions are defined by

$$x^{k+1} = x^k - (J(x^k))^{-1} f(x^k) \quad (2.23)$$

where J represents the Jacobian matrix defined by

$$J(x) = \frac{\partial f(x)}{\partial x} = \begin{bmatrix} \frac{\partial f_1(x)}{\partial x_1} & \frac{\partial f_1(x)}{\partial x_2} & \dots & \frac{\partial f_1(x)}{\partial x_n} \\ \frac{\partial f_2(x)}{\partial x_1} & \frac{\partial f_2(x)}{\partial x_2} & \dots & \frac{\partial f_2(x)}{\partial x_n} \\ \vdots & \vdots & \ddots & \vdots \\ \frac{\partial f_n(x)}{\partial x_1} & \frac{\partial f_n(x)}{\partial x_2} & \dots & \frac{\partial f_n(x)}{\partial x_n} \end{bmatrix} \quad (2.24)$$

### 2.4.3. Relaxation method

If a system has too many initial parameters or system matrix is far away from the diagonal dominance, the above mentioned approaches cannot converge and find a solution. In such cases, iteration should be relaxed for globally converging. In the literature, various relaxation methods exist and almost all of them have the same procedure. The general definition of the relaxation method is described as

$$x^{k+1} = \alpha x^{k+1} + (1 - \alpha) x^k \quad (2.25)$$

where  $\alpha$  represents the relaxation factor and its value is in the range of  $0 < \alpha \leq 1$ . The value of the relaxation factor should be correctly determined in the design stage. If the relaxation factor is selected as 1, this means that there is no relaxation. As the relaxation factor is close to zero, the number of iteration and the computation effort

will be increased. For example, solution set of a nonlinear system respect to iteration number is given in Figure 2.9 to highlight the correct selection of relaxation factor. There is no relaxation in Figure 2.9-(a) and result shows that the nonlinear approach couldn't converge the solution. Then, the relaxation factor is selected as 0.75 in Figure 2.9-(b) and the solution couldn't be converged as well. However, the ripple of the solution is reduced compared to previous one. Later, the relaxation factor is selected as 0.5 and the nonlinear approach can reach a solution after 12 iterations. Next, the relaxation factor is selected as 0.25 and 0.1, respectively and it is seen that the accurate results are obtained with more number of iterations. Here, it is clearly obtained that

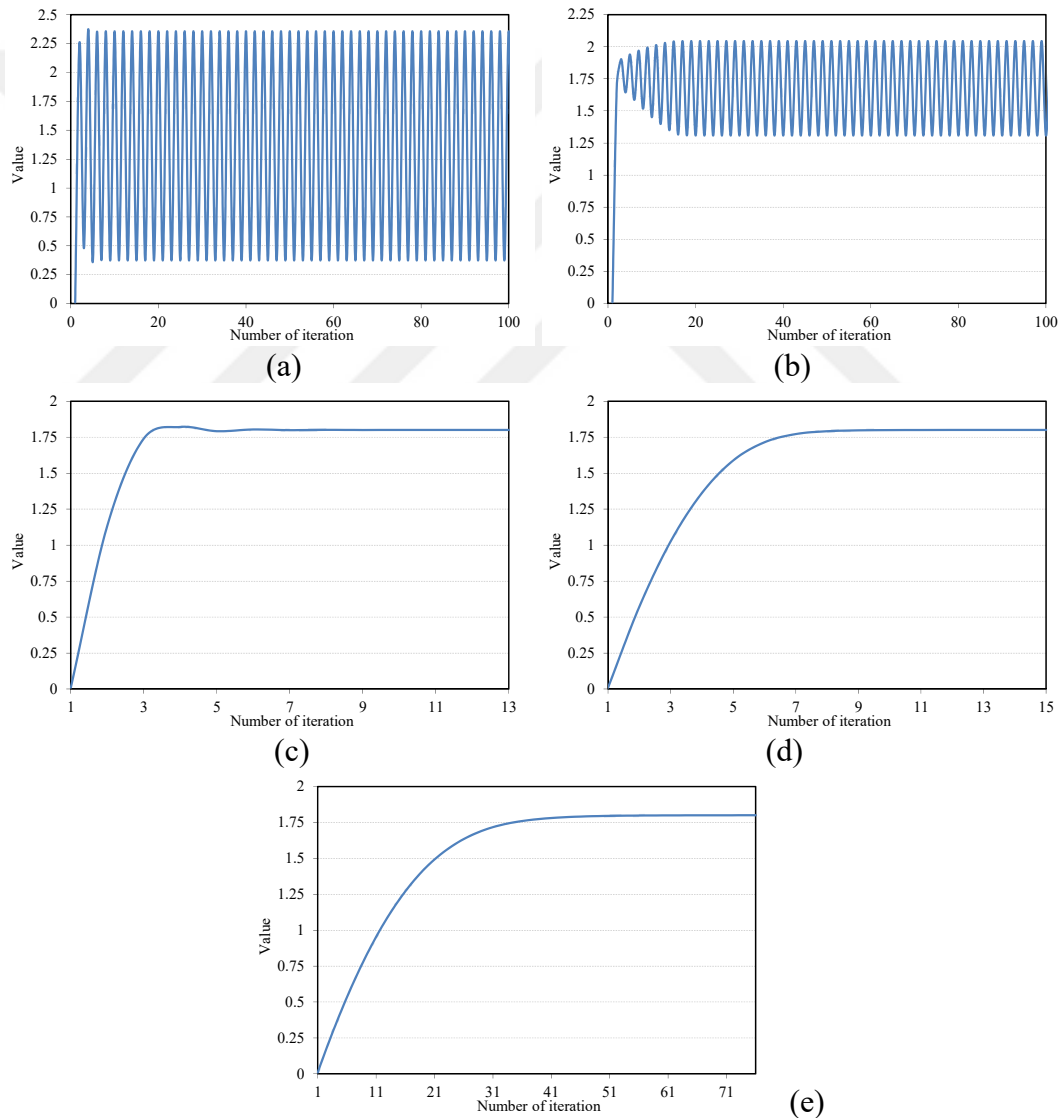


Figure 2.9. Investigation of various relaxation factors: (a)  $\alpha=1$ , (b)  $\alpha=0.75$ , (c)  $\alpha=0.5$ , (d)  $\alpha=0.25$  and (e)  $\alpha=0.1$

the correct selection of the relaxation factor is vital to reduce the computational effort and to obtain the accurate results.

## **2.5. Modeling and Analysis of an AF-ECB**

In this section, modeling, analysis and real time dynamic torque control of a single-rotor and single-stator AF-ECB are presented. Modeling of an AF-ECB is accomplished based on nonlinear magnetic equivalent circuit (MEC) modeling. Braking torque profile of the AF-ECB are obtained by nonlinear MEC modeling and numerical analyses will be carried out by 3D-FEAs to validate the nonlinear MEC modeling and to obtain the braking torque profile. 3D thermal FEAs will be also completed to identify working period at maximum braking torque. A prototype AF-ECB is manufactured based on the analyses, and open-loop torque profile is experimentally verified. Good agreement between the test, 3D-FEA and nonlinear MEC results is achieved. A real time controller is developed and dynamic torque control of the brake for various torque and speed references is also obtained to illustrate the dynamic behaviors of the system.

### **2.5.1. Introduction**

Due to rapid developments in traction applications, AF-ECBs are becoming widely used in commercial trucks. AF-ECBs provide safety working with frictionless braking by using eddy current phenomena. Compared to conventional friction-based braking systems, AF-ECBs have fast response time and therefore they are commonly preferred in medium and high power traction applications in the range of 350 Nm to 3000 Nm. AF-ECBs do not require any maintenance due to noncontact structure and in addition, system failure of ECBs is quite low compared to conventional braking systems [59-62]. The drawback of the AF-ECBs is that the braking torque cannot be obtained at very low speeds so that the conventional braking have to be used in the traction systems. Generally, AF-ECBs are used as an auxiliary braking component to observe the main kinetic power of the system while driving. The layout of the AF-ECB in a traction system is shown in Figure 2.10 [63]. Contrary to conventional friction braking systems, AF-ECBs can be mounted within the driveline or on the gearbox.

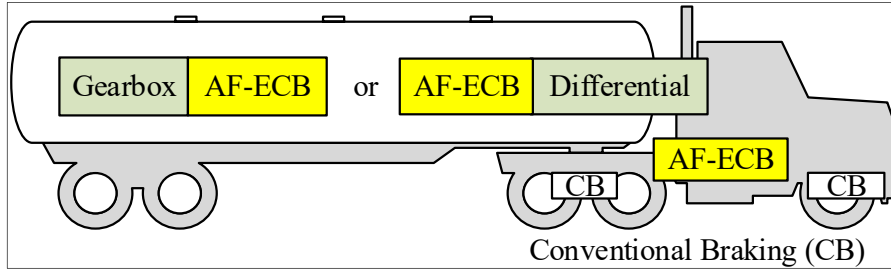


Figure 2.10. Layout of an AF-ECB in a commercial truck [63]

AF-ECBs could have single-rotor single stator, double-rotor single-stator, single-rotor double stator and multi-rotor multi-stator structures. Here, single-rotor single-stator AF-ECB with 8 open-slotted configuration is investigated. 3D AF-ECB structure with the one flux path is given in Figure 2.11. The windings are wound separately and connected in series. The key design parameters of the AF-ECB is given in Table 2.2.

Table 2.2. Key parameters of single-rotor-single-stator AF-ECB

Parameters	Value
Outer diameter	180 mm
Inner diameter	100 mm
Axial air gap	1 mm
Turn number per teeth	200
Stator teeth-to-pole ratio	0.42
Brake disc thickness	15 mm
Maximum speed	1400 min <sup>-1</sup>

The inner-to-outer diameter ratio of the AF-ECB is 0.55, and the brake has 180 mm of outer diameter. Low carbon steel is selected as brake disc material since it is the most suitable and cost-effective material in the market that it has good magnetic and electrical properties to create the eddy current paths. Certificated ST37 material is used in the brake disc and stator. BH curve of ST37 material is given in Figure 2.12. The magnetic permeability of ST37 is 1000 at 639 A/m and resistivity of ST37 is  $100 \times 10^{-9} \Omega \cdot m$  at room temperature. It should be reminded that generally, lamination steels used in the electric machine have maximum magnetic permeability of 5000-8000 and resistivity of  $500 \times 10^{-9} \Omega \cdot m$ .

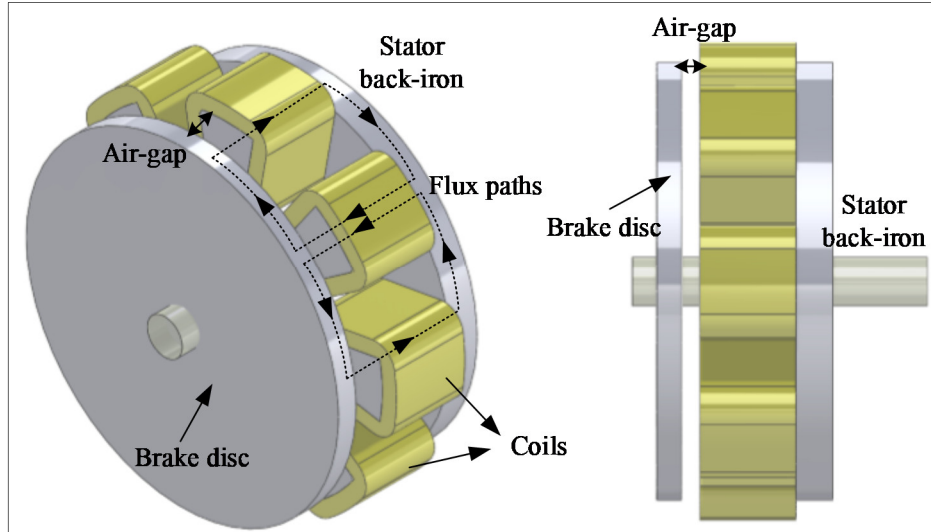


Figure 2.11. 3D model and one flux path of AF-ECB [63]

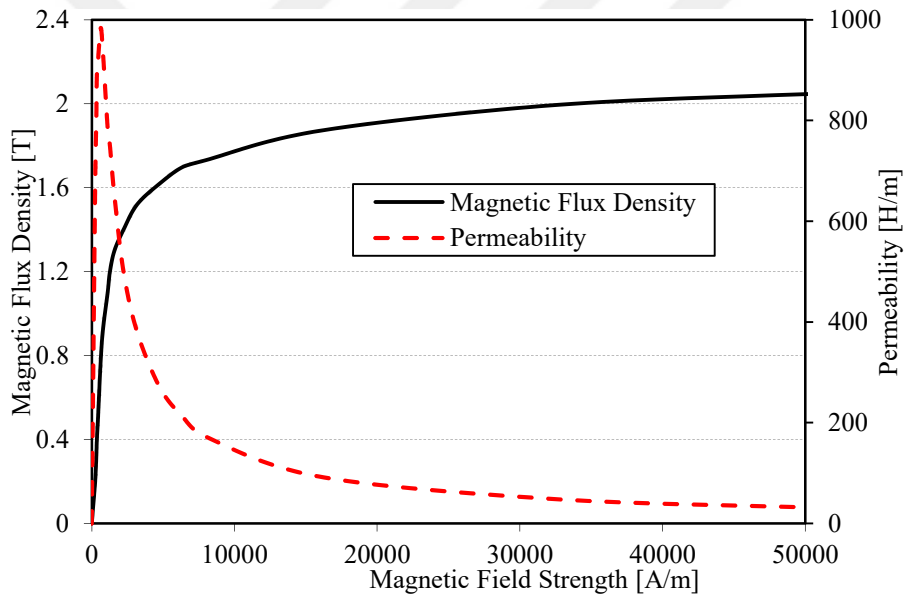


Figure 2.12. BH curve of ST37 low carbon steel

### 2.5.2. Nonlinear MEC modeling

The 3D model of the single-rotor-single-stator AF-ECB is shown in Figure 2.11. Investigated AF-ECB has 8 symmetrical flux paths related to number of slots. Therefore, focusing only one pole is adequate to model and analyze the whole AF-ECB. The 2D symmetry model and the magnetic equivalent circuit modeling is given in Figure 2.13. Notations of the 2D symmetry model are also provided in the figure:  $w_{\text{pole}}$  represents the yoke width,  $w_{\text{st}}$  represents the teeth width,  $\mathcal{R}$  represents the reluctances,  $\phi$  represents the flux and  $\mathfrak{F}$  represents the current linkage.



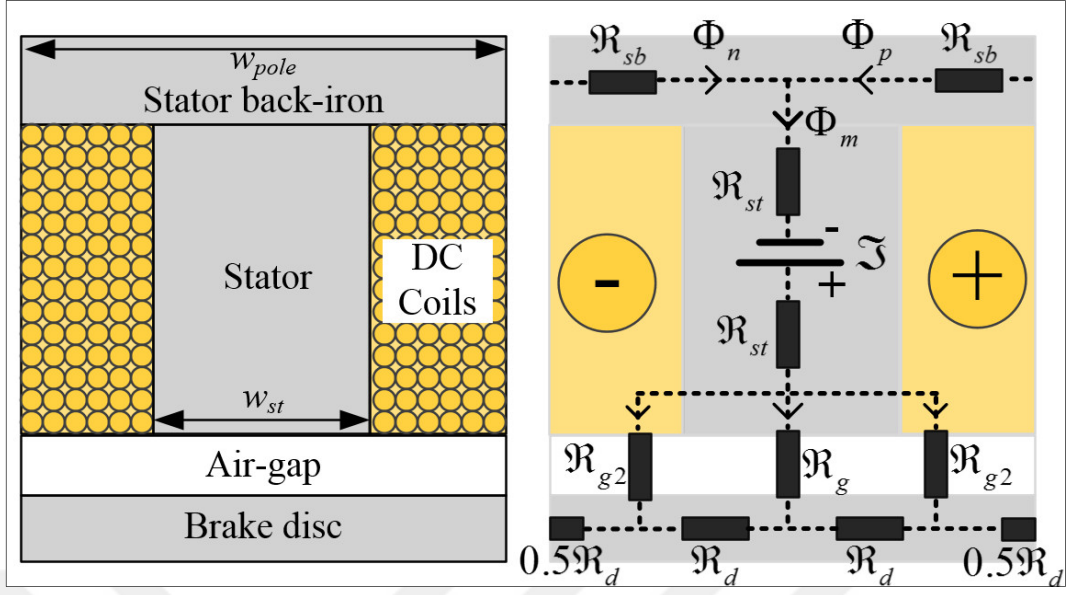


Figure 2.13. 2D symmetry model and the magnetic equivalent circuit modeling of AF-ECB [63]

The governing equations of the braking torque in ECBs were previously investigated in Section 2.1 and it was reported that calculation of magnetic flux density in the brake disc plays important role for the braking torque. Here, the MEC modeling given in Figure 2.13 is used to obtain the magnetic flux density in the brake disc. Gauss-Siedel approach is used as nonlinear solver of the MEC model. Main MEC modeling matrix of the 2D symmetry AF-ECB model is described as

$$\begin{bmatrix} \varphi_p \\ \varphi_n \end{bmatrix} = \begin{bmatrix} \mathfrak{R}_{sb} + \mathfrak{R}_{st} + \mathfrak{R}_g + \mathfrak{R}_d & \mathfrak{R}_{st} + \mathfrak{R}_g \\ \mathfrak{R}_{st} + \mathfrak{R}_g & \mathfrak{R}_{sb} + \mathfrak{R}_{st} + \mathfrak{R}_g + \mathfrak{R}_d \end{bmatrix}^{-1} \begin{bmatrix} \mathfrak{I} \\ \mathfrak{I} \end{bmatrix} \quad (2.26)$$

where  $\mathfrak{R}_{sb}$  represents the yoke reluctance,  $\mathfrak{R}_{st}$  represents the teeth reluctance,  $\mathfrak{R}_g$  represents the air gap reluctance and finally,  $\mathfrak{R}_d$  represents the brake disc reluctance.

The above reluctances are defined as

$$\mathfrak{R}_{sb} = \frac{1}{\mu_0 \mu_{sb}} \frac{l_{sb}}{w_{sb} d} \quad (2.27)$$

$$\mathfrak{R}_{st} = \frac{1}{\mu_0 \mu_{st}} \frac{l_{st}}{w_{st} d} \quad (2.28)$$

$$\mathfrak{R}_g = \frac{1}{\mu_0} \frac{g}{(1+2k_{ff}) w_{st} d} \quad (2.29)$$

$$\mathfrak{R}_d = \frac{1}{\mu_0 \mu_d} \frac{l_d}{w_d d} \quad (2.30)$$

where  $\mu_{sb}$ ,  $\mu_{st}$  and  $\mu_d$  represent the yoke, teeth and the brake disc permeability's, respectively,  $g$  represents the axial air gap length,  $w$  represents the reluctances' width,  $l$  represents the flux length and  $d$  represents the stack length. It has to borne in mind that the stack length is equal to difference between outer and inner radius. In MEC modeling, the fringing flux factor,  $k_{ff}$ , is also used to consider the actual flux path and defined as

$$k_{ff} = 0.5 \frac{g}{\sqrt{w_t d}} \ln \left( \frac{2w_t}{g} \right) \quad (2.31)$$

The main flux path equation is obtained by  $\varphi = \varphi_p + \varphi_n$  and finally, the magnetic flux density in the brake disc is defined as

$$B_g = \frac{\varphi}{(1+2k_{ff}) w_{st} d} \quad (2.32)$$

Nonlinear analysis of AF-ECB is carried out by Gauss-Siedel method. The flowchart of Gauss Siedel approach is given in Figure 2.14. The flowchart consists of two Gauss-Siedel approaches for calculation of the fluxes and magnetic flux densities. The approach starts with the determination of initial values. Next, saturable reluctances are calculated by the initial parameters and flux equations are obtained. The first Gauss-Siedel approach is applied to calculate the fluxes, then the first comparison is made for the computed flux values. If the error between the computed and the previous values are lower than desired, magnetic flux densities are computed and the comparison is performed. The second Gauss-Siedel iteration is evaluated until the desired error is achieved.

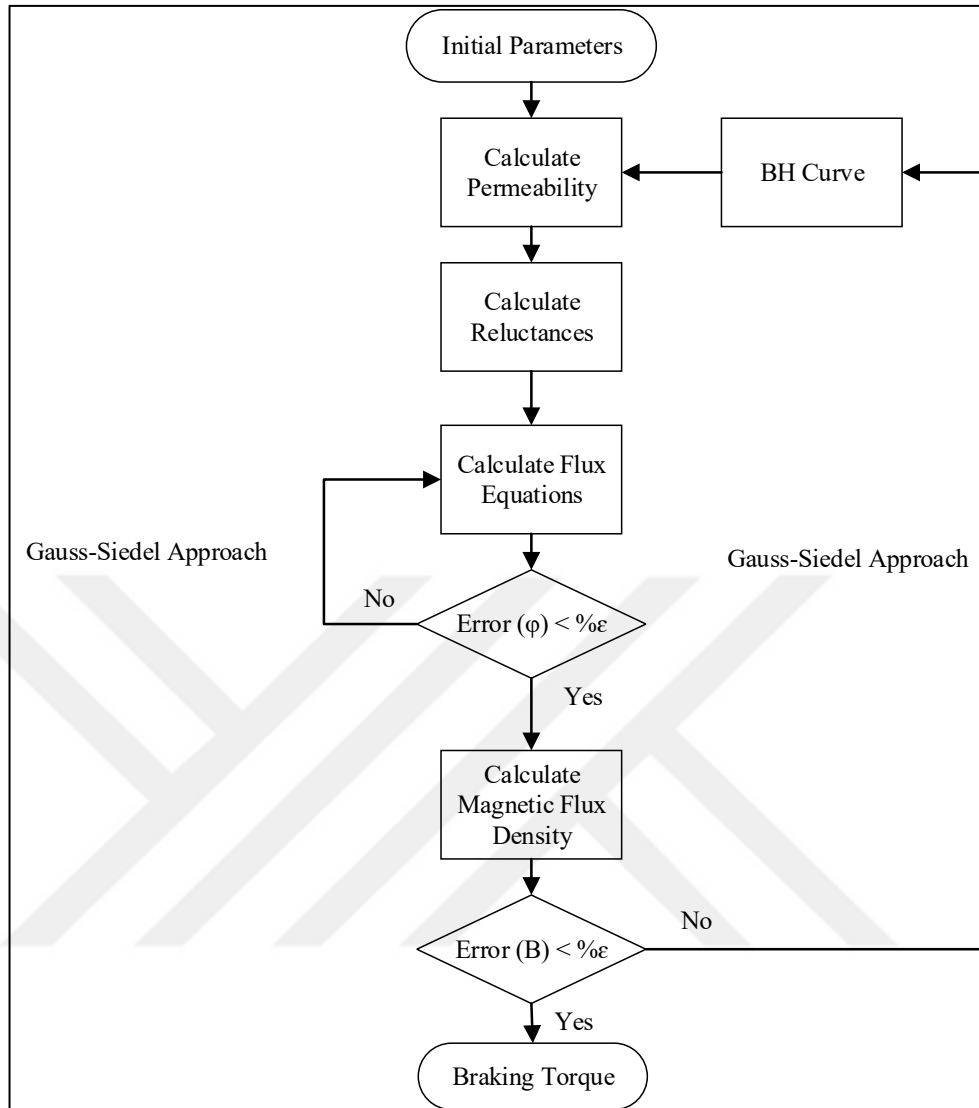


Figure 2.14. The flow chart of Gauss-Siedel approach

The magnetic flux density in the yoke and the stator teeth obtained from nonlinear magnetic modeling at the rated excitation current is given in Figure 2.15. The 1.51 T of magnetic flux density is calculated in the stator teeth while 1.23 T of magnetic flux density is calculated in the yoke. The nonlinear approach is converged a solution in 26 number of iterations and the solution accuracy is below 0.01%.

The braking torque characteristic obtained from nonlinear magnetic modeling at the rated excitation current as a function of rotational speed is given in Figure 2.16. It is seen that linear braking torque region is obtained between the speeds of 0 and 600  $\text{min}^{-1}$ . After the speed of 600  $\text{min}^{-1}$ , stable region is getting dominant. It means that the skin depth is in the decreasing trend and the armature reaction is becoming more effective.

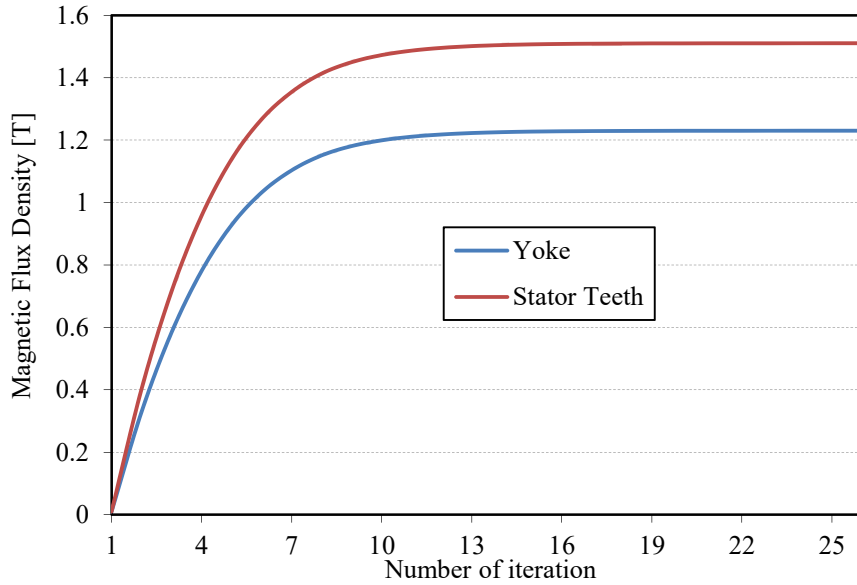


Figure 2.15. The magnetic flux density in the yoke and the stator teeth obtained by nonlinear magnetic modeling

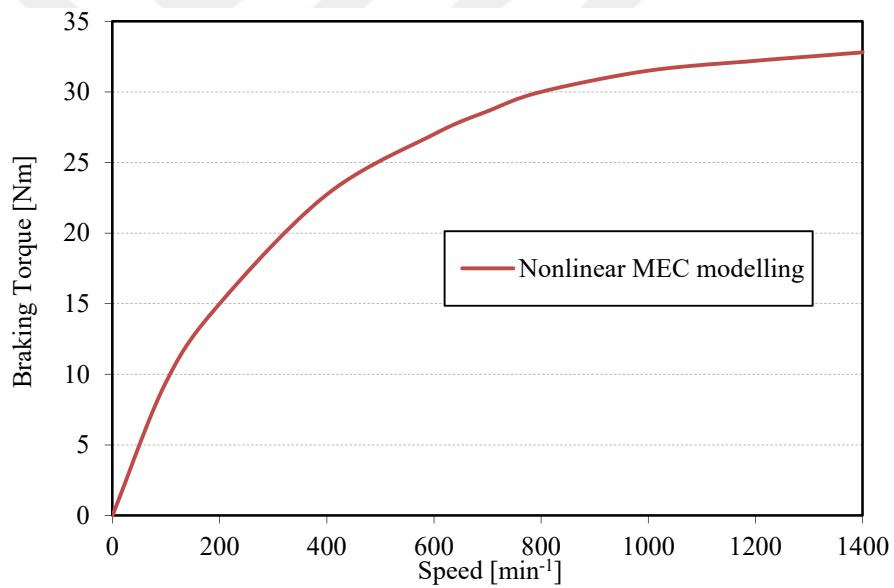


Figure 2.16. Braking torque profile of AF-ECB at rated excitation current

### 2.5.3. 3D-FEA

Due to directions of flux paths and 3<sup>rd</sup> dimensional skin effects, 3D analyses are absolutely required for the AF-ECB. Numerical analyses are carried out by using 3D finite element software by Altair. Special attention is paid to the air gap and winding regions during 3D FEA by increasing calculation steps in order to compute skin effect more accurately. Full and symmetry 3D-FE models as well as mesh structure are all

shown in Figure 2.17. Designed AF-ECB can be analyzed with symmetry model so that computation time can be reduced, and improved mesh profile can easily be implemented. 2<sup>nd</sup> order mesh is applied focusing on the air gap and brake disc regions for high mesh density.

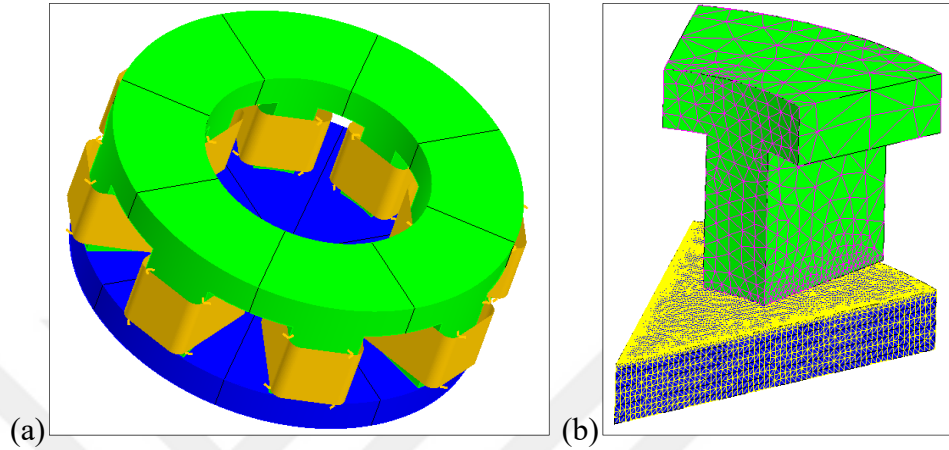


Figure 2.17. (a) Full and (b) symmetry 3D-FE models of AF-ECB

The magnetic flux density profiles of AF- ECB for maximum excitation current at the speed of  $800 \text{ min}^{-1}$  is given in Figure 2.18. It is seen that the maximum flux density in stator teeth is around 1.5 T and this value is well agree with the nonlinear magnetic modeling. In addition, the braking torque profile of AF-ECB must be determined to see the capabilities of the braking torque accurately. Parametric electromagnetic 3D-FEA simulations are completed to obtain braking torque profile. Variation of braking torque for various currents obtained from 3D-FEA is illustrated in Figure 2.19. In the

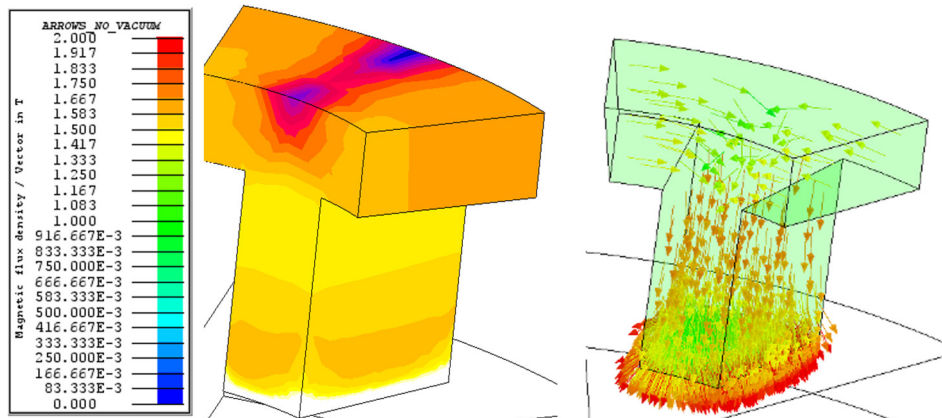


Figure 2.18. Magnetic flux density profiles of AF-ECB for rated excitation current [63]

figure, the braking torque variation for 3, 5 and 7 A excitation currents are provided. The maximum braking torque is obtained as 28 Nm at the speed of 1000  $\text{min}^{-1}$ .

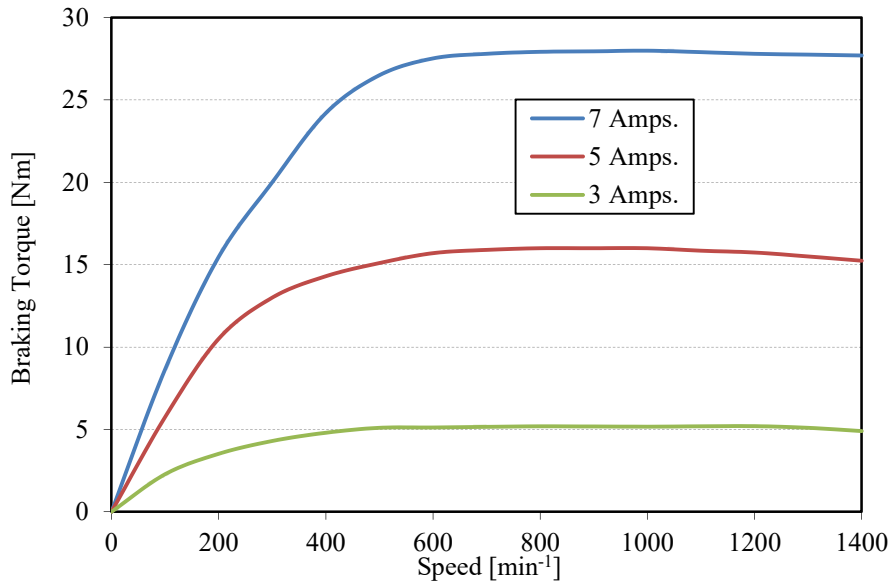


Figure 2.19. Braking torque profiles of AF-ECB for various excitation currents [63]

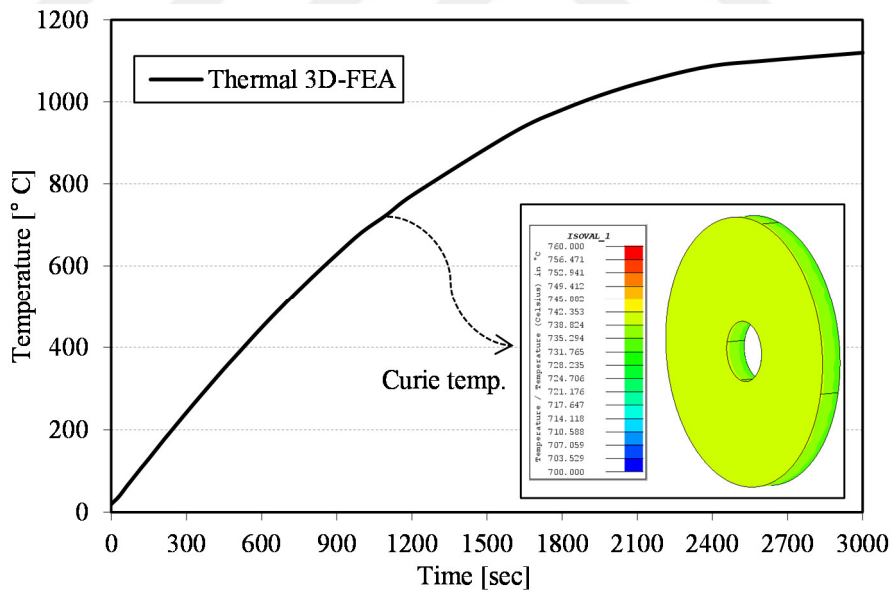


Figure 2.20. Temperature variation of the disc during braking [63]

During braking, temperature is increased rapidly in the brake disc, and temperature variation must be analyzed to determine the maximum braking time. Therefore, a thermal 3D-FEA is performed and temperature variation of the disc for maximum braking torque point is calculated and provided in Figure 2.20. The results show that the brake disc reaches Curie temperature in 1100 seconds. Due to nonventilated rotor

structure of investigated AF-ECB, maximum working temperature must be selected fairly low as to Curie temperature to obtain stable working condition. In this study, maximum working temperature is limited to 200 °C and it defines 170 seconds as maximum braking time. It has to be noted that all experimental studies are performed based on thermal limits of the material.

#### **2.5.4. Prototype, experimental results and comparison**

AF-ECB prototype and a test system are built to validate the design. Manufactured stator, brake disc structure and prototype ECB are demonstrated in Figure 2.21-(a). Stator and brake disc are made by ST37 low carbon steel and stator slots are cut by laser cutting technology. Concentrated windings are employed and connected in series. The test system displayed in Figure 2.21-(b) is manufactured to validate and control the AF-ECB. The test set-up consists of a drive motor, dSPACE 1104 control board, and torque-meter. The drive-motor used in the test system has 0-3000 min<sup>-1</sup> controllable speed range with 47.5Nm torque value with extremely high output torque quality.

Firstly, open-loop responses of the prototype are investigated to validate the braking torque profile obtained from MEC and 3D-FEAs. The tests are performed at the rated current and for various speeds. It should be noticed that temperature variation in the brake disc is not allowed during tests. The comparison of braking torque profiles obtained from nonlinear magnetic modeling, 3D-FEA and the experiments are given in Figure 2.22. In general, good agreement between nonlinear magnetic modeling, 3D-FEA and experiments results is achieved. However, over the speed of 700 min<sup>-1</sup>, the braking torque variation obtained from 3D-FEA is in stable region while the experimental data and the nonlinear magnetic modeling results are still in increasing region. Therefore, it can be stated that at high speeds, nonlinear magnetic modeling give more practical results than the 3D-FEA.

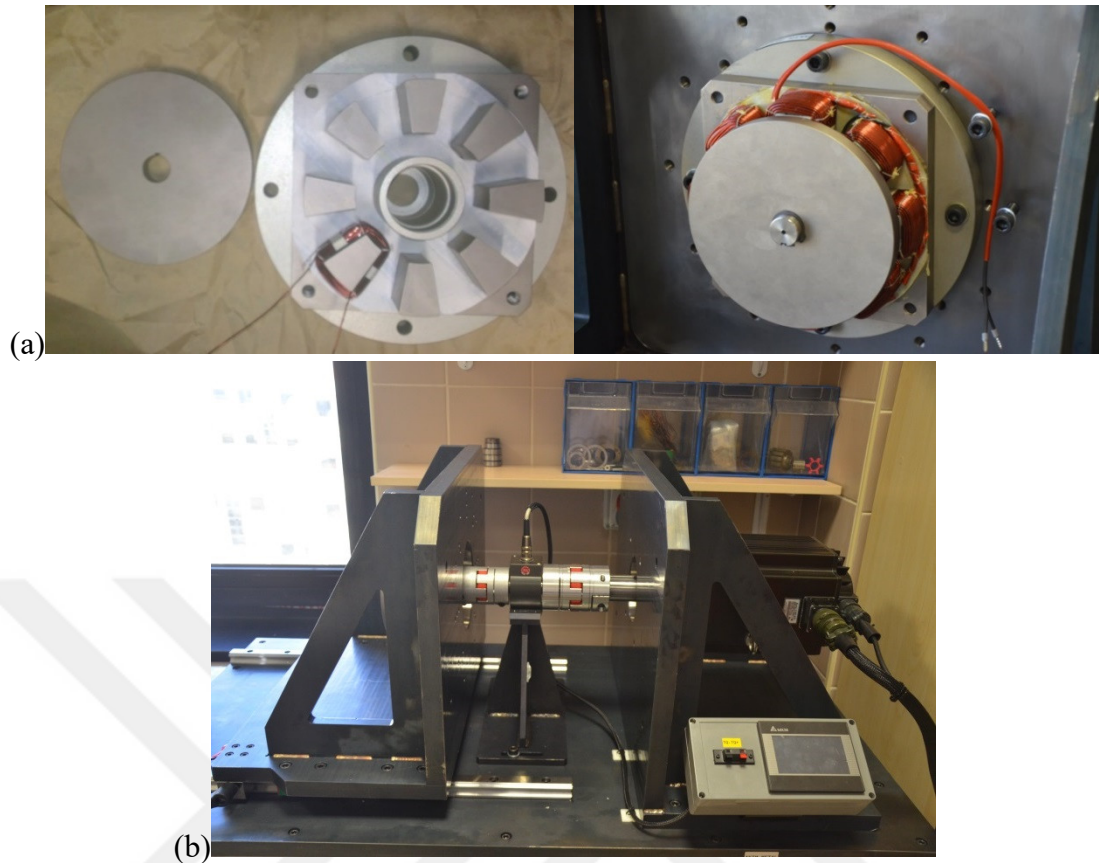


Figure 2.21. (a) Manufactured stator, brake disc and assembled AF-ECB and (b) test setup [63]

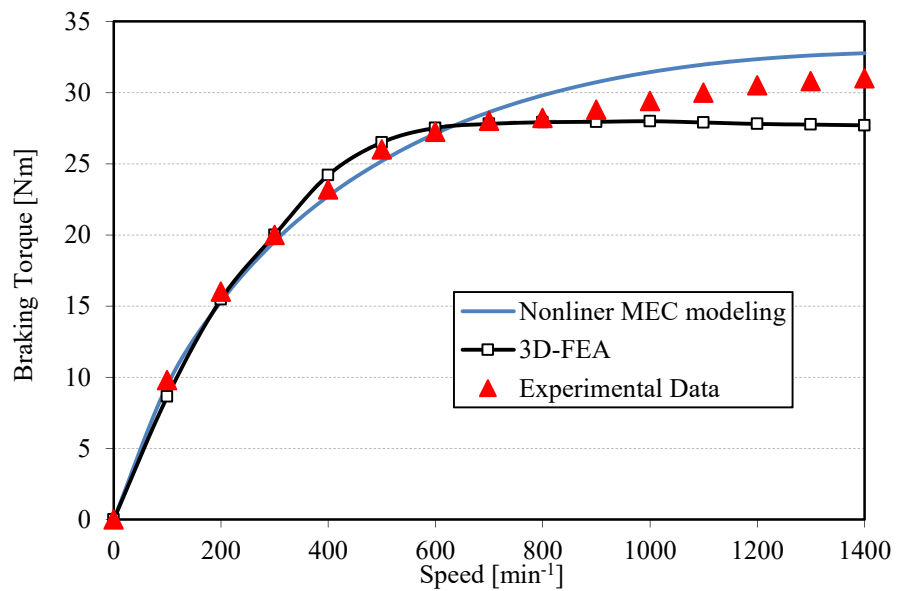


Figure 2.22. Comparison of the braking torque profiles of the AF-ECB obtained from nonlinear magnetic modeling, 3D-FEA and the experiments



Thermal validation is the other key issue in the integrated design process of AF-ECB and thermal analyses must be performed to determine the maximum braking time. Variation of temperature on brake disc is measured by a multi spot infrared thermometer at  $1000 \text{ min}^{-1}$  and the rated excitation current. Comparison of temperature variation obtained by thermal 3D-FEA and experiments is given in Figure 2.23. Results show that the thermal 3D-FEA results match well with the test data. Brake disc temperature is measured  $162 \text{ }^\circ\text{C}$  and calculated  $176 \text{ }^\circ\text{C}$  after 210 seconds at the rated excitation current.

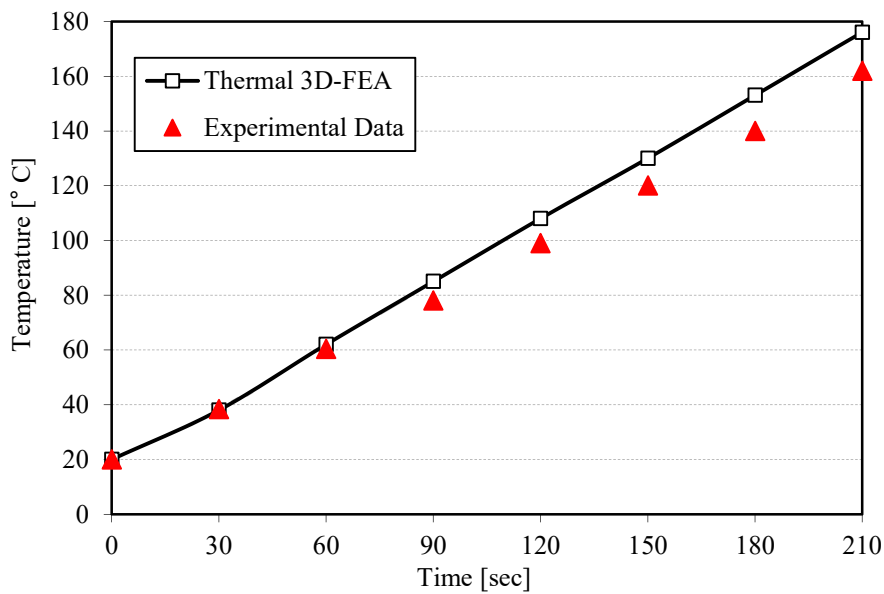


Figure 2.23. Comparison of the temperature rise in the brake disc obtained from thermal 3D-FEA and the experiments [63]

A real time dynamic torque control is performed for the designed AF-ECB to see the dynamic responses. The real time control blocks consist of reference signal selector which provides different torque commands, PI controller and PWM are designed on Simulink and applied by dSPACE 1104 controller board. The overall test system has an H-bridge MOSFET drive, a prototype AF-ECB, a torque meter and a drive servo motor. Real time control system of AF-ECB is illustrated in Figure 2.24. H-bridge MOSFET driver, which supports 5.5 to 55 V range, continuous 9 A current and 40 kHz maximum operating frequency, is employed at 20 kHz PWM frequency. In addition, MOSFETs have  $10 \text{ m}\Omega$  on resistance value which is very low compared to DC coil resistance of  $4.2 \text{ }\Omega$  of the prototype AF-ECB.

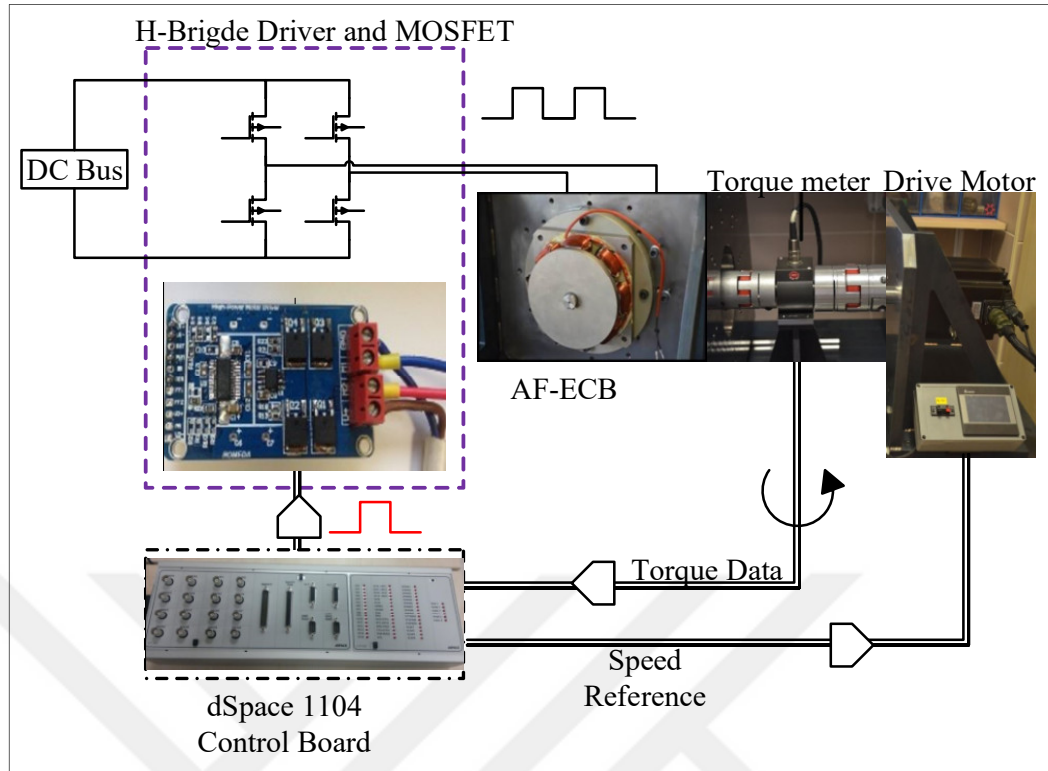


Figure 2.24. Real-time control system of AF-ECB [63]

To perform the dynamic torque control and simulate different industrial scenarios, various speed and torque commands are applied to the system. Waveforms of the speed inputs are applied to drive motor as analog signals via dSPACE 1104. Similarly, the reference torque signals are compared with measured torque data from the torque meter. PI block generates appropriate control signal, which determines the duty cycles of the MOSFETs. Consequently, drive servo motor rotates the AF-ECB at the desired speed values based on the analog signals and the torque reference commands are applied to the AF-ECB when the system rotates at different speeds. Three different torque references (step, sinusoidal and square) and speed values (constant, sinusoidal and triangular) are applied to the AF-ECB system and Table 2.3 shows these torque and speed combinations. In addition, the goal of the dynamic torque control is to indicate that the AF-ECB can be controlled by a basic techniques including PI and to show the dynamic behaviors of the AF-ECB. The proportional parameter of 2 and integral parameter of 0.6 is used under the sample time of 0.001 seconds. It has to be mentioned that there has to be no precise tuning, when the real time control system is fast for the first order systems (RL).

Table 2.3. Reference signals for braking torque and speed values

Speed\Torque	Step	Sinusoidal	Square
Step	✓	✓	✓
Sinusoidal	✓	✓	✓
Triangle	✓	✓	✓

Torque control responses of the AF-ECB at the constant speed of  $1000 \text{ min}^{-1}$  are illustrated in Figure 2.25. As seen from Figure 2.25-(a), torque commands that has 30 Nm at the speed of is tracking the reference signal as desired with no oscillation, no overshoot and zero steady state error. The sine and square wave torque commands which have 30 Nm peak value are applied as a reference signal at the speed of  $1000 \text{ min}^{-1}$  and the test results are given in Figure 2.25-(b and c). Although there is a small deflection on the sine tracking, the torque response is tracking the reference signal as desired. It is clearly shown that square wave trajectory tracking result has no overshoot and no zero steady state error and it is tracking the reference as desired.

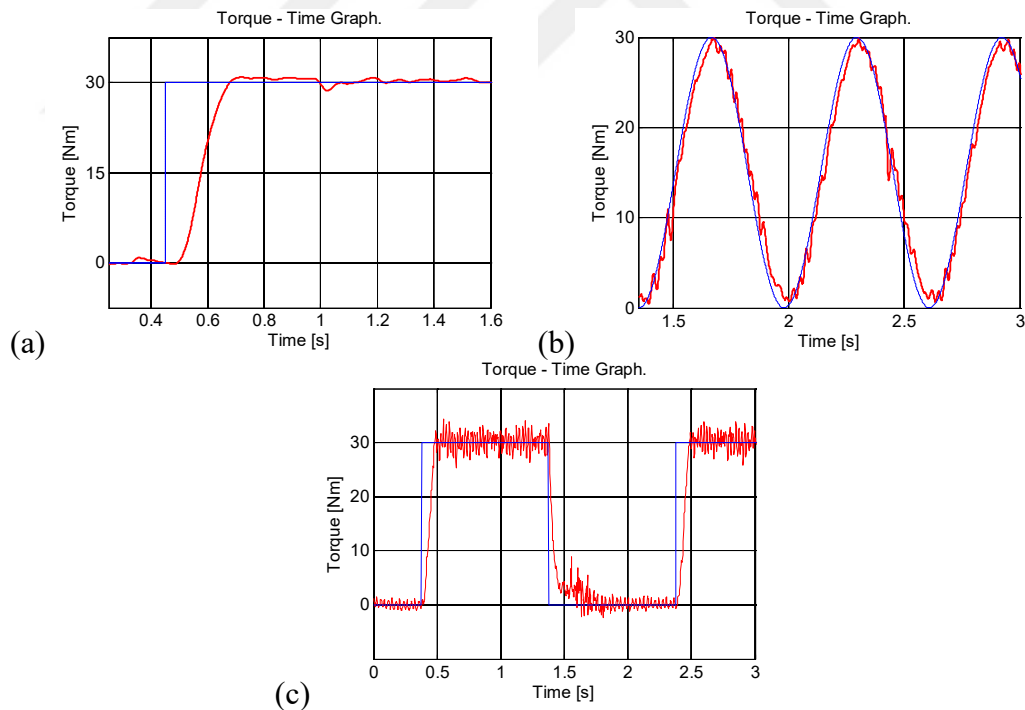


Figure 2.25. Responses of torque control at the speed of  $1000 \text{ min}^{-1}$ : (a) 30 Nm step, (b) 0-30 Nm sine and (c) 0-30 Nm square wave loads [63]

The reference square wave, sine wave and step signal torque commands of 25 Nm peak value are applied to the AF-ECB during sinusoidal speed input. The test results are given in Figure 2.26. It is seen that although the experimental results are

satisfactory, some deflection occurs on the sine trajectory tracking and there exists 4% steady state error on the step response. Moreover, square wave torque response is tracking the reference signal as desired with no oscillation, no overshoot and no zero steady state error.

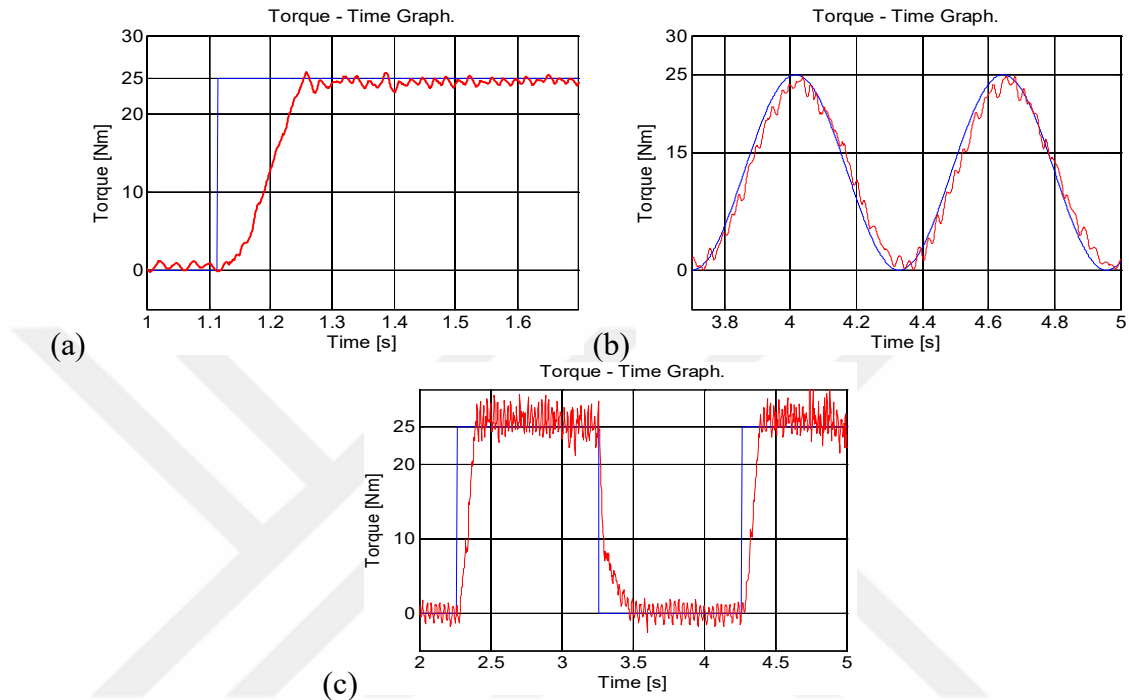


Figure 2.26. Responses of torque control at the 600-1400 of sine speed (a) 25 Nm step, (b) 0-25 Nm sine and (c) 0-25 Nm square wave loads [63]

The sine and the square wave trajectory tracking and the step signal responses are all given in Figure 2.27. Each torque command of 25 Nm peak is applied to the AF-ECB during at triangle speed input. As seen from Figure 2.27, the torque responses are tracking the reference value as expected.

It can be concluded, all test results are acceptable when the system dynamics are considered. The torque responses are tracking the whole reference signal as desired. Although the step responses have no oscillation, no overshoot and zero steady state error, the sine-wave trajectory tracking results have some deflection at changing times. If the optimum PI parameters are determined for all reference torque commands, it can be changed to improve sine-wave trajectory tracking response.

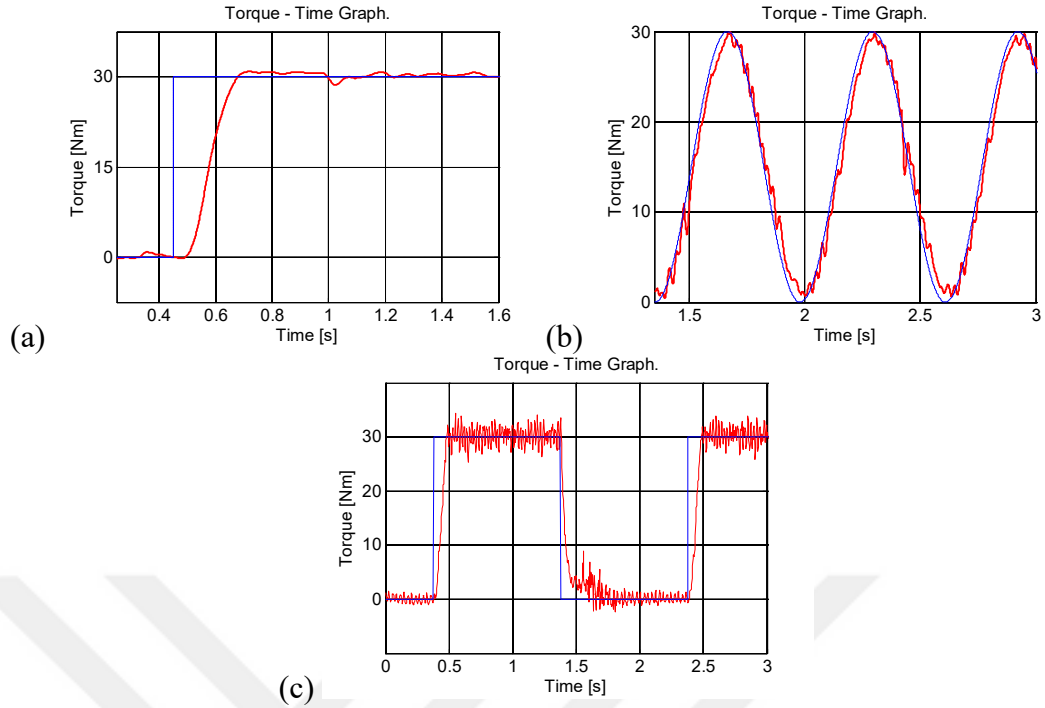


Figure 2.27. Responses of torque control at the 600-1400  $\text{min}^{-1}$  of triangular speed (a) 25 Nm step, (b) 0-25 Nm sine and (c) 0-25 Nm square wave loads [63]

## 2.6. Modeling and Analysis of a Radial-Flux PM-ECB

In this section, modeling and analysis of a radial flux PM-ECB is investigated. A quasi-3-dimensional (3D) analytical modeling approach based on a reluctance network considering the actual structure of the reference PM-ECB is proposed and verified. Gauss-Siedel method is used as nonlinear solver for the reluctance network modeling and the braking torque is calculated considering both skin effect and the armature reaction. The nonlinear analytical modeling is validated by 3D-FEA and the experimental data.

### 2.6.1. Introduction

The radial-flux (RF) PM-ECB is used as a speed limiter of an internal torsional spring lifting system in a household roller shutter. According to the measurements of the roller shutter, a smooth drag force is calculated at 0.65 m/sec, which corresponds to a rotational speed of  $300 \text{ min}^{-1}$ , and the length required for the ECB of the roller shutter is calculated to be 40 mm by [64]

$$T = S\sigma_{F_{\tan}} r \quad (2.33)$$

where  $T$  is the torque,  $S$  is the active rotor surface area,  $r$  is the radius of the air gap, and  $\sigma_{F_{tan}}$  is the tangential stress, which is assumed to be 1.5 kPa.

A 3D view of the RF-PM-ECB is given in Figure 2.28. The brake has eight poles, and two PM stacks are used to obtain the total active axial length. The benefit of using two PM stacks is the easy assembly in automatic production as the magnets are placed in a plastic support. The key parameters of the RF-PM-ECB are given in Table 2.4. The outer diameter of the brake is 32.6 mm, and its total axial length is 55 mm. The dimensions of one piece of permanent magnet are  $4 \times 3 \times 20 \text{ mm}^3$ , and the total PM mass in the RF-PM-ECB is 28.8 g.

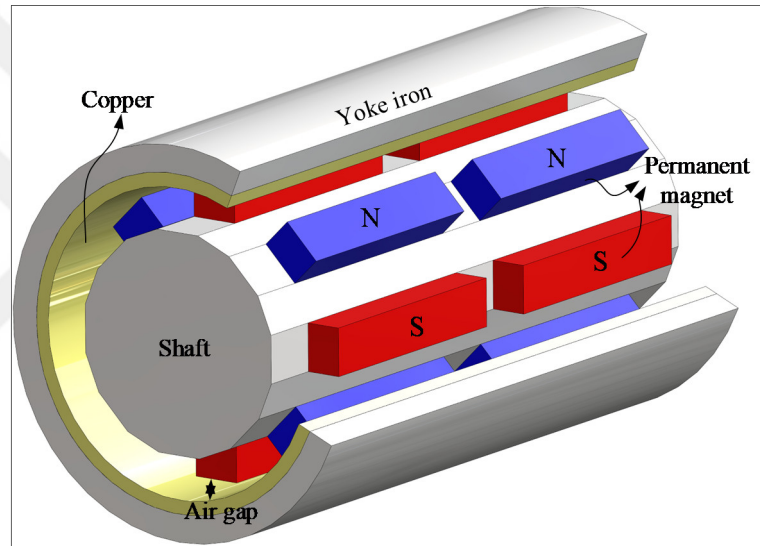


Figure 2.28. 3D view of the RF-PM-ECB

Table 2.4. Key parameters of the PM-ECB

Parameters	Value
Outer radius	32.6 mm
Mechanical air gap	0.5 mm
Total axial PM length	40 mm
Total axial length	55 mm
Overhang length	5 mm
Copper thickness	1.17 mm
Yoke thickness	2.3 mm
Rated speed	$330 \text{ min}^{-1}$

## 2.6.2. Nonlinear 2D reluctance network modeling

The magnetic flux density in the conductive regions should be accurately calculated to obtain a correct braking torque. In this subsection, 2D nonlinear reluctance-network-based magnetic modeling is investigated as an analytical approach. The reluctance network modeling relies on a rectangular-element-based mesh structure over the entire model, and all the mesh structure elements have x- and y-axis reluctances in both positive and negative directions. In the method, the mesh structure is determined by the complexity of the model. By the network model, all flux paths can be determined with a high precision, and predesign outputs can be quickly obtained [65, 66].

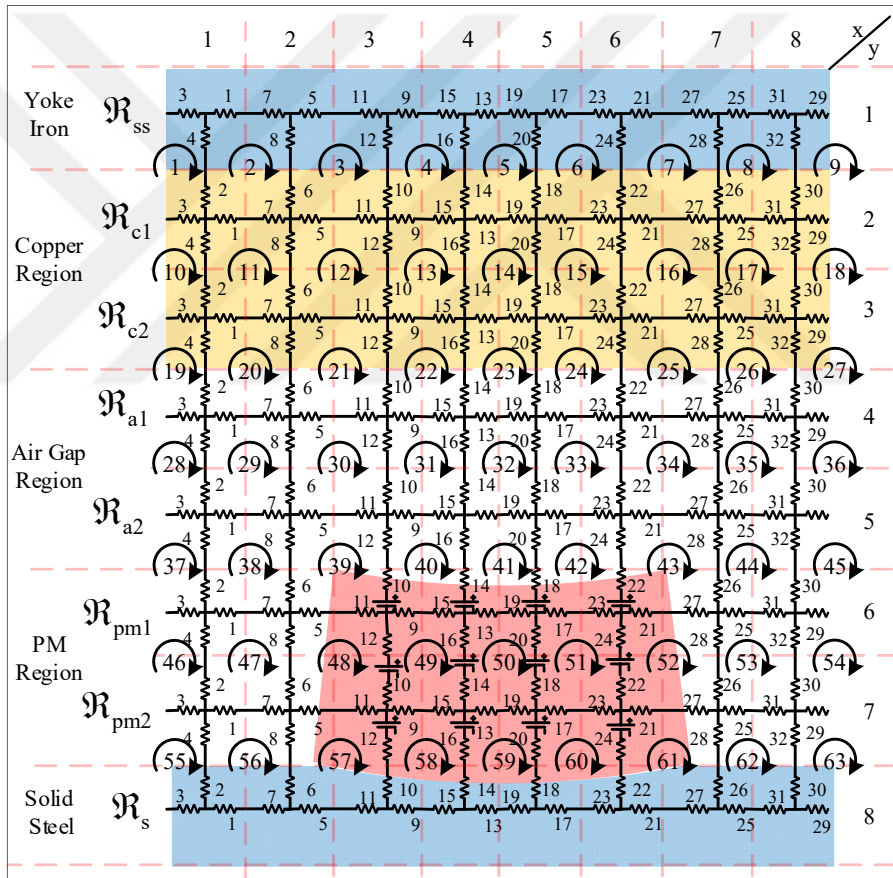


Figure 2.29. 2D reluctance network model of the RF-PM-ECB considering a flat-shaped PM

The RF-PM-ECB has eight poles, and therefore, it can be modeled by a 1/8 symmetric model. A symmetric reluctance network model of the RF-PM-ECB is given in Figure 2.29. All nonmagnetic regions, such as copper, air gap, and PM, are modeled by two

horizontal layers to increase the solution accuracy. In total, a 7-to-9 mesh structure is developed for the symmetry model.

It is important to consider the actual flat-shaped PM geometry in the 2D nonlinear reluctance network model as the PM geometry plays a critical role in the brake performance. The actual flat-shaped PM geometry is linearized and a variable air-gap structure is obtained by an arc-shaped trapezoid PM geometry, which has cylindrical reluctances defined as [66]

$$\mathfrak{R}_x = \frac{1}{\mu_0 \mu_{pm}} \frac{\alpha_{PM}}{\log\left(\frac{r_{PM}}{r_{shaft}}\right) d} \quad (2.34)$$

$$\mathfrak{R}_y = \frac{1}{\mu_0 \mu_{pm}} \frac{1}{\alpha_{PM} d} \log\left(\frac{r_{PM}}{r_{shaft}}\right) \quad (2.35)$$

where  $\mu_{pm}$  is the relative permeability of the PM,  $\alpha_{PM}$  is the PM angular width,  $d$  is the axial length,  $r_{PM}$  is the radius of the PM, and  $r_{shaft}$  is the shaft radius. After calculating the PM cylindrical reluctances, the sub reluctances related to the mesh structure are

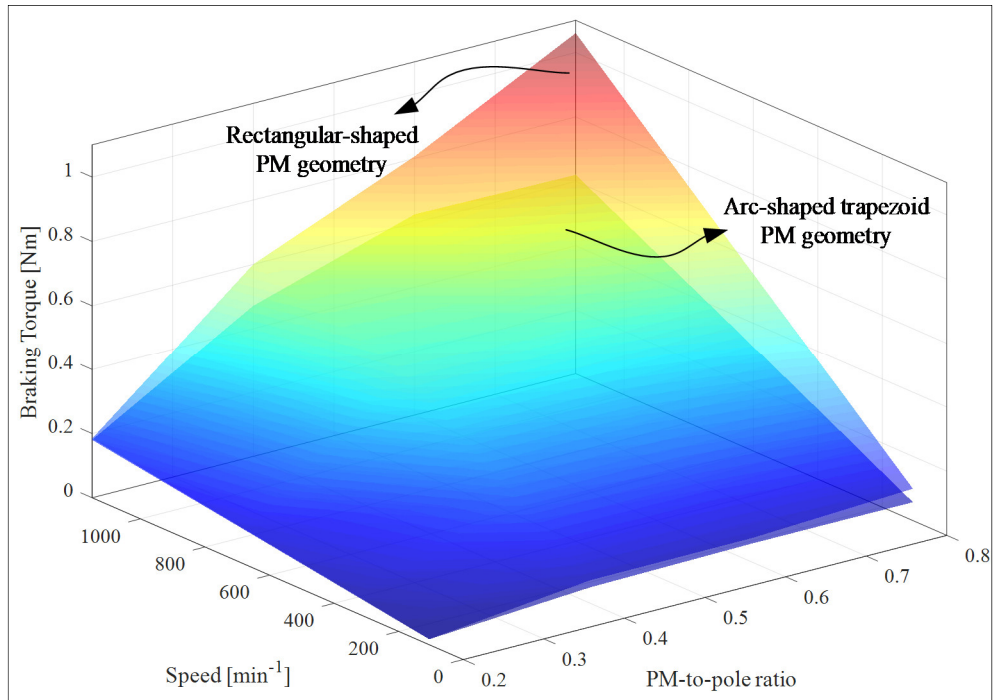


Figure 2.30. Comparison of the braking torque profiles obtained from the rectangular-shaped PM geometry and the arc-shaped trapezoid geometry



distributed. A parametric study is performed to examine the arc-shaped trapezoid PM geometry. The braking torque profiles obtained from the rectangular PM geometry and the arc-shaped trapezoid geometry are given in Figure 2.30. It is clear that the difference between the two geometries is greatly increased when the PM width increases, which is unacceptable. Therefore, considering the actual flat-shaped PM geometry is vital for the analytical approach.

MATLAB<sup>®</sup> software is used to develop the network model and nonlinear analyses. All the reluctances, meshes and current linkages are created automatically with loops after determining the variables. The size of 63×63 main reluctance matrix, the size of the 1×63 current linkage matrix, and the flux matrix related to the rectangular-based meshes are defined as

$$\begin{bmatrix} \varphi_1 \\ \varphi_2 \\ \varphi_3 \\ \vdots \\ \varphi_{63} \end{bmatrix} = \begin{bmatrix} \mathfrak{R}_1 & \mathfrak{R}_{1-2} & \mathfrak{R}_{1-3} & \cdots & \mathfrak{R}_{1-63} \\ \mathfrak{R}_{2-1} & \mathfrak{R}_2 & \mathfrak{R}_{2-3} & \cdots & \mathfrak{R}_{2-63} \\ \mathfrak{R}_{3-1} & \mathfrak{R}_{3-2} & \mathfrak{R}_3 & \cdots & \mathfrak{R}_{3-63} \\ \vdots & \vdots & \vdots & \ddots & \vdots \\ \mathfrak{R}_{63-1} & \mathfrak{R}_{63-2} & \mathfrak{R}_{63-3} & \cdots & \mathfrak{R}_{63} \end{bmatrix}^{-1} \begin{bmatrix} \mathfrak{I}_1 \\ \mathfrak{I}_2 \\ \mathfrak{I}_3 \\ \vdots \\ \mathfrak{I}_{63} \end{bmatrix} \quad (2.36)$$

where  $\varphi$  is the flux,  $\mathfrak{R}$  is the reluctance, and  $\mathfrak{I}$  is the current linkage. The subscripts of the parameters represent the related fluxes and their adjacent fluxes (only for reluctances). For example,  $\mathfrak{R}_{2-3}$  is defined as

$$\mathfrak{R}_{2-3} = \mathfrak{R}_{ss}(8) - \mathfrak{R}_{cl}(6) \quad (2.37)$$

Nonlinear analysis is required since the yoke is made from solid steel and it has naturally eddy-current reaction. In addition, the sensitive model is essential for the optimization problem. A low carbon steel [67] is used in solid steel parts and the resistivity of the yoke is taken as  $25 \times 10^{-8} \Omega \cdot m$ . Gauss-Siedel method with relaxation is preferred for 2D reluctance network model. The flowchart of the nonlinear method for the 2D reluctance network model is given in Figure 2.31. The nonlinear method consists of two Gauss-Siedel stages so that the main iteration calculates the magnetic flux densities and updates the BH curve. In the subiteration, fluxes are updated and calculated. The investigated nonlinear method enables much less time consuming than single iteration (conventional) approach. In MATLAB software, single iteration

Gauss-Siedel method takes 9.8 seconds while the investigated method takes 6.1 seconds. When any optimization process is considered, less time consuming computations play critical role. All required errors ( $\epsilon$ ) in the Gauss-Siedel method are set to 0.0001% and the value of 0.5 relaxation factor is utilized during the design.

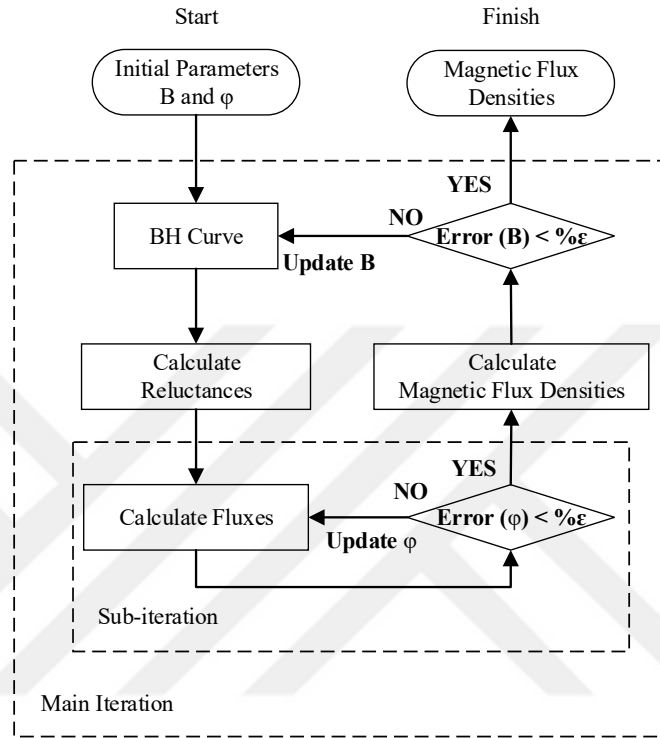


Figure 2.31. The flowchart of the nonlinear method for the 2D reluctance network model

Because of the overhang structure of the PM-ECB, the analytical approach should be improved to obtain correct results in practice. The 3D magnetic flux density profiles obtained by the analytical and 3D-FEA approaches are given in Figure 2.32 to demonstrate the difference. It is clearly seen that the analytical approach does not match the actual 3D model. In this section, the effect of the overhang is taken into account by the well-known Carter's theory [68]. The magnetic thicknesses of the nonmagnetic regions (air gap and copper) are expressed by magnetic equivalents as

$$g_{k_c} + h_{Cu k_c} = (g + h_{Cu}) k_C \quad (2.38)$$

where  $g$  is the air gap,  $h_{Cu}$  is the copper thickness, and  $k_C$  is Carter's factor defined as

$$k_c = \frac{t_1}{t_1 - y_1 (g + h_{Cu})} \quad (2.39)$$

where  $t_1$  is the slot pitch defined as

$$t_1 \approx 2l_{oh} + 0.5l_{stk} \quad (2.40)$$

where  $l_{oh}$  is the axial overhang length and  $l_{stk}$  is the total axial PM length. The factor of  $y_1$  is defined as

$$y_1 = \frac{4}{\pi} \left( \frac{2l_{oh}}{2g} \arctan \left( \frac{2l_{oh}}{2g} \right) - \ln \sqrt{1 + \left( \frac{2l_{oh}}{2g} \right)^2} \right) \quad (2.41)$$

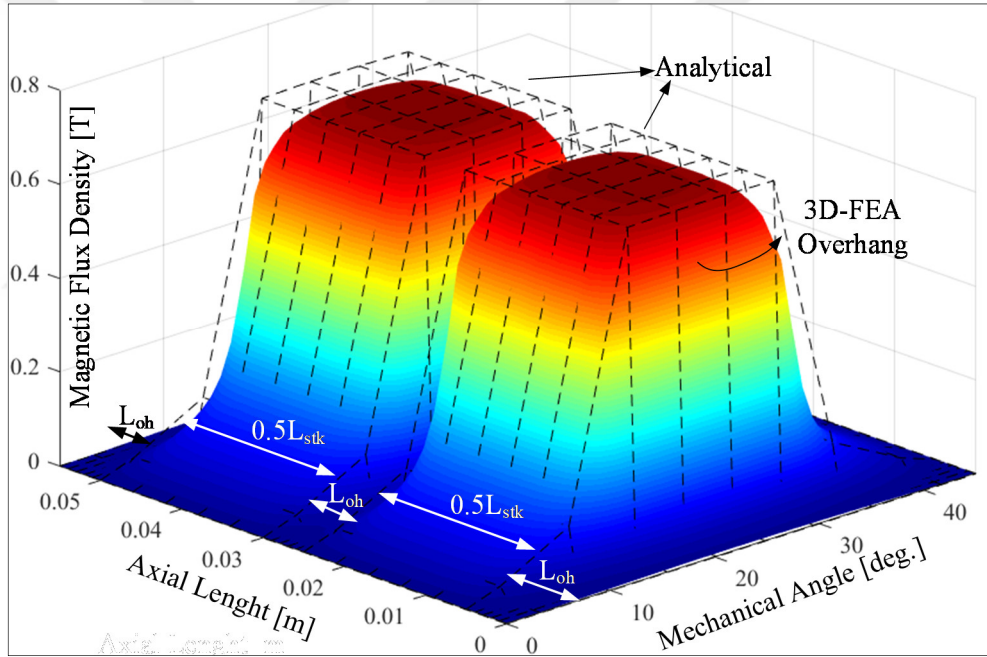


Figure 2.32. 3D Magnetic flux density profile of the reference PM-ECB in the middle of the air gap obtained by the analytical and 3D-FEA considering overhang

The nonlinear 2D reluctance network model is modified and a quasi-3D analytical reluctance network model is achieved. The most important benefit of the quasi-3D analytical approach is the simple and accurate calculation of the braking torque. The following steps are carried out to obtain the braking torque: (1) Calculate the magnetic flux density for all vertical reluctances in the copper and yoke regions, (2) update the magnetic flux densities by armature reaction, (3) calculate the current density

separately for all related reluctances, (4) calculate power for all related reluctances considering their radius, (5) calculate the braking torque for each reluctance as below and sum. To validate the proposed quasi-3D analytical modeling, several design cases are evaluated and the results are compared with the 3D-FEA. The details are given in Table 2.5. It is clearly shown that the quasi-3D analytical approach works as expected.

Table 2.5. Validation of the quasi-3D analytical modeling

	PM-ECB	Design 1	Design 2	Design 3
Total PM mass	28.8 g	28.8 g	28.8 g	28.8 g
PM-to-pole ratio	0.41	0.6	0.2	0.5
Pole number	8	12	16	4
Copper thickness	1.17 mm	1.17 mm	2 mm	0.5 mm
		Braking torque at 330 min <sup>-1</sup>		
Quasi-3D Analytical	0.144 Nm	0.159 Nm	0.6 Nm	0.128 Nm
3D-FEA	0.142 Nm	0.157 Nm	0.59 Nm	0.135 Nm

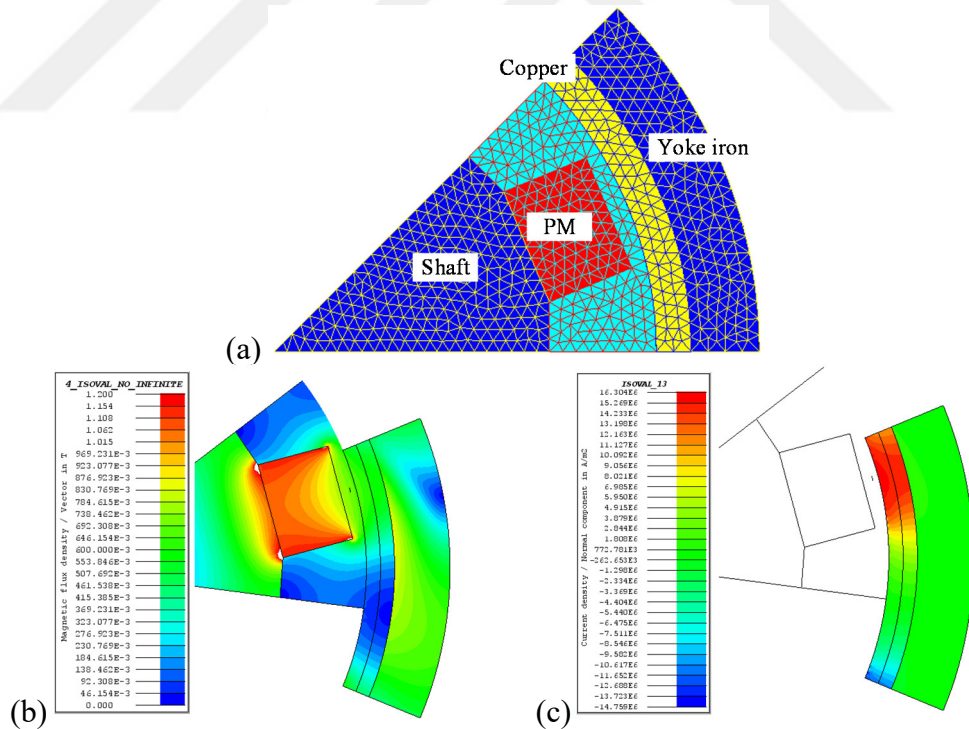


Figure 2.33. 2D-FE symmetry model of the PM-ECB: (a) mesh structure, (b) magnetic flux density profile, and (c) current density profile at the speed of 330 min<sup>-1</sup>

### 2.6.3.3D-FEA

Firstly, 2D-FEA model with mesh profile is described in Figure 2.33-(a) to demonstrate the structure of the PM-ECB. The Altair Flux v11.3 software is used in the FEA simulations. The symmetry model is taken into account, and the magnetic flux density and current density profiles at the speed of  $330 \text{ min}^{-1}$  are given in Figure 2.33-(b)-(c), respectively. The figure shows that the maximum magnetic flux density in the yoke is  $0.7 \text{ T}$ , and the maximum current density in the copper is  $16.3 \times 10^6 \text{ A/m}^2$ .

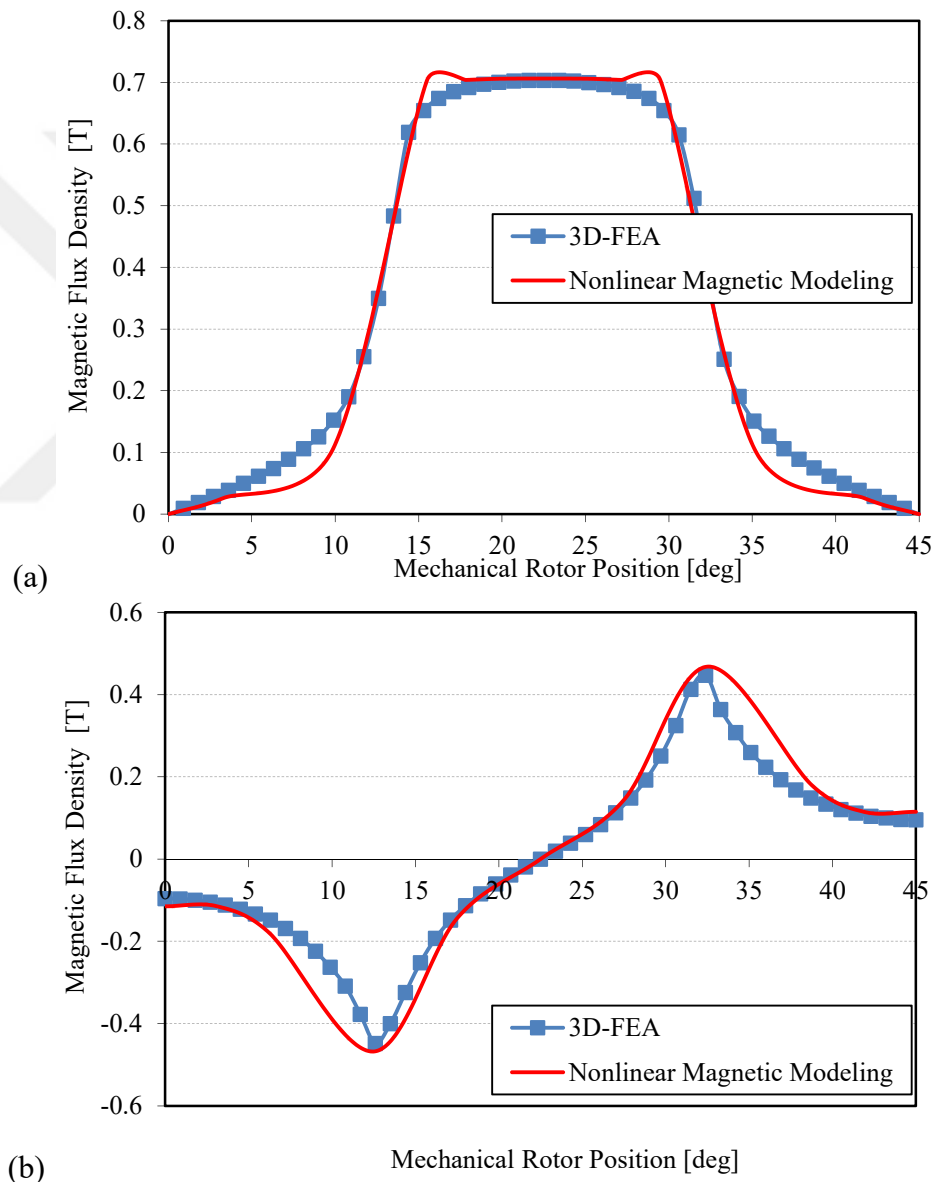


Figure 2.34. Comparison of the reference and the optimized PM-ECB: (a) normal and (b) tangential components of the magnetic flux density in the air gap with both nonlinear reluctance network modeling and 3D-FEA approaches

Comparison of the results obtained from 2D-FEA and the quasi-3D analytical modeling approach is vital to validate the proposed approach. The normal and tangential components of the air gap magnetic flux density profile for the RF-PM-ECB are given in Figure 2.34. The maximum normal magnetic flux density of 0.7 T is both obtained by nonlinear analytical approach and the 3D-FEA. The results obtained from the quasi-3D analytical modeling approach and the 3D-FEA agree quite well.

A series of simulations are carried out by the FEA for validation. To highlight the effect of overhang structure, 2D-FEA, 3D-FEA and 3D-FEA with overhang structures are investigated. The FE models of the RF-PM-ECB are given in Figure 2.35. It is clear that the 2D-FEA is the fastest way among all and the 3D-FEA with overhang structure is the most time consuming approach, which is the most practical one.

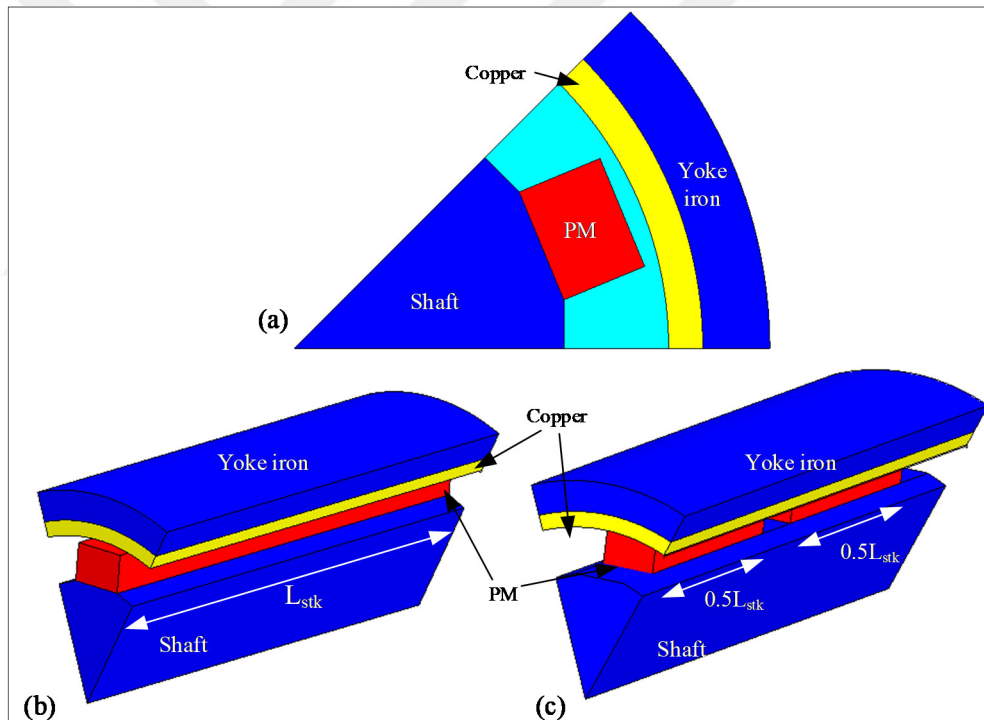


Figure 2.35. FE modeling approaches of PM-ECB: (a) 2D-FEA, (b) 3D-FEA and (c) 3D-FEA with overhang structure

The braking torque profiles obtained from 2D-FEA, 3D-FEA and 3D-FEA with overhang structure are given in Figure 2.36 to highlight the effect of overhang structure. The results show that 2D-FEA and 3D-FEA have close results while 3D-FEA with overhang structure has lower braking torque values than the other approaches. It is seen that investigated PM-ECB should be analyzed by 3D-FEA with

overhang structure. The magnetic flux density distribution of the PM-ECB is illustrated in Figure 2.37. The influence of overhang structure on flux paths is clearly seen from the figure.

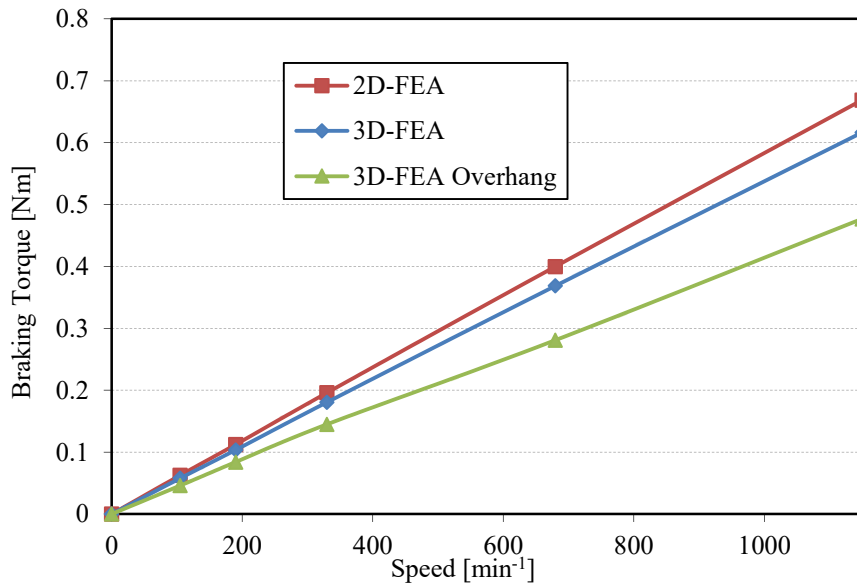


Figure 2.36. Braking torque profiles obtained from 2D-FEA, 3D-FEA and 3D-FEA with overhang structure

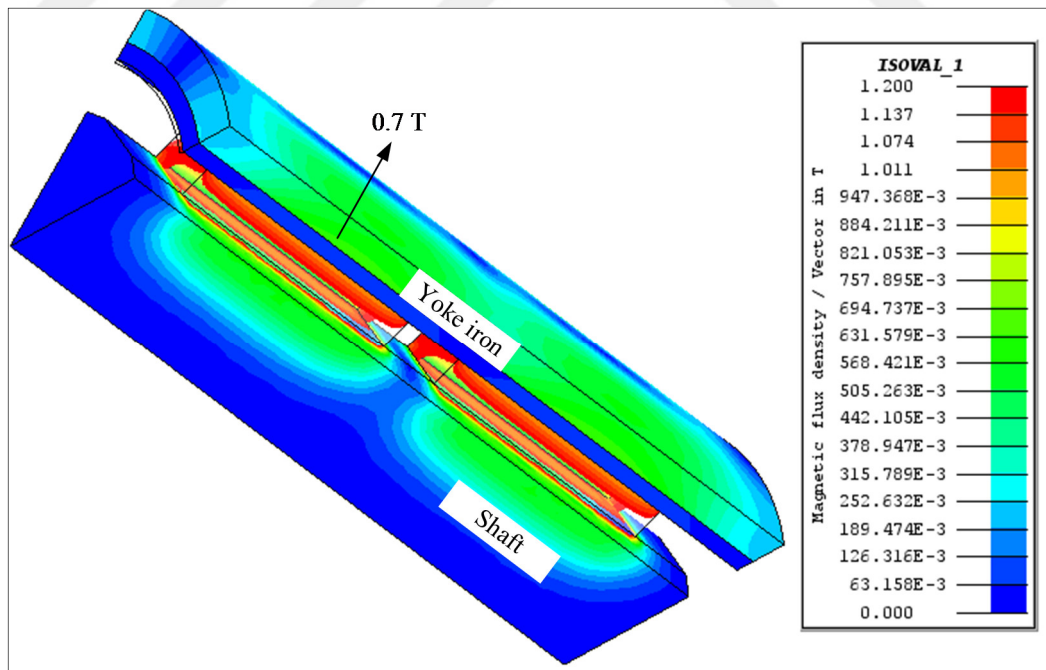


Figure 2.37. 3D magnetic flux density distribution of PM-ECB

#### 2.6.4. Prototype, experimental results and comparison

Prototype of the RF-PM-ECB is given in Figure 2.38. The materials for the reference PM-ECB were selected to be easily available standard materials with standard dimensions. The permanent magnet grade N48 was chosen for the prototype. This material has a remanence flux density from 1.37 to 1.42 T and a coercive field strength  $\geq 955$  kA.

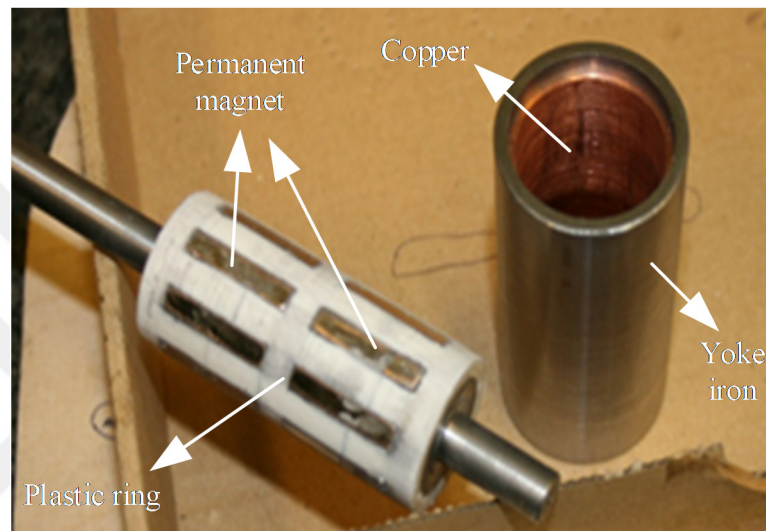


Figure 2.38. Photo of the prototype

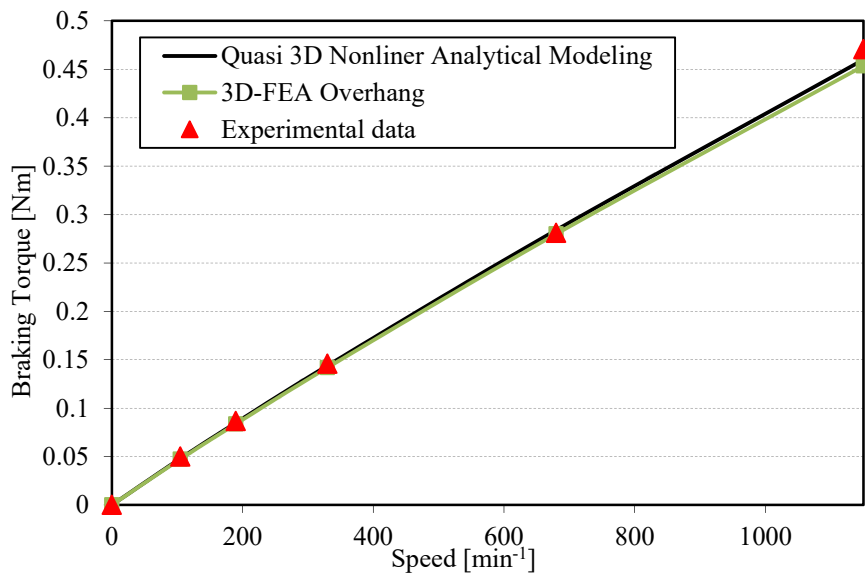


Figure 2.39. Comparison of the braking torque results obtained from the quasi-3D analytical and 3D-FEA and experimental data

The experiments are carried out for various speeds and the measured braking torque values are given in Figure 2.39 together with the quasi-3D analytical approach and the



3D-FEA. The results show that the proposed quasi-3D analytical approach is in agreement with the 3D-FEA and experimental results. Thus, the proposed quasi-3D modeling seems a trustworthy approach. Obviously, it can be used in the modeling and the design of RF-PM-ECBs of this kind.

## **2.7. Summary**

Eddy current braking theory with practical cases were investigated in this chapter. Firstly, braking torque governing approach was explained and the influence of design parameters on braking torque performances was presented. MEC modeling and nonlinear solving methods were investigated and 2 different types of ECBs were modeled and analyzed by nonlinear analytical approach and 3D-FEAs. Experimental verification and comparison of the results obtained from analytical, FEA and tests were also given in this chapter.

### **3. NOVEL NONLINEAR MULTIDISCIPLINARY DESIGN APPROACH**

A new nonlinear multidisciplinary design approach (NMDA) for eddy current brakes particularly for axial-flux (AF) eddy current brakes (ECBs) is presented in this section. The proposed NMDA consists of nonlinear coupled magnetic-thermal-structural modeling. The nonlinear behaviors of the AF-ECB covering the BH curve, resistivity, heat capacity, thermal conductivity and the temperature are jointly analyzed in time domain to investigate the actual brake properties and to determine brake operating range. In this chapter, the nonlinear magnetic modeling based on 2-dimensional (2D) reluctance network is studied by a modified Newton-Raphson method. Further, the nonlinear thermal modeling is carried out by lumped-parameters considering the change of heat capacity, thermal conductivity and temperature and updating the data in the evaluation process. Finally, nonlinear structural modeling is performed to obtain the deflection and the mechanical safety factor of the brake. The nonlinear modeling methods in the proposed NMDA are validated by independent 3D electromagnetic, thermal and structural finite element analyses (FEAs) and the proposed NMDA is tested with two different AF-ECB prototypes. The experimental results confirm that the proposed NMDA has high accuracy, and it provides a fast solution to predict the AF-ECB performance compared to cumbersome and time consuming 3D-FEA approaches.

#### **3.1. Introduction**

Due to the developments in the transportation industry, power usage has been dramatically increased to fulfil the required demand. This increased demand certainly leads to a problem concerning safety. ECBs have a great potential to solve this critical issue. They are auxiliary braking systems which provide frictionless and safe braking in the industry, especially, in commercial trucks, trains, industrial elevators and vehicle test benches. The key benefits of ECBs are fast response time and long life span compared with conventional mechanical brake systems [69, 70].

The working principle of the ECB relies on the same electromagnetic rules valid for electric machines. An ECB has a stationary part with excitation coils and/or magnets and one or more rotating/moving parts. In general, AF-ECBs are preferred because of their high braking torque densities and cooling advantages in rotating industrial applications [35, 44, 63]. The braking energy is released as heat resulting in a temperature rise in the rotating disc. The change of temperature naturally affects the physical parameters including the magnetic electrical and thermal properties [37, 71]. In addition, the brake disc is always under pulling axial force particularly ferromagnetic single-sided brake disc topologies, therefore, stresses should be also investigated for AF-ECBs. Briefly, magnetic and thermal as well as structural behaviors must be considered in the design process of an AF-ECB.

Various papers in the literature on ECBs are focused mostly on the magnetic modeling during the design stage [32, 46, 47, 72, 73]. The thermal modeling is investigated only by a limited number of papers, for example in [30, 37, 71, 74]. The structural issue has become a major issue particularly in AF topologies but this is not covered in details in the previous studies. An AF-ECB forms a multidisciplinary system in which all magnetic, thermal and structural parameters should be considered integrately during the design stage. Generally, FEA software programs in the market are focused on one physical problem as: electromagnetic or thermal or structural or aerodynamics etc. However, multidisciplinary system should be integrately analyzed to determine the whole output performances and limitations. For example, the designers cannot correctly determine the maximum braking time by only thermal FEA or the designers cannot compute the braking torque decreasing ratio in time by only electromagnetic FEA. It has to be pointed out that only limited number of software packages can offer multiphysics modeling. The handicaps of these are: they do not offer a cost-effective solution and highly experienced personnel is needed to use these software packages and multiphysics analysis specially for transient cases is a time consuming process. From the point of computation time, if the designers would like to make an optimization related to a multiphysics problem, it would probably take several months to solve. However, analytical-based multidisciplinary optimization by the proposed NMDA takes only days and does not require costly FEA tools. Therefore, analytical-

based coupled-design methods can be a good solution to tackle the above mentioned lacks.

In this chapter, a new nonlinear multidisciplinary modeling approach considering the magnetic, thermal and structural issues together is proposed and presented for the first time. Single-disc single-stator configuration of the AF-ECB is analyzed utilizing the proposed NMDA. Two different AF-ECBs with 4.5 kW and 10.5 kW braking powers are investigated by 3D electromagnetic, thermal and structural FEAs for the validation. The experimental verification of the proposed NMDA is also presented for these two cases.

### 3.2. Novel NMDA

The novel NMDA aims to consider the magnetic, thermal and structural aspects of an AF-ECB to determine the actual brake performance completely. The proposed NMDA is illustrated in Figure 3.1. The multidisciplinary design is carried out in the time domain as a quasi-transient analysis to define the braking torque, braking time, temperature variation, deflection and safety factor of the AF-ECB. The multidisciplinary design starts with the determination of the initial parameters as geometric parameters, speed, excitation current, braking time, initial temperature, magnetic flux density, resistivity, and thermal conductivity etc. In the first step, non-

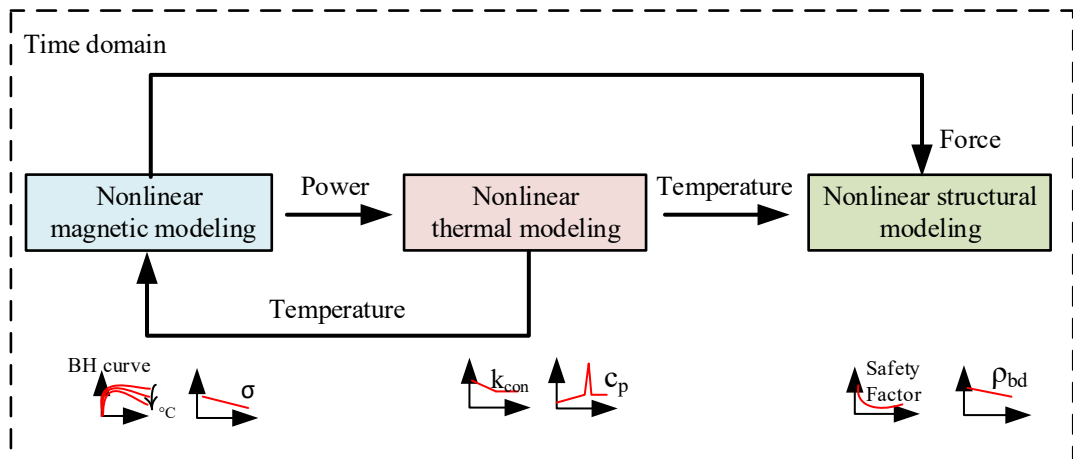


Figure 3.1. The novel NMDA.  $\sigma$  is the conductivity,  $k_{con}$  is the thermal conductivity,  $c_p$  is the heat capacity,  $\rho_{bd}$  is the volume density of the brake disc

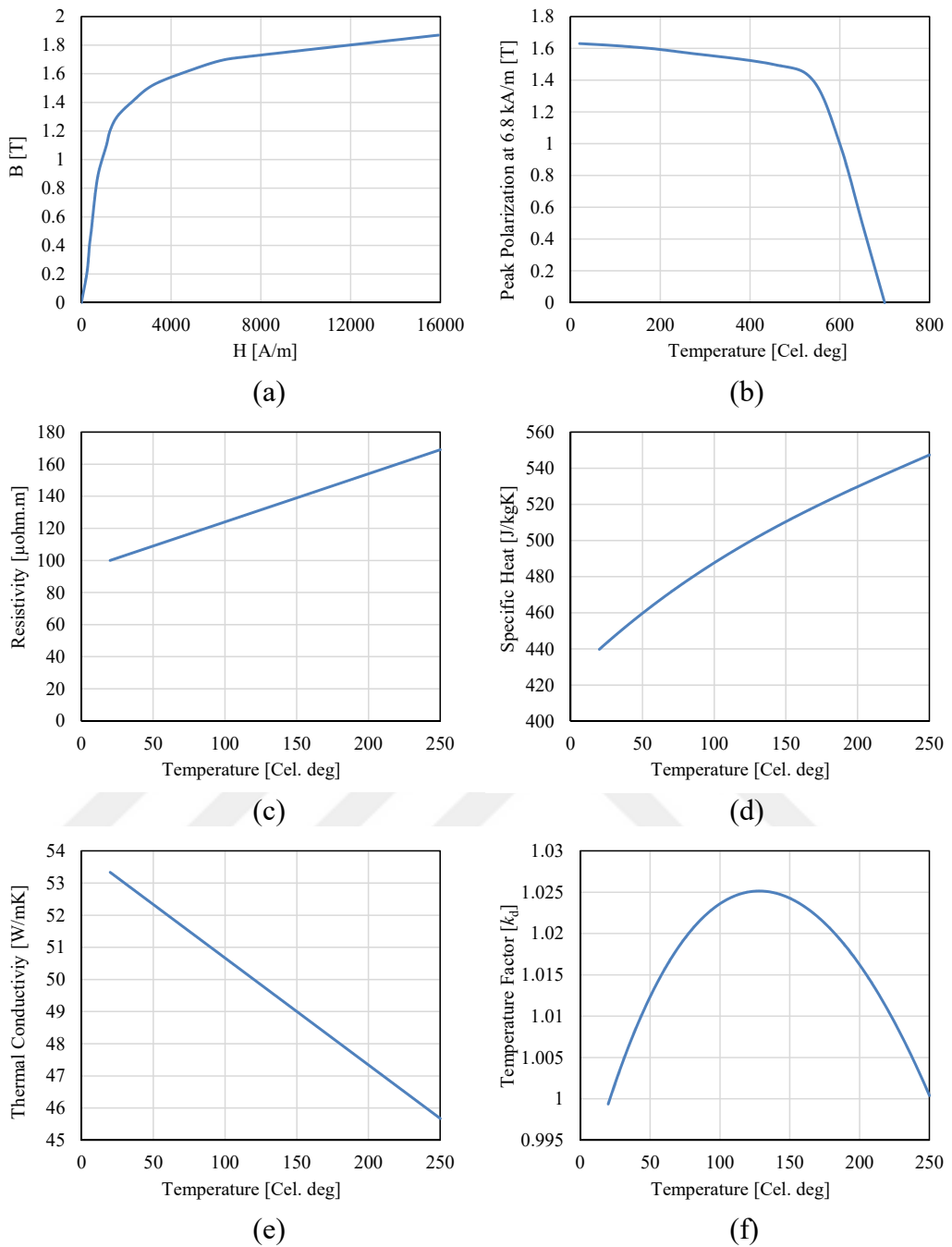


Figure 3.2. Variation of nonlinear parameters of ST37: (a) BH curve at room temperature, (b) effect of temperature on peak polarization [67] (c) resistivity, (d) heat capacity, (e) thermal conductivity and (f) temperature factor

linear magnetic modeling is evaluated and the braking torque, power dissipation in the brake disc and the force affecting the disc are calculated. Then, the power dissipation is used in the nonlinear thermal modeling as an input source to calculate the disc temperature by thermal lumped parameter model. The calculated temperature affects the heat capacity, thermal conductivity, BH curve, resistivity, density and temperature

factor of the AF-ECB. In the last step, the force created is used in a nonlinear structural modeling to calculate the deflection and the safety factor of the disc. The nonlinear parameters are updated in each time-step, which is one second for all analyses, and this process is repeated until the specified error is fulfilled. Details about nonlinear parameters (BH curve, resistivity, heat capacity and temperature factor) are all provided in Figure 3.2.

### 3.2.1. Nonlinear magnetic modeling

In this case, the nonlinear magnetic modeling is carried out by 2D reluctance network approach. The AF machines can be modeled by 2D approaches [77-79] so that the 2D linearized symmetry model of AF-ECB is used in the proposed NMDA. The 2D symmetry model, which is related to the slot number, consists of one stator tooth and one slot. The network model is a kind of analytical meshing approach in which the x- and y-axis reluctances are placed in the defined regions as required. The number of regions used in the model is 12 and the regions are described here. The symmetry and the reluctance network models of an open-slot AF-ECB are illustrated in Figure 3.3. Two parameters are used in the reluctance notation,  $\mathfrak{R}_{i,j}$ , where  $i$  represents the region and  $j$  represents the ranking info. The ranking is assigned with respect to anticlockwise rotation from 1 to 4. 12 flux loops are also defined according to the regions and finally a main matrix is created to solve the network modeling described as

$$\begin{bmatrix} \varphi_1 \\ \varphi_2 \\ \varphi_3 \\ \vdots \\ \varphi_{12} \end{bmatrix} = \begin{bmatrix} \mathfrak{R}_1 & \mathfrak{R}_{1-2} & \mathfrak{R}_{1-3} & \cdots & \mathfrak{R}_{1-12} \\ \mathfrak{R}_{2-1} & \mathfrak{R}_2 & \mathfrak{R}_{2-3} & \cdots & \mathfrak{R}_{2-12} \\ \mathfrak{R}_{3-1} & \mathfrak{R}_{3-2} & \mathfrak{R}_3 & \cdots & \mathfrak{R}_{3-12} \\ \vdots & \vdots & \vdots & \ddots & \vdots \\ \mathfrak{R}_{12-1} & \mathfrak{R}_{12-2} & \mathfrak{R}_{12-31} & \cdots & \mathfrak{R}_{12} \end{bmatrix}^{-1} \begin{bmatrix} 0 \\ 0.5\mathfrak{I} \\ 0.5\mathfrak{I} \\ \vdots \\ 0 \end{bmatrix} \quad (3.1)$$

where the flux loops are represented by  $\varphi$ , reluctances by  $\mathfrak{R}$  and current linkages are symbolized by  $\mathfrak{I}$ . The subnumber of the reluctances describes related flux loop numbers. For example,  $\mathfrak{R}_1$  represents the reluctances linked only by the first flux loop ( $\varphi_1$ ) and  $\mathfrak{R}_{1-2}$  represents the mutual reluctances of the first ( $\varphi_1$ ) and the second ( $\varphi_2$ ) flux loop.  $\mathfrak{R}_1$  and  $\mathfrak{R}_{1-2}$  are described by

$$\mathfrak{R}_1 = \mathfrak{R}_{1,3} + \mathfrak{R}_{1,4} + \mathfrak{R}_{4,2} + \mathfrak{R}_{4,3} \quad (3.2)$$

$$\mathfrak{R}_{1-2} = \mathfrak{R}_{1,4} + \mathfrak{R}_{4,2} . \quad (3.3)$$

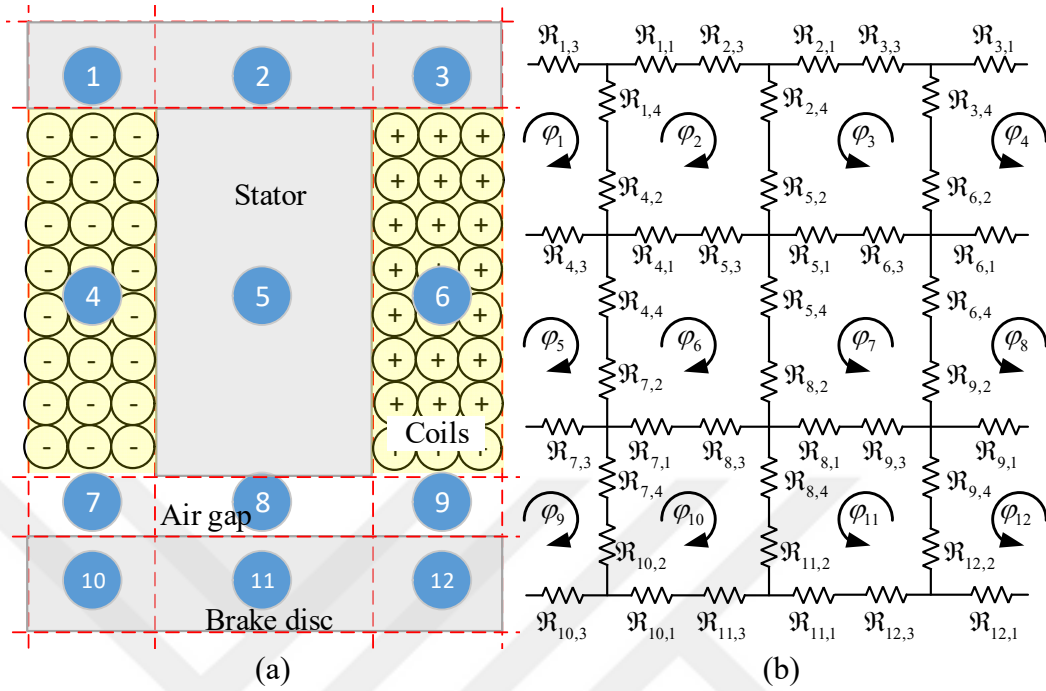


Figure 3.3. (a) 2D symmetry and (b) reluctance network model of the AF-ECB

A modified Newton-Raphson method is applied to the reluctance network model as a nonlinear solver. The flowchart of the Newton-Raphson method is given in Figure 3.4. The Newton-Raphson method starts with setting initial parameters. The reluctances are firstly calculated based on the initial parameters from the material BH curve. Then, Newton-Raphson functions and their differentials are derived and the magnetic flux density of the reluctances are calculated. Next, the error on the magnetic flux density is compared with a certain value and if it is below than desired, the Newton-Raphson's iteration is finished and the braking torque, power dissipation in the disc and affected force on the disc are calculated. Otherwise, the process goes back to the beginning and the reluctances are updated by the BH curve using previously calculated values. This process continues until the desired accuracy is obtained.

The Newton-Raphson method is a kind of root finding algorithm and is an iterative method, which is described by the first order Taylor series [80]. There are some disadvantages in the Newton-Raphson method such as the need for initial guess and derivative problems. If the initial guesses of unknowns are far away from roots or the derivatives of functions are close to zero, the Newton-Raphson method cannot

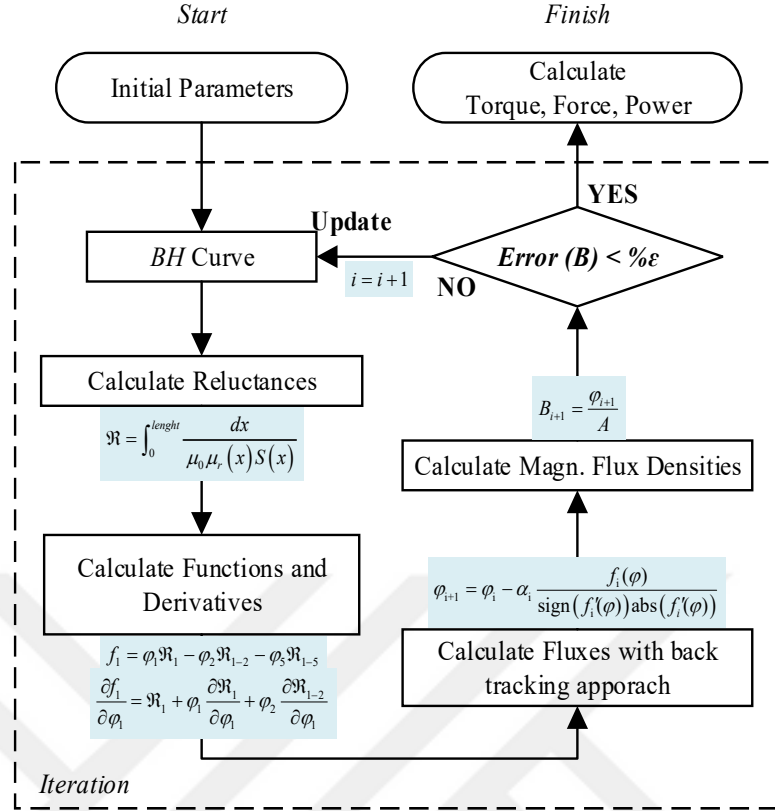


Figure 3.4. Flowchart of the nonlinear magnetic modeling for AF-ECBs

convergence and fails [81]. Therefore, the Newton-Raphson method needs an extension for global convergence. In the literature, various hybrid Newton-Raphson methods exist [82-84]. In this study, the Newton-Raphson method is extended by a back tracking approach. The modified Newton-Raphson method is defined as

$$x_{k+1} = x_k - \alpha_k \frac{f_k(x)}{\text{sign}(f'_k(x)) \text{abs}(f'_k(x))} \quad (3.4)$$

where  $k$  is the iteration round number,  $\alpha$  is a relaxation factor between 0 and 1. The principle of this method is relied on tracking the derivative of the function and determining of the slope of its derivatives by positive or negative sign. Thereby, the Newton-Raphson method always can converge.

The arrangement of the functions and their derivatives is an important stage of the Newton-Raphson method. For instance, the first Newton-Raphson function derived from (1) is defined as



$$f_1 = \varphi_1 \mathfrak{R}_1 - \varphi_2 \mathfrak{R}_{1-2} - \varphi_5 \mathfrak{R}_{1-5} \quad (3.5)$$

where  $f_1$  is the function of the first flux loop. Other Newton-Raphson functions are also described by using this manner. The derivative of the first function is described as

$$\frac{\partial f_1}{\partial \varphi_1} = \mathfrak{R}_1 + \varphi_1 \frac{\partial \mathfrak{R}_1}{\partial \varphi_1} + \varphi_2 \frac{\partial \mathfrak{R}_{1-2}}{\partial \varphi_1} \quad (3.6)$$

where the fifth flux loop is eliminated since  $\mathfrak{R}_{1-5}$  is a nonmagnetic reluctance. In this manner, all functions and their derivatives are constructed, and all flux loops are calculated. In the following step, the magnetic flux densities of the reluctances are calculated. After that, the braking torque can be obtained from the power dissipation in the disc defined as

$$P_{\text{disc}} = \int_V \rho J^2 dV = \rho J^2 (r_o^2 - r_i^2) \pi d \quad (3.7)$$

where  $\rho$  is the conductivity,  $d$  is the thickness,  $r_o$  is the outer radius and  $r_i$  is the inner radius of the disc and  $J$  is the current density defined as

$$J = \sigma (r\omega \times B_n) e^{-d/\delta} \quad (3.8)$$

where  $r$  is the disc mean radius,  $\omega$  is the electrical angular speed,  $B_n$  is the normal component of magnetic flux density and  $\delta$  is the skin depth for nonlinear case defined as

$$\delta = \sqrt{\frac{2H_0}{\sigma\omega B_s}} \quad (3.9)$$

where  $H_0$  is the peak value of applied surface magnetic field and  $B_s$  is the saturation value of magnetic flux density. The eddy current reaction (armature reaction), namely the magnetic flux density variation as a function of speed, has influence on the magnetic flux density that it should be investigated as

$$B_n = B_0 e^{-R_m} \quad (3.10)$$

where  $B_0$  is the magnetic flux density at zero speed, and  $R_m$  is the magnetic Reynolds number defined as

$$R_m = \sigma v_c \mu_0 l_c \quad (3.11)$$

where  $v_c$  is the characteristic velocity  $v_c = \omega_{el}r/Q$  where  $\omega_{el}$  is the electrical angular speed,  $r$  is the brake disc radius and  $Q$  is the slot number,  $\sigma$  is the brake disc conductivity,  $\mu_0$  is the vacuum permeability, and  $l_c$  is characteristic length obtained by disc volume  $V_{disc}$  divided by its air gap surface  $S_{disc}$  ( $l_c = V_{disc}/S_{disc}$ ). It has to borne in mind that as the speed of the ECB increases, the skin depth, current density, and air gap flux density decrease, too. If the disc thickness is approximately the same as the penetration depth at the investigated operation speed, the proposed calculation scheme works well. If the speed is increased to a point where the penetration depth is considerably lower than the disc thickness, then the approach where magnetic field analysis or Faraday's law and Ampere's law are coupled is required to get accurate enough results [44, 85]. For the structural analyses, the affected force on the disc is defined as

$$F = B_{ave} 2\pi r (r_o - r_i) / \mu_0 \quad (3.12)$$

where  $B_{ave}$  is the average magnetic flux density. At the end of this step, the braking torque, power dissipation in the disc and affected force on the disc are calculated.

### 3.2.2. Nonlinear thermal modeling

The temperature variation in the disc should be investigated in AF-ECBs since a great amount of energy turn into heat during the braking and the temperature rise affects the electrical, magnetic and structural properties of the material. The nonlinear thermal modeling is investigated by thermal lumped-parameter in the proposed NMDA. The schematic drawing of single-disc-single-stator AF-ECB and the corresponding lumped-parameter thermal network are given in Figure 3.5. The T-equivalent circuit modeling approach is used because of the AF geometry [86, 87]. The thermal network consists of nine nodes: 1) disc, 2) air gap, 3) stator teeth, 4) slot windings, 5) yoke, 6) frame and 7-8-9) shaft.

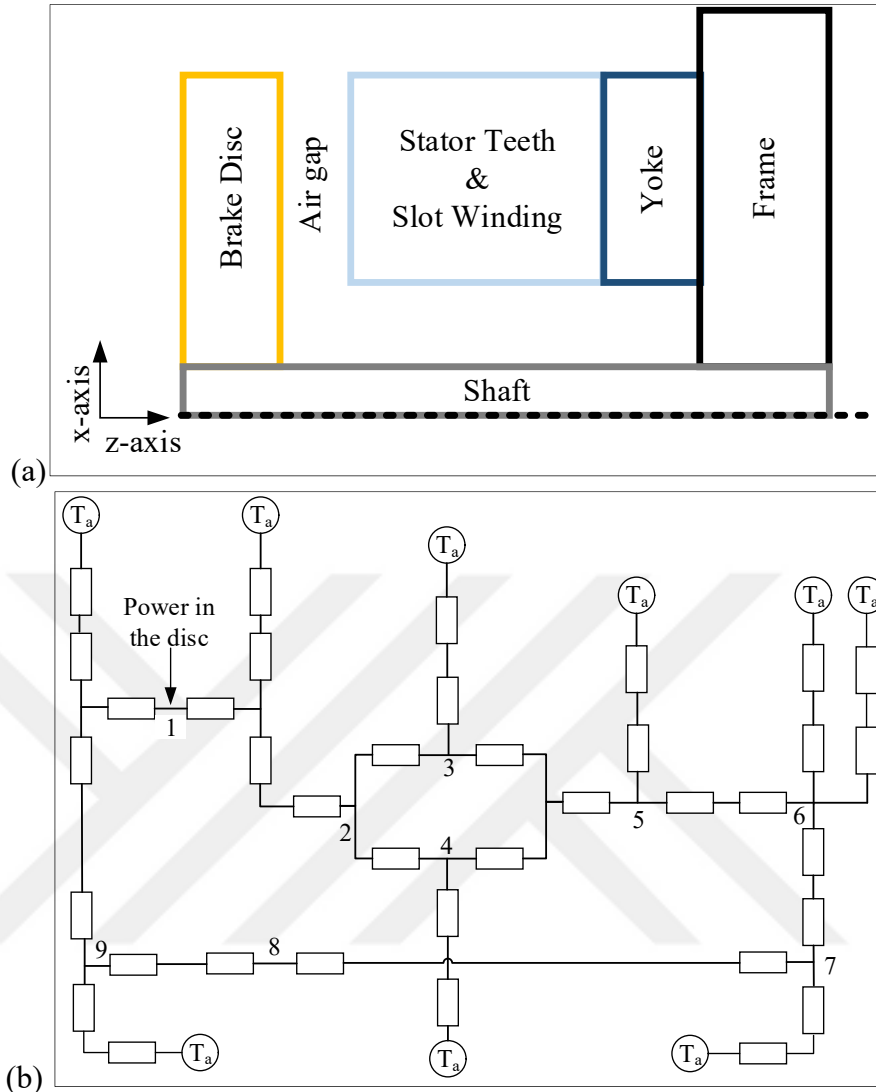


Figure 3.5. (a) The schematic drawing and (b) thermal resistance network of AF-ECB.  $T_a$  represents the ambient temperature

For the transient analysis, the temperature rise of each node is calculated with the matrix equation defined as

$$\frac{d}{dt}(\Delta T) = C^{-1}(P - G \cdot \Delta T) \quad (3.13)$$

where  $t$  is the time,  $\Delta T$  is the temperature rise vector,  $C$  is the thermal capacitance matrix,  $P$  is the power loss vector and  $G$  is the thermal conductance matrix defined as

$$G = \begin{bmatrix} \sum_{i=1}^n \frac{1}{R_{1,i}} & -\frac{1}{R_{1,2}} & -\frac{1}{R_{1,3}} & \cdots & -\frac{1}{R_{1,n}} \\ -\frac{1}{R_{2,1}} & \sum_{i=1}^n \frac{1}{R_{2,i}} & -\frac{1}{R_{2,3}} & \cdots & -\frac{1}{R_{2,n}} \\ -\frac{1}{R_{3,1}} & -\frac{1}{R_{3,2}} & \sum_{i=1}^n \frac{1}{R_{3,i}} & \cdots & -\frac{1}{R_{3,n}} \\ \vdots & \vdots & \vdots & \ddots & \vdots \\ -\frac{1}{R_{n,1}} & -\frac{1}{R_{n,2}} & -\frac{1}{R_{n,3}} & \cdots & \sum_{i=1}^n \frac{1}{R_{n,i}} \end{bmatrix} \quad (3.14)$$

where  $n$  is the node number and  $R$  is the thermal resistance. The subscripts in  $R$  define the total thermal resistance between the two nodes. In the nonlinear thermal modeling, conduction and convection are taken into account. The conductive and convective thermal resistances are defined by

$$R = \frac{l}{k_{\text{con}}(T)S} \quad (3.15)$$

$$R_{\text{conv}} = \frac{1}{h(\omega)A} \quad (3.16)$$

where  $l$  is the length of the heat flow,  $k_{\text{con}}$  is the thermal conductivity,  $h$  is the convection coefficient,  $S$  is the cross-sectional area.

The convective thermal resistances in the brake disc are the most important components of the thermal network. As the brake disc is rotating, convection exists between the brake disc and the stator as well in radial and axial directions between the brake disc and the ambient. The convection coefficient in the air gap between the brake disc and stator is calculated by the following set of equations [88]

$$\text{Re} = \frac{vg}{\nu_{\delta}} \quad (3.17)$$

$$\text{Ta} = \text{Re}^2 \frac{g}{r_0} \quad (3.18)$$

$$\text{Nu} = \begin{cases} 2, & \text{Ta} < 1700 \\ 0.128\text{Ta}^{0.367}, & 1700 < \text{Ta} < 10^4 \\ 0.409\text{Ta}^{0.241}, & 10^4 < \text{Ta} < 10^7 \end{cases} \quad (3.19)$$

where Re is the Reynolds number, v is the circumferential speed of the brake disc, g is the axial air gap length,  $\nu_\delta$  is the kinematic viscosity of the air, Ta is the Taylor numbers and Nu is the Nusselt numbers. The heat coefficient of the air gap between the brake disc and the stator is finally defined as

$$h_{\text{air}} = \frac{\text{Nu}\lambda_{\text{air}}}{g} \quad (3.20)$$

The convection coefficient between the brake disc and the ambient has radial and axial directions. The convection coefficient in axial direction is calculated by the following set of equations [88]

$$\text{Laminar Flow } (\text{Re}_{\text{ax}} < 3 \times 10^5), \text{ Cm}_{\text{ax}} = \frac{3.87}{\text{Re}_{\text{ax}}^{0.5}} \quad (3.21)$$

$$\text{Turbulent Flow } (\text{Re}_{\text{ax}} > 3 \times 10^5), \text{ Cm}_{\text{ax}} = \frac{0.146}{\text{Re}_{\text{ax}}^{0.2}} \quad (3.22)$$

$$\text{Nu}_{\text{ax}} = \frac{\text{Pr Re}_{\text{ax}} \text{ Cm}_{\text{ax}}}{2\pi} \quad (3.23)$$

where  $\text{Cm}_{\text{ax}}$  is the axial flow coefficient and Pr is the average Prandtl number. The forced convection coefficient in axial direction is defined as

$$h_{\text{ax}} = \frac{\text{Nu}_{\text{ax}} \lambda_{\text{air}}}{r_o} \quad (3.24)$$

The convection coefficient in radial direction is calculated by the following set of equations

$$\text{Gr} = \frac{\rho_d^2 g_f \beta \Delta T (l_c)^3}{\mu_d^2} \quad (3.25)$$

$$\text{Nu}_{\text{rad}} = 0.18 \left( \text{Pr} \left( 0.5 \text{Re}_{\text{rad}}^2 + \text{Gr} \right) \right)^{0.315} \quad (3.26)$$

where Gr is the Grashof number,  $\rho_d$  is the mass density of the air,  $g_f$  is the gravitational attraction force,  $\beta$  coefficient of cubical expansion,  $l_c$  is the characteristic length. Finally, the convection coefficient in radial direction is defined as

$$h_{\text{rad}} = \frac{\text{Nu}_{\text{rad}} \lambda_{\text{air}}}{2r_o} \quad (3.27)$$

The thermal contact resistances caused by the contact transitions are modeled in a similar manner by substituting the convection coefficient with the contact heat transfer coefficient. The nonlinear thermal modeling starts with setting the initial parameters. Firstly, all thermal resistances are derived and the temperatures are calculated by (13). Then, the calculated temperature info is shared with the nonlinear magnetic and the structural modeling. In the next time step, the nonlinear parameters are updated by the new temperature and power info, and the progress is repeated. It has to be reminded that the power dissipation calculated in the nonlinear magnetic modeling is used as power source in the thermal network. The critical temperature in the brake disc is checked at each time step and if it is larger than desired, the analysis fails. In the proposed NMDA, the maximum disc temperature is limited to 160 °C for security in the lab facilities.

### 3.2.3. Nonlinear structural modeling

The deflection and the fatigue analyses are crucial design steps of AF electric machines which must be investigated to define the life span of the disc. The structural modeling is also important for the AF-ECB that this issue does not receive the attention in most papers in the literature.

In the proposed NMDA, affected force and stresses on the disc are calculated to define the deflection and the safety factor of the disc. The general formula of the deflection on the outer radius of the disc is related to bending described as [89]

$$s = \frac{Fr^3}{3E_m I_m} \quad (3.28)$$

where  $F$  is the affected force in axial direction,  $E_m$  is the modulus of elasticity and  $I_m$  is area moment of inertia of the disc. Simple fluctuating loading is examined for fatigue analysis by Soderberg failure criterion [89] defined as

$$\frac{\sigma_a}{S_e} + \frac{\sigma_m}{S_y} = \frac{1}{n} \quad (3.29)$$

where  $\sigma_a$  is the amplitude stress,  $\sigma_m$  is the midrange stress,  $S_e$  is the endurance limit,  $S_y$  is the yield stress and  $n$  is the factor of safety. In AF-ECBs, the bending stress affects the disc and it can be assumed that  $\sigma_a$  and  $\sigma_m$  is equal. The bending stress of the disc is defined as

$$\sigma_b = \frac{M z}{I_m} \quad (3.30)$$

where  $M$  is the bending moment,  $z$  is the vertical distance away from the neutral axis. The endurance limit is defined as

$$S_e = k_a k_b k_c k_d k_e k_f S'_e \quad (3.31)$$

where  $k_a$  is the surface condition modification factor,  $k_b$  is the size modification factor,  $k_c$  is the load modification factor,  $k_d$  is the temperature modification factor,  $k_e$  is the reliability factor,  $k_f$  is miscellaneous-effects modification factor and  $S'_e$  is the test specimen endurance limit.

The surface factor,  $k_a$ , is described as  $k_a = a S_{ut}^b$  where  $S_{ut}$  is the tensile stress,  $a$  and  $b$  are the surface finish factors which are obtained from material properties. The size factor,  $k_b$ , is defined as  $k_b = 1.24 \times d^{-0.107}$ . The load modification factor,  $k_c$ , is equal to 1 due to bending of the disc. The temperature factor,  $k_d$ , is defined as

$$k_d = 0.99 + 2.25 \times 10^{-9} T - 2.8 \times 10^{-6} T^2 + 6.1 \times 10^{-4} T^3 \quad (3.32)$$

where  $25 \leq T \leq 250$  is the temperature of the disc in Celsius degrees. The reliability factor,  $k_e$ , is described as  $k_e = 1 - 0.08 z_a$  where  $z_a$  is the transformation variable. During the multidisciplinary analyses,  $z_a$  is taken as 3.091 which is equal to 99.9% of

reliability. The miscellaneous-effects modification factor,  $k_f$ , is equal to 1 thus there is no notch in the disc. The test specimen endurance limit,  $S'_e$ , is described by

$$S'_e = 0.5S_{ut} \quad (3.33)$$

The nonlinear structural modeling has two inputs as affected force computed from magnetic modeling and temperature in the disc computed from thermal modeling. In each time step, the deflection and the safety factor are recalculated by Equation (4.28)-(4.31) and reflected as output of the proposed NMDA.

### 3.2.4. Results of NMDA

Variation of the outputs of the AF-ECB is presented to highlight the proposed NMDA. The actual brake performance can be obtained by the proposed NMDA and the variation of the outputs of the brake can be attained. For instance, the variation of the braking torque and the temperature in time is given in Figure 3.6 in per unit and the brake operation range can easily be determined by the proposed NMDA. In addition, variations in the slot opening and pole shape are also examined in the proposed NMDA. For example, the influence of tooth shape on the braking torque (Figure 3.7) and the improvements of the braking time with the disc thickness can also be obtained by the proposed approach.

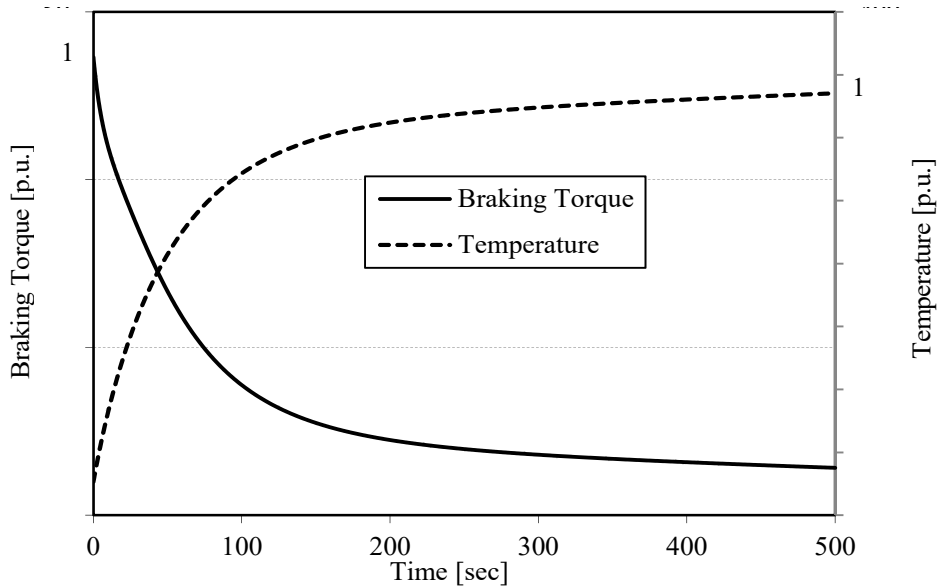


Figure 3.6. Variation of braking torque and temperature in time



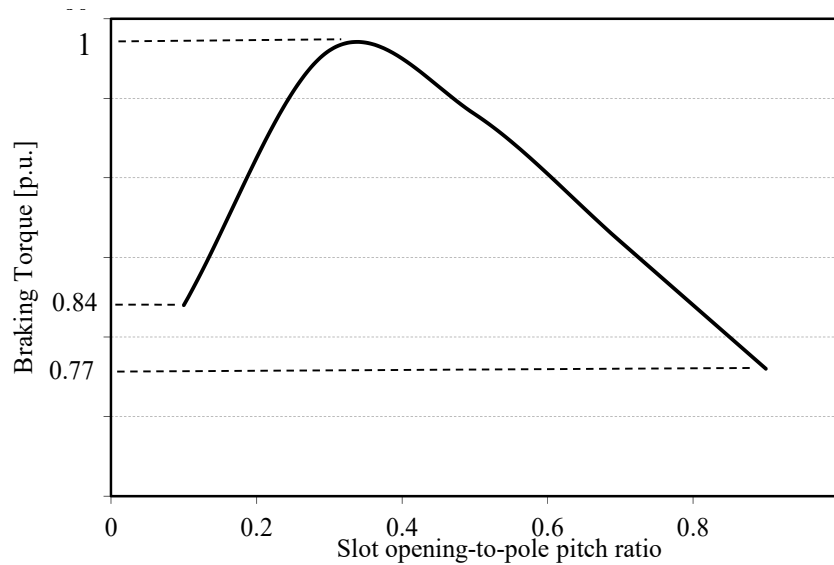


Figure 3.7. Influence of slot opening-to-pole pitch ratio on braking torque

### 3.3. Case Studies

The two case studies are investigated in this section to validate the proposed NMDA. The investigated AF-ECBs have different geometric structures and are designed for test benches and auxiliary brake for light commercial trucks. They consist of single-disc-single-stator configuration with eight open-slot teeth. The design parameters of two cases are explained and results obtained from 3D electromagnetic, thermal and structural FEAs are compared with the proposed NMDA. It has to be stated that FEA simulations are carried out independently so that the proposed multidisciplinary approach is set for only 30 seconds to verify the modeling approaches in the proposed NMDA. Therefore, the results obtained from FEAs and the NMDA are given with numbers in this section.

In this section, actual verification of the proposed NMDA is performed by experiments for investigated two cases and comparison of the proposed NMDA and 3D-FEAs are completed. Transient 3D electromagnetic FEA is performed for a specified time to obtain the braking torque and 3D thermal FEA is carried out for the whole braking time. Transient electromagnetic and thermal FEA are time consuming progresses. Comparison of computation time of the proposed NMDA and 3D-FEAs are given in Appendix. The braking torque and the temperature on the outer surface of the disc are measured during the tests and the results obtained from experiments are compared with

the proposed NMDA and 3D-FEAs. The braking torque is measured with a sensitive torque meter and the temperature is measured with multi spots infrared thermometer and thermocouples. It should be stated that for the security reasons and long term use, the maximum allowed temperature in the disc is limited as 160 °C. The braking time of experiments are set to 360 seconds for all cases.

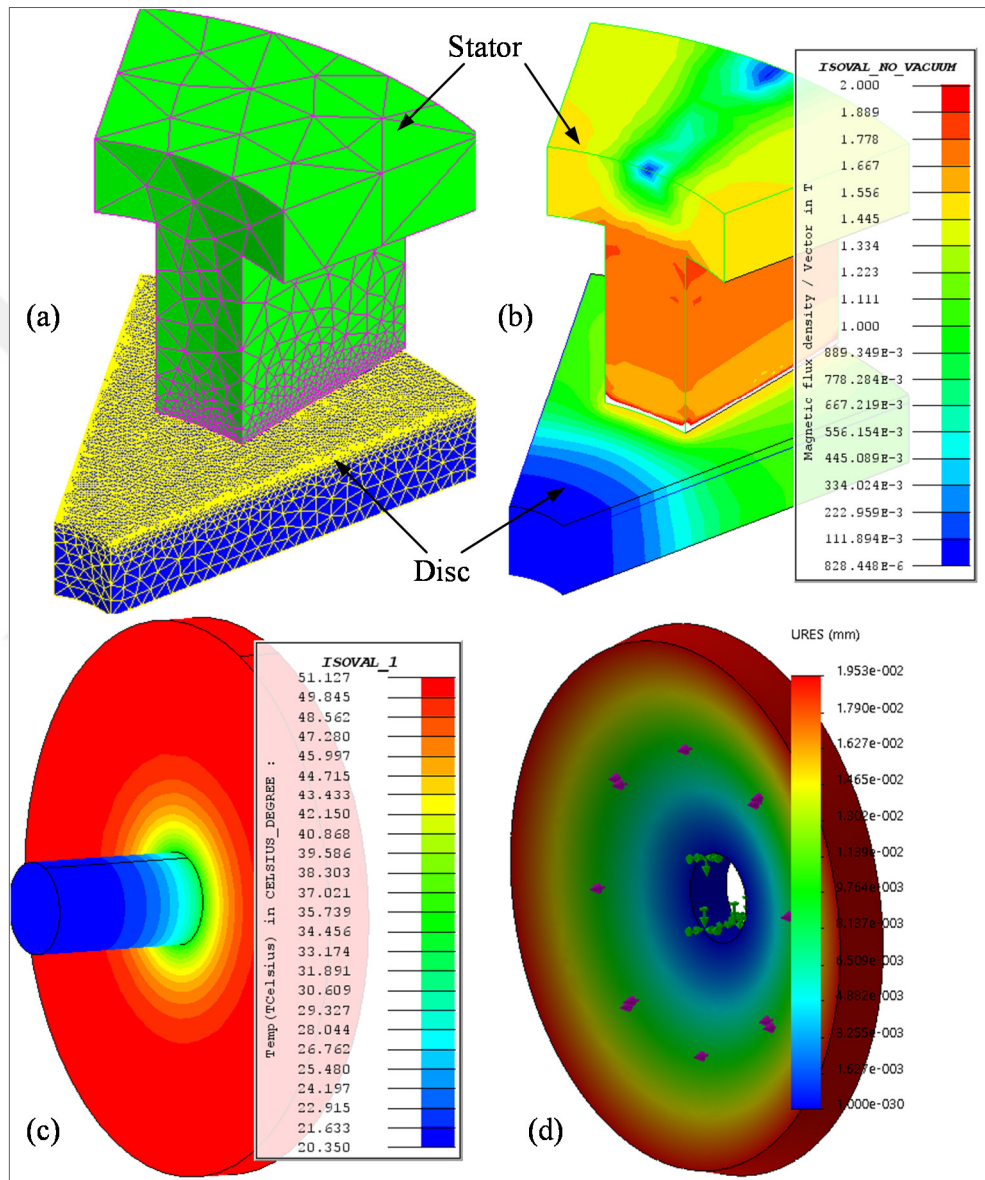


Figure 3.8. 4.5 kW of AF-ECB: (a) FE model with mesh profile, (b) magnetic flux density, (c) thermal and (d) structural profiles

### 3.3.1. Case-1: 4.5 kW AF-ECB

As a first case, a previously designed and validated 4.5 kW AF-ECB is investigated with the proposed NMDA. The ST37, low carbon steel, is selected as disc material

since it has low resistivity and good permeability properties. The rated speed and current of the AF-ECB are  $1400 \text{ min}^{-1}$  and 7 DC A, respectively. The dimensions and design details of Case-1 were previously provided in Table 2.2.

The 3D electromagnetic FE model of the Case-1 with mesh profile is given in Figure 3.8-(a). High mesh density is applied in the air gap and on the disc eddy-current surface to obtain correct results. The magnetic flux density, temperature and deflection profiles obtained from 3D-FEAs are given in Figure 3.8-(b)-(d). The results obtained from the proposed NMDA and the 3D-FEAs are given in Table 3.1. It can be seen that all results obtained from the proposed NMDA and the 3D-FEAs correlate well. The most of the results have under 5% of error between the proposed NMDA and 3D-FEA. A 9% of error is obtained for the maximum deflection. However, it is still in acceptable level since the deflection value is small. In addition, the factor of the safety for the Case I is quite well for the infinite life span. Detail performance experimental comparison of Case-1 can be found in [63].

Table 3.1. Comparison of the results for Case-1

	The proposed NMDA	3D-FEA	% Error
Braking torque	29.4 Nm	30.5 Nm	4%
Teeth mag. flux. dens.	1.57 T	1.54 T	2%
Power effecting on disc	4.31 kW	4.47 kW	4%
Force effecting on disc	5556 N	5480 N	1.3%
Disc temp. rise after 30 s.	30 °C	31.27 °C	4%
Maximum deflection	0.0212 mm	0.0195 mm	9%
Factor of safety	5.1	5.36	5%

The prototype of Case-1 and test setup are shown in Figure 3.9. The disc, stator with windings and assembled AF-ECB are shown in the figure. The concentrated windings are employed and connected in series. The drive-motor in the test system has 0–3000  $\text{min}^{-1}$  speed range with 47.5 Nm torque value.

The experiments are performed at the speed of  $1400 \text{ min}^{-1}$  for various excitation currents (3, 5 and 7 DC A). The braking torque and temperature variations are given in Figure 3.10. The braking torque obtained from 3D-FEA is not given in for better view. It is seen that generally the braking torque and temperature variations obtained

from the proposed NMDA and the experiments are in good agreement although temperature variations obtained from 3D-FEA disagree with the experimental results.

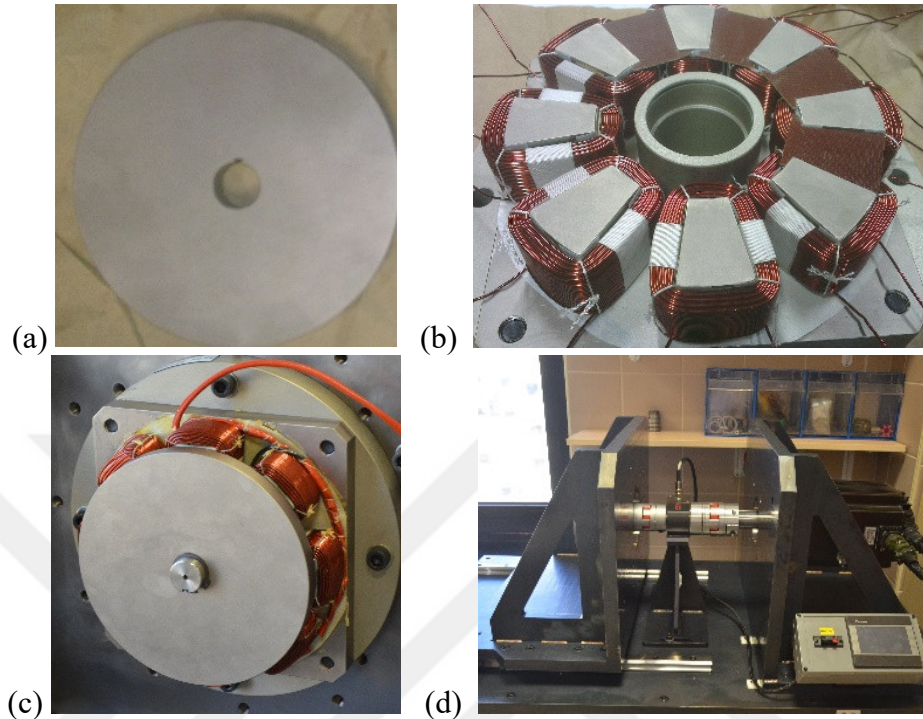


Figure 3.9. 4.5 kW AF-ECB prototype: (a) Disc, (b) stator with windings, (c) assembled prototype, and (d) test system

As mentioned in the above, the maximum allowed temperature in the disc is set to 160 °C therefore the experiments for various currents have different braking times. For the 7 A of excitation current, the maximum temperature has been reached in 180 seconds. For the 5 A of excitation current, the maximum temperature has been reached in 360 seconds. For the lowest case, there is no temperature problem. The braking torque is reduced by around 4% for 7 A and 5 A, and 1.5% for 3 A. The detail comparison of results at the speed of 1400 min<sup>-1</sup> is given in Table 3.2. Almost, under 5% error is obtained between the proposed NMDA and the experiments. Temperature rise after braking time is also given in the table and it is obtained that the proposed NMDA provides better results than 3D-FEA. It can be concluded that Case-1 has maximum 180 seconds of braking time at the rated speed and the excitation current when the temperature limit is 160 °C.

Table 3.2. Results for Case-1

	The proposed NMDA	3D-FEA	Experiment
Braking torque -7 A	29.16 Nm	30.5 Nm	30 Nm
Braking torque -5 A	17.45 Nm	18.6 Nm	17.6 Nm
Braking torque -3 A	6.33 Nm	6.7 Nm	5.9 Nm
Temp. rise – 7 A	125 °C	150 °C	131 °C
Temp. rise – 5 A	126 °C	152 °C	129 °C
Temp. rise – 3 A	44 °C	59 °C	39 °C

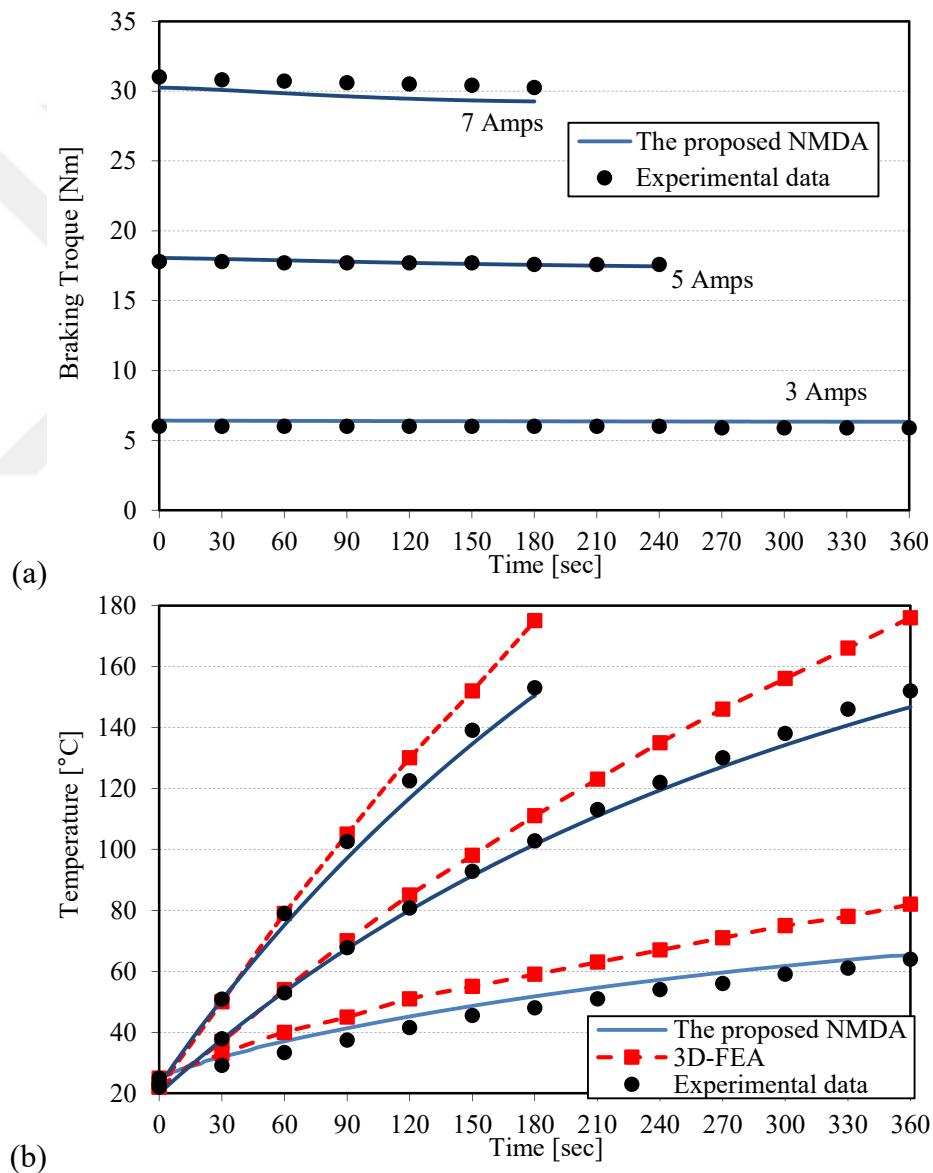


Figure 3.10. (a) Braking torque and (b) temperature variations for various excitation currents at the speed of  $1400 \text{ min}^{-1}$

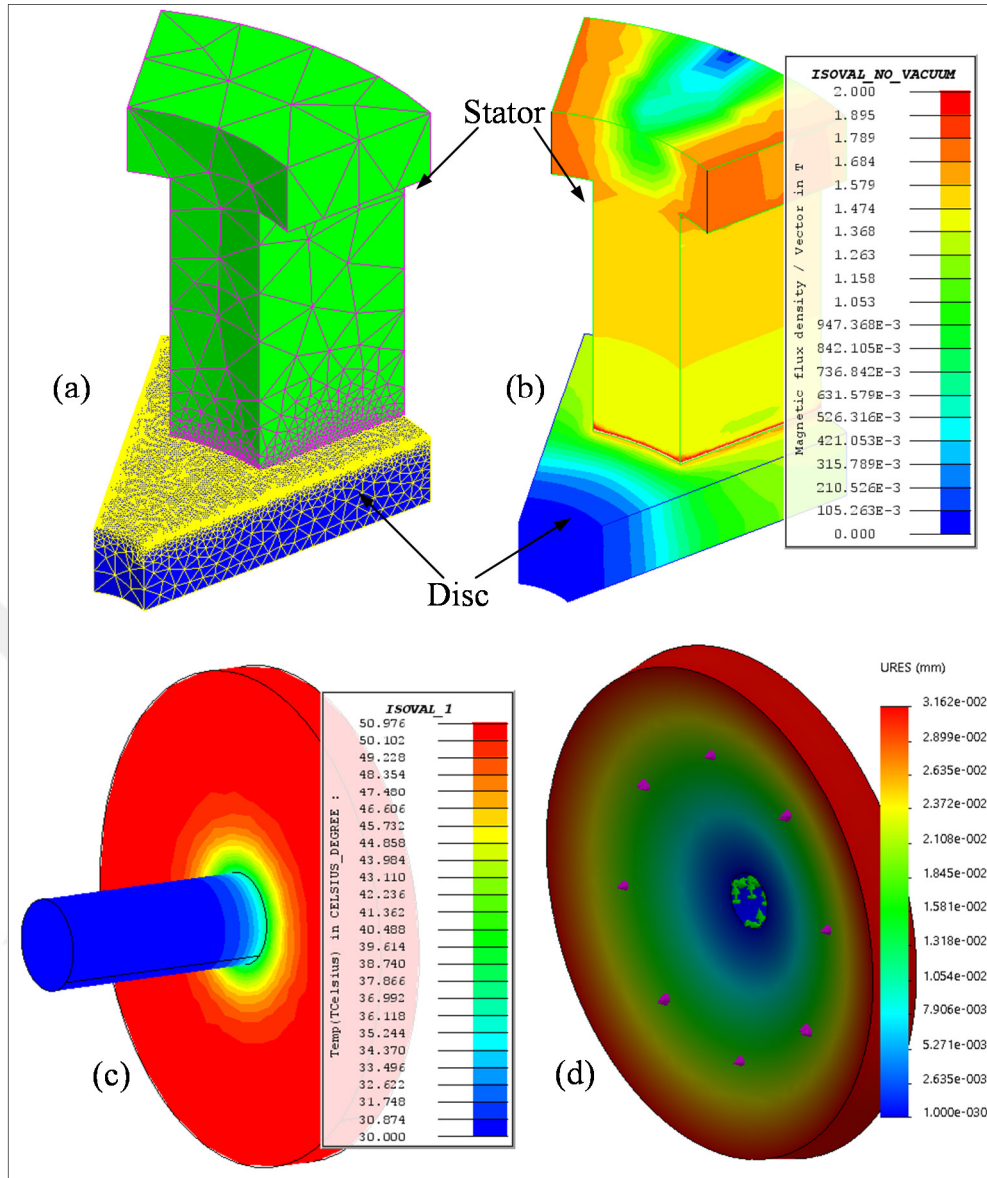


Figure 3.11. 10.5 kW of AF-ECB: (a) FE model with mesh profile, (b) magnetic flux density, (c) thermal and (d) structural profiles

### 3.3.2. Case-2: 10.5 kW AF-ECB

As a second case, a 10.5 kW AF-ECB is designed to test the validity of the proposed NMDA. The design parameters of the Case-2 are given in Table 3.3. The ST37 is also used as disc material. The rated speed of the Case-2 is  $1000 \text{ min}^{-1}$  and the rated excitation current is 20 DC A.

Table 3.3. The design parameters of Case-2

Outer radius	135 mm
Number of slots	8
Inner radius	80 mm
Disc thickness	25 mm
Teeth-to-pole ratio	0.555
Yoke thickness	25 mm
Axial air gap length	0.9 mm

The FE model of the Case-2 with mesh profile is given in Figure 3.11-(a). The same approach described in the previous subsection is also carried out for Case-2. The magnetic flux density, temperature and deflection profiles are given in in Figure 3.11-(b)-(d). The results obtained from the proposed NMDA and the 3D-FEAs are given in Table 3.4. It can be seen that all results obtained from the proposed NMDA agree with the 3D-FEAs. The results have around 5% of error between the proposed NMDA and 3D-FEA. The factor of safety for Case-2 is also good that it provides infinite life span.

Table 3.4. Comparison of the results for Case-2

	The proposed NMDA	3D-FEA	% Error
Braking torque	86.15 Nm	89.9 Nm	5%
Teeth mag. flux. dens.	1.39 T	1.46 T	5%
Power effecting on disc	4.31 kW	4.47 kW	4%
Force effecting on disc	13.86 kN	14.59 kN	5%
Disc temp. rise after 30 s.	28.25 °C	31 °C	5.6%
Maximum deflection	0.0297 mm	0.0316 mm	6%
Factor of safety	4.621	4.3	7.4%

The prototype of Case-2 and test setup are shown given in Figure 3.12. The stator, windings and assembled AF-ECB with test setup are shown in the figure. The concentrated windings are employed and connected in series. The drive-motor in the test system has 0–3000 min<sup>-1</sup> speed range with 100 Nm torque value.

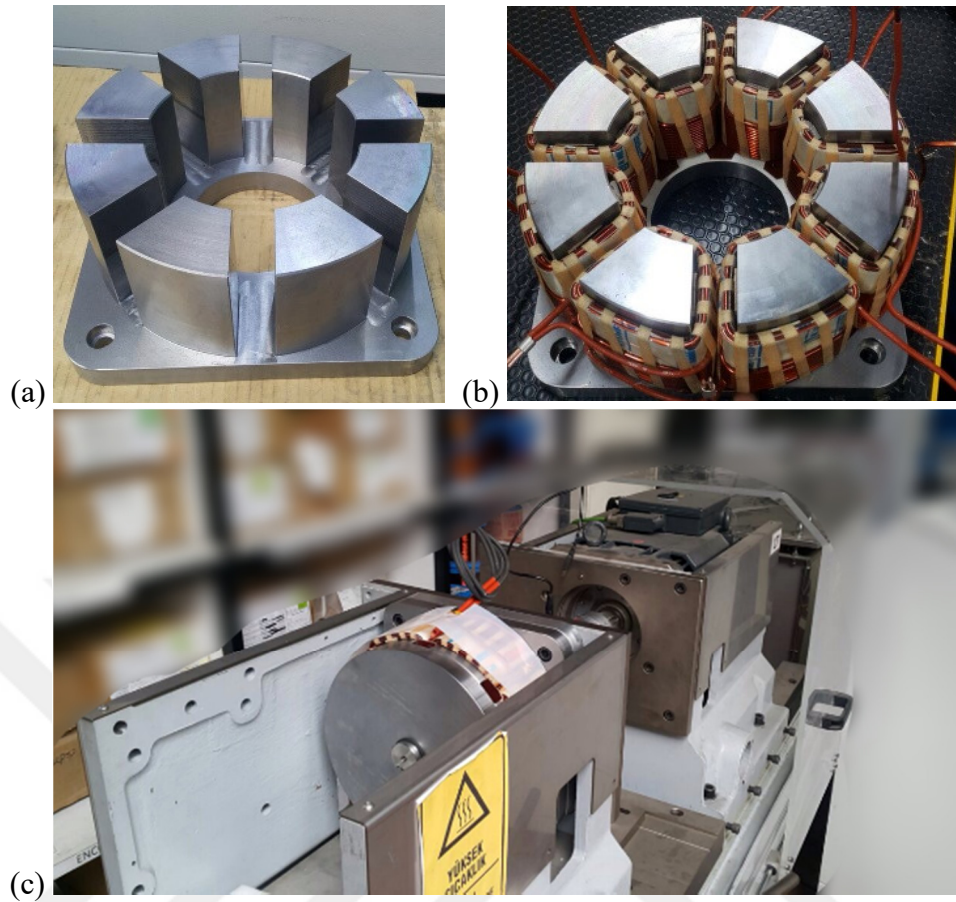


Figure 3.12. 10.5 kW AF-ECB prototype: (a) Stator core made of solid ST37, (b) stator with windings, (c) assembled prototype and test system

The experiments are performed at the speed of  $1000 \text{ min}^{-1}$  for 20 DC A of excitation current. (Due to the lab facility's limitation in the factory, only 20 DC A is investigated.) The braking torque and temperature variations are measured and the results are given in Figure 3.13. The braking torque obtained from 3D-FEA is not shown in the figure since the results are close to each other. It is seen that the results obtained from the proposed NMDA and the experiments are well matched. The braking torque is reduced by c. 2.3% at the end of the time. The 87.72 Nm of braking torque is measured while the 85.43 Nm of braking torque is obtained by the proposed NMDA and 89.9 Nm of braking torque is computed by 3D-FEA. After 300 seconds, the temperature on the outer surface of this disc is measured as  $160 \text{ }^\circ\text{C}$  while  $164 \text{ }^\circ\text{C}$  is obtained by the proposed NMDA and  $186 \text{ }^\circ\text{C}$  is computed by 3D-FEA. The results show that 3D-FEA gives unpractical results as the time progressed. As the temperature



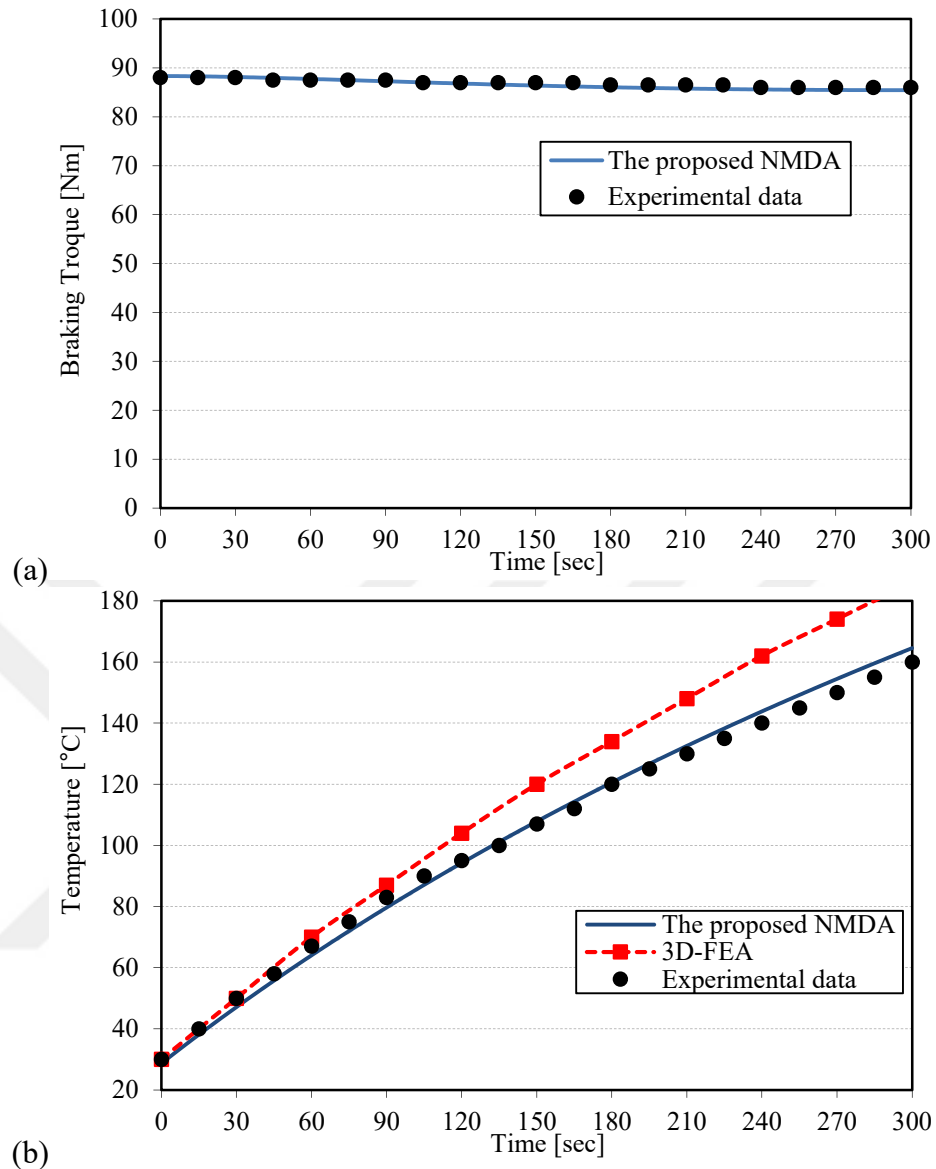
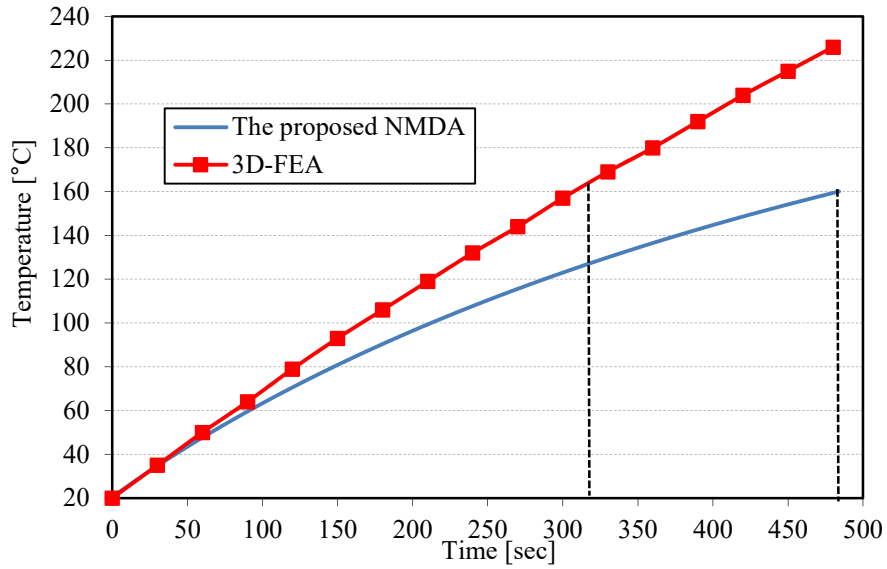
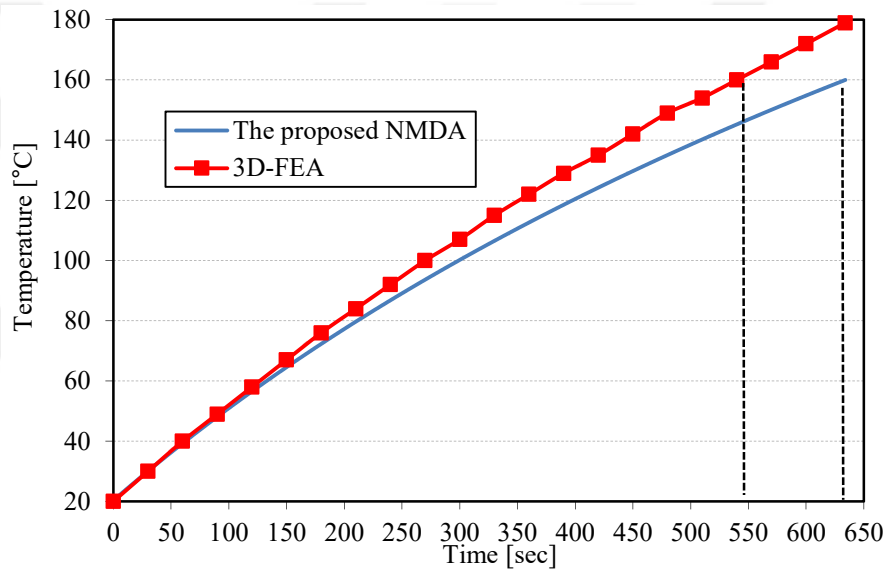


Figure 3.13. (a) The braking torque and (b) temperature variations of 10.5 kW AF-ECB at the speed of  $1000 \text{ min}^{-1}$  and the excitation current of 20 A

rise should be considered correctly to determine the braking time, it is not possible to obtain it by 3D-FEA. Temperature variation obtained from the proposed NMDA follows the actual brake performance. As a conclusion, maximum braking time of Case-2 is 180 seconds at the rated speed and the excitation current when the temperature limit is  $160 \text{ }^\circ\text{C}$ .



(a)



(b)

Figure 3.14. Temperature variation of (a) Case-1 and (b) Case-2 when the brake disc thickness are doubled at the rated speed and excitation current

### 3.3.3. Investigation of braking time by the proposed NMDA

As mentioned in the previous section, braking time of the AF-ECBs relies on the temperature limit in the brake disc. Due to lab facilities, here the temperature limit is set to 160 °C and maximum braking time of cases are determined. In some cases, more braking time might be needed or application might allow higher temperatures. In such cases, the parameters of the designs should be updated. It is certain that the brake disc thickness is the simplest parameter as the increase of the thickness provides more braking time. This modification can be easily done by the proposed NMDA. In both

cases, the brake disc thickness is doubled (Case-1: to 30 mm and Case-2: to 50 mm) and the same temperature limit is practiced. Temperature variations obtained from the proposed NMDA and the 3D-FEA are given in Figure 3.14. By this modifying, the difference between the proposed NMDA and 3D-FEA comes clearer. The results are summarized as follows:

- 483 seconds of braking time for Case-1 is obtained by the proposed NMDA while 310 seconds of braking time is obtained by 3D-FEA. Consider that the proposed NMDA gives more practical results, the 3D-FEA has 35% difference from the proposed NMDA. Maximum braking time increases from 180 to 483 seconds by the proposed NMDA for Case-1.
- For Case-2, 634 seconds of braking time is achieved by the proposed NMDA while 540 seconds of braking time of obtained with 3D-FEA. The difference between the proposed NMDA and the 3D-FEA is 15% and the braking time is nearly doubled.

### **3.4.Summary**

In this chapter, a novel NMDA is proposed for AF-ECBs. The proposed NMDA consists of integrated nonlinear magnetic, thermal and structural modeling and aims to find the actual brake performance. The BH curve, resistivity, thermal conductivity, density etc. of the material are all coupled to the temperature in the time domain. The nonlinear magnetic modeling is investigated by 2D reluctance network approach and modified Newton-Raphson method is applied as nonlinear solver. The nonlinear thermal modeling is carried out with thermal lumped-parameter and structural modeling is examined with bending and fatigue analyses. The braking torque, temperature in the disc, safety factor, and deflection of the disc are all obtained as functions of time in the proposed NMDA. 3D electromagnetic, thermal and structural FEAs are carried out to validate the nonlinear modeling approaches in the proposed NMDA. 4.5 kW and 10.5 kW AF-ECBs are experimentally tested, and braking torque and temperature variations are compared with the proposed NMDA and the 3D-FEA simulations. The results obtained from the experiments and the NMDA are all found to be in good agreement. However, results obtained from 3D-FEAs do not reflect the actual brake performance. Braking time of AF-ECBs is investigated by increasing the brake disc thickness and the results also confirm that the 3D-FEA does not provide

practical results. It can be concluded that the proposed NMDA is a very effective method for the AF-ECB design and determine the limitations.



## **4. A NEW AF-PMA-ECB AND ITS DESIGN OPTIMIZATION**

This chapter proposes a multiobjective design optimization of a new axial-flux (AF) permanent magnet assisted (PMA) eddy-current brake (ECB) by nonlinear network based analytical modeling. The magnets in the proposed new AF-PMA-ECB topology are placed into slot openings to increase the braking torque capability as opposed to conventional magnet less ECB topologies. The proposed new AF-PMA-ECB is modeled by a reluctance network approach and Newton-Raphson approach is preferred as nonlinear solver. A multiobjective particle swarm optimization (MO-PSO) is developed and applied to two different cases: The first aims to 28 Nm of braking torque and the second targets to the maximum braking torque of 47.5Nm (also limited to 47.5 Nm by test setup) with minimum ampere-turns and total PM mass. The optimized models are obtained by nondominating results in 3-dimensional (3D) Pareto surfaces and analytical results are compared by 3D finite element analyses (3D-FEA). One of the optimized cases is specifically manufactured and experimentally verified. The results obtained from analytical, 3D-FEA and the tests agree well and it is shown that the investigated design procedure is very effective and fast to obtain the optimized design parameters compared to 3D-FEA.

### **4.1. Introduction**

In general, most ECBs in the literature and in the market consist of only DC windings. Nowadays, the conventional ECB structures have not been used as frequently as before due to rapid developments in the field of ECBs and demand in electrical applications. PM-and-PMA-ECBs are promising area of research for the future applications due to the benefits in control particularly in PMA topologies and high-efficiency systems [37, 45, 75]. PMA-ECB could have radial-flux or axial-flux structures and linear or rotational movements. However, accomplishing the optimum design parameters, especially optimum magnet geometry, is vital for all PMA-ECB topologies.

In this chapter, a new AF-PMA-ECB design approach is presented. The proposed AF-PMA-ECB is analytically modeled and two different optimized designs are proposed

to obtain the rated braking torque and the maximum braking torque. In addition, this chapter demonstrates that optimizing the magnet dimensions is crucial in the AF-PMA-ECB design and MO-PSO enables so as to get the design parameters more quickly compared to the transient time-consuming 3D-FEA simulations.

#### 4.2. The Proposed AF-PMA-ECB

The proposed AF-PMA-ECB topology has a single-rotor-single-stator configuration and the structure is illustrated in Figure 4.1-(a). It has to be pointed out that the topology could have multi-stator multi-rotor configuration. PM magnetizations, excitation coils and flux paths are provided in Figure 4.1-(b). Without excitation current, the magnet driven flux completes its path during yoke. PM flux can be altered by DC

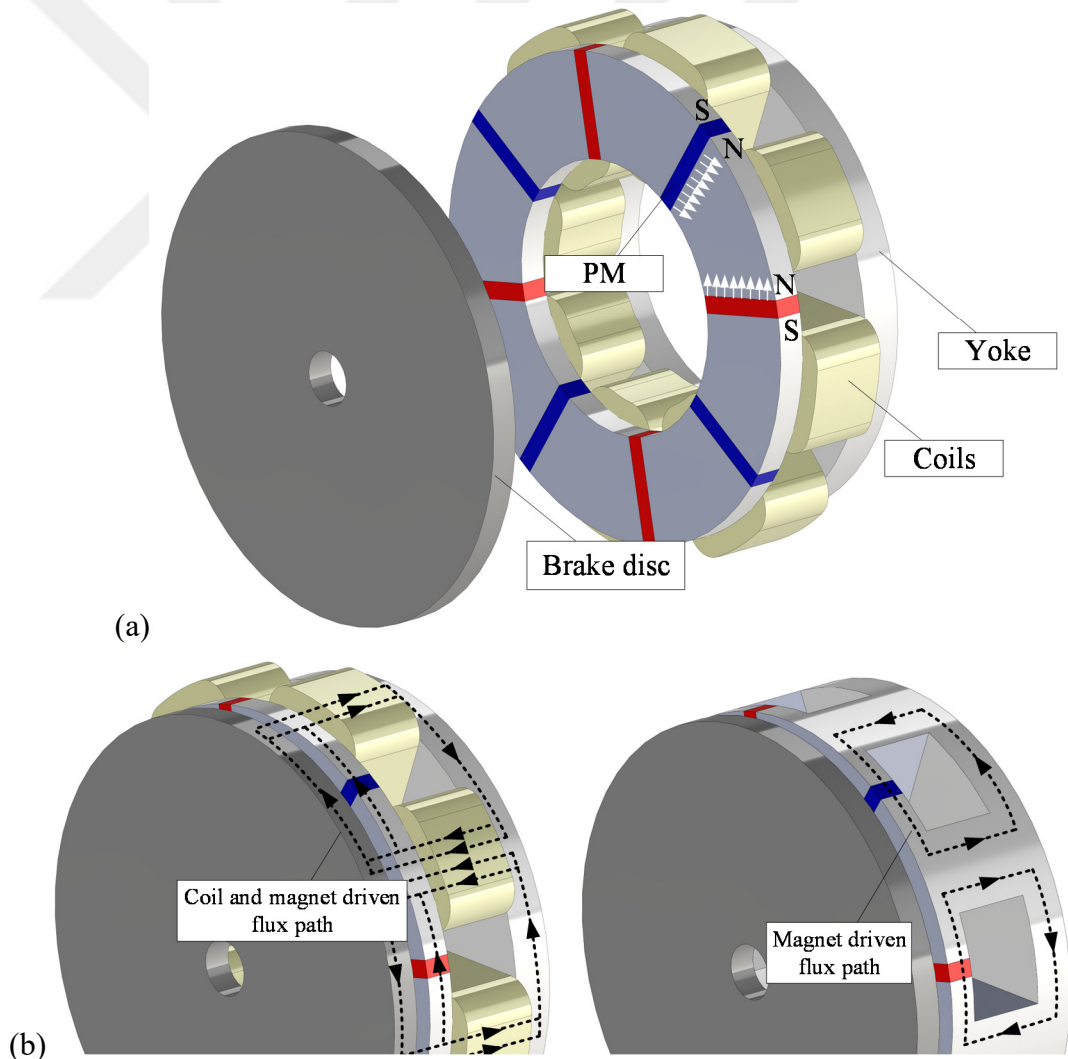


Figure 4.1. (a) The proposed AF-PMA-ECB topology and (b) its flux paths

excitation during braking operation in this topology and it is possible to fully control the braking torque without external mechanisms as to [30, 31, 36, 76]. In this state, the design of the magnet size is critical since the PMs directly affect the working principle and controllability of the ECB. If the magnet size is not big enough, the capability of the proposed brake cannot be fully utilized. In addition, if the PM size is larger than the optimum dimensions, some PM flux will complete its path over the yoke generating over saturation of the core and the benefits of the proposed model cannot be fully demonstrated. Therefore, it is critical that the PM size should be optimized precisely.

The key parameters of the proposed AF-PMA-ECB are provided in Table 4.1. The brake has 180-to-100 mm of outer-to-inner diameter with an axial air-gap of 1 mm. The brake disc has a thickness of 15 mm. NdFeB magnets are used in the slots openings to switch the flux directions. The low carbon steel material is used as rotor and stator materials. The rated speed of the brake is selected as  $1000 \text{ min}^{-1}$ .

Table 4.1. Key parameters of the proposed AF-PMA-ECB

Parameter	Value
Outer diameter	180 mm
Inner diameter	100 mm
Axial air gap	1 mm
Resistivity of the brake disc	$100 \times 10^{-9} \Omega\text{m}$
Stator and brake disc material	Low carbon steel ST37
Brake disc thickness	15 mm
Number of slots	8
PM Relative permeability	1.05
PM Br	1.1 T

### 4.3. Analytical Modeling of the Proposed AF-PMA-ECB

Before the optimization, an accurate analytical model should be developed so as to obtain correct results and examine the whole alternative design cases. Due to AF structure, 3D analysis is required for the proposed AF-PMA-ECB. 3D analysis can be performed by FEM software tools or 3D field analysis [35] or quasi 2D analytical modeling, which is consists of superposition of several 2D linear models [77].

Reduction approach of 3D to 2D linearized geometry for AF machines is well covered in the literature that the determination of the computation planes (slices) is important to get the correct results. Most papers in literature report that 5 and more planes give accurate results [77, 78, 90]. Therefore, 6 number of computation planes are selected for the proposed AF-PMA-ECB.

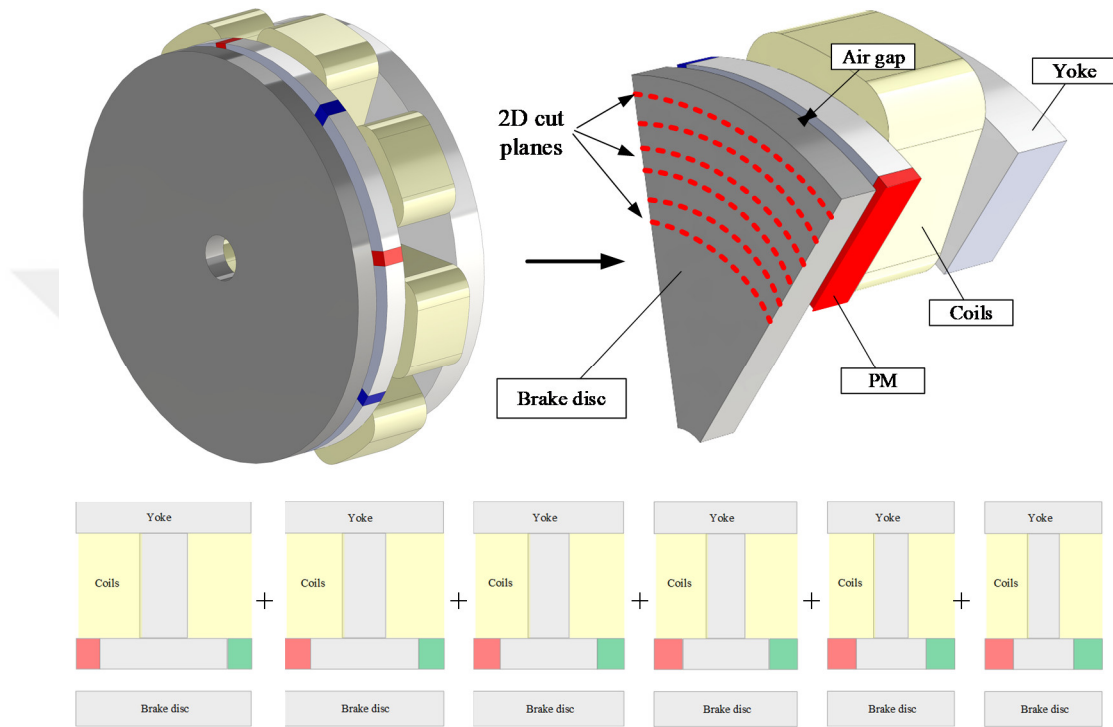


Figure 4.2. Reduction of 3D AF-PMA-ECB geometry to 2D linearized symmetry models

Analytical modeling of AF-PMA-ECB is performed by 2D reluctance network modeling approach. The reluctance network modeling presented here is similar to meshing method, which can easily be implemented to all types of electric machines. In this approach, firstly meshing points are assigned to the critical regions and then meshing lines are drawn to generate the rectangular-shaped mesh structures. The mesh structure could have x and/or y axes reluctance components and all mesh structures are linked to mesh fluxes and current linkages.

The AF-PMA-ECB structure has 8 slots and due to symmetry it can be modeled by focusing only one. The symmetric reluctance network model of the AF-PMA-ECB is illustrated in Figure 4.3. The DC excitation coils are not shown in the figure for a better



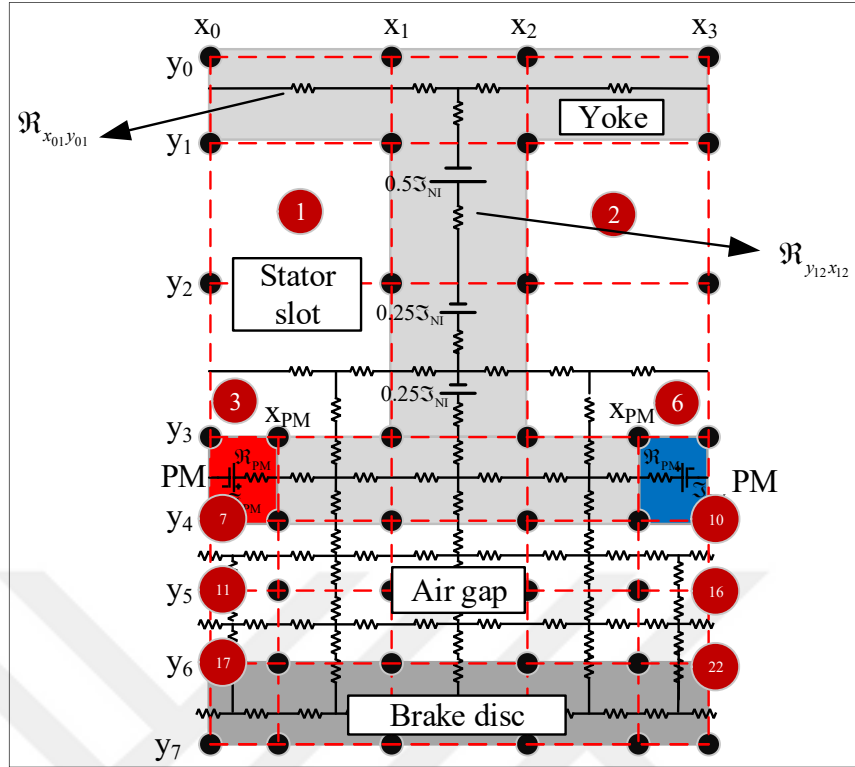


Figure 4.3. The reluctance network model of the proposed AF-PMA-ECB (focusing only symmetry model). The DC excitation coils are not shown for better demonstration

demonstration. The black circles represent the mesh points and red labels represent the mesh fluxes. The air gap in the model meshed by 2 horizontal layers to improve the accuracy of the results. The yoke and the stator slot regions are simply meshed to avoid heavily computation. The size of a  $22 \times 22$  main reluctance matrix and the size of a  $1 \times 22$  current linkage vector are generated that the aim is to solve this matrix to find the mesh flux vector. The reluctances are defined by their x and y axes mesh info. To give an example, the PM reluctance is defined as

$$\mathcal{R}_{PM} = \frac{1}{\mu_0 \mu_{PM}} \frac{x_{PM} - x_0}{(y_4 - y_3)d} \quad (4.1)$$

where  $\mu_0$  is the vacuum permeability,  $\mu_{PM}$  is the PM permeability and  $d$  is the depth, which equals to outer-to-inner radius difference. The saturable reluctances are defined as a function of magnetic field strength in the network model. For example, the stator yoke reluctance is defined as

$$\Re_{x_0 y_0} (H_{x_0 y_0}) = \frac{B_{x_0 y_0}}{H_{x_0 y_0}} \frac{x_1 - x_0}{(y_2 - y_1) d} \quad (4.2)$$

The saturable reluctances are expressed as a function of H since the nonlinear analysis can converge the solution faster with this approach. This issue will be covered in the next section. The HB curve of the low carbon steel used here is presented in Figure 4.4. Y-axis could look better as from 0 to 350 kA/m

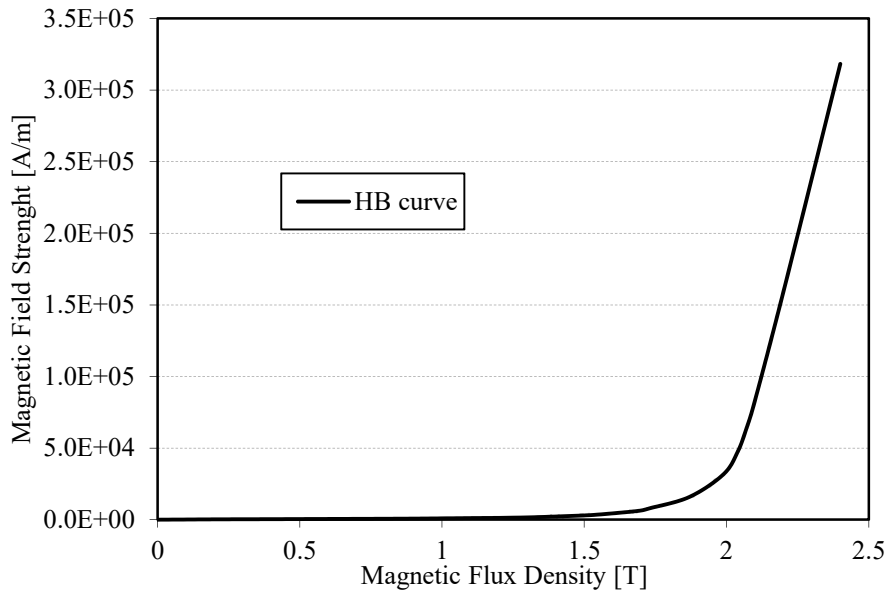


Figure 4.4. HB curve of the low carbon steel used in the AF-PMA-ECB

#### 4.4. Nonlinear Analysis of the Proposed AF-PMA-ECB

The Newton-Raphson method with back-tracking approach is used as nonlinear solver for reluctance network model. The classical Newton-Raphson method has converging problem when the model has numerous initial parameters. Due to selection of arbitrary initial parameters, the model could have nontrivial dynamics. Therefore, the Newton-Raphson is modified by back-tracking method described as

$$x_{k+1} = x_k - \alpha_k \frac{f_k(x)}{\text{sign}(f'_k(x)) \text{abs}(f'_k(x))} \quad (4.3)$$

where k is the iteration number,  $\alpha$  is a relaxation factor between 0 and 1. The aim of this modification is to follow the derivative of the function to assign the slope sign into the convergence problem.

As mentioned in Chapter 2, the magnetic flux density in the conductive part plays a very critical role in governing equations. Therefore, the magnetic flux density distribution should be accurately calculated. The Newton-Raphson method is an iteration based root find algorithm and its flowchart is given in Figure 4.5. The Newton-Raphson method starts with initialization of parameters and network reluctances are calculated by initial parameters in the first iteration and magnetic flux densities of saturable reluctances are obtained by flux functions and its derivatives. In each iteration, saturable reluctances are updated by HB curve until the desired error is reached. It has to be pointed out that HB curve is preferred since it is more suitable for the Newton-Raphson functions derivatives.

The important stage of the Newton-Raphson method is the calculation of functions and their derivatives. As seen from Figure 4.3, mesh fluxes have a symmetry that the 1<sup>st</sup> flux mesh is equal to 2<sup>nd</sup> flux mesh and 3<sup>rd</sup> flux mesh is equal to 6<sup>th</sup> flux mesh etc. Therefore, definition of the left side or right side Newton-Raphson functions and derivatives is enough for the whole model. The 1<sup>st</sup> function and its derivative are described as

$$f_1 = \varphi_1 \mathfrak{R}_1 + \varphi_2 \mathfrak{R}_{1-2} - \varphi_3 \mathfrak{R}_{1-3} - \varphi_4 \mathfrak{R}_{1-4} \quad (4.4)$$

$$\frac{\partial f_1}{\partial \varphi_1} = \mathfrak{R}_1 + \varphi_1 \frac{\partial \mathfrak{R}_1}{\partial \varphi_1} + \varphi_2 \frac{\partial \mathfrak{R}_{1-2}}{\partial \varphi_1} + \varphi_4 \frac{\partial \mathfrak{R}_{1-4}}{\partial \varphi_1} \quad (4.5)$$

where  $\varphi$  is the mesh flux,  $\mathfrak{R}_1$  notation represents the sum of the reluctances in the first mesh flux while  $\mathfrak{R}_{1-2}$  notation represents the mutual reluctances of 1<sup>st</sup> and 2<sup>nd</sup> mesh fluxes. The 3<sup>rd</sup> function and its derivative are described as

$$f_3 = \varphi_3 \mathfrak{R}_3 - \varphi_1 \mathfrak{R}_{3-1} - \varphi_4 \mathfrak{R}_{3-4} - \varphi_7 \mathfrak{R}_{3-7} \quad (4.6)$$

$$\frac{\partial f_3}{\partial \varphi_3} = \mathfrak{R}_3 + \varphi_3 \frac{\partial \mathfrak{R}_3}{\partial \varphi_3} + \varphi_4 \frac{\partial \mathfrak{R}_{3-4}}{\partial \varphi_4} + \varphi_7 \frac{\partial \mathfrak{R}_{3-7}}{\partial \varphi_7} . \quad (4.7)$$

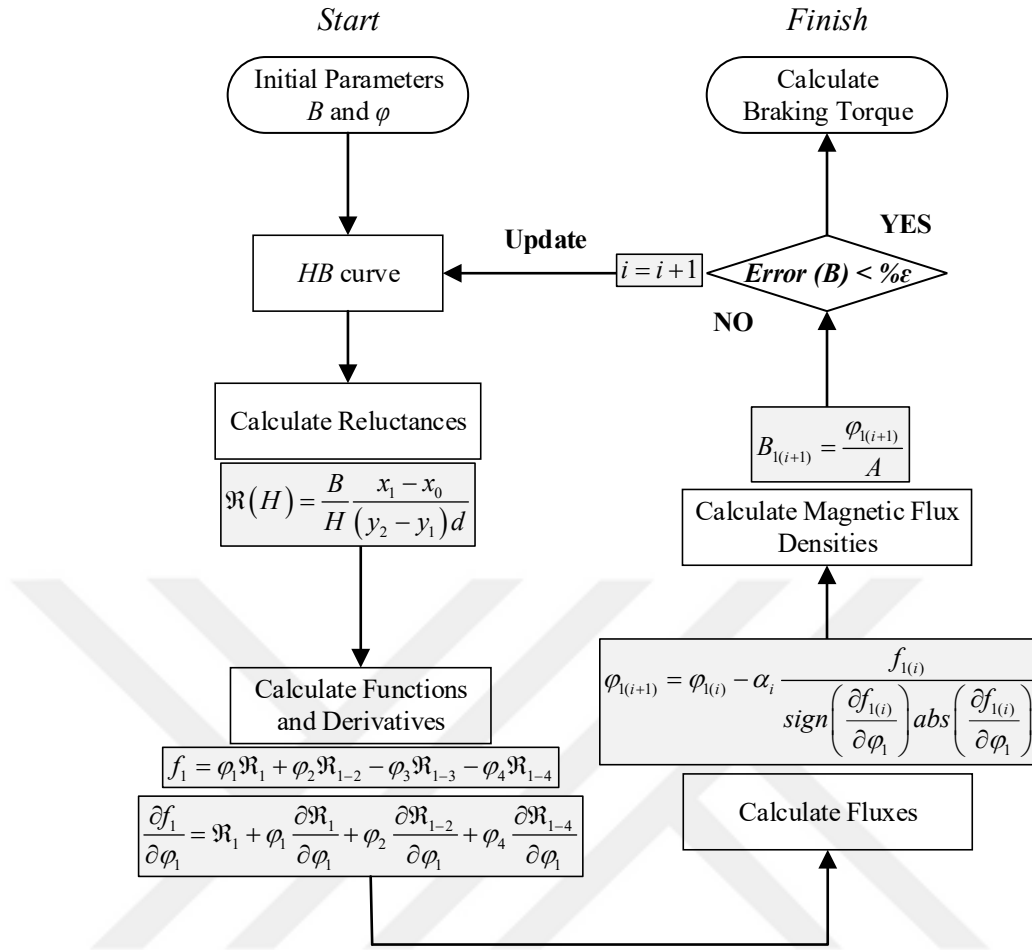


Figure 4.5. The flow chart of the Newton-Raphson method

The 4<sup>th</sup> function and its derivative are defined as

$$f_4 = \varphi_4 \mathfrak{R}_4 - \varphi_1 \mathfrak{R}_{4-1} - \varphi_3 \mathfrak{R}_{4-3} + \varphi_5 \mathfrak{R}_{4-5} - \varphi_8 \mathfrak{R}_{4-8} \quad (4.8)$$

$$\frac{\partial f_4}{\partial \varphi_4} = \mathfrak{R}_4 + \varphi_4 \frac{\partial \mathfrak{R}_4}{\partial \varphi_4} + \varphi_1 \frac{\partial \mathfrak{R}_{4-1}}{\partial \varphi_1} + \varphi_3 \frac{\partial \mathfrak{R}_{4-3}}{\partial \varphi_3} + \varphi_5 \frac{\partial \mathfrak{R}_{4-5}}{\partial \varphi_5} + \varphi_8 \frac{\partial \mathfrak{R}_{4-8}}{\partial \varphi_8} \quad (4.9)$$

The 7<sup>th</sup> function and its derivative are defined as

$$f_7 = \varphi_7 \mathfrak{R}_7 - \varphi_3 \mathfrak{R}_{7-3} - \varphi_8 \mathfrak{R}_{7-8} - \varphi_{11} \mathfrak{R}_{7-11} - \varphi_{12} \mathfrak{R}_{7-12} \quad (4.10)$$

$$\frac{\partial f_7}{\partial \varphi_7} = \mathfrak{R}_7 + \varphi_7 \frac{\partial \mathfrak{R}_7}{\partial \varphi_7} + \varphi_3 \frac{\partial \mathfrak{R}_{7-3}}{\partial \varphi_3} + \varphi_8 \frac{\partial \mathfrak{R}_{7-8}}{\partial \varphi_8} \quad (4.11)$$

The 8<sup>th</sup> function and its derivative are defined as

$$f_8 = \varphi_8 \mathfrak{R}_8 - \varphi_4 \mathfrak{R}_{8-4} - \varphi_7 \mathfrak{R}_{8-7} + \varphi_9 \mathfrak{R}_{8-9} - \varphi_{13} \mathfrak{R}_{8-13} \quad (4.12)$$

$$\frac{\partial f_8}{\partial \varphi_8} = \mathfrak{R}_8 + \varphi_8 \frac{\partial \mathfrak{R}_8}{\partial \varphi_8} + \varphi_4 \frac{\partial \mathfrak{R}_{8-4}}{\partial \varphi_4} + \varphi_7 \frac{\partial \mathfrak{R}_{8-7}}{\partial \varphi_7} + \varphi_9 \frac{\partial \mathfrak{R}_{8-9}}{\partial \varphi_9} \quad (4.13)$$

The 11<sup>th</sup>, 12<sup>th</sup> and 13<sup>th</sup> mesh fluxes only consist of air gap reluctances so that there is not derivative functions. These functions are defined as

$$f_{11} = \varphi_{11} \mathfrak{R}_{11} - \varphi_7 \mathfrak{R}_{11-7} - \varphi_{12} \mathfrak{R}_{11-12} - \varphi_{17} \mathfrak{R}_{11-17} \quad (4.14)$$

$$f_{12} = \varphi_{12} \mathfrak{R}_{12} - \varphi_7 \mathfrak{R}_{12-7} - \varphi_{11} \mathfrak{R}_{12-11} - \varphi_{18} \mathfrak{R}_{12-18} \quad (4.15)$$

$$f_{13} = \varphi_{13} \mathfrak{R}_{13} - \varphi_8 \mathfrak{R}_{13-8} - \varphi_{12} \mathfrak{R}_{13-12} + \varphi_{14} \mathfrak{R}_{13-14} - \varphi_{19} \mathfrak{R}_{13-19} \quad (4.16)$$

The 17<sup>th</sup> function and its derivative are given as

$$f_{17} = \varphi_{17} \mathfrak{R}_{17} - \varphi_{11} \mathfrak{R}_{17-11} - \varphi_{18} \mathfrak{R}_{17-18} \quad (4.17)$$

$$\frac{\partial f_{17}}{\partial \varphi_{17}} = \mathfrak{R}_{17} + \varphi_{17} \frac{\partial \mathfrak{R}_{17}}{\partial \varphi_{17}} + \varphi_{18} \frac{\partial \mathfrak{R}_{17-18}}{\partial \varphi_{18}} \quad (4.18)$$

The 18<sup>th</sup> function and its derivative are defined as

$$f_{18} = \varphi_{18} \mathfrak{R}_{18} - \varphi_{12} \mathfrak{R}_{18-12} - \varphi_{17} \mathfrak{R}_{18-17} - \varphi_{19} \mathfrak{R}_{18-19} \quad (4.19)$$

$$\frac{\partial f_{18}}{\partial \varphi_{18}} = \mathfrak{R}_{18} + \varphi_{17} \frac{\partial \mathfrak{R}_{18-17}}{\partial \varphi_{17}} + \varphi_{19} \frac{\partial \mathfrak{R}_{18-19}}{\partial \varphi_{19}} \quad (4.20)$$

Finally, the 19<sup>th</sup> function and its derivative are expressed as

$$f_{19} = \varphi_{19} \mathfrak{R}_{19} - \varphi_{13} \mathfrak{R}_{19-13} - \varphi_{18} \mathfrak{R}_{19-18} + \varphi_{20} \mathfrak{R}_{19-20} \quad (4.21)$$

$$\frac{\partial f_{19}}{\partial \varphi_{19}} = \mathfrak{R}_{19} + \varphi_{19} \frac{\partial \mathfrak{R}_{19-18}}{\partial \varphi_{19}} + \varphi_{18} \frac{\partial \mathfrak{R}_{19-18}}{\partial \varphi_{18}} + \varphi_{20} \frac{\partial \mathfrak{R}_{19-20}}{\partial \varphi_{20}} \quad (4.22)$$

The derivative terms should be resolved in the Newton-Raphson approach. For example, the derivative of tooth reluctance  $\mathfrak{R}_{y_{12}x_{12}}$  with respect to 1<sup>st</sup> mesh flux is stated as

$$\frac{\partial \mathfrak{R}_{y_{12}x_{12}}}{\partial \phi_1} = \frac{\partial \mathfrak{R}_{y_{12}x_{12}}}{\partial H_{y_{12}x_{12}}} \frac{\partial H_{y_{12}x_{12}}}{\partial B_{y_{12}x_{12}}} \frac{\partial B_{y_{12}x_{12}}}{\partial \phi_{y_{12}x_{12}}} \frac{\partial \phi_{y_{12}x_{12}}}{\partial \phi_1} \quad (4.23)$$

where  $\phi_{y_{12}x_{12}}$  is the flux related to reluctance. The term  $\partial H_{y_{12}x_{12}}/\partial B_{y_{12}x_{12}}$  is obtained by HB curve. The other terms in Equation (4.23) are defined as

$$\frac{\partial \mathfrak{R}_{y_{12}x_{12}}}{\partial H_{y_{12}x_{12}}} = \frac{1}{B_{y_{12}x_{12}}} \frac{y_1 - y_2}{(x_2 - x_1)d} \quad (4.24)$$

$$\frac{\partial B_{y_{12}x_{12}}}{\partial \phi_{y_{12}x_{12}}} = \frac{1}{(x_2 - x_1)d} \quad (4.25)$$

$$\frac{\partial \phi_{y_{12}x_{12}}}{\partial \phi_1} = 1 \quad (4.26)$$

By the above approach, all functions and their derivatives are obtained and calculated.

#### 4.5. MO-PSO of the Proposed AF-PMA-ECB

The particle swarm algorithm is selected for the multiobjective optimization because of its simple and effective structure [91, 92]. The particle swarm algorithm is a metaheuristic optimization method, which is inspired by the social behaviour of bird flocking and fish schools. In the PSO, all particles share their experiences with the population (swarm), and each particle updates its position ( $x$ ) and velocity ( $v$ ) by personal (pbest) and global (gbest) best solutions. The particle swarm algorithm can be explained by only two equations defined as

$$v_i^{k+1} = \xi_{iw} v_i^{k+1} + c_1 r_1 (pbest_i^k - x_i^k) + c_2 r_2 (gbest_i^k - x_i^k) \quad (4.27)$$

$$x_i^{k+1} = x_i^k + v_i^{k+1} \quad (4.28)$$

where  $k$  is the iteration number,  $i$  is the particle index,  $\xi_{iw}$  is the inertia weight,  $c_1$  and  $c_2$  are the personal and global acceleration coefficients, and  $r_1$  and  $r_2$  are randomly

generated numbers between 0 and 1. In the PSO,  $\xi_{iw}$  is taken as 0.5, and its damping rate, which is the reduction rate from one iteration to the next, is taken as 0.99. The coefficients of  $c_1$  and  $c_2$  are taken as 1 and 2, respectively.

The basic flow chart of the particle swarm algorithm is given in Figure 4.6. The particle swarm algorithm is an iterative process where the optimization starts with problem definition and PSO initialization. In the PSO initialization, the positions and velocities of particles are randomly created. The initial values of  $g_{best}$  and  $p_{best}$  are taken as  $+\infty$  or  $-\infty$ . This depends on the problem definition, that is, whether minimization or maximization is the task. After initialization, velocity and position are calculated for each particle, respectively, and the cost function is evaluated by particle position, which is a vector with values of the variables. After obtaining the cost function,  $p_{best}$

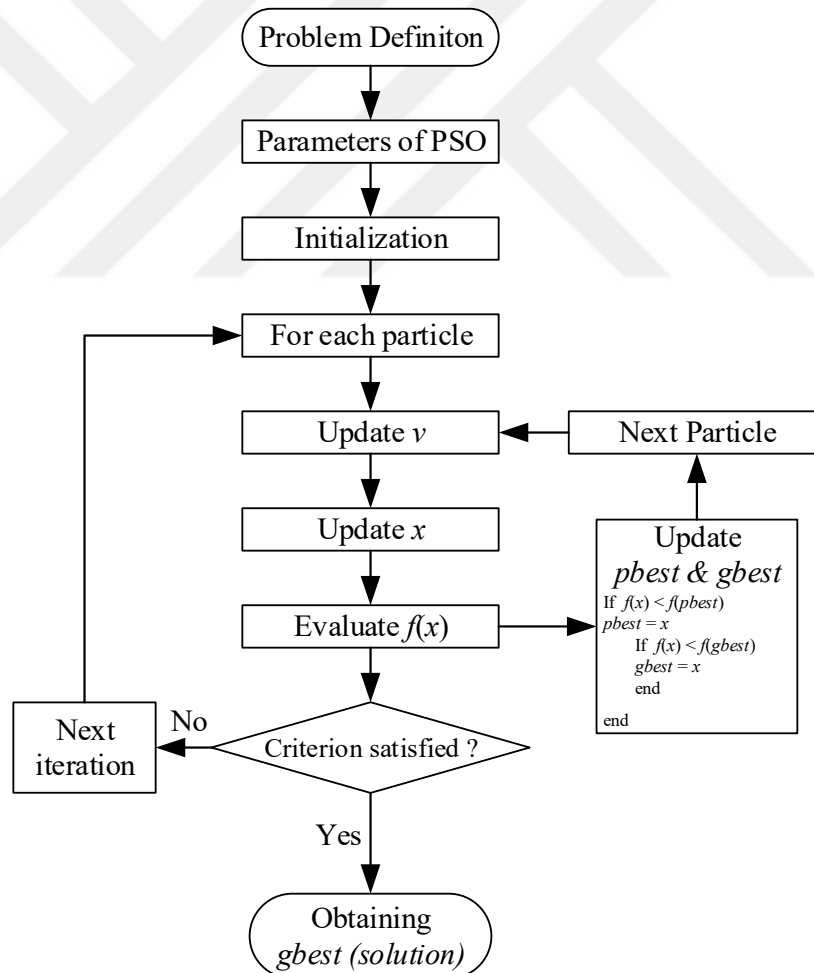


Figure 4.6. Flowchart of the particle swarm optimization

and gbest values are checked and updated if necessary. This loop is performed for all particles. Next, the optimization termination criteria are checked, and the process is repeated until the final number of iterations is reached. Finally, the gbest solution is assigned as the optimum design, and the optimum design parameters are obtained by the gbest position.

The nonlinear analytical model is adapt to the MO-PSO and 500 the size of population and repository and 100 the number of iterations are used in the optimization. The stator tooth-to-pole ratio, PM-to-slot ratio and PM height are selected as variables and minimum-maximum values are given in Table 4.2. The outer-to-inner diameter, the current density in the coils, air gap length and the brake disc properties are fixed during optimization. MO-PSO has three cost functions as braking torque, total PM mass and total ampere-turns. In this study, two design cases are targeted to test the analytical approach and MO-PSO. The Case-1 aims the 28 Nm of braking torque with minimum ampere-turns and the Case-2 goals maximum braking torque, which is set to 47.5 Nm due to the test setup properties (Table 4.3).

Table 4.2. Variable parameters of MO-PSO

Parameters	Minimum	Maximum
Tooth-to-pole ratio	0.3%	0.85%
PM-to-slot ratio	0.05%	0.9%
PM height	0.5 mm	10 mm

Table 4.3. Cost functions of MO-PSO

Cost Function	Case-1	Case-2
Braking torque	28 Nm	47.5 Nm
Total PM mass	Minimum	Minimum
Total ampere-turns	Minimum	Minimum

The 3D-Pareto surfaces obtained from MO-PSO of Case-1 and Case-2 are given in Figure 4.7 and Figure 4.8, respectively. The nondominating design alternatives are presented in the figures. The nondominating solutions are chosen by a roulette wheel genetic operator [91, 92]. It should be noticed that in the figures: 1<sup>st</sup> objective is absolute difference between rated and computed braking torques, 2<sup>nd</sup> objective is total



PM mass, 3<sup>rd</sup> objective is the total ampere-turns. To clarify the selection criterion, the PM width info also is given in the 3D-Pareto surfaces with color bar.

Before explaining the selection criteria, it should be stated that the 1<sup>st</sup> function is the dominant cost function of the MO-PSO. The following matters are taken into considerations for selecting the optimized design point: (1) the optimized design should provide the rated braking torque, (2) PM geometry shouldn't be so small to avoid the PM demagnetization, and (3) the total ampere-turns and total PM mass should be as small as possible. The optimized (selected) design points are marked in the figures.

The target braking torque for Case-1 is 28 Nm while the optimized design has 28.2 Nm which is below 1% of difference. The Case-2 aims to reach the 47.5 Nm in MO-PSO and the optimized design has 48.28 Nm of braking torque which means nearly 2% difference. These results agree well with the targets and errors are in acceptable levels. The PM height, PM-to-slot ratio, total PM mass and ampere-turns of the optimized design parameters are all given in Table 4.4.

Table 4.4. Optimized Design Parameters

Cost Function	Case-1	Case-2
Braking torque	28.2 Nm	48.28 Nm
Tooth-to-pole ratio	0.722	0.475
PM-to-slot ratio	0.18	0.21
PM height	8.1 mm	10 mm
Total PM mass	54.28 g	151.25 g
Total ampere-turns	996 A-turns	1324 A-turns

#### 4.6. 3D-FEA Validation of the Optimized AF-PMA-ECBs

The validation of the optimized cases is critical in order to prove the investigated design approach. The 3D-FEA simulations are carried out at the speed of 1000 min<sup>-1</sup>. It should be noticed that one transient 3D-FEA simulation, which consists of 250 time steps, takes nearly 59 hours by i7-6700HQ processor with 32 GB of RAM computer.

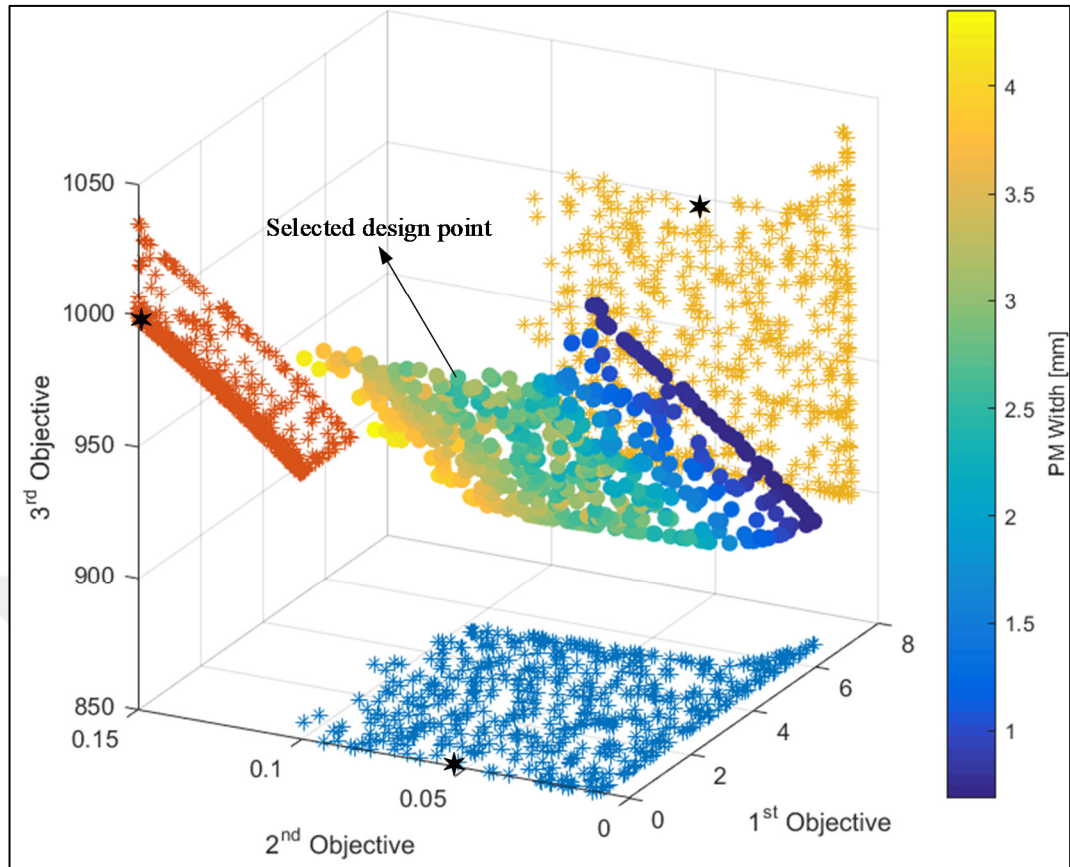


Figure 4.7. 3D-Pareto surface of the Case-1

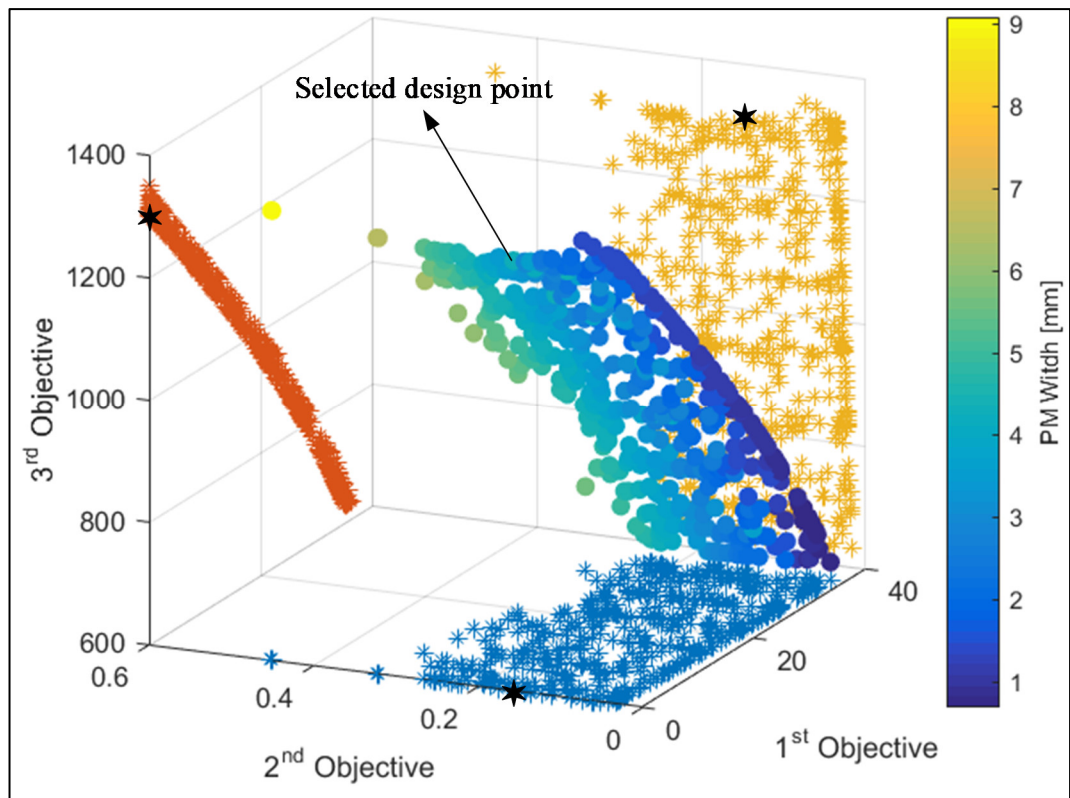


Figure 4.8. 3D-Pareto surface of the (a) Case-2

The symmetry 3D-FEA model and mesh profile of the optimized cases at the time zero are shown in Figure 4.9. Air gap is meshed with 2 layers to increase the accuracy of analyses. The magnetic flux density value of yoke, tooth and the brake disc of the cases are also illustrated in Figure 4.9. The comparison of the magnetic flux densities of the yoke, tooth and the brake disc obtained from 3D-FEA and nonlinear analytical approach are given in Table 4.5. Close results are obtained between the nonlinear analytical approach and 3D-FEA even in the saturation region of BH curve.

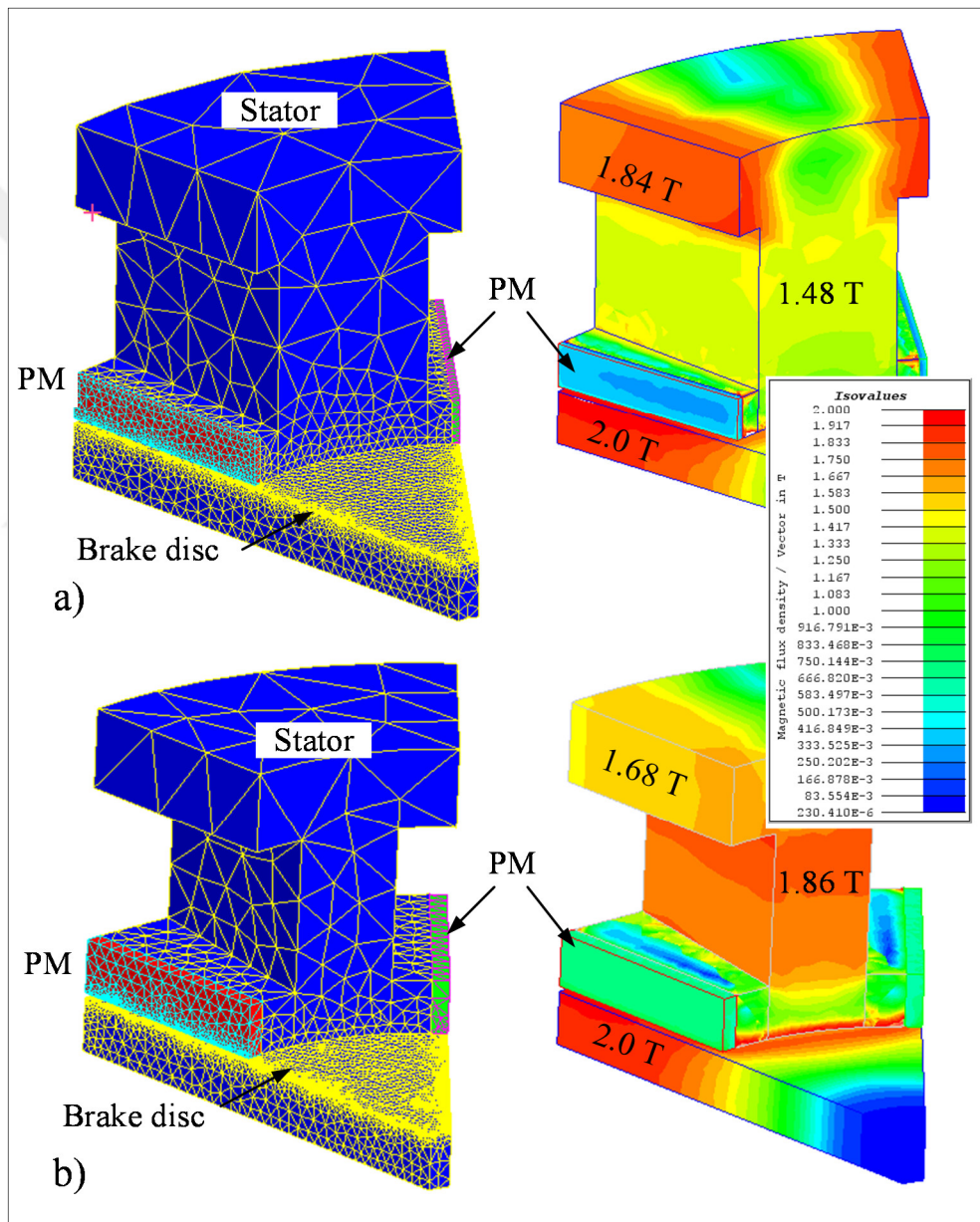


Figure 4.9. 3D-FEA model with mesh structure, and magnetic flux density profile of (a) Case-1 and (b) Case-2 at the time zero PM width

Table 4.5. Results comparison

	Case-1		Case-2	
	FEA	Analytical	FEA	Analytical
Yoke	1.84 T	1.91 T	1.68 T	1.77 T
Tooth	1.48 T	1.52 T	1.86 T	1.81 T
Brake disc	2.0 T	1.93 T	2.02 T	2.08 T

The transient responses for both cases are given in Figure 4.10. 60 milliseconds of analysis time is performed to demonstrate the transient and steady state regions for both cases. It is obtained that Case-1 has 27.3 Nm of braking torque and Case-2 has 48.5 Nm of braking torque at the rated speed of  $1000 \text{ min}^{-1}$ . The results show that investigated approach works quite well, and MO-PSO and 3D-FEA provide close results with reasonable errors.

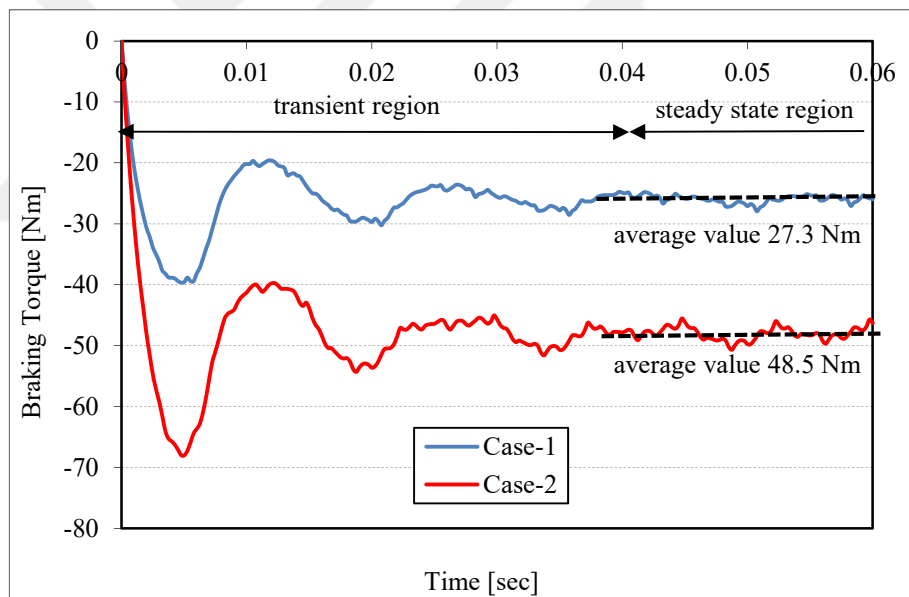


Figure 4.10. Transient variation of braking torque for Case-1 and Case-2 obtained from 3D-FEA

As mentioned earlier, the magnetic flux density in the air gap decreases with the increase of the speed due to armature reaction. This case is considered by magnetic Reynolds number in the analytical approach. Magnetic flux density variation of both cases obtained from mean radius are given in Figure 4.11 to demonstrate its influence. It is clear that armature reaction is dominant for both cases and the average magnetic flux density over one pole-pitch decreases by 45% for Case-1 and 53% for Case-2. In

addition, current density variation for both cases is also given in Figure 4.12. It is clearly seen that brake disc of Case-1 has more current density than the Case-2, which results in more braking torque for Case-1.

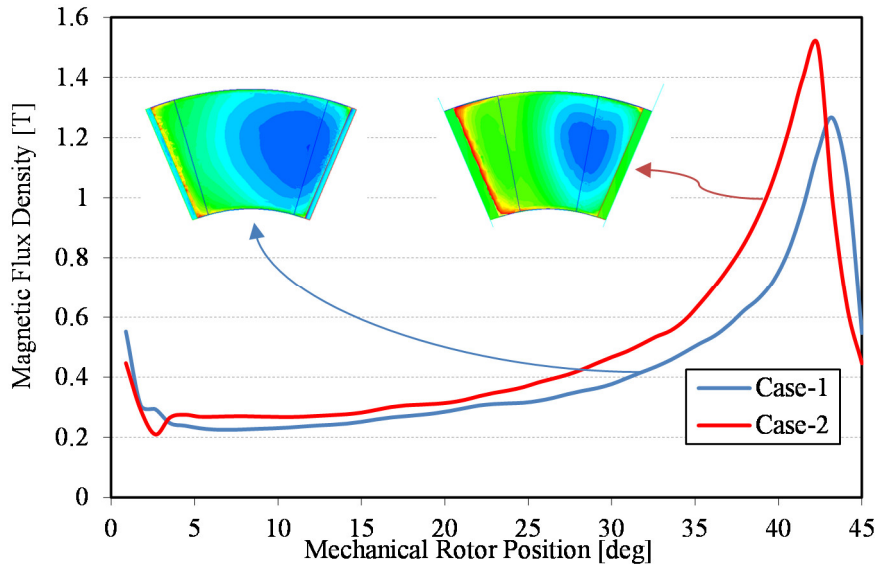


Figure 4.11. Magnetic flux density variation of Case-1 and Case-2 for one-pole pitch at the steady state

#### 4.7. Summary

A nonlinear analytical design approach of the proposed new AF-PMA-ECB is presented by particle swarm based multiobjective optimization in this chapter. Two design alternatives are targeted for the efficient usage of the magnets in the proposed AF-PMA-ECB topology presented. The nonlinear reluctance network modeling approach are implement into the optimization process and the optimum design parameters are determined by nondominating 3D-Pareto surfaces. The optimized designs are validated by transient 3D-FEAs. The results indicate that the proposed design approach works quite well and is a speedy design method compared to cumbersome transients 3D-FE simulations.

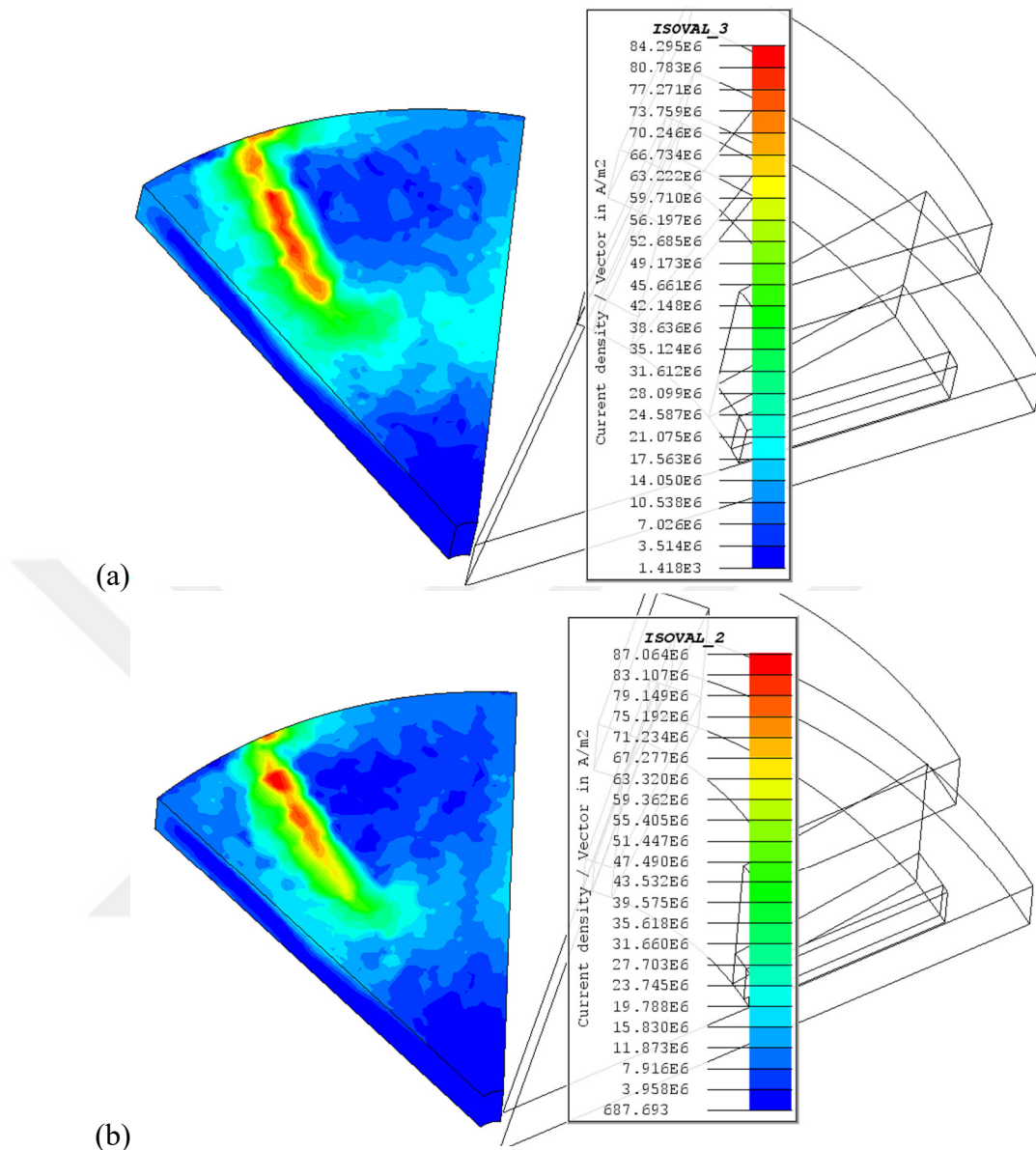


Figure 4.12. Current density variation of (a) Case-1 and (b) Case-2

## **5. NMDA OF THE NEW AF-PMA-ECB**

This chapter explores a nonlinear multidisciplinary design approach (NMDA) of the proposed new axial-flux permanent magnet assisted eddy current brake (AF-PMA-ECB). The optimized design “Case-2” presented in the previous chapter is investigated by NMDA and the output performances of braking torque variation, temperature rise in the brake disc, magnets and the coils in time are obtained. The NMDA presented in Chapter 3 is revised for the proposed AF-PMA-ECB topology. It is an important stage that the definition of the working limitation of the proposed AF-PMA-ECB has to be clarified before manufacturing since the braking torque and temperature variations in time cannot be obtained by 3-dimensional finite elements method (3D-FEM). Only, multiphysics coupled FEM software can solve the problem but such kind of software is not a cost-effective solution and require significant experience. Therefore, the proposed NMDA is applied to the new AF-PMA-ECB to determine the working limitations.

### **5.1. NMDA of the Proposed AF-PMA-ECB**

As explored in Chapter 3, the NMDA is an integrated design approach, which targets to analyze an AF-ECB by coupled nonlinear magnetic-thermal-structural modeling to clarify the actual brake performances. The multidisciplinary design is carried out in the time domain to define the braking torque, braking time, temperature variation, deflection and safety factor of the AF-ECB. The details of the NMDA was given in Chapter 3. In this chapter, the presented NMDA in Chapter 3 is revised for the proposed AF-PMA-ECB. The revised NMDA is illustrated in Figure 5.1. It has to be stated that the proposed brake consists of magnets in the slot openings and PMs are very sensitive to temperature. Therefore, temperature rise of the magnets has to be followed during analysis. In the revised NMDA, the nonlinear magnetic modeling investigated in Chapter 4 is used and additionally, PM properties are updated by the temperature rise. The nonlinear structural modeling is used as presented in the Chapter 3. The nonlinear thermal modeling is revised for the proposed AF-PMA-ECB to compute the temperature rise of the magnets and its effect. The details about nonlinear

behaviors of low carbon steel (BH curve, resistivity, heat capacity and temperature factor) were all given in Figure 3.2. The demagnetization curves of N30UH type NdFeB is provided in Figure 5.2 [93].

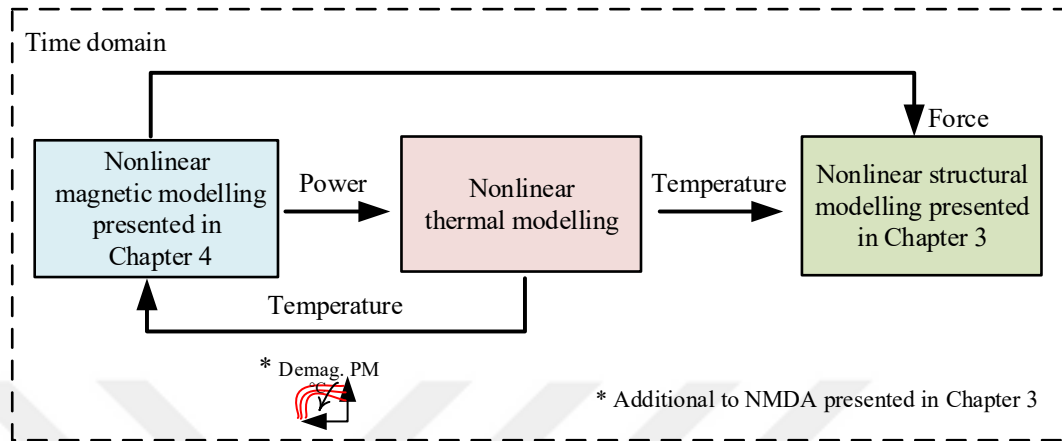


Figure 5.1. The revised NMDA. Demagnetization curve of the PM is updated by temperature rise

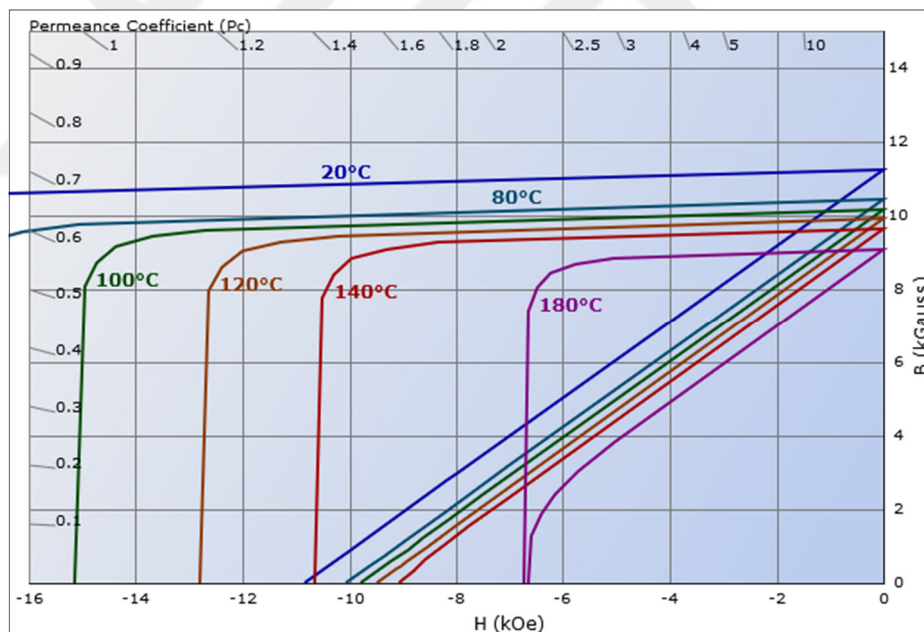


Figure 5.2. Demagnetization curves of the N30UH grade NdFeB [93]

### 5.1.1. Nonlinear magnetic modeling

Analytical modeling of the proposed AF-PMA-ECB is performed by 2D reluctance network modeling approach as presented in Chapter 4. Briefly, the reluctance network modeling presented here is a kind of meshing method that model could have x and/or y axes reluctance components and all mesh structures are linked to mesh fluxes and



current linkages. Symmetry model and the magnetic modeling of the proposed AF-PMA-ECB is given in Figure 5.3.

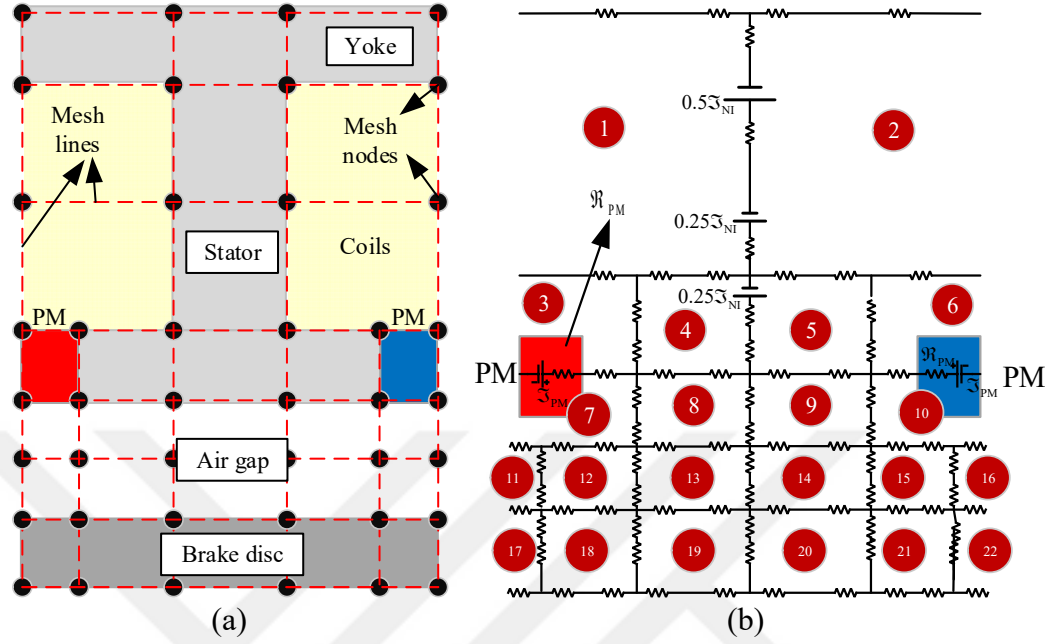


Figure 5.3. (a) Symmetry model and (b) the magnetic modeling of the proposed AF-PMA-ECB

The magnetic modeling approach presented in the previous chapter is used in this section. The size of a  $22 \times 22$  main reluctance matrix and the size of a  $1 \times 22$  current linkage vector are generated. The aim is to solve this matrix to find the mesh flux vector. The reluctances are defined by their x and y axes mesh info. The revised part of the magnetic modeling is adding temperature effect to PM properties. The reluctance of PM is here defined as

$$\mathfrak{R}_{PM}(T) = \frac{1}{\mu_0 \mu_{PM}(T)} \frac{x_{PM} - x_0}{(y_4 - y_3)d} \quad (5.1)$$

$$\mu_{PM}(T) = \frac{Br(T)}{\mu_0 H(T)} = \frac{Br_{int}(100+a)}{\mu_0 Hc_{int}(100+b)} \quad (5.2)$$

where  $Br_{int}$  is remanent induction at room temperature,  $Hc_{int}$  is the intrinsic coercivity,  $a$  is the temperature coefficient of remanent induction and  $b$  is the temperature coefficient of intrinsic coercivity. The temperature characteristics of NdFeB grades are

given in Table 5.1. By this table, the influence of temperature on PM properties can be considered in the nonlinear magnetic modeling.

Table 5.1. Temperature characteristics of NdFeB grades

Magnet Type	Rev.Temp.Coeff. of Induction (Br), a, %/ °C (20-100 °C)	Rev.Temp.Coeff. of Coercivity (Hci), b, %/ °C (20-100 °C)	Max. Working Temperature
	-0.12	-0.6	80 °C
M	-0.12	-0.58	100 °C
H	-0.11	-0.58	120 °C
SH	-0.1	-0.55	150 °C
UH	-0.09	-0.52	180 °C
EH	-0.085	-0.5	200 °C
VH/ AH	-0.08	-0.45	230 °C

A modified Newton-Raphson method and the functions and derivatives presented in Chapter 4 is used in this section and the braking torque variation is obtained by the same approaches.

### 5.1.2. Nonlinear thermal modeling

The temperature variation in the disc and also in the PM should be investigated in the proposed AF-PMA-ECB to determine the braking torque variation and working limitations. The nonlinear thermal modeling is investigated by thermal lumped-parameter in the revised NMDA as well. The schematic drawing of the proposed AF-PMA-ECB and the corresponding lumped-parameter thermal network are given in Figure 3.5. The T-equivalent circuit modeling approach is used because of the AF geometry. The thermal network consists of nine nodes: 1) disc, 2) air gap, 3) PM, 4) teeth tips, 5) stator teeth, 6) slot windings, 7) yoke, 8) frame and 9-10-11) shaft.

For the transient analysis, the temperature rise of each node is calculated with the matrix equation defined as

$$\frac{d}{dt}(\Delta T) = C^{-1}(P - G \cdot \Delta T) \quad (5.3)$$

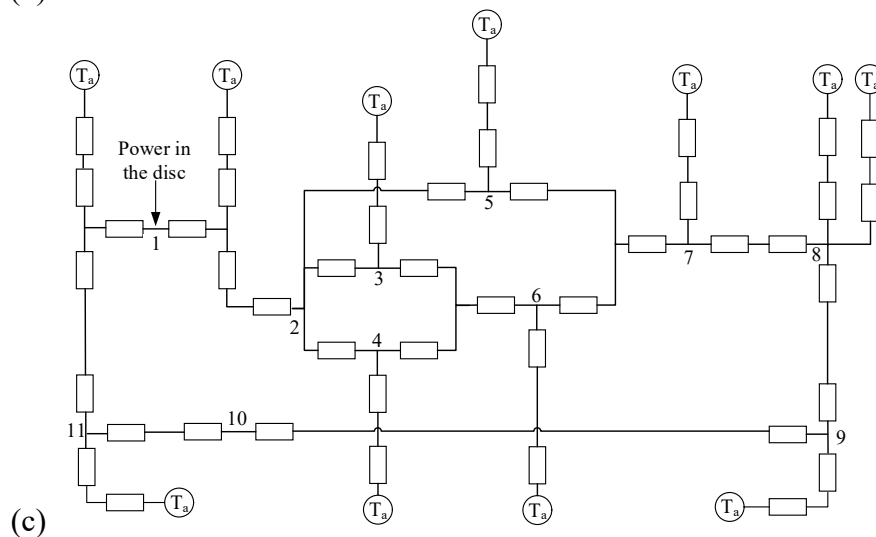
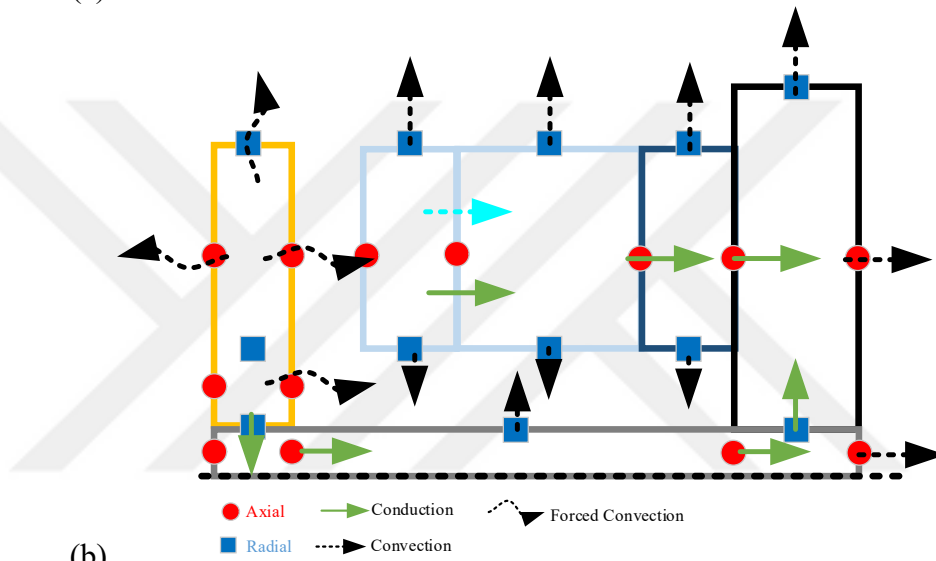
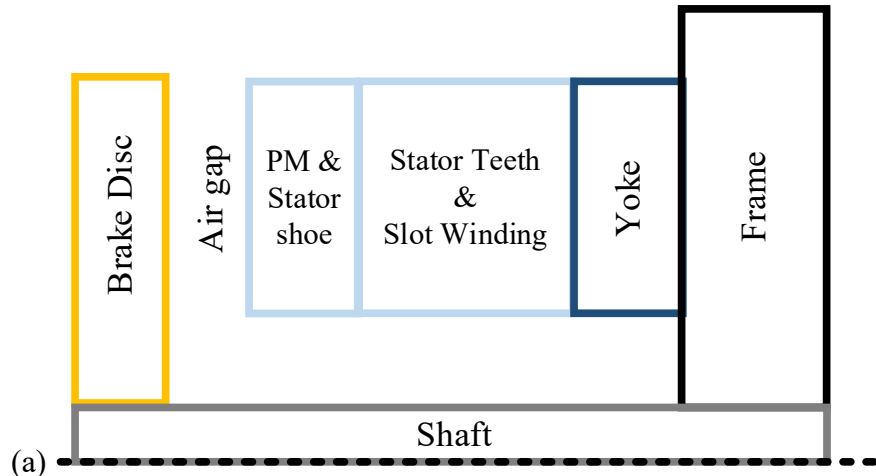


Figure 5.4. (a) The schematic drawing and (b) heat transfer flow definition and (c) thermal resistance network of the proposed AF-PMA-ECB.  $T_a$  represents the ambient temperature

where  $t$  is the time,  $\Delta T$  is the temperature rise vector,  $C$  is the thermal capacitance matrix,  $P$  is the power loss vector and  $G$  is the thermal conductance matrix defined as

$$G = \begin{bmatrix} \sum_{i=1}^n \frac{1}{R_{1,i}} & -\frac{1}{R_{1,2}} & -\frac{1}{R_{1,3}} & \cdots & -\frac{1}{R_{1,n}} \\ -\frac{1}{R_{2,1}} & \sum_{i=1}^n \frac{1}{R_{2,i}} & -\frac{1}{R_{2,3}} & \cdots & -\frac{1}{R_{2,n}} \\ -\frac{1}{R_{3,1}} & -\frac{1}{R_{3,2}} & \sum_{i=1}^n \frac{1}{R_{3,i}} & \cdots & -\frac{1}{R_{3,n}} \\ \vdots & \vdots & \vdots & \ddots & \vdots \\ -\frac{1}{R_{n,1}} & -\frac{1}{R_{n,2}} & -\frac{1}{R_{n,3}} & \cdots & \sum_{i=1}^n \frac{1}{R_{n,i}} \end{bmatrix} \quad (5.4)$$

where  $n$  is the node number and  $R$  is the thermal resistance. The subscripts in  $R$  define the total thermal resistance between the two nodes. In the nonlinear thermal modeling, conduction and convection thermal resistances are used and the same definitions described in Chapter 3 were used. The nonlinear thermal modeling starts with setting the initial parameters. Firstly, all thermal resistances are derived and the temperatures are calculated. Then, the calculated temperature info is shared with the nonlinear magnetic and the structural modeling. In the next time step, the nonlinear parameters are updated by the new temperature and power info, and the progress is repeated. The critical temperature in the brake disc and PM is checked at each time step and if it is larger than desired, the analysis fails.

### 5.1.3. Nonlinear structural modeling

The deflection and the fatigue analyses have to be considered to define the mechanical limitations in all kind of electric machines. The structural modeling is also important for the proposed AF-PMA-ECB. In the revised NMDA, affected force and stresses on the disc are calculated to define the deflection and the safety factor of the disc as presented in Chapter 3. The general formula of the deflection on the outer radius of the disc and fatigue analysis by Soderberg failure criterion are defined

$$s = \frac{Fr^3}{3E_m I_m} \quad (5.5)$$

$$\frac{\sigma_a}{S_e} + \frac{\sigma_m}{S_y} = \frac{1}{n} \quad (5.6)$$

where  $F$  is the affected force in axial direction,  $E_m$  is the modulus of elasticity and  $I_m$  is area moment of inertia of the disc,  $\sigma_a$  is the amplitude stress,  $\sigma_m$  is the midrange stress,  $S_e$  is the endurance limit,  $S_y$  is the yield stress and  $n$  is the factor of safety. The details were previously presented in Chapter 3.

## 5.2. Investigation of the Optimized AF-PMA-ECB by NMDA

The optimized design Case-2 presented in Chapter 4 is investigated by the NMDA in this section. Hereafter, the optimized Case-2 is named as optimized AF-PMA-ECB. The 3-dimensional (3D) model of the optimized brake is given in Figure 5.5. The key parameters of the optimized AF-PMA-ECB is also given Table 5.2. The inner to outer radius ratio of the optimized AF-PMA-ECB is found to be 0.55 and the stator teeth-to-pole ratio is 0.475. The N30UH type NdFeB magnets are used in the slot openings

Table 5.2. Key parameters of the optimized AF-PMA-ECB

Parameter	Value
Outer diameter	180 mm
Inner diameter	100 mm
Stator teeth-to-pole ratio	0.475
Axial air gap	1 mm
Number of slots	8
Turn number in the slot	172×2
Maximum current density in the coil	10 A/mm <sup>2</sup>
Stator and brake disc material	ST37
Brake disc thickness	15 mm
Number of magnets	8
PM Type	N30UH
PM Size	6.18×10×40 mm <sup>3</sup>
PM Br at room temperature	1.1 T
PM Hc at room temperature	860/m

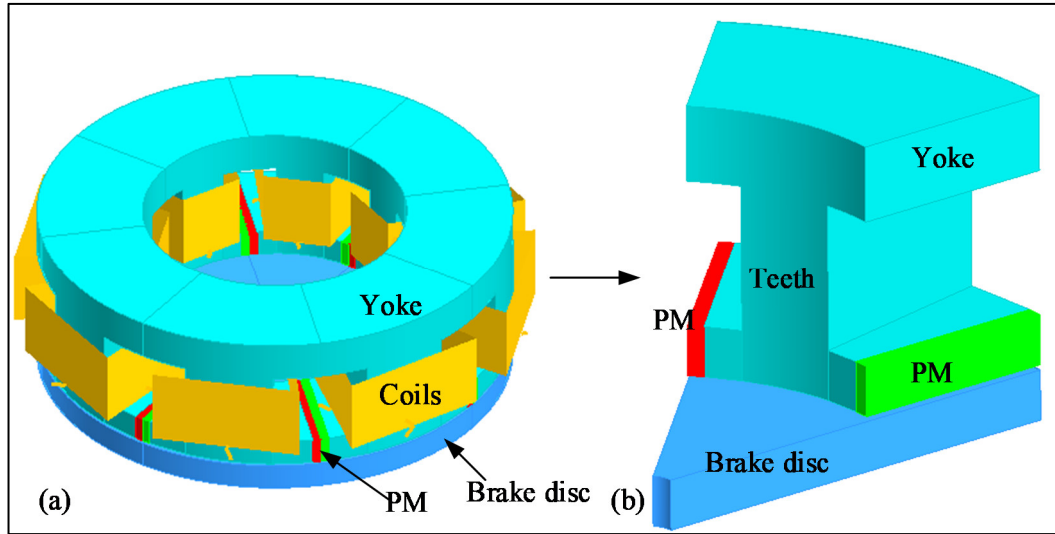


Figure 5.5. (a) The 3D model and (b) symmetry model of the optimized AF-PMA-ECB

and the optimized PM size is  $6.18 \times 10 \times 40 \text{ mm}^3$ . The number of 344 coil turns are wound in each slot and the allowed maximum current density in the coils is set to  $10 \text{ A/mm}^2$ , which is equal to the excitation current of 7.7 A. The working speed range of the optimized AF-PMA-ECB varies from 500 to  $2000 \text{ min}^{-1}$  due to lab facilities.

6 different scenarios are performed by the proposed NMDA. The studied cases of the optimized AF-PMA-ECB is given in Table 5.3. In the first 3 scenarios, the speed is fixed to  $1000 \text{ min}^{-1}$  and the excitation current is adjusted to 3.5 A, 5.8 A and 7.7 A, respectively. It has to be borne in mind that the excitation current is independent from temperature rise in first 3 cases. In the last 3 scenarios, the speed is varied to 500, 1000 and  $2000 \text{ min}^{-1}$  and the rated excitation current is applied with considering the temperature rise in the coils, which means that the excitation current is dependent to

Table 5.3. Studied scenarios of the optimized AF-PMA-ECB

Scenario	Speed [ $\text{min}^{-1}$ ]	Current [A]
A	1000	7.7 A fixed
B	1000	5.8 A fixed
C	1000	3.5 A fixed
D	500	7.7 A at the initial
E	1000	7.7 A at the initial
F	2000	7.7 A at the initial

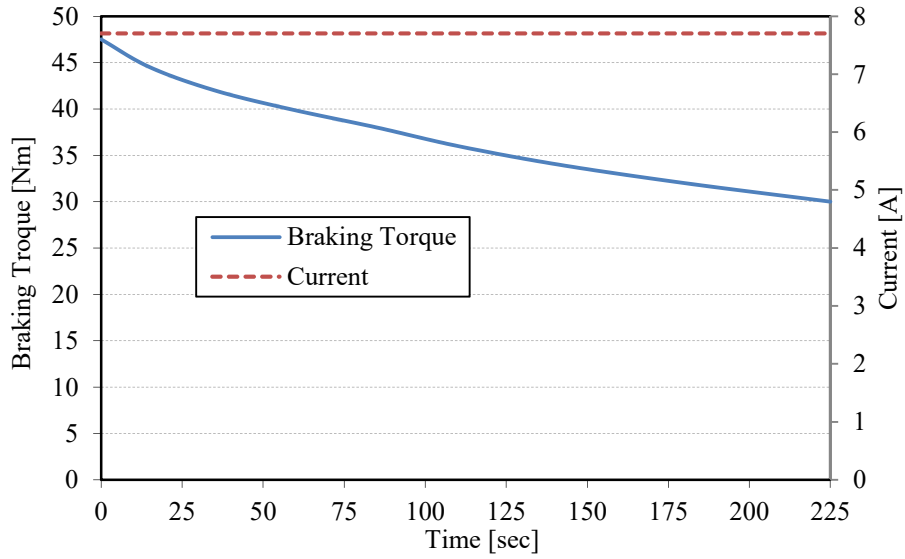


Figure 5.6. Braking torque variation of the optimized AF-PMA-ECB for Scenario-A ( $1000 \text{ min}^{-1}$  and  $7.7 \text{ A}$  fixed)

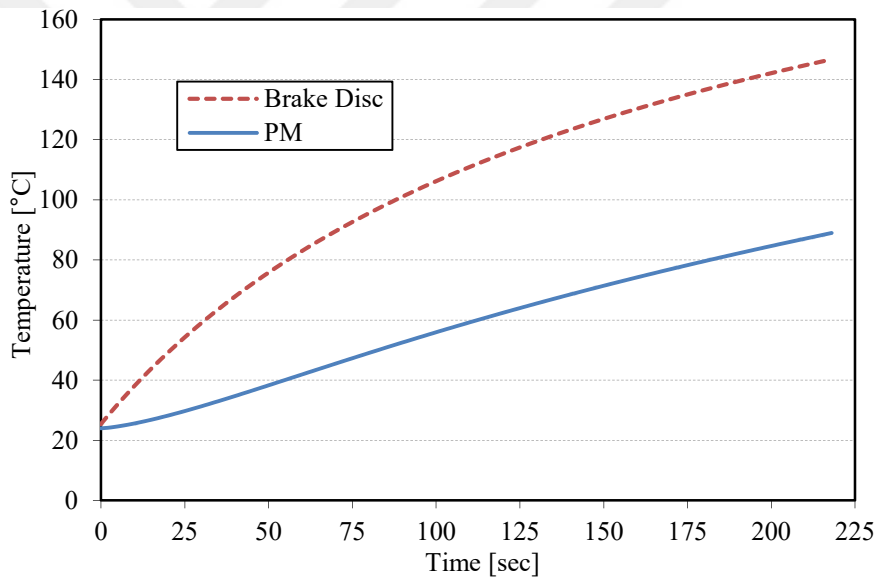


Figure 5.7. Temperature variation of the brake disc and the PM for Scenario-A ( $1000 \text{ min}^{-1}$  and  $7.7 \text{ A}$  fixed)

the temperature. The speed and the current information of the studied cases can be found in Table 5.3.

The braking torque and temperature variations obtained from Scenario-A are given in Figure 5.6 and Figure 5.7, respectively. The simulation time is set to 225 seconds and the speed is set to  $1000 \text{ min}^{-1}$  during NMDA. The results given in Figure 5.6 show that the braking torque is  $47.6 \text{ Nm}$  at the beginning and after 225 seconds is reduced to  $30 \text{ Nm}$ . The reducing percentage of the braking torque is  $36.84$  after 225 seconds. The

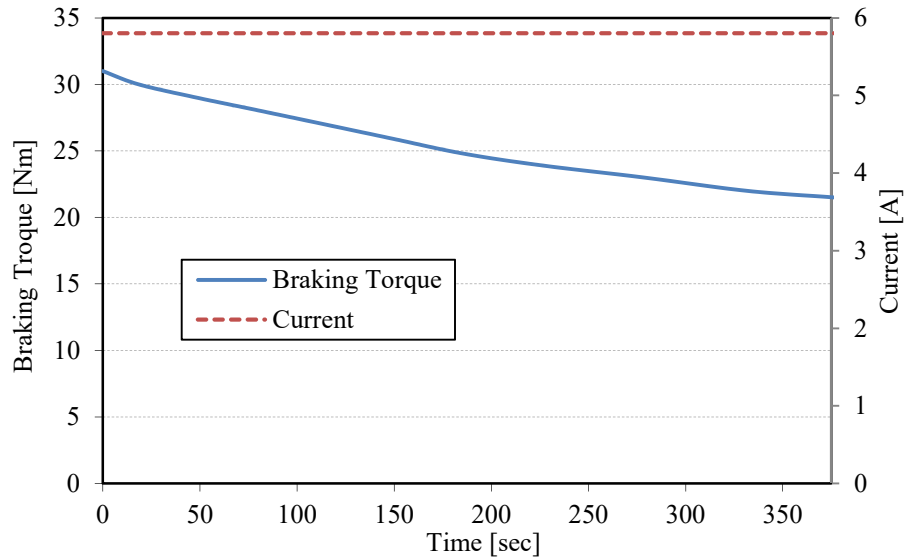


Figure 5.8. Braking torque variation of the optimized AF-PMA-ECB for Scenario-B ( $1000 \text{ min}^{-1}$  and 5.8 A fixed)

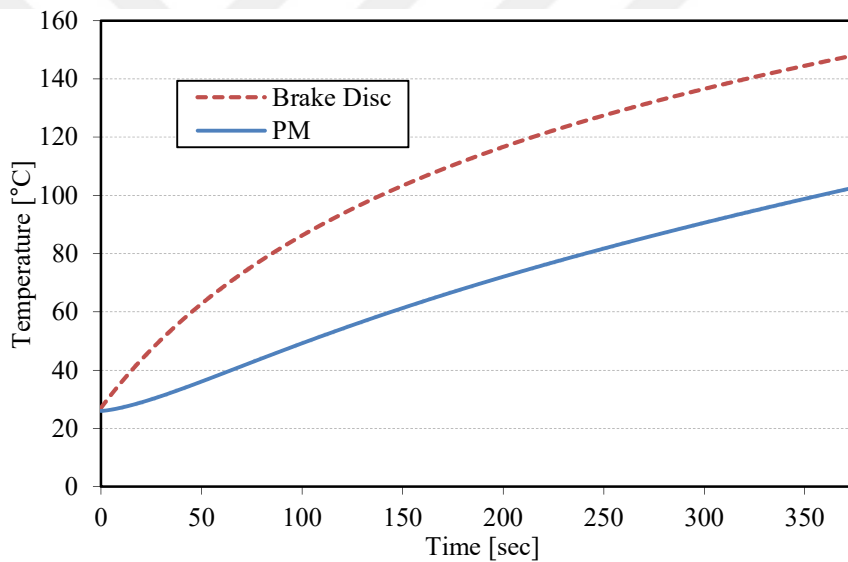


Figure 5.9. Temperature variation of the brake disc and the PM for Scenario-B ( $1000 \text{ min}^{-1}$  and 5.8 A fixed)

temperature variation of the brake disc and the PM are given in Figure 5.7. The results show that temperature rise of the brake disc and the PM are  $126 \text{ }^\circ\text{C}$  and  $67 \text{ }^\circ\text{C}$  respectively.

The braking torque and temperature variations obtained from Scenario-B are given in Figure 5.8 and Figure 5.9, respectively. The simulation time is set to 375 seconds and the speed is set to  $1000 \text{ min}^{-1}$  during NMDA. The results given in Figure 5.8 show that the braking torque is 31 Nm at the beginning and after 375 seconds is reduced to 22 Nm. The braking torque is reduced by 29%. The temperature variation of the brake



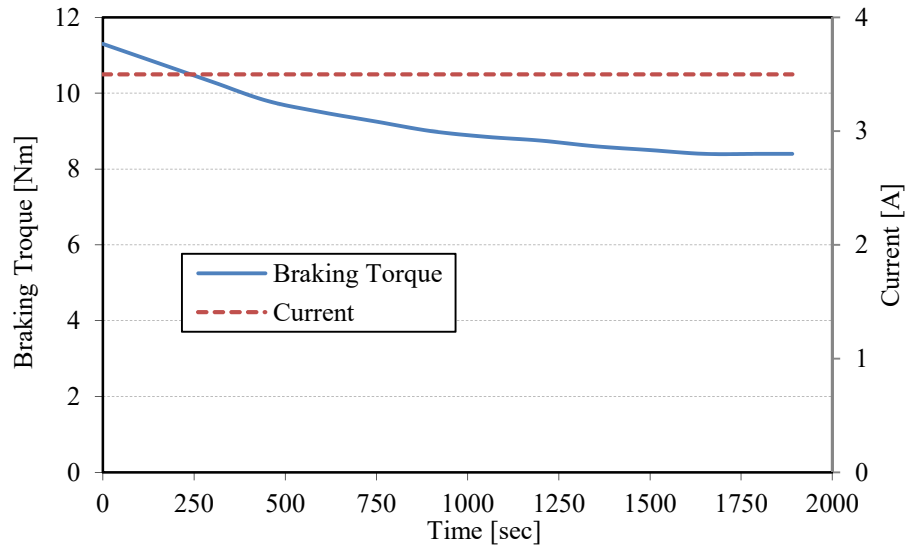


Figure 5.10. Braking torque variation of the optimized AF-PMA-ECB for Scenario-C ( $1000 \text{ min}^{-1}$  and  $3.5 \text{ A}$  fixed)

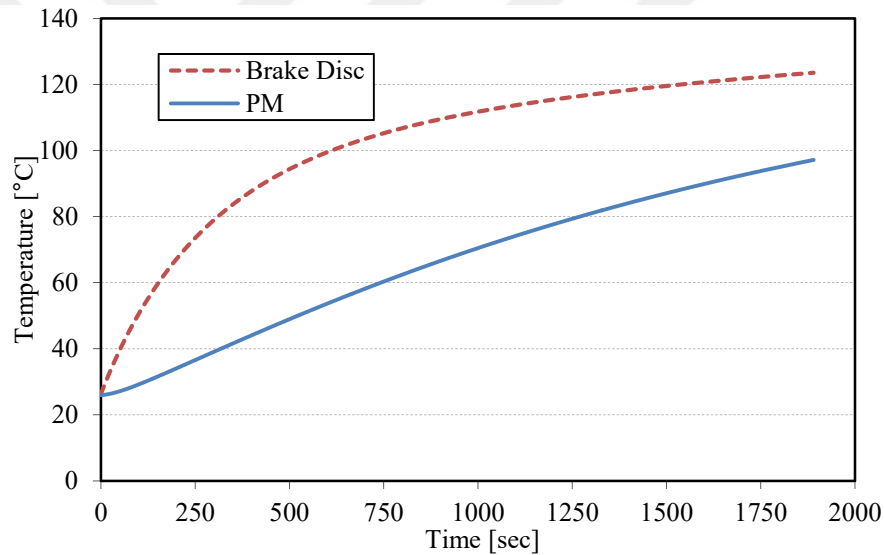


Figure 5.11. Temperature variation of the brake disc and the PM for Scenario-C ( $1000 \text{ min}^{-1}$  and  $3.5 \text{ A}$  fixed)

disc and the PM are given in Figure 5.9. The results show that temperature rise of the brake disc and the PM are  $150 \text{ }^\circ\text{C}$  and  $101 \text{ }^\circ\text{C}$  respectively.

The braking torque and temperature variations obtained from Scenario-C are given in Figure 5.10 and Figure 5.11, respectively. The simulation time is set to 1890 seconds and the speed is set to  $1000 \text{ min}^{-1}$  during NMDA. The results given in Figure 5.10 show that the braking torque is  $11 \text{ Nm}$  at the beginning and after 1890 seconds is reduced to  $8.4 \text{ Nm}$ . The temperature variation of the brake disc and the PM are given

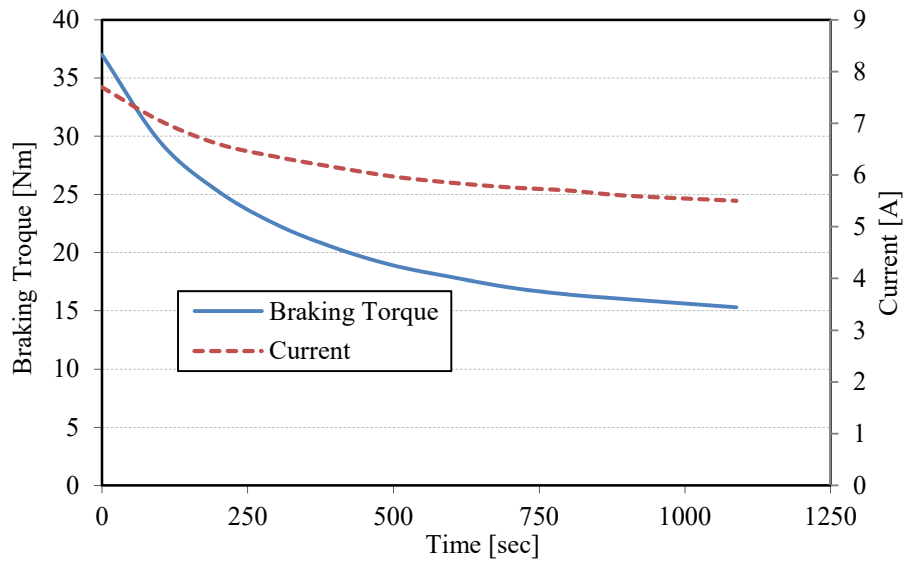


Figure 5.12. Braking torque variation of the optimized AF-PMA-ECB for Scenario-D ( $500 \text{ min}^{-1}$  and  $7.7 \text{ A}$  initial)

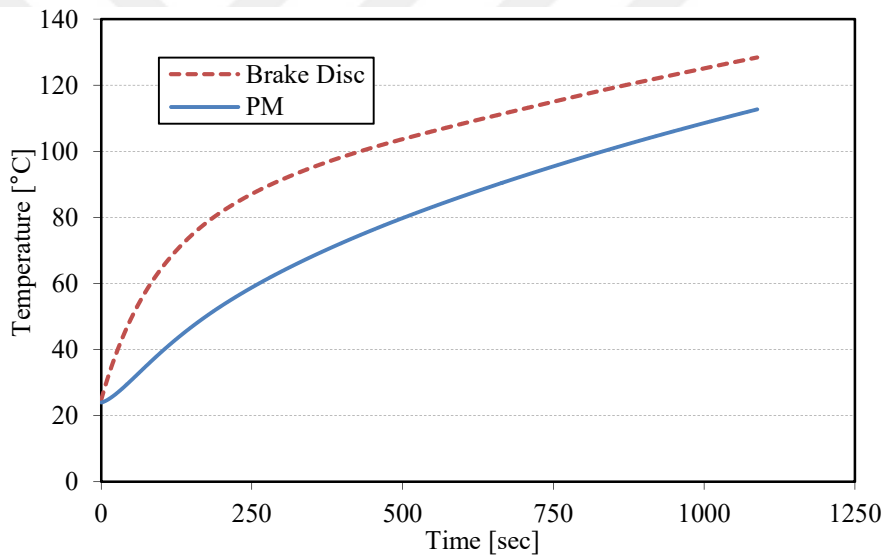


Figure 5.13. Temperature variation of the brake disc and the PM for Scenario-D ( $500 \text{ min}^{-1}$  and  $7.7 \text{ A}$  initial)

in Figure 5.11. The results show that temperature rise of the brake disc and the PM are  $131 \text{ }^\circ\text{C}$  and  $103 \text{ }^\circ\text{C}$ .

The braking torque, excitation current and the temperature variations obtained from Scenario-D are given in Figure 5.12 and Figure 5.13, respectively. The simulation time is set to 1100 seconds and the excitation current at the room temperature is set to  $7.7 \text{ A}$  and the speed is set to  $500 \text{ min}^{-1}$  during NMDA. The results show that the braking torque is  $37 \text{ Nm}$  at the beginning and after 1100 seconds, is reduced to  $15.3 \text{ Nm}$ . Nearly 58.3% of braking torque reduction is achieved. In Scenario-D, the excitation current

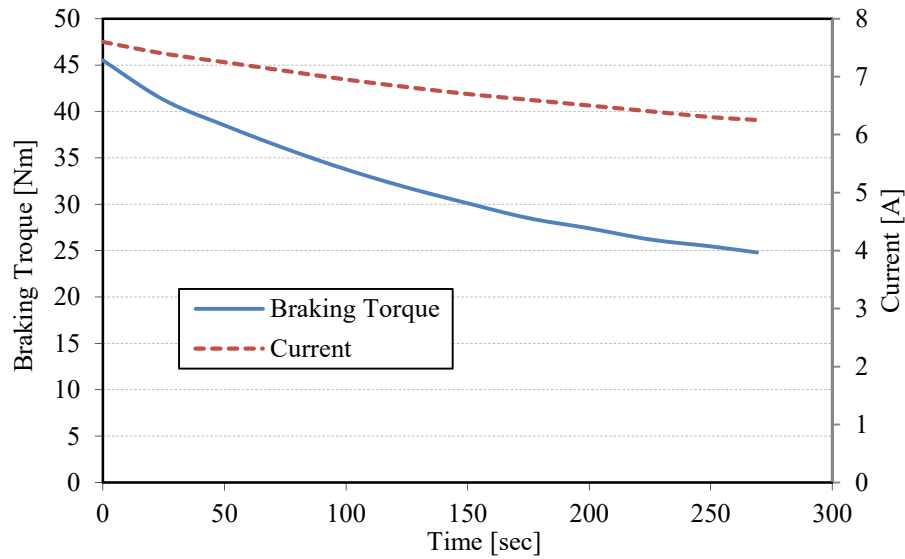


Figure 5.14. Braking torque variation of the optimized AF-PMA-ECB for Scenario-E ( $1000 \text{ min}^{-1}$  and  $7.7 \text{ A}$  initial)

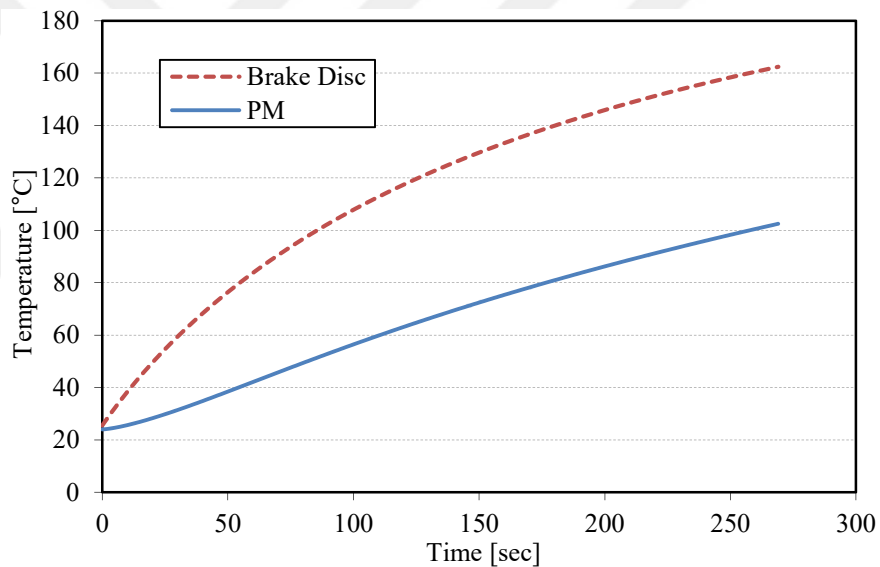


Figure 5.15. Temperature variation of the brake disc and the PM for Scenario-E ( $1000 \text{ min}^{-1}$  and  $7.7 \text{ A}$  initial)

also dependent to the temperature rise. The excitation current is  $7.7 \text{ A}$  in the beginning and finally is reduced to  $5.5 \text{ A}$ . The temperature variation of the brake disc and the PM are given in Figure 5.13. The results show that temperature rise of the brake disc and the PM are  $115 \text{ }^\circ\text{C}$  and  $85 \text{ }^\circ\text{C}$ .

The braking torque, excitation current and the temperature variations obtained from Scenario-E are given in Figure 5.14 and Figure 5.15, respectively. The simulation time is set to 275 seconds and the excitation current at the room temperature is set to  $7.7 \text{ A}$

and the speed is set to  $1000 \text{ min}^{-1}$  during NMDA. The results show that the braking torque is  $47.5 \text{ Nm}$  at the beginning and after 275 seconds, is reduced to 25. Nearly 47% of braking torque reduction is achieved. In Scenario-E, the excitation current also dependent to the temperature rise. The excitation current is  $7.7 \text{ A}$  in the beginning and finally is reduced to  $6.25 \text{ A}$ . The temperature variation of the brake disc and the PM are given in Figure 5.15. The results show that temperature rise of the brake disc and the PM are found to be  $141 \text{ }^\circ\text{C}$  and  $83 \text{ }^\circ\text{C}$  respectively.

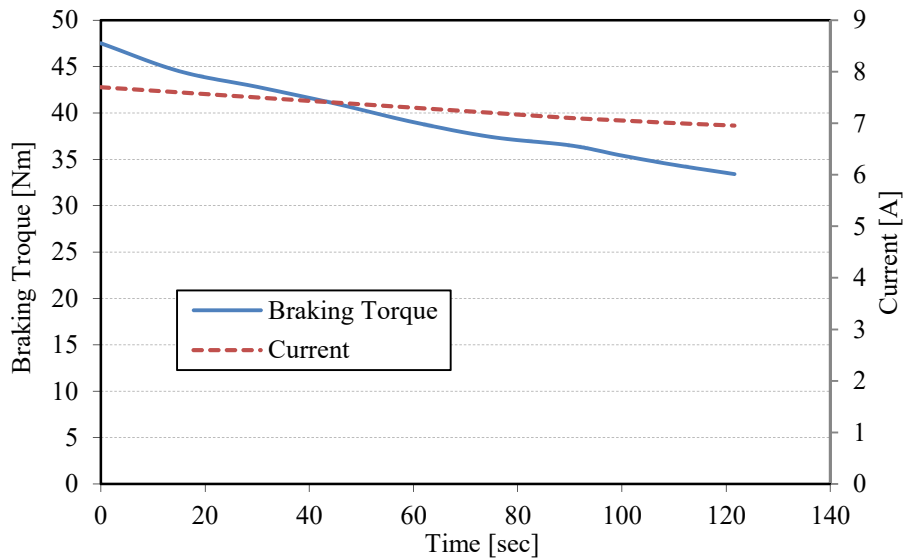


Figure 5.16. Braking torque variation of the optimized AF-PMA-ECB for Scenario-F ( $2000 \text{ min}^{-1}$  and  $7.7 \text{ A}$  initial)

The braking torque, excitation current and the temperature variations obtained from Scenario-F are given in Figure 5.16 and Figure 5.17, respectively. The simulation time is set to 120 seconds and the excitation current at the room temperature is set to  $7.7 \text{ A}$  and the speed is set to  $2000 \text{ min}^{-1}$  during NMDA. The results show that the braking torque is  $47.5 \text{ Nm}$  at the beginning and after 120 seconds, is reduced to  $33.4 \text{ Nm}$ . In Scenario-F, the excitation current also dependent to the temperature rise that the excitation current is  $7.7 \text{ A}$  in the beginning and finally is reduced to  $6.95 \text{ A}$ . The temperature variation of the brake disc and the PM are given in Figure 5.17. The results show that temperature rise of the brake disc and the permanent magnets are obtained to be  $160 \text{ }^\circ\text{C}$  and  $80 \text{ }^\circ\text{C}$ .

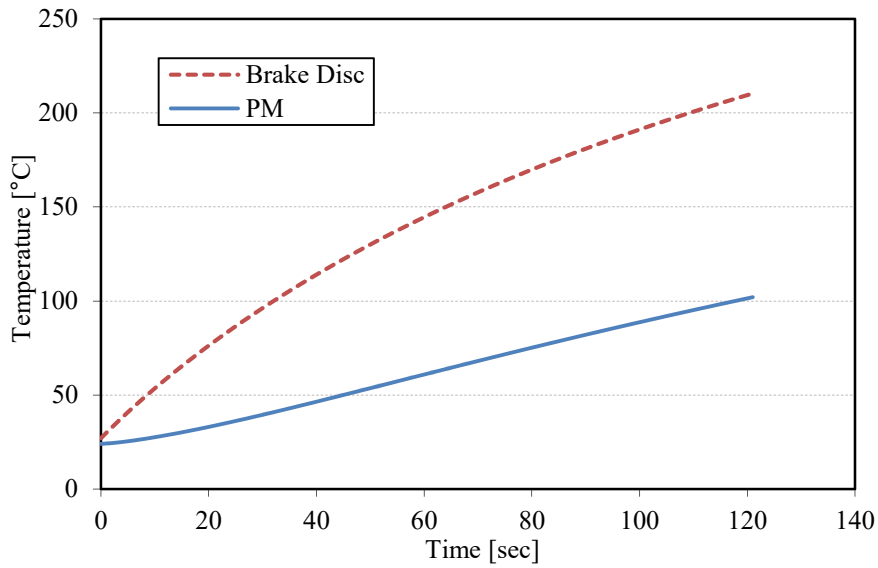


Figure 5.17. Temperature variation of the brake disc and the PM for Scenario-F ( $2000 \text{ min}^{-1}$  and  $7.7 \text{ A}$  initial)

### 5.3. Summary

In this chapter, the optimized AF-PMA-ECB is investigated by the proposed NMDA. The proposed NMDA presented in Chapter 4 is revised for the optimized AF-PMA-ECB topology that the temperature effect on PM properties is considered in the revised NMDA. The NMDA is nonlinear magnetic, thermal and structural coupling modeling and aims to find the actual brake performance. The optimized AF-PMA-ECB is investigated by 6 different working cases. The braking torque and the temperature rise for brake disc and PM are summarized for all scenarios and the reduction rate of the braking torque for all cases are also provided in this chapter.

## **6. THE PROTOTYPE AND EXPERIMENTAL WORK**

The last chapter of this thesis deals with the prototype manufacturing and the experimental work. The optimized AF-PMA-ECB investigated in the previous chapter is manufactured and a special test set up system is prepared for the experimental work. The tests are performed in two stages: (1) cold-case test and (2) hot-case test. During cold-case experimental work, the temperature rise in the brake disc is not allowed, therefore, the tests are carried out in very short of time. The cold-case, temperature-independent, studies aim to compare the results obtained from experimental work, 3D-FEA and the nonlinear magnetic modeling. The second stage tests are the hot-case experimental work. In this stage, the temperature effect on the brake disc, permanent magnets and the coils are allowed. The braking torque and the temperature rise were measured in time and the experimental results are compared with the proposed NMDA and FEA simulations.

### **6.1. Prototype of the optimized AF-PMA-ECB**

The prototype of the optimized AF-PMA-ECB is manufactured and tested to validate the results obtained from nonlinear magnetic modeling, the proposed NMDA and 3D-FEA. Manufactured stator, windings and the magnets of the novel AF-PMA-ECB are illustrated in Figure 6.1. ST37, low carbon steel, material is used as stator and the rotor material in the prototype. Concentrated windings are employed and connected in series. The N30UH type NdFeB magnets are placed into the slot openings and attached with a special magnet glue material.

### **6.2. Test Setup**

The test system is displayed in Figure 6.2. The setup consists of a drive motor, a prototype, a torque meter and a dSPACE control board. The drive motor has 47.5 Nm of rated torque with 3000 min<sup>-1</sup> of maximum speed. The torque meter has 0-50 Nm of sensing range with high accuracy. The torque data is acquired by dSPACE control board.

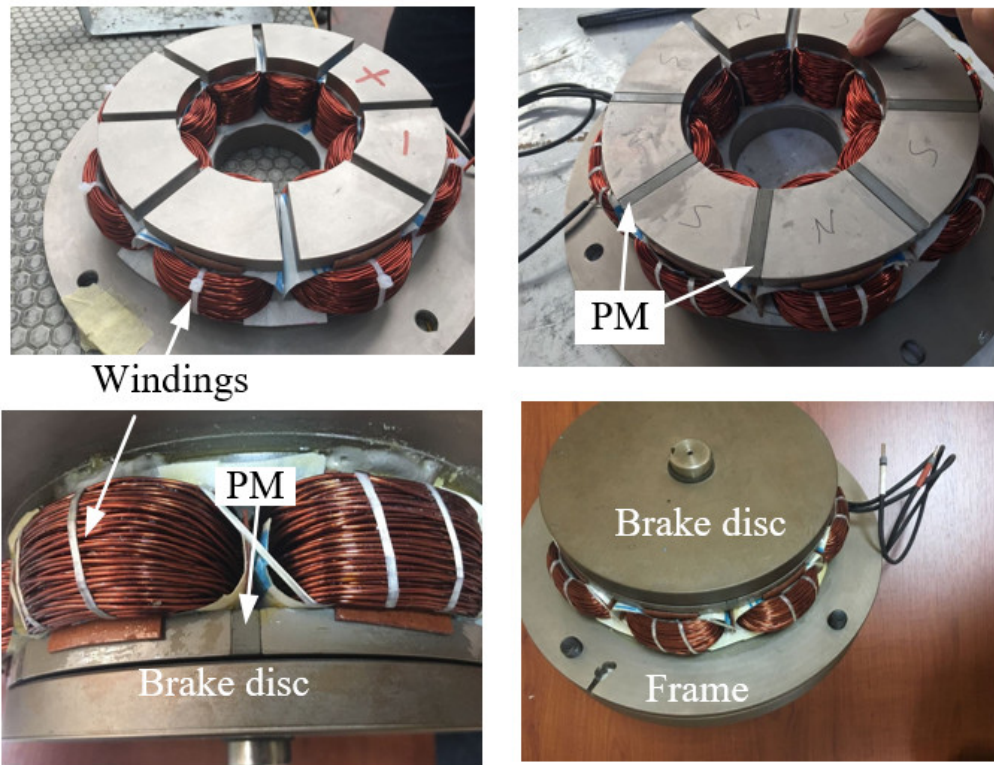


Figure 6.1. Prototype of the optimized AF-PMA-ECB

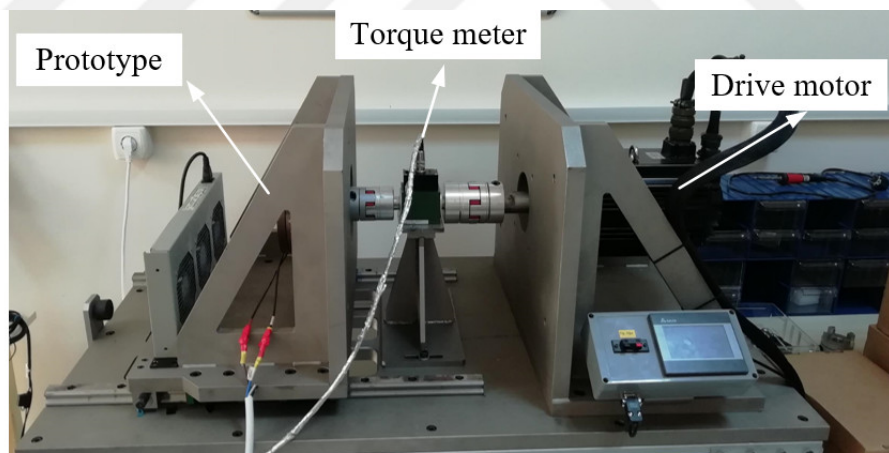


Figure 6.2. Test setup

### 6.3. Cold-Case Experimental Work

Firstly, cold-case experimental study has been investigated to compare the results with nonlinear magnetic modeling's and 3D-FEAs' results. It has to be reminded that all cold-case experimental studies are performed at room temperature and the temperature affect in the brake disc, magnets and coils are not allowed. Because a high energy occurs during braking, experiments are carried out individually during a short time

period and enough time is set between each test to be sure to start at room temperature disc.

The experiments are carried out at various currents and various speeds. It has to be noticed that 7.7 DC A is the rated (maximum) excitation current, which is equal to 10 A/mm<sup>2</sup> of current density in the coils. The results obtained from the experimental work, 3D-FEA and nonlinear magnetic modeling approach (previously presented in Chapter 4) are all given from Figure 6.3 through Figure 6.6 at different speeds. It is clearly seen that the results obtained from the nonlinear magnetic modeling approach,

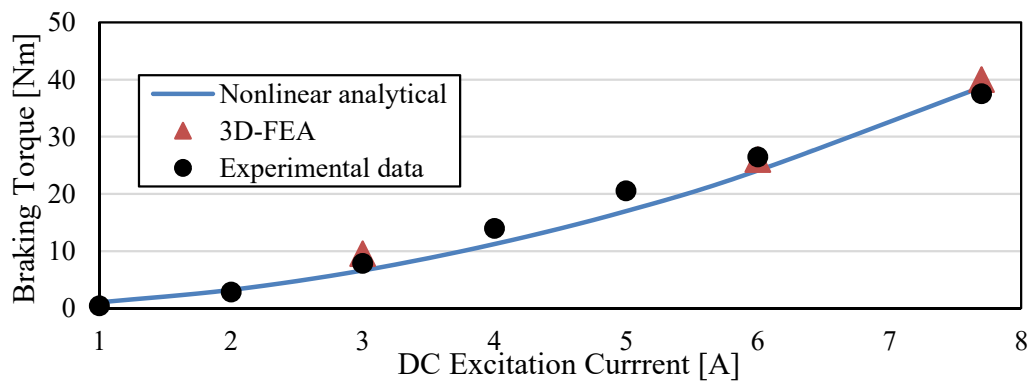


Figure 6.3. Braking torque comparison at the speed of 500 min<sup>-1</sup>

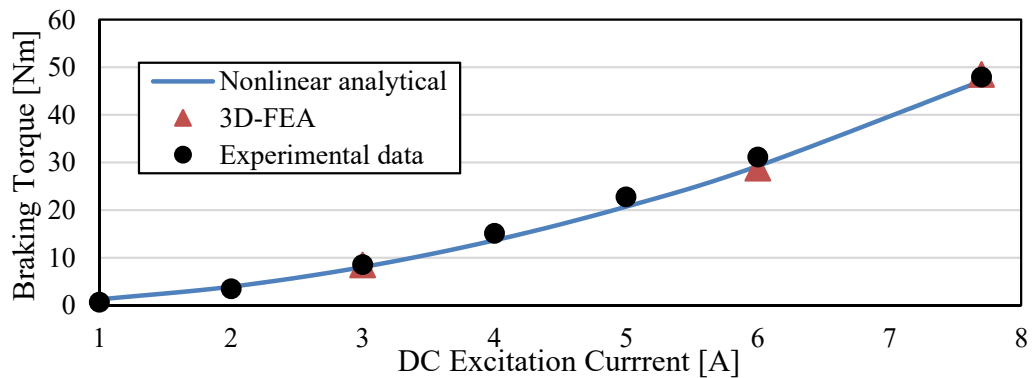


Figure 6.4. Braking torque comparison at the rated speed of 1000 min<sup>-1</sup>

3D-FEA and experiments are in good agreement at the speed of 500 and 1000 min<sup>-1</sup>. Some errors between the proposed design approach and the experimental results are achieved for higher excitation currents at the speed of 2000 and 3000 min<sup>-1</sup>. The reason of these errors can be fixed by updating the Reynolds number or changing the magnetic modeling approach to solve the Maxwell equations. It has to be stated that without no excitation current, magnet driven flux does not affect the torque, and



this also confirms the control benefit of the proposed AF-PMA-ECB. In addition, it can be stated that PMs in the slots increase the braking torque capability of the brake. It can be concluded that the manufactured AF-PMA-ECB provided stable braking torque between 1000 and 3000  $\text{min}^{-1}$  rotational speeds.

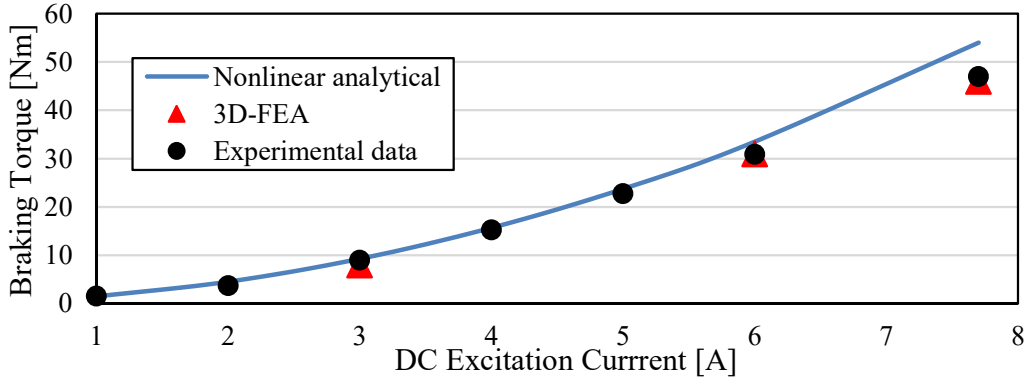


Figure 6.5. Braking torque comparison at the speed of 2000  $\text{min}^{-1}$

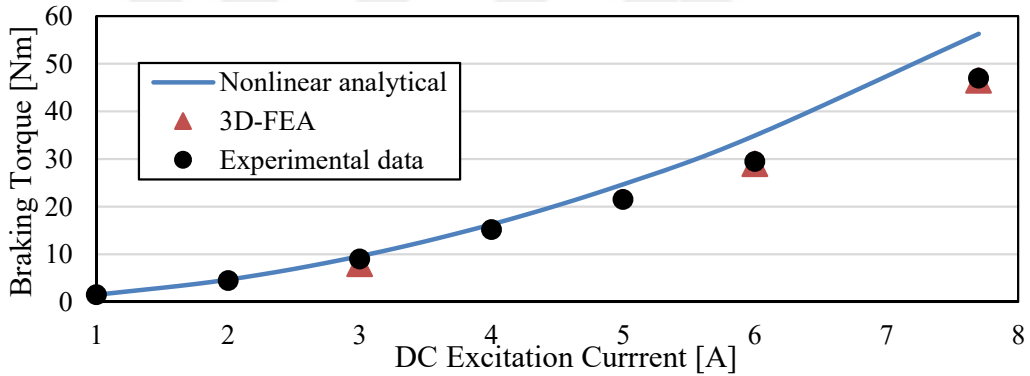


Figure 6.6. Braking torque comparison at the speed of 3000  $\text{min}^{-1}$

#### 6.4. Hot-Case Experimental Work

After cold-case studies, the test setup is revised for the hot-case experimental work that during hot-case test, temperature rise in the brake disc, magnets and the coils should be carefully tracked. The revised test setup with temperature measuring and capturing tools are given in Figure 6.7. Thermal camera is used in the test system to capture the thermal image of the prototype during braking. A thermocouple is attached to the magnet surface by special thermal paste and two laser-spot infrared thermometers are used to measure the temperature rise in the brake disc and the PM. The dSPACE board is also used in the system to get the temperature rise, excitation current variation and the braking torque variation during the test.

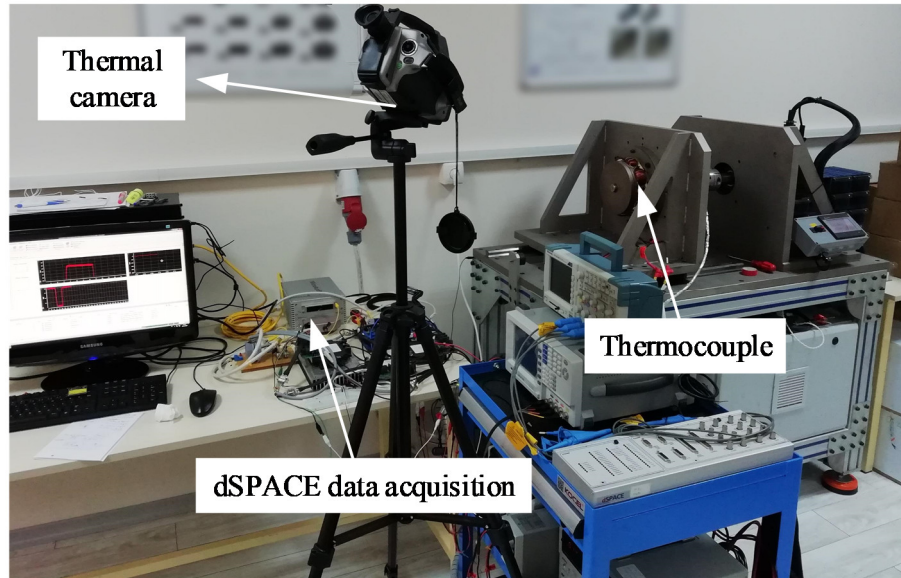


Figure 6.7. The revised test setup with temperature measuring and capturing tools

As previously presented in Chapter 5, the number of 6 scenarios were performed by NMDA and in this section, these scenarios are experimentally tested and the experimental results are compared with the NMDA results. As a reminder, in the first 3 scenarios (A-B-C), the rotational speed is fixed to  $1000 \text{ min}^{-1}$  and the excitation current is set to 3.5, 5.8 and 7.7 A, respectively. In the last 3 scenarios, the excitation current is dependent to temperature and initially set to 7.7 A, and the rotational speed is set to 500, 1000 and  $2000 \text{ min}^{-1}$ , respectively.

The braking torque variation and temperature rise variation of the brake disc and PM for all scenarios are given from Figure 6.8 to Figure 6.19, respectively. It is obtained that the results obtained from experiments generally agree well with the proposed NMDA. It can be clearly stated that the proposed NMDA works well for the PM-ECB proposed in this thesis.

For Scenario-A, the braking torque variation is given in Figure 6.8. It is seen that the results obtained from experiments and the proposed NMDA agree well. Initially, the braking torque is 47.5 Nm and reduced to 30 Nm after 225 seconds. The temperature rise of the brake disc and magnets is given in Figure 6.9. The brake disc temperature reaches  $150 \text{ }^{\circ}\text{C}$  and the magnets temperature reaches  $88 \text{ }^{\circ}\text{C}$  after 225 seconds of braking time.

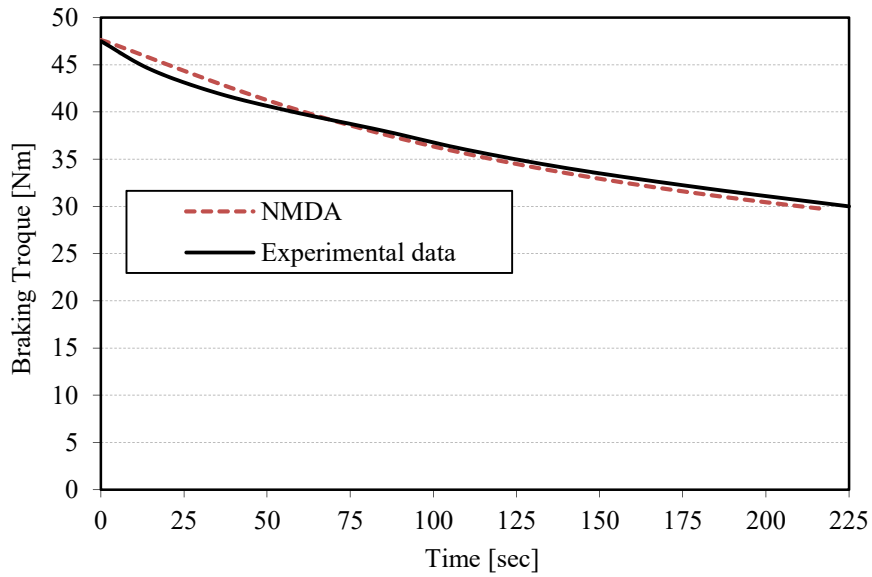


Figure 6.8. Braking torque variation for Scenario-A ( $1000 \text{ min}^{-1}$  and  $7.7 \text{ A}$  fixed)

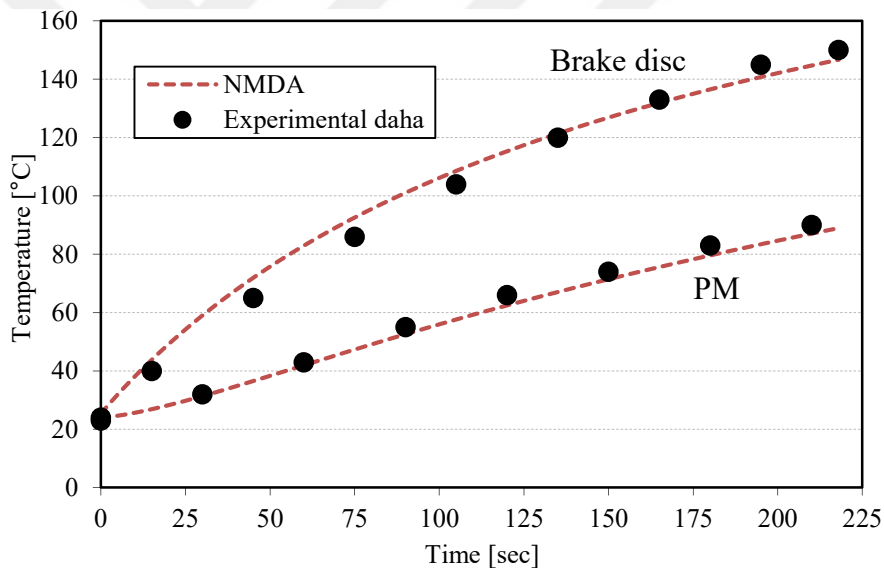


Figure 6.9. Temperature rise of the brake disc and PM for Scenario-A ( $1000 \text{ min}^{-1}$  and  $7.7 \text{ A}$  fixed)

For Scenario-B, the braking torque variation is given in Figure 6.10. In this case, the results obtained from the proposed NMDA are in good agreement with the experimental results. However, nearly 7% error with respect to experimental results is observed by the NMDA results. It can be said it is still in acceptable. The braking torque is measured as  $29 \text{ Nm}$  in the beginning of the test and after 380 seconds it is reduced to  $19.35 \text{ Nm}$ . The temperature rise of the brake disc and the magnets is given

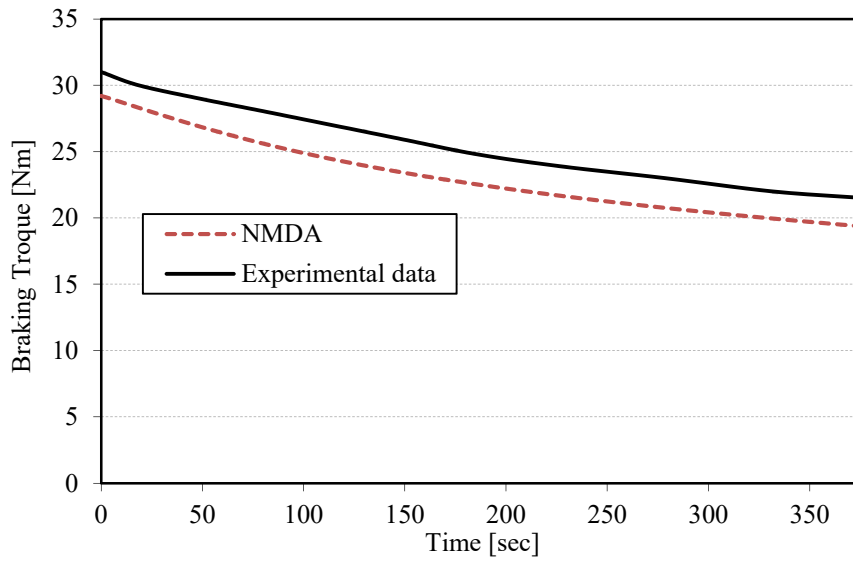


Figure 6.10. Braking torque variation for Scenario-B ( $1000 \text{ min}^{-1}$  and  $5.8 \text{ A}$  fixed)

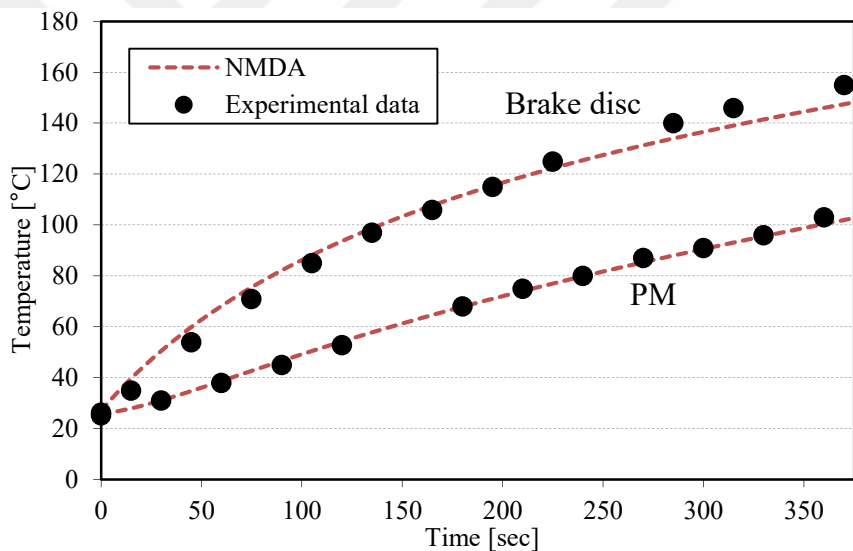


Figure 6.11. Temperature rise of the brake disc and PM for Scenario-B ( $1000 \text{ min}^{-1}$  and  $5.8 \text{ A}$  fixed)

in Figure 6.11. It is seen that the brake disc temperature reaches  $155 \text{ }^\circ\text{C}$  and the magnet temperature reaches  $105 \text{ }^\circ\text{C}$  after 380 seconds of braking time.

As for the Scenario-C, the braking torque variation is given in Figure 6.12. It can be seen that the results obtained from experiments and the proposed NMDA are in good agreement. Almost perfect matched has been achieved. The braking torque is measured as  $11.3 \text{ Nm}$  in the beginning of the test and is reduced to  $8.4 \text{ Nm}$  after 1890 seconds. The temperature rise of the brake disc and magnets is given in Figure 6.13. It

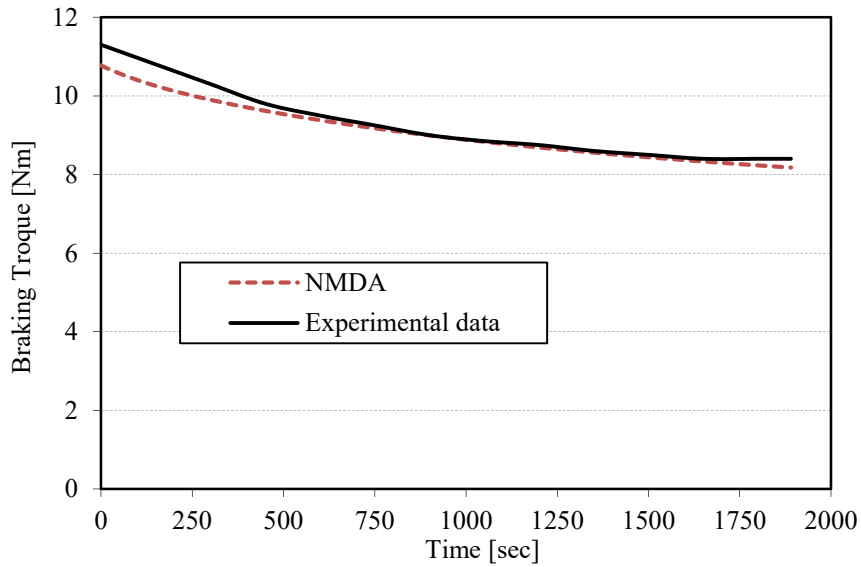


Figure 6.12. Braking torque variation for Scenario-C ( $1000 \text{ min}^{-1}$  and  $3.5 \text{ A}$  fixed)

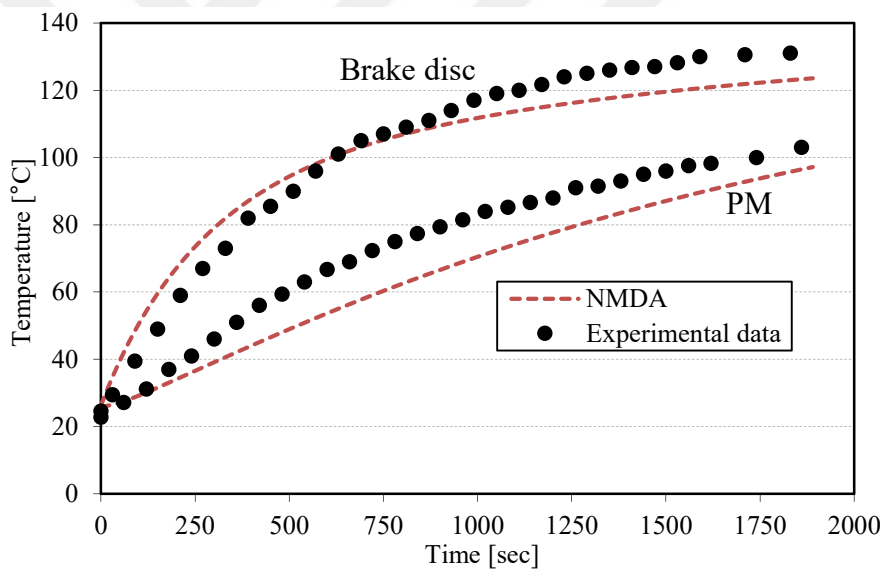


Figure 6.13. Temperature rise of the brake disc and PM for Scenario-C ( $1000 \text{ min}^{-1}$  and  $3.5 \text{ A}$  fixed)

is seen that temperature rise of the brake disc and PM are correctly computed by the proposed NMDA for this test case. The temperature rise for the brake disc is measured as  $108 \text{ }^\circ\text{C}$  while it is computed as  $99 \text{ }^\circ\text{C}$  by the proposed NMDA. In addition, the temperature rise for the PM is measured as  $80 \text{ }^\circ\text{C}$  while it is computed as  $74 \text{ }^\circ\text{C}$  by the proposed NMDA.

The braking torque variation is given in Figure 6.14 for Scenario-D. It is observed that the results obtained from experiments and the proposed NMDA are match well. The

braking torque is measured as 37 Nm in the beginning of the test and the torque is reduced to 15.3 Nm after 1088 seconds of operation. The temperature rise of the brake disc and the magnets is displayed in Figure 6.15. Good agreement between the experimental results and the NMDA results is attained. The temperature of the brake disc is measured as 135 °C while it is computed as 128 °C by the proposed NMDA after 1088 seconds. The temperature of the magnets is also measured as 123 °C while it is computed as 105 °C by the proposed NMDA approach.

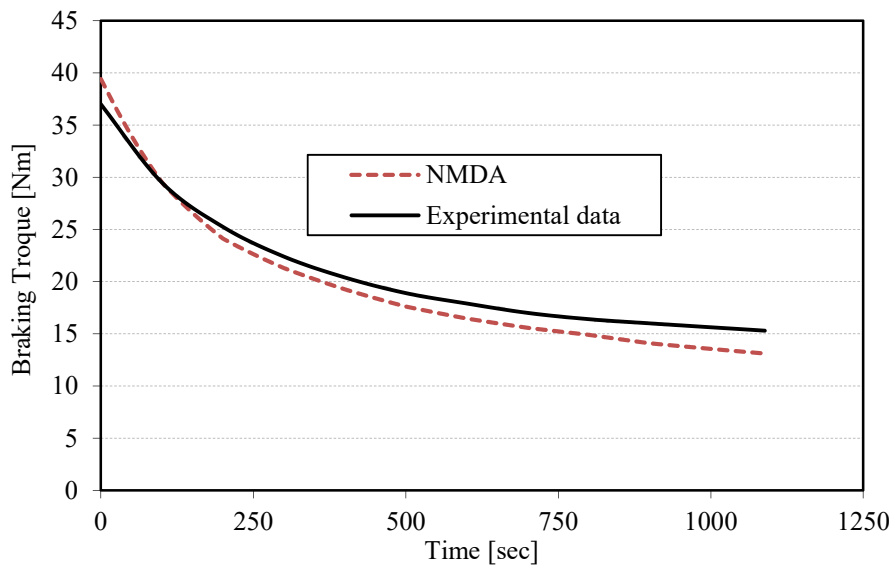


Figure 6.14. Braking torque variation for Scenario-D (500 min<sup>-1</sup> and 7.7 A initial)

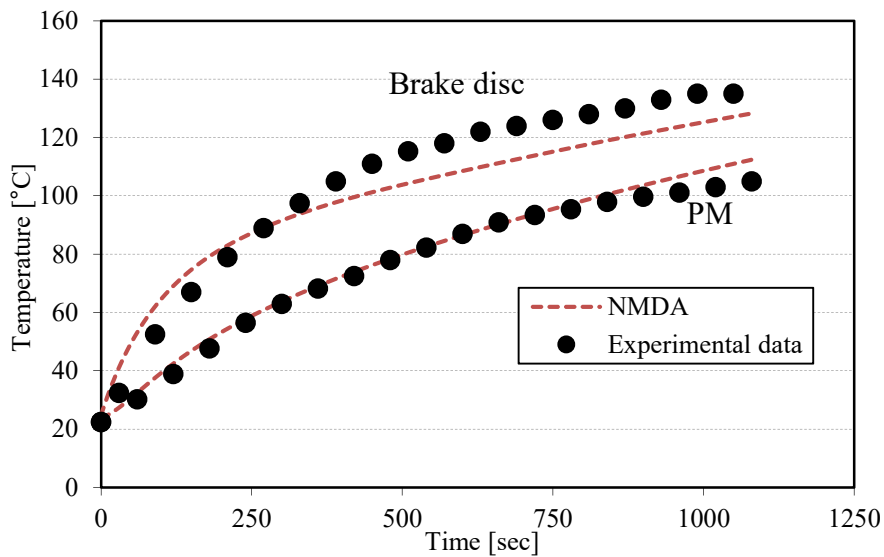


Figure 6.15. Temperature rise of the brake disc and PM for Scenario-D (500 min<sup>-1</sup> and 7.7 A initial)

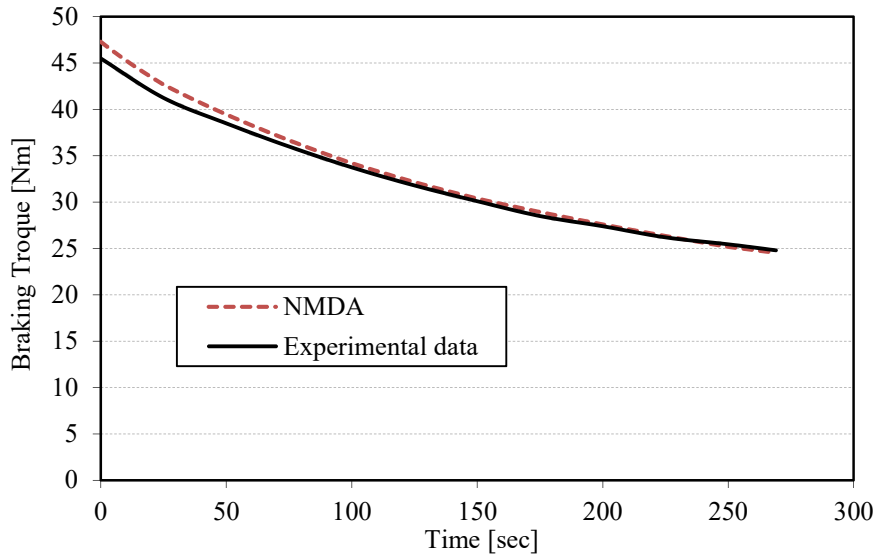


Figure 6.16. Braking torque variation for Scenario-E ( $1000 \text{ min}^{-1}$  and  $7.7 \text{ A}$  initial)

For Scenario-E, the braking torque variation is given in Figure 6.16. The results obtained from experiments and the proposed NMDA are perfectly matched. The braking torque is measured as  $47 \text{ Nm}$  in the beginning of the test and after 270 seconds it is reduced to  $25 \text{ Nm}$ . The temperature rise of the brake disc and magnets is given in Figure 6.17. It can be concluded that the results obtained from the experiments and the proposed NMDA are in good agreement. The brake disc temperature is measured as  $161 \text{ }^\circ\text{C}$  while it is computed as  $158 \text{ }^\circ\text{C}$  by the proposed NMDA. The temperature of the PM is measured as  $103 \text{ }^\circ\text{C}$  while it is computed as  $101 \text{ }^\circ\text{C}$  by the proposed NMDA.

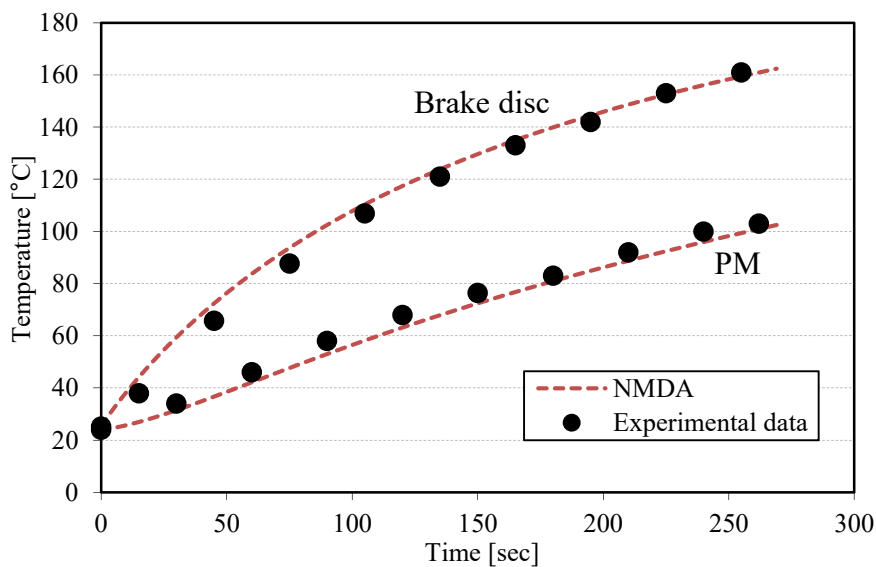


Figure 6.17. Temperature rise of the brake disc and PM for Scenario-E ( $1000 \text{ min}^{-1}$  and  $7.7 \text{ A}$  initial)

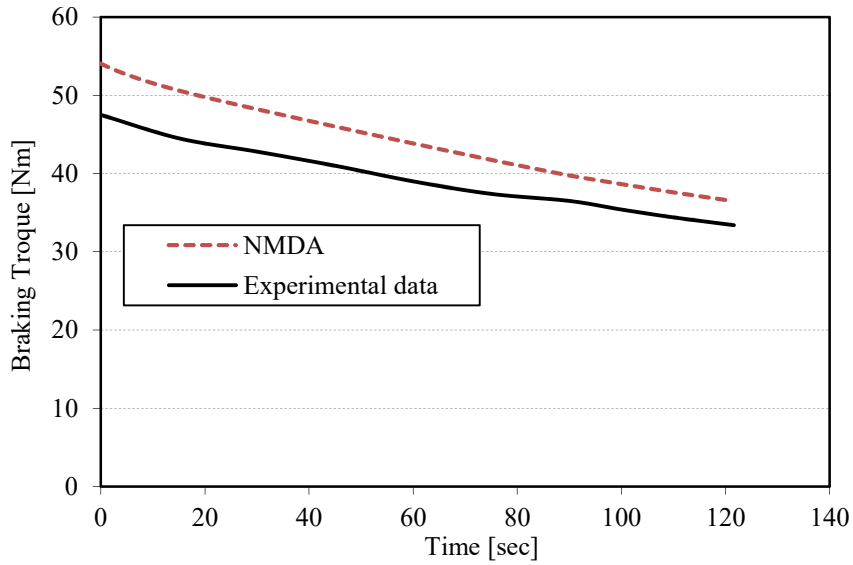


Figure 6.18. Braking torque variation for Scenario-F ( $2000 \text{ min}^{-1}$  and  $7.7 \text{ A}$  initial)

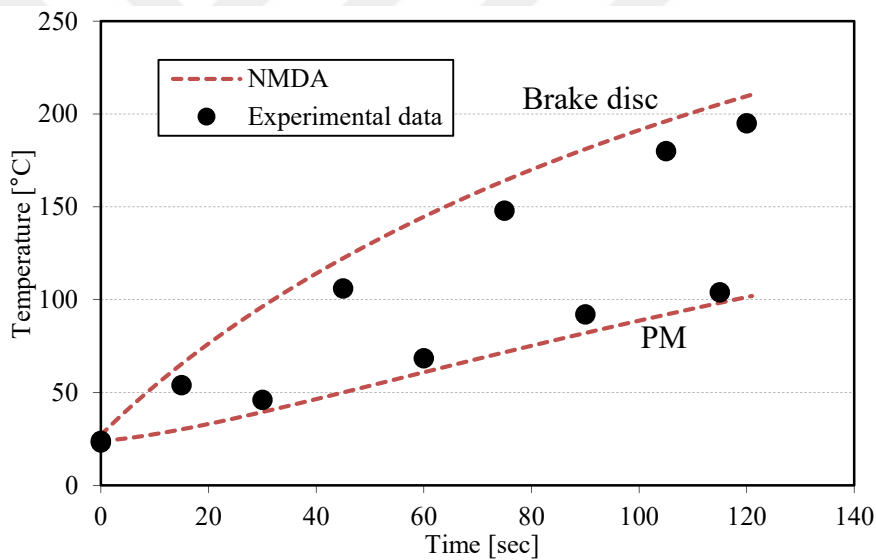


Figure 6.19. Temperature rise of the brake disc and PM for Scenario-F ( $2000 \text{ min}^{-1}$  and  $7.7 \text{ A}$  initial)

The braking torque variation for Scenario-F is shown in Figure 6.18. The results obtained from experiments and the proposed NMDA do not match well at the rotational speed of  $2000 \text{ min}^{-1}$  due to the armature reaction becoming dominant since the Reynolds numbers have to be updated for high speeds. The braking torque is measured as  $47.5 \text{ Nm}$  in the beginning of the test and it is reduced to  $33.4 \text{ Nm}$  after 121 seconds. The braking torque is computed as  $54 \text{ Nm}$  by the proposed NMDA and it is reduced to  $36.6 \text{ Nm}$ . The temperature rise of the brake disc and magnets obtained from experiments and the proposed NMDA are in good agreement. It can be stated



that the temperature rise increases rapidly in time and it has to be followed carefully. Thermal images of the prototype for Scenario-F are shown in Figure 6.20. The thermal image is captured at the beginning of the test, after 40, 74 and 120 seconds, respectively. It is seen that the thermal images also agree well with the results obtained from the proposed NMDA.

### 6.5. Summary

The optimized AF-PMA-ECB investigated in Chapter 5 was manufactured and tested in the laboratory. Detailed experimental work of the prototype has been performed and presented in this chapter. Two test stages, (1) cold-case (temperature independent) and (2) hot case (temperature dependent), were performed to validate the results obtained from the proposed nonlinear magnetic modeling, 3D-FEA and the proposed NMDA. For cold-case experimental studies, the results obtained from experiments were in big harmony with the results obtained from nonlinear magnetic modeling and the 3D-FEA

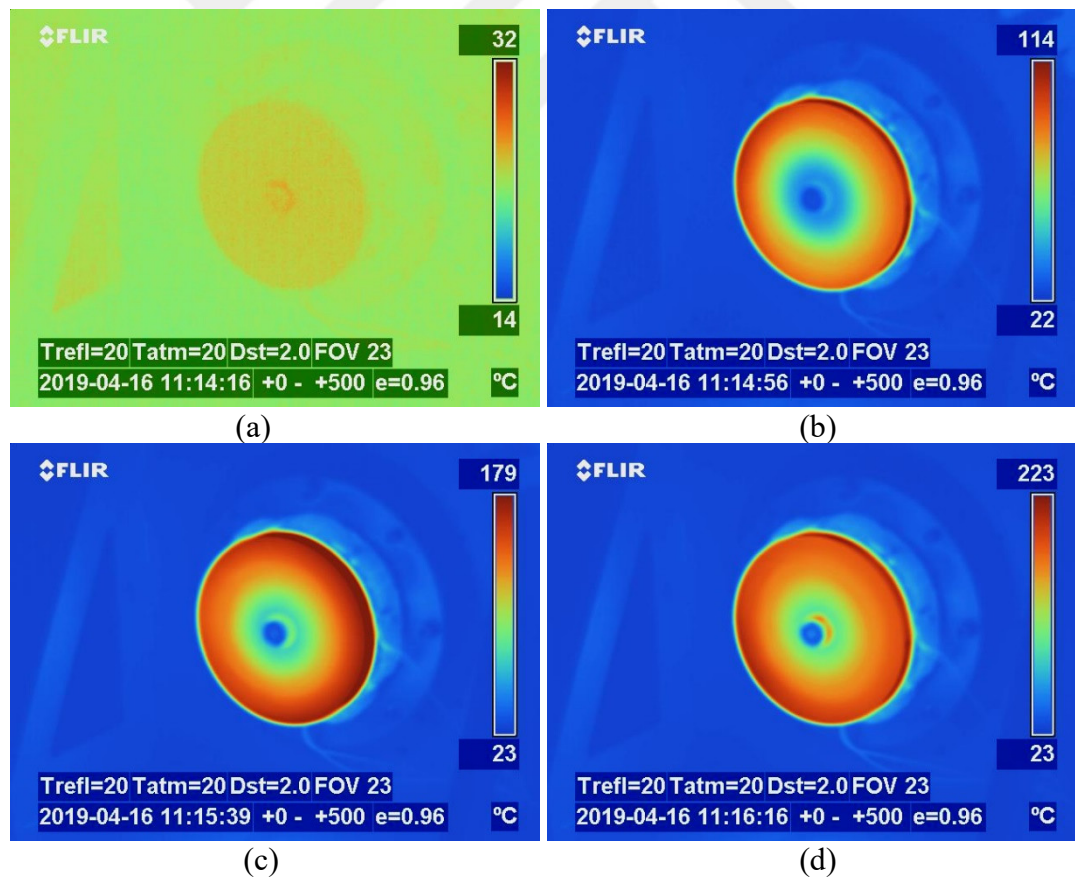


Figure 6.20. Thermal image of the prototype: (a) in the beginning, (b) after 40 seconds, (c) after 74 seconds and (d) after 120 seconds of braking

For the hot-case experimental studies, various scenarios were performed. It is shown that the experimental results agree well with the results obtained from NMDA. It can be concluded that the proposed nonlinear magnetic modeling and the proposed NMDA provide practical results and NMDA can be used to determine the working limits of the eddy current brakes proposed.



## 7. CONCLUSIONS AND RECOMMENDATIONS

In this thesis, a new axial flux permanent magnet assisted eddy current brake topology was proposed to eliminate the control drawbacks of the permanent magnet eddy current brakes and to highlight the advantages of the proposed topology as to conventional eddy current brakes. This thesis consisted of 4 main stages: (1) investigation of eddy current brakes, (2) proposing the new multidisciplinary design methodology, (3) presenting the new axial flux permanent magnet assisted eddy current brake and (4) manufacturing and experimental validation of the prototype.

The first stage of the thesis focused on the design and analyses of eddy current brakes. Eddy current theory, influence of geometric parameters on brake performance and nonlinear analytical magnetic modeling approach of eddy current brakes were clarified. Two different cases, axial flux and radial flux eddy current brakes, were modeled and analyzed by nonlinear magnetic modeling approach and 3-dimensional finite element methods, and the magnetic brakes are experimentally verified. The first stage of the thesis has disclosed some design and control aspects. The following conclusions can be obtained from this section:

- Eddy current brakes having ferromagnetic rotors have to be modeled with nonlinear magnetic modeling approaches. The permeability in the ferromagnetic rotor has a great influence on braking torque calculation and it has to be computed precisely.
- Similarly, radial flux eddy current brakes, axial flux eddy current brakes can also be modeled by 2D modeling approaches.
- Gauss-Siedel approach with relaxation can be preferred if the main solving matrix has such unknown reluctances.
- A comprehensive reluctance network modeling is necessary for permanent magnet eddy current brakes to consider the actual magnet shape.

- Unsophisticated control techniques are not essential for eddy current brakes. The proportional or proportional-integral control is sufficient for the dynamic torque control. For extreme cases, nonlinear based control methods are required.

The second phase of the thesis aimed to propose a new multidisciplinary design approach for eddy current brakes to obtain the actual brake performance in time and to determine the working limits. With the new proposed multidisciplinary design approach, working limits of the eddy current brakes can be determined. A 4.5 kW and a 10.5 kW conventional and magnet-less axial flux eddy current brakes were explored by the new design methodology and the results obtained from the new design technique agreed well with the experimental data. It was shown that the proposed nonlinear multidisciplinary design approach can provide actual brake behaviors with high accuracy.

The third phase of the thesis presented the new axial flux permanent magnet assisted eddy current brake topology. The proposed new axial flux permanent magnet assisted eddy current brake was firstly presented and the working principle of the proposed brake was introduced. Multiobjective design optimization of the proposed brake topology was carried out for two different design cases, and the optimized designs obtained from multiobjective optimization were verified by 3-dimensional finite element analyses. It was shown that the magnet size is very important in the proposed new eddy current brake topology to obtain the maximum braking torque profile.

The last stage of this thesis targeted the nonlinear multidisciplinary design approach of the optimized axial flux permanent magnet eddy current brake and the experimental study. The optimized proposed brake was evaluated by the nonlinear multidisciplinary design approach and the number of 6 different scenarios were performed by the design approach. The following conclusions can be drawn from the proposed new eddy current brake, its nonlinear multidisciplinary design approach and the experimental studies:

- The proposed new eddy current brake topology can provide higher braking torque characteristic as to magnetless eddy current brakes when the optimum magnet size is determined.

- External devices are no longer necessary to control the braking torque in the proposed permanent magnet assisted eddy current brake topology.
- The new eddy current brake topology has significant advantages over the permanent magnet eddy current brakes and magnetless eddy current brakes such as increased braking torque density/profile, increased efficiency and eliminated external control system.
- The actual eddy current brake performances can be obtained by the proposed nonlinear multidisciplinary design approach. Particularly for eddy current brakes having permanent magnets, the temperature variation in magnets have to be correctly computed in the proposed design approach. The braking torque reduction and temperature rise in time were experimentally proven.

## REFERENCES

- [1] <https://www.machinedesign.com/archive/basics-electromagnetic-clutches-and-brakes> (Last Visited: 15.06.2019)
- [2] [https://en.wikipedia.org/wiki/Eddy\\_current\\_brake](https://en.wikipedia.org/wiki/Eddy_current_brake) (Last Visited: 15.06.2019)
- [3] <https://www.electric-brake.com> (Last Visited: 15.06.2019)
- [4] <https://www.machinedesign.com/motion-control/what-s-difference-between-torque-control-solutions> (Last Visited: 15.06.2019)
- [5] <https://sepac.com/electromagnetic-brakes/magnetically-engaged> (Last Visited: 15.06.2019)
- [6] <https://www.magtrol.com/product/hysteresis-brakes> (Last Visited: 02.07.2019)
- [7] Morris D. K., Lister G. A., The eddy current brake for testing the motors, *Journal of the Institution of Electrical Engineers*, 1905, **35**(175), 445-468.
- [8] Moore A. D., Eddy current in disks: Driving and damping forces and torques, *Transactions of the American Institute of Electrical Engineers*, 1947, **66**(1), 1-11.
- [9] Symthe W. R., On eddy currents in a rotating disk, *Electrical Engineering*, 1942, **66**(9), 681-684.
- [10] McConnel H. M., Eddy-current phenomena in ferromagnetic materials, *Transactions of the American Institute of Electrical Engineers*, 1954, **73**(3), 226-235.
- [11] Davies E. J., An experimental and theoretical study of eddy-current couplings and brakes, *IEEE Transactions on Power Apparatus and Systems*, 1963, **83**(67), 401-419.
- [12] Gonen D., Stricker S., Analysis of an eddy-current brake, *IEEE Transactions on Power Apparatus and Systems*, 1965, **84**(5), 357-361.
- [13] Schieber D., Braking torque on rotating sheet in stationary magnetic field, *Proceedings of the Institution of Electrical Engineers*, 1974, **121**(2), 117-122.
- [14] Ripper M. D., Endean V. G., Eddy-current braking-torque measurements on a thick copper disc, *Proceedings of the Institution of Electrical Engineers*, 1975, **122**(3), 301-302.

- [15] Schieber D., Optimal dimensions of rectangular electromagnet for braking purposes, *IEEE Transactions on Magnetics*, 1975, **11**(3), 948-952.
- [16] Singh A., Theory of eddy-current brakes with rotating disc, *Proceedings of the Institution of Electrical Engineers*, 1977, **124**(4), 373-376.
- [17] Venkataratnam K., Raju R. D., Analysis of eddy-current brakes with nonmagnetic rotors, *Proceedings of the Institution of Electrical Engineers*, 1977, **124**(1), 67-71.
- [18] Bigeon J., Sabonnadiere J., Coulomb J., Finite element analysis of an electromagnetic brake, *IEEE Transactions on Magnetics*, 1983, **19**(6), 2632-2634.
- [19] Zhi-ming S., De-xin X., Cheng-qian H., The finite element solution of transient axisymmetrical nonlinear Eddy-current field problems, *IEEE Transactions on Magnetics*, 1985, **21**(6), 2303-2306.
- [20] Wouterse J. H., Critical torque and speed of eddy current brake with widely separated soft iron poles, *IEEE Proceedings B – Electric Power Applications*, 1991, **138**(4), 153-158.
- [21] Nehl T. W., Lequesne B., Gangla V., Gutkowski S. A., Robinson M. J., Sebastian T., Nonlinear two-dimensional finite element modeling of permanent magnet eddy current couplings and brakes, *IEEE Transactions on Magnetics*, 1994, **30**(5), 3000-3003.
- [22] Albertz D., Dappen S., Henneberger G., Calculation of the 3D nonlinear eddy current field in moving conductors and its application to braking systems, *IEEE Transactions on Magnetics*, 1996, **32**(3), 768-771.
- [23] Lequesne B., Liu B., Nehl T. W., Eddy-current machines with permanent magnets and solid rotors, *IEEE Transactions on Industrial Applications*, 1997, **33**(5), 1289-1294.
- [24] Muramatsu K., Takahashi N., Hashio T., Yamada C., Ogawa M., Kobayashi S., Kuwahara T., 3-D eddy current analysis in moving conductor of permanent magnet type of retarder moving coordinate system, *IEEE Transactions on Energy Conversion*, 1999, **14**(4), 1312-1317.
- [25] Jang S-M., Jeong S-S., Cha S-D., The application of linear Halbach array to eddy current rail brake system, *IEEE Transactions on Magnetics*, 2001, **37**(4), 2627-2629.
- [26] Jang S-M., Lee S-U., Comparison of three types of permanent magnet linear eddy-current brakes according to magnetization pattern, *IEEE Transactions on Magnetics*, 2003, **39**(5), 3004-3006.
- [27] Anwar S., A parametric model of an eddy current electric machine for automotive braking applications, *IEEE Transactions on Control Systems Technology*, 2004, **12**(3), 422-427.

- [28] Gay S. E., Ehsani M., Parametric analysis of eddy-current brake performance by 3-D finite-element analysis, *IEEE Transactions on Magnetics*, 2006, **42**(2), 319-328.
- [29] Gosline A., Hayward V., Eddy current brakes for haptic interfaces: Design, identification, and control, *IEEE/ASME Transactions on Mechatronics*, 2008, **13**(6), 669-677.
- [30] Ye L., Li D., Ma Y., Jiao B., Design and performance of a water-cooled permanent magnet retarder for heavy vehicles, *IEEE Transactions on Energy Conversion*, 2011, **26**(3), 953-958.
- [31] Shin H-J., Choi J-Y., Cho H-W., Jang S-M., Analytical torque calculations and experimental testing of permanent magnet axial eddy current brake, *IEEE Transactions on Magnetics*, 2013, **49**(7), 4152-4155.
- [32] Karakoc K., Suleman A., Park E. J., Optimized braking torque generation capacity of an eddy current brake with the application of time-varying magnetic fields, *IEEE Transactions on Vehicular Technology*, 2014, **63**(4), 1530-1538.
- [33] Kou B., Jin Y., Zhang H., Zhang L., Zhang H., Analysis and design of hybrid excitation linear eddy current brake, *IEEE Transactions on Energy Conversion*, 2014, **29**(2), 496-506.
- [34] Yazdanpanah R., Mirsalim M., Hybrid electromagnetic brakes: Design and performance evaluation, *IEEE Transactions on Energy Conversion*, 2015, **30**(1), 60-69.
- [35] Lubin T., Rezzoug A., 3-D analytical model for axial-flux eddy-brake couplings and brakes under steady-state conditions, *IEEE Transactions on Magnetics*, 2015, **51**(10), ASN: 8203712.
- [36] Ye L., Cao M., Liu Y., Li D., Multi-field coupling analysis and demagnetization experiment of permanent magnet retarder for heavy vehicles, *IEEE Access*, 2018, **7**, 50734-50745.
- [37] Jin Y., Li L., Kou B., Pan D., Thermal analysis of a hybrid excitation linear eddy current brake, *IEEE Transactions on Industrial Electronics*, 2019, **66**(4), 2987-2997.
- [38] <https://tr.telma.com/entreprise/historique> (Last Visited: 15.06.2019)
- [39] <https://norwoodequipment.com/telma> (Last Visited: 15.06.2019)
- [40] Thompson M. T., Practical Issues in the Use of NdFeB Permanent Magnets in Maglev, Motors, Bearings, and Eddy Current Brakes, *Proceedings of the IEEE*, 2009, **97**(11), 1758-1767.
- [41] Dorrell D. G., Hsieh M-F., Popescu M., Evans L., Staton D. A., Grout V., A Review of the Design Issues and Techniques for Radial-Flux Brushless Surface



- and Internal Rare-Earth Permanent-Magnet Motors, *IEEE Transactions on Industrial Electronics*, 2011, **58**(9), 3741-3757.
- [42] Capponi F. G., Donato G. D., Caricchi F., Recent Advances in Axial-Flux Permanent-Magnet Machine Technology, *IEEE Transactions on Industry Applications*, 2012, **48**(6), 2190-2205.
- [43] <http://www.voith.com/ca-en/voith-magnetarder-bus/voith-magnetarder-bus-25620.html> (Last Visited: 15.06.2019)
- [44] Yazdanpanah R., Mirsalim M., Axial-flux wound-excitation eddy-current brakes: Analytical study and parametric modeling, *IEEE Transactions on Magnetics*, 2014, **50**(6), ASN: 8000710.
- [45] Kou B., Jin Y., Zhang H., Zhang L., Zhang H., Nonlinear analytical modeling of hybrid-excitation double-sided linear eddy-current brake, *IEEE Transactions on Magnetics*, 2015, **51**(11), ASN: 8003404.
- [46] Sharif S., Shari, K., Performance analysis of a cylindrical eddy current brake y current brake, *IET Electric Power Applications*, 2012, **6**(9), 661-668.
- [47] Cho S., Liu H-C., Ahn H., Lee J., Lee H.-W., Eddy current brake with a two-layer structure: Calculation and characterization of braking performance, *IEEE Transactions on Magnetics*, 2017, **53**(11), ASN: 8110205.
- [48] Pyrhönen J., Nerg J., Kurronen P., Lauber U., High-speed high output solid-rotor induction-motor technology for gas compression, *IEEE Transactions on Industrial Electronics*, 2010, **57**(1), 272–280.
- [49] Agarwal P. D., Eddy-current losses in solid and laminated iron, *Transactions of the American Institute of Electrical Engineers, Part I: Communication and Electronics*, 1959, **78**(2), 169-181.
- [50] Wang A., Ji Y., Soong L., Comparison of five topologies for an interior permanent-magnet machine for a hybrid electric vehicle, *IEEE Transactions on Magnetics*, 2011, **47**, 3606-3609.
- [51] Galioto S. J., Reddy P.B., El-Refaie A., Alexander J. P., Effect of magnet types on performance of high-speed spoke interior-permanent-magnet machines designed for traction applications, *IEEE Transactions on Industry Applications*, 2015, **51**, 2148-2160.
- [52] Bentouati S., Zhu Z. Q., Howe D., Influence of design parameters on the starting torque of a single-phase PM brushless DC motor, *IEEE Transactions on Magnetics*, 2000, **36**(5), 3533-3536.
- [53] Pluk K. J. W., Jansen J. W., Lomonova E. A., Hybrid analytical modeling: Fourier modeling combined with mesh-based magnetic equivalent circuits, *IEEE Transactions on Magnetics*, 2015, **51**(8), 1-10.

- [54] Ouagued S., Diriye A. A., Amara Y., Barakat G., A general framework based on a hybrid analytical model for the analysis and design of permanent magnet machines, *IEEE Transactions on Magnetics*, 2015, **51**(11), 1-4.
- [55] Chen H., Li Z., Flux characteristics analysis of single-phase tubular permanent magnet linear motor, *IEEE Transactions on Applied Superconductivity*, 2018, **28**(3), ASN: 5200106.
- [56] Chen Q., Liu G., Zhao W., Shao M., Nonlinear adaptive lumped parameter magnetic circuit analysis for spoke-type fault-tolerant permanent-magnet motors, *IEEE Transactions on Magnetics*, 2013, **49**(9), 5150-5157.
- [57] Fu W. N., Ho S. L., Dynamic demagnetization computation of permanent magnet motor using finite element method with normal demagnetization curves, *IEEE Transactions on Applied Superconductivity*, 2010, **20**(3), 851-855.
- [58] Derbas H. W., Williams J. M., Koenig A. C., Pekarek S. D., A comparison of nodal- and mesh-based magnetic equivalent circuit models, *IEEE Transactions on Energy Conversion*, 2009, **24**(2), 388-396.
- [59] Anwar S., Zheng B., An antilock-braking algorithm for an eddy-current-based brake-by wire system, *IEEE Transactions on Vehicular Technology*, 2007, **56**(3), 1100-1107.
- [60] Wang P. J., Chiueh S. J., Analysis of eddy current brakes for high speed railway, *IEEE Transactions on Magnetics*, 1998, **34**(4), 1237-1239.
- [61] Zamani A., Design of a controller for rail eddy current brake system, *IET Electric System Transportation*, 2014, **4**(2), 38-44.
- [62] Adly A., Abd-El-Hafiz S., Speed-range-based optimization of nonlinear electromagnetic braking systems, *IEEE Transaction on Magnetics*, 2007, **43**(6), 2606-2608.
- [63] Gulec M., Yolacan E., Aydin M., Design, Analysis and Real Time Dynamic Torque Control of Single-Rotor-Single-Stator Axial Flux Eddy Current Brake, *IET Electric Power Applications*, 2016, **10**(9), 869-876.
- [64] Pohjonen L., Roller shape with brake, 2016, U. S. Patent No. 2016/0245018 A1, *U. S. Patent and Trademark Office*.
- [65] Bruzzese C., Zito D., Tessarolo A., Finite reluctance approach: A systematic method for the construction of magnetic network-based dynamic models of electrical machines, *AEIT Annual Conference*, Trieste, Italy, 18-19 Sept. 2014.
- [66] Perho J., Reluctance Network for Analysing Induction Machines, Ph.D. dissertation, Helsinki University of Technology, Department of Electrical and Communication Engineering, Espoo, Finland, 2002.

- [67] Boehm A., Hahn I., Measurement of magnetic properties of steel at high temperatures, *40<sup>th</sup> Annual Conference of the IEEE Industrial Electronics Society*, Dallas, TX, USA, 29 October-1 November 2014.
- [68] Pyrhönen J., Ruuskanen V., Nerg J., Puranen J., Jussila H., Permanent-magnet length effects in ac machines, *IEEE Transactions on Magnetics*, 2010, **46**(10), 3783-3789.
- [69] Valderas D., Mesa I., Adín I., Lehmann H., Lancaster G., Stark O., Baldauf W., Portillo J. D., Modeling eddy current brake emissions for electromagnetic compatibility with signaling devices in high-speed railways, *IEEE Transaction on Vehicular Technology*, 2017, **66**(11), 9743-9752.
- [70] Mouton Z, Kamper M. J., Modeling and optimal design of an eddy current coupling for slip-synchronous permanent magnet wind generators, *IEEE Transactions on Industrial Electronics*, 2014, **61**(7), 3367-3376.
- [71] Zhang K., Li D., Du X., Zheng R., Numerical analysis and experimentation of a novel self-excited and liquid-cooled eddy current retarder, *IEEE Transactions on Energy Conversion*, 2014, **29**(1), 196-203.
- [72] Dai X., Liang Q., Cao J., Long Y., Mo J., Wang S., Analytical modeling of axial-flux permanent magnet eddy current couplings with a slotted conductor topology, 2016, *IEEE Transactions on Magnetics*, **52**(2), ASN: 8000315.
- [73] Wang J., Zhu J., A simple method for performance prediction of permanent magnet eddy current couplings using a new magnetic equivalent circuit model, *IEEE Transactions on Industrial Electronics*, 2018, **65**(3), 2487-495.
- [74] Zhang K., Li D., Zheng R., Yin W., Design and performance of a self-excited and liquid-cooled electromagnetic retarder, *IEEE Transactions on Vehicular Technology*, 2015, **64**(1), 13-20.
- [75] Gulec M., Aydin M., Modelling and analysis of a new axial flux permanent magnet biased eddy current brake, *22<sup>nd</sup> International Conference on Electrical Machines*, Lausanne, Switzerland, 4-7 September 2016.
- [76] Shin K., Park H., Cho H., Choi J., Semi-Three-Dimensional Analytical Torque Calculation and Experimental Testing of an Eddy Current Brake With Permanent Magnets, *IEEE Transactions on Applied Superconductivity*, 2018, **28**(3), ASN: 5203205.
- [77] Parviainen A., Niemela M., Pyrhönen J., Modeling of axial flux permanent-magnet machines, *IEEE Transactions on Industrial Applications*, 2004, **40**(5), 1333-1340.
- [78] Gulec M., Aydin M., Implementation of different 2D finite element modelling approaches in axial flux permanent magnet disc machines, *IET Electric Power Applications*, 2018, **12**(2), 195-202.

- [79] Kano Y., Kosaka T., Matsui N., A simple nonlinear magnetic analysis for axial-flux permanent-magnet machines, *IEEE Transactions on Industrial Electronics*, 2010, **57**(6), 2124-2133.
- [80] Hameyer K., Belmans R., *Numerical Modelling and Design of Electrical Machines and Devices*, WIT Press, Southampton, UK, 1999.
- [81] Rosu M., Zhou P., Lin D., Ionel D., Popescu M., Blaabjerg F., Rallabandi V., Staton D., *Multiphysics Simulation by Design for Electrical Machines, Power Electronics and Drives*, Wiley-IEEE Press, New Jersey, USA, 2018.
- [82] Yao W., Jin J., Krein P. T., Magill M. P., A finite-element-based domain decomposition method for efficient simulation of nonlinear electromechanical problems, *IEEE Transactions Energy Conversion*, 2014, **29**(2), 309-319.
- [83] Demenko A., Wojciechowski R., Loop analysis of multi-branch, multi-node nonlinear circuits using singular formulation, *COMPEL - The international journal for computation and mathematics in electrical and electronic engineering*, 2009, **28**(3), pp. 691-699, 2009.
- [84] Vande-Sande H., Henrotte F., Hameyer K., The Newton-Raphson method for solving non-linear and anisotropic time-harmonic problems, *COMPEL - The international journal for computation and mathematics in electrical and electronic engineering*, 2004, **23**(4), 950-958.
- [85] Meier S., Hahn I., Modeling single and double stator axial eddy current brakes considering current displacement, magnetic leakage, fringing and saturation using coupled electric and magnetic equivalent circuits, *40<sup>th</sup> Annual Conference of the IEEE Industrial Electronics Society*, Dallas, TX, USA, 29 October -1 November 2014.
- [86] Nerg J., Rilla M., Pyrhonen J., Thermal analysis of radial-flux electrical machines with a high power density, *IEEE Transactions on Industrial Electronics*, 2008, **55**(10), 3543-3354.
- [87] Rostami N., Feyzi M. R., Pyrhönen J., Parviainen A., Niemela M., Lumped-parameter thermal model for axial flux permanent magnet machines, *IEEE Transactions on Magnetics*, 2013, **49**(3), 1178-1184.
- [88] Saari J., Thermal modelling of high-speed induction machines,” Ph.D. dissertation, Acta Polytechnica Scandinavica, Espoo, Finland, 1995.
- [89] Budynas R., Nisbett K., *Shigley’s Mechanical Engineering Design*, 8<sup>th</sup> ed., McGraw–Hill Primis, USA, 2006.
- [90] Hemeida A., Lehtikoinen A., Rasilo P. , Vansompel H., Belahcen A., Arkkio A., Sergeant P., A Simple and Efficient Quasi-3D Magnetic Equivalent Circuit for Surface Axial Flux Permanent Magnet Synchronous Machines, *IEEE Transactions on Industrial Electronics*, 2018, **Early Access**, DOI: 10.1109/TIE.2018.2884212.

- [91] Kennedy J., Eberhart E., Particle swarm optimization, *IEEE International Conference on Neural Networks*, Perth, WA, Australia, 27 November - 1 December 1995.
- [92] Coello C., Pulido G. T., Lechuga M. S., Handling multiple objectives with particle swarm optimization, *IEEE Transactions on Evolutionary Computation*, 2004, **8**(3), 256-279.
- [93] <https://www.kjmagnetics.com/bhcurves.asp> (Last visited: 15/06/2019)



## PUBLICATIONS AND WORKS

- [1] **Gulec M.**, Aydin M., Janne N., Lindh P., Pyrhönen J., Nonlinear Multidisciplinary Design Approach for Axial-Flux Eddy Current Brakes, *IEEE Transactions on Energy Conversion*, 2019, Accepted for publication, DOI: 10.1109/TEC.2019.2923675.
- [2] Boduroglu A., **Gulec M.**, Demir Y., Yolacan E., Aydin M., A New Asymmetric Planar V-Shaped Magnet Arrangement for A Linear PM Synchronous Motor, *IEEE Transactions on Magnetics*, 2019, **55**(7), ASN: 8105905.
- [3] Barış A., **Güleç M.**, Demir Y., Aydın M., Doğrusal Sürekli Mıknatıslı Senkron Motorun Doğrusal Olmayan Manyetik Eşdeğer Devre ve Sonlu Elemanlar Tabanlı Tasarımı, *EMO Bilimsel Dergi*, 2018, **8**(15), 97-102.
- [4] **Gulec M.**, Aydin M., Implementation of Different 2D Finite Element Modelling Approaches in Axial Flux Permanent Magnet Disc Machines, *IET Electric Power Applications*, 2018, **12**(2), 195-202.
- [5] Yildiriz E., **Gulec M.**, Aydin M., An Innovative Dual-Rotor Axial-Gap Flux-Switching Permanent-Magnet Machine Topology With Hybrid Excitation, *IEEE Transactions on Magnetics*, 2018, **54**(11), 1-5.
- [6] **Güleç M.**, Aydin M., Electromagnetic Brake System (Elektromanyetik Fren Sistemi in Turkish), Turkish Patent and Trade Mark Office, Registration No: 2016 08459 Granted Date: 2018/11/21.
- [7] **Gulec M.**, Aydin M., Lindh P., Pyrhönen J., Investigation of Braking Torque Characteristic for a Double-Stator Single-Rotor Axial-Flux Permanent-Magnet Eddy-Current Brake, *IEEE International Conference on Electrical Machines*, Dedeağaç, Greece, 3-6 September 2018.
- [8] **Gulec M.**, Yolacan E., Aydin M., Design and Comparison of Radial Flux Magnetic Levitation Systems Based on Conventional and Buried Permanent Magnet Types Rotors, *IEEE International Conference on Electrical Machines*, Dedeağaç, Greece, 3-6 September 2018.
- [9] **Gulec M.**, Yolacan E., Demir Y., Ocak O., Aydin M., Modeling based on 3D finite element analysis and experimental study of a 24-slot 8-pole axial-flux permanent-magnet synchronous motor for no cogging torque and sinusoidal back EMF, *Turkish Journal of Electrical Engineering & Computer Sciences*, 2016, **24**, 262-275.

- [10] Aydın M., **Gulec M.**, A New Coreless Axial Flux Interior Permanent Magnet Synchronous Motor with Sinusoidal Rotor Segments, *IEEE Transactions on Magnetics*, 2016, **52**(7), 1-5.
- [11] **Gulec M.**, Yolacan E., Aydın M., Design, Analysis and Real Time Dynamic Torque Control of Single-Rotor-Single-Stator Axial Flux Eddy Current Brake, *IET Electric Power Applications*, 2016, **10**(9), 869 – 876.
- [12] **Güleç M.**, Aydın M., Eksenel Akıllı Açık Oluklu bir Girdap Akım Freninde Doğrusal Olmayan Manyetik Modelleme Yöntemlerinin Karşılaştırılması", *Elektrik-Elektronik ve Bilgisayar Mühendisliği Sempozyumu*, Bursa, Turkey, 1-3 December 2016.
- [13] Aydın M., **Gulec M.**, Demir Y., Akyuz B., Yolacan E., Design and Validation of a 24-Pole Coreless Axial Flux Permanent Magnet Motor for A Solar Powered Vehicle, *IEEE International Conference on Electric Machines*, Lausanne, Switzerland, 4-7 September 2016.
- [14] **Gulec M.**, Aydın M., Modelling and Analysis of a New Axial Flux Permanent Magnet Biased Eddy Current Brake", *IEEE International Conference on Electric Machines*, Lausanne, Switzerland, 4-7 September 2016.
- [15] **Güleç M.**, Aydın M., Tek-Rotor Tek-Stator Yapısına Sahip Eksenel Akıllı Elektromanyetik Bir Frenin Modellenmesi, Analizi ve Gerçek Zamanda Moment Denetimi, *Otomatik Kontrol Türk Milli Komitesi Ulusal Konferansı*, Denizli, Turkey, 10-12 September 2015.
- [16] **Gulec M.**, Aydın M., 2D Finite Element Modelling Approach for Axial Flux Permanent Magnet Synchronous Motors, *IEEE International Magnetic Conference*, Beijing , Republic of China, 11-15 May 2015.
- [17] **Gulec M.**, Aydın M., Magnet asymmetry in reduction of cogging torque for integer slot axial flux permanent magnet motors, *IET Electric Power Applications*, 2014, **8**(5), 189-198.
- [18] Aydın M., **Gulec M.**, Reduction of Cogging Torque in Double-Rotor Axial-Flux Permanent-Magnet Disk Motors: A Review of Cost-Effective Magnet-Skewing Techniques with Experimental Verification, *IEEE Transactions on Industrial Electronics*, 2014, **61**(9), 5025-5034.
- [19] **Gulec M.**, Yolacan E., Aydın M., Design and control of an 8-slot radial flux magnetic bearing, *IEEE International Symposium on Power Electronics, Electrical Drives, Automation and Motion*, Ischia , Italy, 18-20 June 2014.
- [20] **Gulec M.**, Aydın M., Design and Simulation of an Axial Gap Electromagnetic Brake with Flux 3D FEA Package, *Flux Conference*, Munichen, Germany, 15-16 October 2014.

- [21] **Gulec M.**, Aydin M., Modelling and Design of Active Magnetic Bearings Based on Magnetic Circuit and 2D Finite Element Analysis, *International Conference on Research and Education in Mechatronics*, Vienna, Austria, 6-7 June 2013.
- [22] **Gulec M.**, Yolacan E., Aydin M., Radyal Bir Aktif Manyetik Yatak Tasarımı, Modellenmesi ve Bulanık Mantık ile Konum Denetimi, *Otomatik Kontrol Türk Milli Komitesi Ulusal Konferansı*, Malatya, Turkey 26-28 September 2013.
- [23] **Güleç M.**, Aydin M., Ocak O., Yolacan E., Sürekli Mıknatıslı Disk Motorların Tasarımı ve Üretimi, *Otomatik Kontrol Türk Milli Komitesi Ulusal Konferansı*, Niğde, Turkey, 11-13 October 2012.
- [24] **Gulec M.**, Aydin M., Influence of Magnet Grouping in Reduction of Cogging Torque for A Slotted Double-Rotor Axial-Flux PM Motor, *IEEE International Symposium on Power Electronics, Electrical Drives, Automation and Motion*, Sorrento, Italy, 19-22 June 2012.
- [25] **Güleç M.**, Aydin M., Manyetik Yatakların Manyetik Devre ve 2B Sonlu Elemanlar Yöntemi ile Modellenmesi ve Tasarımı, *Elektrik - Elektronik ve Bilgisayar Mühendisliği Sempozyumu*, Bursa, Turkey, 26 November-1 December 2012.



## **CURRICULUM VITAE**

Mehmet Güleç received the B.S. and M.S. degrees in mechatronics engineering from Kocaeli University, Kocaeli, Turkey, in 2010 and 2013, respectively. He is currently working as a Research Assistant at the Department of Mechatronics Engineering, Kocaeli University and a Visiting Researcher at the Laboratory of Electrical Drives Technology, Lappeenranta University of Technology, Lappeenranta, Finland and a R&D engineer at MST ArGe Ltd., which is a spin-off company from Mechatronics Engineering Department at Kocaeli University. His research interests include modeling, simulation and design of electromagnetic systems and mechatronics.

